Low-Reynolds-Number gravity-driven migration and deformation of bubble(s) and/or solid particle(s) near a deformable free surface

Marine Guemas

To cite this version:

Marine Guemas. Low-Reynolds-Number gravity-driven migration and deformation of bubble(s) and/or solid particle(s) near a deformable free surface. Fluid mechanics [physics.class-ph]. Ecole Doctorale Polytechnique, 2014. English. NNT : . tel-01137987

HAL Id: tel-01137987
https://theses.hal.science/tel-01137987v1

Submitted on 31 Mar 2015

École Polytechnique
Laboratoire d'Hydrodynamique

Thèse présentée pour obtenir le grade de

DOCTEUR DE L'ÉCOLE POLYTECHNIQUE
Spécialité : Mécanique

par

Marine Guémas

Low-Reynolds-Number gravity-driven migration and deformation of bubble(s) and/or solid particle(s) near a deformable free surface

Soutenue le 21 Novembre 2014 devant le jury composé de

M. Henry Power	rapporteur	University of Nottingham, Nottingham
M. Christophe Josserand	rapporteur	Université Pierre et Marie Curie, Paris
M. Eric Climent	examinateur	IMFT, Toulouse
M. Jean-Marc Flesselles	examinateur	Saint-Gobain Recherche, Aubervilliers
M. Huai-Zhi Li	examinateur	Université de Lorraine, Nancy
M. Franck Pigeonneau	directeur de thèse	Saint-Gobain Recherche, Aubervilliers
M. Antoine Sellier	directeur de thèse	École Polytechnique, Palaiseau
M. François Feuillebois	invité	LIMSI, Orsay

Remerciement

En premier lieu, j'aimerais remercier tous les membres du jury pour m'avoir fait l'honneur de participer à l'évaluation de mon travail de thèse. Merci à Henry Power et Christophe Josserand pour avoir accepter d'être rapporteur, à Huai-Zhi Li, Jean-Marc Flesselles et au président du jury Eric Climent pour avoir accepter d'examiner mon travail de thèse et à Francois Feuillebois en tant que membre invité pour avoir participé à la discussion finale qui fut, grâce à l'ensemble des questions posées par les membres du jury, passionnante.

Cette thèse a été financé par Saint-Gobain Recherche et je remercie mon responsable Saint-Gobain et codirecteur de thèse Franck Pigeonneau pour son implication et son soutient scientifique qui m'ont permit de mieux comprendre les enjeux industriels de cette thèse.

Un grand merci à mon codirecteur Antoine Sellier pour avoir dirigé mes travaux avec patience et humour tous au long de cette thèse ainsi que pour le soutient scientifique et moral dans les moments de doute. L'organisation du congrès BeTeQ 2013 fut une expérience humaine et scientifique très enrichissante.

Je remercie Emmanuelle Gouillart en tant que directrice du laboratoire Surface du Verre et Interface (SVI) de Saint-Gogain Recherche pour l'aspect scientifique du mélange réactionnel qu'est le verre, et pour m'avoir aidé à faire le lien entre la partie académique de ma thèse et l'interêt industriel. Merci à Jean-Marc Flesselles (Saint-Gobain Recherche) et à Christophe Clanet (LadhyX) pour leurs remarques et conseils lors de mes points de thèse.

Merci aussi à tous les permanents anciens et nouveaux du laboratoire SVI, Pierre Jop, Marie-Hélène Chopinet, Etienne Barthel, Davy Delmas, Serguei Grachev, Jérémie Teisseire, Irina Gozhyk, Alban Sauret, Ekaterina Burov, Hervé Montigaud pour les discussions autour des travaux de recherche en rapport au verre ce qui m'a permis de mieux comprendre la complexité de ce matériau, à Raphael et Emmanuel pour les discussions sécurités.

Merci aux thésards de SVI et EV, Corinne, William et Isabelle dont la vision chimiste m'ont beaucoup aidé à comprendre et compléter mes connaissances sur le verre.

Je remercie tous les membres permanents du LadhyX, les chercheurs et chercheuses et en particulier Camille Duprat, Jean-Marc Chomaz, Sabine Ortiz, Patrick Huerre, Charles Baroud, Emmanuelle De Langre et Lutz Lesshaft pour les discussions scientifiques enrichissantes. Merci aussi à l'équipe administrative, Delphine, Sandrine, Thérèse, Judith, Caroline et le service informatique Daniel et Toai sans qui cette thèse numérique n'aurait pas eu lieu. Merci aux thésards numéricien du LadhyX pour les conseils et le partage des *connaissances, merci Gaetan, Mathieu, Miguel, Juanluca, Franz, Fabien, Nicolas, Xavier, Eunok, Chakri.*

Dans un registre plus léger, j'aimerais remercier toutes les personnes du LadhyX pour l'ambiance conviviale et chaleureuse où les pauses café sont un endroits de plaisir, de partage et de rire.

Pour les discussions passionnantes en salle café et les débats, merci à David, Jérémy, Tonio et Sabine. À la team foot du labo, merci Caroline, Baptiste, Loic, Remi, Etienne, Adrien, Gaetan, Manu, Juno, Mathieu, Pierre-Brice, Philippe et Lionel, à la team footing Sabine, Eunok, Eline, Caroline Frot et Fabien. Pour les conseils de recherche d'emploi, merci Nicolas Dovetta. Merci à Avin pour les blagues, à Eline pour l'enthousiasme et à ma guide coréenne Eunok pour sa bonne humeur permanente.

Un grand merci à Sabine pour son soutient et réconfort tout au long de ma période de rédaction, ainsi qu'à mes collègues de bureau Eunok, Gaetan et Mathieu et aussi à Avin, Julie, Jeremy, Caroline C., Caroline F., Nicolas D., Franz et Etienne.

Merci à tous les membres de SVI sans exceptions pour les pauses cafés et la bonne humeur dans le laboratoire. Merci aux post-doc (ancien et nouveaux) de SVI, en particulier Jalila Boujlel pour ses connaissances sur le mélange, son réconfort et sa technique de gestion du stress lors de la rédaction. Un gros merci au thésards (ancien et nouveaux) de SVI et EV, à Corinne, Jean-Yvon, Barbara, Isabelle, William, Gauthier, Yann, Aymeric, Théo, Jean, Katia, Océane, Thomas pour les soirée cultures et restaurants mémorables et aussi pour le soutient mutuel lors de coup dur.

Un énorme merci à tous mes amis parisiens, Rachel, Jérome, Sarah, Armandine, Raphael, Julie, Julia, Tanguy, Victor, Anne, Théo, Valentin sans qui les sorties à Paris n'auraient pas eu la même saveur et surtout pour avoir supporté mes humeurs pendant ma dernière année de thèse.

Enfin, je voudrais remercier ma famille qui m'a toujours soutenue et encouragée pendant ces trois années, pour avoir organisé un sublime pot de thèse et avoir été présente pour ma soutenance sachant qu'elle était en anglais. Voir cette fierté dans vos yeux m'a vraiment fait comprendre à quel point ce jour était incroyable.

Merci aussi à mon compagnon Yohann qui a toujours été là, dans les moments de joie et les moments plus durs pour discuter, faire l'intendance, me rassurer.

Contents

Introduction

This thesis is related to industrial issues encountered in the glass melting process. Glass is industrially made in large tanks where chemical reactions occur to form a molten silicate at high temperature. This dynamics is indeed highly complex involving mass transfer, chemical reactions, two-phase or three phase flows. A huge quantity of bubbles with unmolten sand grains are then created. The remove of these impurities is achieved by increasing the temperature and adding chemical agents to either dissolve gases or further increase the bubble size to speed up the buoyancy effect. In certain conditions, a foam layer can occur at the top of the molten glass bath creating a thermal screen and reducing the energetic efficiency of glass furnaces [15]. The foam creation is a balance between the bubble source coming from the bulk (actually, the relevant quantity is the superficial gas velocity [27]) and lifetimes of bubble at the free surface of glass bath. Understanding and quantifying this complex balance is an important issue for the furnaces design.

Apart form the glass melting, phase separation is involved in other applications such as microfluidics [33]-[1], industrial extraction processes (oil and gases) [23], stabilizing foam and mixing in food engineering [4], volcano eruption [24]-[22], and so on. Behind these processes, the important scientific subject is the interaction of particles (bubbles, solid particles) with a free surface. The dynamics of bubbles (burst or coalescence) is the milestone of the phase separation. The main feature of this physics in the glass melting context is that the liquid is highly viscous (indeed molten glass at 1400°C is 10^4 times more viscous than water at 20°C!).

The film dynamics in Stokes flow has been extensively investigated through various purposes. Experimentally, the coalescence of a drop with a liquid-liquid interface has been examined by Hartland for the drop shape [10], the film thickness [11] and the film rupture [12] and it has been shown that the film thickness is non uniform the film being thinner at the edge of the drop. In the same spirit of the first work of Hartland, Princen [28] described carrefully the drop shape at a fluid-fluid interface. Using simple arguments, he predicted a thinning rate of the liquid film in the framework of lubrication theory initially developed by Reynolds [30]. Assuming a constant liquid film, he pointed out that the thinning rate is inversely proportional to the area of the spherical cap creating by the inclusion at the fluid-fluid surface. His work has been further extended by Hartland [13] by developing a local lubrication model. Later, Lin and Slattery [20] provided a new lubrication model showing the gradient of surfactant is enough to consider the immobilization of fluid-fluid interfaces. More recent works in the same spirit can be found in the book of Slattery et al. [31].

Previous works have been mainly focused in liquids with a moderate dynamic viscosity and for interface without mobility. In the case of a high viscous liquid and a shear free interface, the dynamics of liquid film drainage behaves differently. One of the first contributions, Debrégeas et al. [7] studied the drainage of bubble at the free surface of silicon oil. He showed that the liquid film decays exponentially with time. More recently, Kocarkova [17] and Kocarkova et al. [16] developed an experiment to study the drainage in molten glass. They found the exponential decrease of the liquid film. Moreover, an important effect of the bubble size has been also clearly observed and explained. Furthermore, unmolten silicate stuck between the bubble and the free surface have been also experimentally observed by Grynberg [8] in molten glass. Grynberg [8] have shown that the velocity of the bubbles rising toward the free surface is indeed affected by the solid bodies.

A large number of numerical and theoretical studies are also available in the interface dynamics.

Lee, Chadwick and Leal [19] examined the solid sphere interaction with a fluid-fluid interface and, appealing to the perturbation method called the method of reflections (see details in [9]), obtained the drag force and the hydrodynamic torque exerted on a solid sphere experiencing a rigid-body motion near the fluid-fluid interface. Similarly, a far-field approximation of the flow has been employed by Berdan and Leal [2] for a distant solid sphere interacting with a weakly disturbed free surface and these authors determined the corrected force and free surface shape using cylindrical coordinates. Moreover, the thermocapillary migration of a spherical bubble moving normally to a flat fluid-fluid interface has been investigated using the bipolar coordinates by Meyyappan and Wilcox [21]. Appealing to those coordinates introduced by Stimson and Jeffery [32], Meyyappan and Wilcox [21] obtained the zeroth-order flow solution (no interfaces deformation). In addition, an asymptotic expansion at small deformation in terms of the capillary number (the number comparing the viscous force to the capillary force) has been developed by Chervenivanova and Zapryanov [5] for a droplet moving toward a free surface using bipolar coordinates to obtain the corrected force and velocity. However, the theoretical work done in [5] exhibits a non zero slope of the interface at the $(z'Oz)$ axis and therefore the obtained results exhibits a non physical behavior.

Lee and Leal [18] numerically extended the work of Berdan and Leal for a solid sphere near a free surface using the boundary-integral formulation to determine the free surface shapes. A numerical study performed by Chi and Leal in [6] examines the case of a viscous deformable drop through a deformable interface combining the Boundary Element Method (BEM) with the lubrification theory. Manga [22] also appealed to the BEM to study bubbles passing through a fluid-fluid interface. The drainage of a bubble near a free surface has been examined by Howell [14] using a lubrication model but when restricting attention to a bidimensional bubble. Neglecting the gravity and assuming that the interface deformation is small, Howell [14] showed that for an axisymmetric bubble, the film drains as an algebraic function of time. The results obtained by Howell has been invalidated by the previously mentioned experimental results of Debrégeas [7] and by a recent numerical work of Pigeonneau and Sellier [26] which examined the bubble-free surface interaction and the time-dependent film thickness using the boundary-element method together with the lubrification theory. This last work has been achieved at different Bond number (the number comparing the gravity term to the surface tension term) for a bubble and a free surface having identical uniform surface tension. It confirmed that the film drainage exhibits an exponential decay in time. Moreover, the case of droplet interacting with a fluid-fluid interface has been investigated by Bonhomme and Magnaudet [3] using two kinds of numerical methods (the volume of fluid method and the phase field technique) and an experimental system. This last contribution is not limited to low-Reynolds-number flows.

Despite all available contributions, the interaction between bubble(s) and/or solid particle(s) close to a free surface has been poorly addressed. Unfortunately, such a case occurs in the melting glass process when unmolten grains of sand interact with bubble(s) near the surface of the glass bath. Moreover, the theory of particle or bubble immerged in a liquid near a surface are not fully understood. Since the surface tension in molten glass is actually dependent of the gas nature [25], the change of surface tension is an important issue to be investigated. Accordingly, the purpose of the thesis work is threefold: (i) Numerical analysis of rising bubbles with or without particles, (ii) theoretical system of a particle or a bubble in limit of small interface deformation (iii) bubble drainage behavior with unequal surface tensions.

In the present problem, the rising of bubble(s) and/or solid particle(s) driven by gravity toward a free surface in a highly viscous liquid has been therefore investigated before the interface breaks under the pressure exerted by the rising bubble (or solid particle).
The liquid is of high viscosity and the typical size of the particles is sufficiently small so that the Reynolds number is low as compared with unity. The flow is then governed by the Stokes equations which are the linearized counterpart of the more-involved Navier-Stokes equations. Since inertial effects are neglected, the interfacial dynamics is here only governed by the capillary forces modeled by the surface tension (taken uniform in the present problem), the gravity forces and the viscous forces induced by the flow. In practice, the Bond number compares the gravity term with the capillary term while the capillary number compares the viscous term with the capillary term. For particles with negligible inertia both numbers are of the same order of magnitude in the glass melting application.

As experiments in molten glass for several particles (bubbles and/or solid bodies) interacting with a free surface are difficult to perform, the present dynamics of bubble(s) and solid particle(s) near a free surface is here numerically investigated in 2d-axisymmetric configuration appealing to the Boundary Element Method. Furthermore, the limitating case of a vanishing Bond number has been asymptotically examined in case of one bubble or one solid particle near a free surface at small Bond number (interfaces being then weakly disturbed).

The present thesis consists in two parts. The first one examines the bubble-free surface interaction using a numerical approach and also the case of a bubble or a solid sphere near a free surface through an asymptotic analysis in 2D-axisymmetric configurations. The second part extends the numerical study of the first part to the case of $M \geq 1$ bubble(s) and $N \geq 1$ solid particle(s) near a free surface in 2d-axysimmetric configurations.

Chapter 1 addresses the problem of a bubble or a solid sphere rising toward a free surface interface. Two phenomena are then examined: the surface shape dynamics and the time-dependent thickness (so-called drainage) of the liquid film stuck between the bubble and the free surface. The conservation equations are formulated in the framework of Stokes regime. These general equations are completed with boundary conditions.

The numerical procedure is described in Chapter 2. The axisymmetric formulation of the boundary-integral equations is introduced. The scheme used to discretize these equations and to track in time the interfaces is presented. Furthermore, benchmark tests are performed to select suitable numerical parameters for the investigation of the bubble-free surface interaction.

Numerical results are displayed and discussed in Chapter 3. The sensitivity of the surface shapes and drainage to a change of surface tension is examined. The film thinning rate has then been calculated and compared against experimental results obtained in molten glass. In addition, from a relation between the contact area of the film and the film thinning rate, the predictions obtained using the Princen and Mason [29] model for a bubble-free surface hydrostatic system (the bubble and the free surface are in contact with a liquid film without thickness) and our "final"computed shapes are compared.

In Chapter 4 and Chapter 5, an asymptotic analysis is developed for a bubble or a solid sphere near a free surface when the surfaces are weakly deformed with the assumptions of small Bond and Capillary numbers. Chapter 4 introduces the perturbation method applied to asymptotically predict each interface shape and the flow versus the Bond number. The asymptotic analysis is restricted to the determination of the bubble and free surface shapes at a given bubble location. It is then checked and new results are given in Chapter 5.

In the second part, the case of bubble(s) and/or solid particle(s) near a free surface is numerically investigated in 2D-axisymmetric configurations.

Chapter 6 extends the boundary-integral formulation for the case of a cluster made of bubble(s) and/or solid particle(s) by appealing to relevant auxiliary flows. In Chapter 7, we presents numerical results for two particles (bubble(s) and/or solid body(ies)) interacting with a free surface. First, the case of two bubbles have been studied and the sensitivity to the computed shapes as well as the drainage to the change of surface tension has been examined. The case of two bubbles with different size is also investigated through the surface tension effect. Second, the challenging case of solid body(ies) pushed by a bubble near a free surface has been finally examined for different Bond number, solid body number and size.

Bibliography

[1] M. Abkarian, A. B. Subramaniam, S.-H. Kim, R. J. Larsen, S.-M. Yang, and H. A. Stone. Dissolution arrest and stability of particle-covered bubbles. *Phys. Rev. lett.*, 99(18):188301, 2007.

[2] C. Berdan and L. G. Leal. Motion of a sphere in the presence of a deformation interface. I. Perturbation of the interface from flat: The effects on drag and torque. *J. Colloid Interface Sci.*, 87:62–80, 1982.

[3] R. Bonhomme, J. Magnaudet, F. Duval, and B. Piar. Inertial dynamics of air bubbles crossing a horizontal fluid-fluid interface. *J. Fluid Mech.*, 707:405–443, 9 2012.

[4] I. Cantat, S. Cohen-Addad, F. Elias, F. Graner, R. Höhler, O. Pitois, F. Rouyer, A. Saint-Jalmes, et al. *Les Mousses : structure et dynamique*. Belin, August 2010.

[5] E. Chervenivanova and Z. Zapryanov. On the deformation of two droplets in a quasisteady Stokes flow. *Int. J. Multiphase Flow*, 11:721–738, 1985.

[6] B. K. Chi and L. G. Leal. A theoretical study of the motion of a viscous drop toward a fluid interface at low Reynolds number. *J. Fluid Mech.*, 201:123–146, 1989.

[7] G. Debrégeas, P.-G. de Gennes, and F. Brochard-Wyart. The life and death of “bare” viscous bubbles. *Science*, 279:1704–1707, 1998.

[8] J. Grynberg. *Mécanismes physiques et chimiques mis en jeu lors de la fusion du mélange SiO2-Na2CO3.* PhD thesis, Université Pierre et Marie Curie - Paris VI, 2012.

[9] J. Happel and H. Brenner. *Low Reynolds number hydrodynamics.* Martinus Nijhoff Publishers, The Hague, 1983.

[10] S. Hartland. The coalescence of a liquid drop at a liquid-liquid interface. Part I: Drop shape. *Trans. Instn Chem. Engrs*, 45:T97–T101, 1967.

[11] S. Hartland. The coalescence of a liquid drop at a liquid-liquid interface. Part II: Film thickness. *Trans. Instn Chem. Engrs*, 45:T102–T108, 1967.

[12] S. Hartland. The coalescence of a liquid drop at a liquid-liquid interface. Part III: Film rupture. *Trans. Instn Chem. Engrs*, 45:T109–T114, 1967.

[13] S. Hartland. The profile of the draining film between a fluid drop and a deformable fluid-liquid interface. *Chem. Eng. J.*, 1:67–75, 1970.

[14] P. D. Howell. The draining of a two-dimensional bubble. *Journal of Engineering Mathematics*, 35:251–272, 1999.

[15] J. Kappel, R. Conradt, and H. Scholze. Foaming behaviour on glass melts. *Glastech. Ber.*, 60:189–201, 1987.

[16] H. Kočárková, F. Rouyer, and F. Pigeonneau. Film drainage of viscous liquid on top of bare bubble: Influence of the bond number. *Phys. Fluids*, 25(2):022–105, 2013.

[17] H. Kočárková. *Stabilité des mousses de verre: Expériences à l’échelle d’une bulle ou d’un film vertical.* PhD thesis, Université Paris-Est, 2011.

[18] L.G. Leal and S.H. Lee. The motion of a sphere in the presence of a deformable interface. ii. a numerical study of the translation of a sphere normal to an interface. *J. Colloid Interface Sci.*, 87(1):61 – 81, 1982.

[19] S.H. Lee, R.S. Chadwick, and L.G. Leal. Motion of a sphere in the presence of a plane interface. part 1. an approximate solution by generalization of the method of lorentz. *J. Fluid Mech.*, 93(04):705–726, 1979.

[20] C.-Y. Lin and J.C. Slattery. Thinning of a liquid film as a small drop or bubble approaches a solid plane. *AIChE J.*, 28(1):147–156, 1982.

[21] R. Shankar Subramanian M. Meyyeppan, W. R. Wilcox. Thermocapillary migration of a bubble normal to a plane surface. *J. Colloid Interface Sci.*, 83:199–208, 1981.

[22] M. Manga. *the motion of deformable drops and bubbles at low Reynolds numbers: Application to selected problems in geology and geophysics.* PhD thesis, Harvard University, 1994.

[23] A. Nguyen and H.J. Schulze. *Colloidal Science of Flotation.* Surfactant Science. CRC Press, 2003.

[24] C. T. Nguyen, H. M. Gonnermann, Y. Chen, C. Huber, A. A. Maiorano, A. Gouldstone, and J. Dufek. Film drainage and the lifetime of bubbles. *Geochemistry, Geophysics, Geosystems*, 14(9):3616–3631, 2013.

[25] V. I. Nizhenko and Yu. I. Smirnov. Surface phenomena and interfacial interaction at the glass-liquid tin-gas phase interface. *Powder Metallurgy and Metal Ceramics*, 42(3-4):171–179, 2003.

[26] F. Pigeonneau and A. Sellier. Low-Reynolds-Number gravity-driven migration and deformation of bubbles near a free surface. *Phys. Fluids*, 23:092302, 2011.

[27] Laurent Pilon. *Foams in Glass Manufacturing*, pages 355–409. John Wiley & Sons, Ltd, 2012.

[28] H. M. Princen. Shape of a fluid drop at a liquid-liquid interface. *J. Colloid Interface Sci.*, 18:178–195, 1963.

[29] H. M. Princen and S.G. Mason. Shape of a fluid drop at a liquid-liquid interface. I. Extension and test of two-phase theory. *J. Colloid Interface Sci.*, 20(2):156–172, 1965.

[30] O. Reynolds. On the theory of lubrication and its application to mr. beauchamp tower's experiments, including an experimental determination of the viscosity of olive oil. *Proceedings of the Royal Society of London*, 40(242-245):191–203, 1886.

[31] J. C. Slattery, L. Sagis, and E.-S. Oh. *Interfacial Transport Phenomena.* Springer, 2007.

[32] M. Stimson and G. B. Jeffery. The motion of two spheres in a viscous fluid. *Prod. R. Soc. London, Serie A*, 111:110–116, 1926.

[33] H.A. Stone and S. Kim. Microfluidics: basic issues, applications, and challenges. *AIChE J.*, 47(6):1250–1254, 2001.

Part I

One bubble interacting with a free surface

Chapter 1

Governing Problem and advocated boundary approach

Contents

In this chapter, we introduce the problem of a bubble immersed in a viscous flow and rising toward a free surface in a 2d axisymmetric configuration. Assuming that the Reynolds number is small, we give the governing equations and the corresponding boundary-integral equations. These equations are solved using a boundary integral technique in Chapter 2.

1.1 Addressed time-dependent problem

In this chapter, we focus on a bubble immersed in a Newtonian fluid flow and driven by buoyancy forces toward a free surface.

As sketched in Figure 1.1, we consider the 2d-axisymmetric geometry of a bubble B_1 immersed in a time-dependent Newtonian fluid occupying the domain $\mathcal{D}(t)$ with uniform density ρ_l and viscosity μ bounded by a free surface and subject to a uniform gravity field $\mathbf{g} = -g\mathbf{e}_z$ with magnitude $g > 0$. The ambient fluid above the free surface is a gas with uniform pressure p_0 and both the temperature T_1 and the pressure p_1 inside the bubble are assumed to be uniform and time-independent. The bubble surface $S_1(t)$ and the free surface $S_0(t)$ have uniform surface tension $\gamma_1 > 0$ and $\gamma_0 > 0$, respectively. These surface tensions γ_0 and γ_1 are not necessarily equal (see Chapter 3).

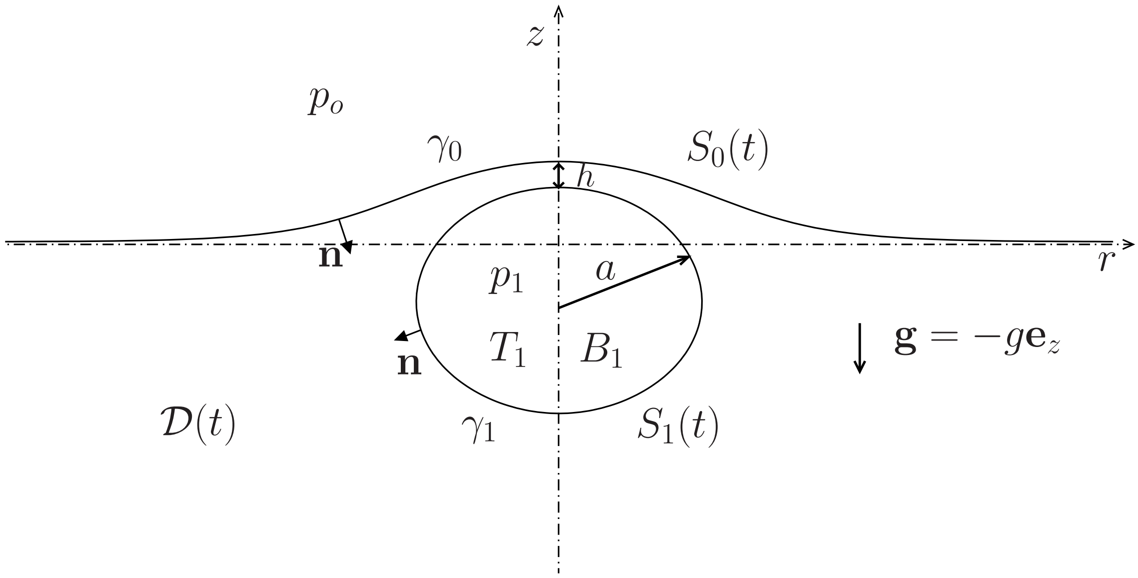

Figure 1.1: A bubble B_1 ascending, under a uniform gravity field $\mathbf{g}$ toward a free surface $S_0(t)$.

As buoyancy effects drive the bubble toward the free surface, the shape of each surface evolves in time. At initial time, the bubble is distant and spherical with radius a while the free surface is the $z = 0$ plane. At any time t, the deformed bubble surface $S_1(t)$ and free surface $S_0(t)$ are axisymmetric having identical axis of revolution parallel with the gravity $\mathbf{g}$. The distance between the bubble surface and the free surface is denoted by h along the z axis.

The Reynolds number Re is a dimensionless quantity defined as the ratio of the inertial force to viscous force which allows us to characterize different flow regimes and is here expressed as follows

$$\mathrm{Re} = \frac{\rho_l U a}{\mu} \tag{1.1}$$

with $U = \rho_l g a^2/3\mu$ the typical velocity of a spherical bubble with radius a rising through a liquid in an infinite domain and which is also the typical magnitude of the liquid velocity in our problem.

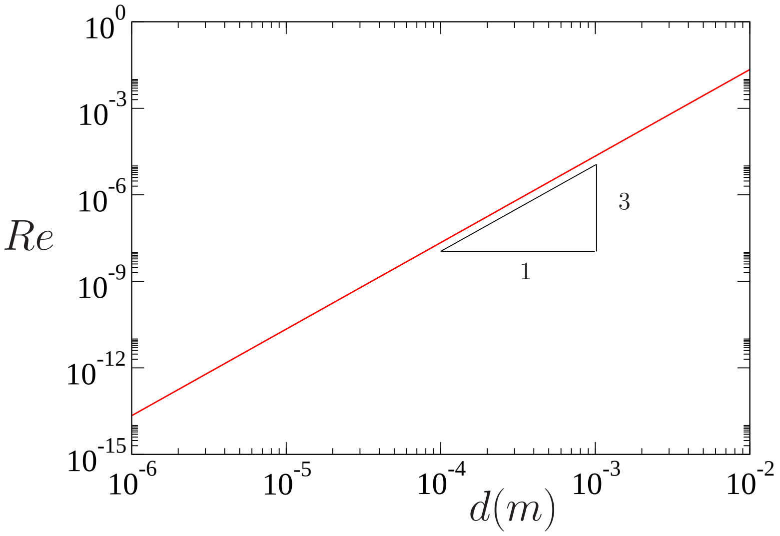

Figure 1.2: Case of the unbounded molten glass: Reynolds number $\mathrm{Re} = \rho_l^2 g a^3/3\mu^2$ versus the bubble diameter d in meters.

The Reynolds number Re is calculated from (1.1) versus the bubble diameter d (in meter) and the result is depicted in Figure 1.2 in the case of a molten glass of viscosity 10 Pa.s (at 1400°C) and density $\rho_l = 2350$ kg.m^{-3} for which the bubble sizes usually observed lie in the range $10^{-6}\,m < d < 10^{-2}\,m$.

Note that the Reynolds number is small in the molten glass, i.e. $\mathrm{Re} \ll 1$. Accordingly the viscous terms here dominate and all inertial effects are neglected.

As the bubble rises through the fluid, two different regimes are experimentally observed in [12]: first the bubble is not sensitive to the free surface and experiences a free ascension in the surrounding liquid, then the bubble motion is reduced by the free surface. Such a second step corresponds to the drainage of the film between the bubble and the free surface.

Note that one here investigates a time-dependent problem by tracking in time the interface evolution. This is achieved by appealing to the linear Stokes equations in axisymmetric configuration. Furthermore, one assumes a dynamic equilibrium of the bubble-free surface interfaces at each time step. Therefore, it is needed to solve the steady Stokes equations to precisely obtain the interfaces at each time step.

1.2 Formulation at each time step

The liquid surrounding the bubble is isotherm, incompressible and Newtonian. It has velocity $\mathbf{u}$, density ρ_l, viscosity μ and pressure P. Since ρ_l is uniform (homogeneous liquid) the mass continuity equation reads

$$\nabla \cdot \mathbf{u} = 0 \quad \text{in } \mathcal{D}(t). \tag{1.2}$$

In the limit of small Reynolds number (see previous section §1.1) the convective acceleration term $\mathbf{u} \cdot \nabla \mathbf{u}$ is neglected compared with the viscous term $\mu \nabla^2 \mathbf{u}$. In addition, we assume quasi-steady deformations of the bubble and the free surface. Then the usual unsteady Navier-Stokes equations governing the flow $(\mathbf{u}, p)$ are replaced with the following quasi-steady Stokes equations

$$\boldsymbol{\nabla} \cdot \mathbf{u} = 0 \quad \text{and} \quad \mu \boldsymbol{\nabla}^2 \mathbf{u} = \boldsymbol{\nabla} P + \rho_l \mathbf{g} \quad \text{in } \mathcal{D}(t). \tag{1.3}$$

For the Newtonian liquid, the stress tensor $\boldsymbol{\sigma}$ reads

$$\boldsymbol{\sigma} = -P\mathbf{I} + \mu \left(\boldsymbol{\nabla}\mathbf{u} + \boldsymbol{\nabla}\mathbf{u}^T \right) \tag{1.4}$$

with $\mathbf{I}$ the 3x3 identity matrix. Setting $\mathbf{x} = \mathbf{OM}$ and

$$P = p + \rho_l \mathbf{g} \cdot \mathbf{x} \tag{1.5}$$

with p the so-called dynamic pressure, one then arrives for $(\mathbf{u}, p)$ at the steady Stokes equations

$$\boldsymbol{\nabla} \cdot \mathbf{u} = 0 \quad \text{and} \quad \mu \boldsymbol{\nabla}^2 \cdot \mathbf{u} = \boldsymbol{\nabla} p \ \ \text{in } \mathcal{D}(t). \tag{1.6}$$

Finally, boundary conditions are required to solve the aforementioned Stokes equations (1.6). Far from the bubble the liquid is at rest. One then requires that

$$(\mathbf{u}, p) \to (\mathbf{0}, 0) \text{ as } |\mathbf{x}| \to \infty. \tag{1.7}$$

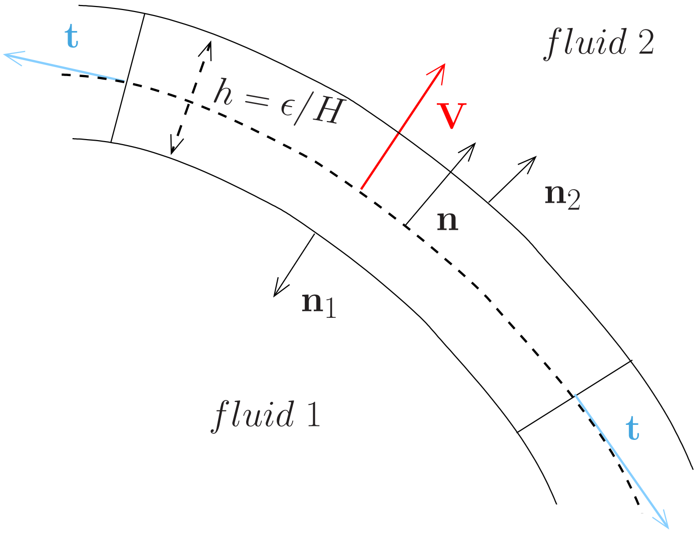

Figure 1.3: Surface layer between two fluids with H the mean curvature and a typical thickness $h = \epsilon/H$.

The bubble and free surfaces are gas-liquid interfaces. Since the physical properties are different in a gas and in a liquid, the pressure and velocity must satisfy a jump at those boundaries. Consider, as sketched in Figure 1.3, an ideal surface layer between two fluids with a typical thickness h small compared to $1/H$ with H the surface mean curvature. The tangent vector $\mathbf{t}$ at the interface and the unit normal $\mathbf{n}_1$ and $\mathbf{n}_2$ are directed into the fluid 1 and the fluid 2, respectively. If h tends to zero, one gets a interface with the material velocity vector $\mathbf{V}$ and a unit normal vector $\mathbf{n}$ directed from the fluid 1 to the fluid 2 selected so that H is positive. Designating the stress jump at the interface as $[\![\,\boldsymbol{\sigma}\,]\!]\cdot\mathbf{n} = (\boldsymbol{\sigma}_2 - \boldsymbol{\sigma}_1)\cdot\mathbf{n}$ with $\boldsymbol{\sigma}_2$ and $\boldsymbol{\sigma}_1$ the stress tensors in the liquid phase and the gaseous phase, respectively, the fundamental stress jump condition given in [11] then writes

$$[\![\,\boldsymbol{\sigma}\,]\!]\cdot\mathbf{n} + \mathbf{grad}_S[\gamma] - \gamma(\boldsymbol{\nabla}_S\cdot\mathbf{n})\mathbf{n} = 0 \quad \text{on } \Sigma_i(\mathcal{D}) \tag{1.8}$$

where $\mathbf{grad}_S = (\mathbb{1} - \mathbf{nn})\cdot\mathbf{grad}$ is the surface gradient, $-[\boldsymbol{\nabla}_S\cdot\mathbf{n}]/2 = H$ is the local average curvature with $\boldsymbol{\nabla}_S\cdot\mathbf{n}$, the surface divergence of the unit normal $\mathbf{n}$ and γ denotes the surface tension.

Assuming a uniform surface tension γ on the interface, $\mathbf{grad}_S[\gamma]$ vanishes and since $\boldsymbol{\sigma}_1$ the stress tensor of the gaseous phase is $\boldsymbol{\sigma}_1 = -p_m\,\mathbf{I}$, one then arrives at

$$\boldsymbol{\sigma}\cdot\mathbf{n} = (\rho_l\mathbf{g}\cdot\mathbf{x} - p_m + \gamma_m\boldsymbol{\nabla}_S\cdot\mathbf{n})\,\mathbf{n} \quad \text{on } S_m \text{ for } m = 0,1 \quad . \tag{1.9}$$

Recall here that our liquid flow has velocity $\mathbf{u}$, pressure $p + \rho_l\mathbf{g}\cdot\mathbf{x}$ and stress tensor $\boldsymbol{\sigma} - (\rho_l\mathbf{g}\cdot\mathbf{x})\,\mathbf{I}$ with $\boldsymbol{\sigma} = \boldsymbol{\sigma}_2$. The far-field behavior for $(\mathbf{u}, p)$ shows that the pressure p_0 above the interface vanishes far from the bubble-free surface interaction. This implies that $p_0 = 0$ everywhere. Moreover, appealing to (1.9), the force exerted on the bubble surface S_1 is (because p_1 and γ_1 are uniform)

$$\int_{S_1}\boldsymbol{\sigma}\cdot\mathbf{n}\,dS - \int_{S_1}(\rho_l\mathbf{g}\cdot\mathbf{x})\cdot\mathbf{n}\,dS = \gamma_1\int_{S_1}(\boldsymbol{\nabla}_S\cdot\mathbf{n})\,\mathbf{n}\,dS\,. \tag{1.10}$$

In addition, $\int_{S_1}(\boldsymbol{\nabla}_S\cdot\mathbf{n})\mathbf{n}\,dS = 0$[1] for a closed surface S_1.

Consequently, (1.10) implies that

$$\int_{S_1}\boldsymbol{\sigma}\cdot\mathbf{n}\,dS = \rho_l V_b\mathbf{g} \tag{1.15}$$

---

[1] Having $\mathcal{C}$, the entire contour of $\partial\mathcal{D}_l$ closed with $\mathbf{t}$ its normal vector oriented to the outside of $\partial\mathcal{D}_l$. Therefore, on each point of $\mathcal{C}$ is applied a linear density stress $\gamma\mathbf{t}$ with γ the constant surface tension forces such as

$$\oint_{\mathcal{C}}\gamma\mathbf{t}\,dl = \int_{\Sigma(\mathcal{D})}\gamma(\boldsymbol{\nabla}_S\cdot\mathbf{n})\mathbf{n}\,dS \tag{1.11}$$

with $\Sigma(\mathcal{D})$ the entire surface.

Let us consider a sphere separated in two hemispheres of surface S_1 and S_2, respectively with the associated tangents vectors t_1 and t_2 defined as follows

$$\mathbf{t}_1 = -\mathbf{e}_z \quad \text{on } S_1\,, \qquad \mathbf{t}_2 = \mathbf{e}_z \quad \text{on } S_2. \tag{1.12}$$

Recalling (1.11), one obtains

$$\oint_{\mathcal{C}}\gamma\mathbf{t}\,dl = \oint_{\mathcal{C}_1}\gamma\,\mathbf{e}_z dl - \oint_{\mathcal{C}_2}\gamma\mathbf{e}_z\,dl = 0. \tag{1.13}$$

One therefore demonstrates that the surface divergence equal zero on a closed surface S

$$\int_{\Sigma(\mathcal{D})}\gamma(\boldsymbol{\nabla}_S\cdot\mathbf{n})\mathbf{n}\,dS = 0 \tag{1.14}$$

with V_b the bubble volume.

There is no liquid transfer accross the bubble surface S_1 and the free surface S_0. Accordingly, the normal component of the fluid velocity here satisfies the boundary conditions

$$\mathbf{V} \cdot \mathbf{n} = \mathbf{u} \cdot \mathbf{n} \quad \text{on } S_m \text{ for } m = 0, 1 \tag{1.16}$$

with $\mathbf{V}$ the material velocity on each surface S_m.
Assuming a constant bubble volume, one also requires that

$$\int_{S_m} \mathbf{u} \cdot \mathbf{n}\, dS = 0 \quad \text{on } S_m \text{ for m=0,1.} \tag{1.17}$$

The $m = 1$ case holds because of (1.16) on S_1 and the conservation of the bubble volume while the case $m = 0$ is subsequently obtained by using (1.2) and (1.7)[2].

For symmetry reasons, the hydrodynamic force $\mathbf{F}$ exerted on the bubble migrating near the free surface takes the following form

$$\mathbf{F} = \int_{S_1(t)} \boldsymbol{\sigma} \cdot \mathbf{n}\, dS = -4\pi\mu U a \lambda\, \mathbf{e}_z \tag{1.20}$$

with $U > 0$ the typical bubble velocity and $\lambda > 0$ a so-called drag coefficient which of course depends upon the bubble shape and location.

Finally, neglecting the bubble inertia, one requires a force-free bubble (it is for symmetry reasons also torque-free [18]) at any time. Accordingly, the following additional relation is requested

$$\int_{S_1(t)} \boldsymbol{\sigma} \cdot \mathbf{n}\ dS - \rho_l V_b \mathbf{g} = \mathbf{0} \tag{1.21}$$

with $V_b = 4\pi a^3/3$ the constant volume of the bubble and a the bubble radius at initial time. Observe that this relation turns out to be (1.15). Substituting V_b by its expression and recalling (1.20), we obtain

$$\mu U \lambda = \frac{\rho_l g a^2}{3}. \tag{1.22}$$

Note that (1.22) holds at any time.

---

[2] Indeed, the unsteady mass continuity equation writes

$$\frac{d}{dt}\left(\int_{\mathcal{D}(t)} \rho_l d\Omega\right) = \int_{\mathcal{D}(t)} \frac{\partial \rho_l}{\partial t} d\Omega + \int_{\mathcal{D}(t)} \rho_l (\mathbf{u} \cdot \mathbf{n}) dS \tag{1.18}$$

Since the liquid has constant mass and density ρ_l, one gets

$$\frac{d}{dt}\left(\int_{\mathcal{D}(t)} \rho_l d\Omega\right) = \rho_l \int_{S_0 \cup S_1} \mathbf{u} \cdot \mathbf{n} dS \tag{1.19}$$

because $|\mathbf{u}|$ decays at infinity to zero (using (1.6) and (1.7)) sufficiently fast.

Summary of the advocated problem

In the addressed problem, the dynamics of each interface (bubble boundary and free surface) in time is sought by tracking in time the entire boundary $\partial\mathcal{D} = S_0 \cup S_1$ for a bubble ascending toward a free surface. To summarizep, at each time step, one solves the following steady Stokes equations and far-field behavior

$$\boldsymbol{\nabla}\cdot\mathbf{u} = 0, \quad \mu\boldsymbol{\nabla}^2\mathbf{u} = \boldsymbol{\nabla}p \;\text{ in } \mathcal{D}(t), \qquad (\mathbf{u}, p) \to (\mathbf{0}, 0) \text{ as } |\mathbf{x}| \to \infty. \tag{1.23}$$

The boundary condition at each interface also provides the traction there using the relations

$$\boldsymbol{\sigma}\cdot\mathbf{n} = (\rho_l\mathbf{g}\cdot\mathbf{x} - p_m + \gamma_m\boldsymbol{\nabla}_S\cdot\mathbf{n})\,\mathbf{n} \quad \text{on } S_m \text{ for } m = 0, 1 \tag{1.24}$$

where we take $p_0 = 0$. Finally, when $(\mathbf{u}, p)$ has been obtained, one gets the normal component of the material velocity $\mathbf{V}$ on each surface through the relation

$$\mathbf{V}\cdot\mathbf{n} = \mathbf{u}\cdot\mathbf{n} \quad \text{on } S_m \text{ for } m = 0, 1. \tag{1.25}$$

Enforcing a time-independent bubble volume, one also gets the additional relations

$$\int_{S_m} \mathbf{u}\cdot\mathbf{n}\, dS = 0 \;\text{ on } S_m \text{ for m=0,1.} \tag{1.26}$$

As already observed, the boundary condition (1.24) on the bubble surface S_1 also yields to the condition of force-free bubble

$$\int_{S_1(t)} \boldsymbol{\sigma}\cdot\mathbf{n}\; dS - \rho_l V_b\mathbf{g} = \mathbf{0}. \tag{1.27}$$

It is interesting to remark that whereas Stokes equations are linear equations, non linear terms still occur at the boundary through the $(\boldsymbol{\nabla}_S\cdot\mathbf{n})\mathbf{n}$ term which needs to be carefully investigated.

Normalized Problem

In the case of a non-deformable(spherical) bubble translating in an *unbounded* viscous liquid at the velocity $U\mathbf{e}_z$, [9]-[20] predicts that $\lambda = 1$. Therefore, a non-deformable bubble migrates far from the free surface under the uniform gravity $\mathbf{g} = -g\mathbf{e}_z$ at the velocity $U_\infty\mathbf{e}_z$ with $U_\infty = \rho_l g a^2/(3\mu)$. The stress jump boundary conditions (1.9) are

$$\boldsymbol{\sigma}\cdot\mathbf{n} = (\gamma_m\boldsymbol{\nabla}_s\cdot\mathbf{n} + \rho_l\mathbf{g}\cdot\mathbf{x} - p_m)\,\mathbf{n} \quad \text{on } S_m \text{ for } m = 0, 1 \tag{1.28}$$

with p_1 the pressure inside the bubble and p_0 the ambient pressure above the interface which is here $p_0 = 0$. We introduce the dimensionless quantities, normalized by the particle diameter $d = 2a$ as follows

$$\boldsymbol{\sigma} \equiv \frac{\mu U}{d}\overline{\boldsymbol{\sigma}}\,, \qquad \mathbf{u} \equiv \;\; U\overline{\mathbf{u}}\,, \qquad \boldsymbol{\nabla}_s \equiv \frac{\overline{\boldsymbol{\nabla}_s}}{d}\,, \qquad \mathbf{x}\cdot\mathbf{e}_z \equiv d\,z. \tag{1.29}$$

Substituting the normalized variables in (1.28), we obtain the normalized stress jump boundary condition

$$\mu U\,\overline{\boldsymbol{\sigma}}\cdot\mathbf{n} = [\gamma_m\,(\overline{\boldsymbol{\nabla}_s}\cdot\mathbf{n}) - \rho_l g d^2\, z - d\, p_m]\cdot\mathbf{n} \text{ on } S_m \text{ for } m = 0, 1 \tag{1.30}$$

where $d\,p_m = \mu U \gamma_1 \overline{p}_m$ are the constant normalized pressure quantities. For further convenience, we henceforth remove the bar above the normalized terms and consider that from now, one only deals with normalized equations. The relation (1.30) on the free surfaces becomes

$$\boldsymbol{\sigma} \cdot \mathbf{n} = \frac{1}{\mathrm{Ca}_0} \left(-12\, \mathrm{Bo}_0\, z + \boldsymbol{\nabla}_S \cdot \mathbf{n} \right) \mathbf{n} \quad \text{on } S_0 \tag{1.31}$$

and in a similar fashion, expresses on the bubble as

$$\boldsymbol{\sigma} \cdot \mathbf{n} = \frac{1}{\mathrm{Ca}_1} \left(-12\, \mathrm{Bo}_1\, z - p_1 + \boldsymbol{\nabla}_S \cdot \mathbf{n} \right) \mathbf{n} \quad \text{on } S_1 \tag{1.32}$$

where we introduced five dimensionless numbers. The first one, the Bond number Bo_0, associated with the surface tension of the free surface γ_0 compares the gravity term $(\rho_l \mathbf{g} \cdot \mathbf{x}) \cdot \mathbf{n}$ with the capillary term $\gamma_0 (\boldsymbol{\nabla}_S \cdot \mathbf{n})\, \mathbf{n}$. The second one is the capillary number Ca_0 based on the free surface comparing the viscous term $\boldsymbol{\sigma} \cdot \mathbf{n}$ with the capillary term $\gamma_0 (\boldsymbol{\nabla}_S \cdot \mathbf{n})\, \mathbf{n}$. Taking d as typical length and U as velocity scale, these numbers actually read

$$\mathrm{Bo}_0 = \frac{\rho_l g a^2}{3 \gamma_0}, \quad \mathrm{Ca}_0 = \frac{\mu U}{\gamma_0}. \tag{1.33}$$

Two additionnal Bond number Bo_1 and capillary number Ca_1, both based on the bubble surface tension γ_1, are also introduced as

$$\mathrm{Bo}_1 = \frac{\rho_l g a^2}{3 \gamma_1}, \quad \mathrm{Ca}_1 = \frac{\mu U}{\gamma_1}. \tag{1.34}$$

Finally, we also introduce the surface tension ratio $\hat{\gamma}$ as

$$\hat{\gamma} = \frac{\gamma_0}{\gamma_1}, \ \gamma_1 > 0 \tag{1.35}$$

Of course, the capillary numbers Ca_0, Ca_1 and Bond numbers Bo_0, Bo_1 are related through the surface tension ratio $\hat{\gamma} = \gamma_0 / \gamma_1$ using the relations

$$\mathrm{Bo}_0 = \frac{\mathrm{Bo}_1}{\hat{\gamma}}, \quad \mathrm{Ca}_0 = \frac{\mathrm{Ca}_1}{\hat{\gamma}}. \tag{1.36}$$

Note that for a bubble rising through an *unbounded* liquid at velocity $U_\infty = \rho_l g a^2 / (3\mu)$, one gets $\mathrm{Bo}_{1\infty} = \mathrm{Ca}_{1\infty}$ (similarly $\mathrm{Bo}_{0\infty} = \mathrm{Ca}_{0\infty}$) while the drag force coefficient is $\lambda_b = 1$. According to the force balance (1.22) on the bubble, the Bond number is actually related in the addressed problem to the Capillary number since $\lambda_b U \mu = \rho_l g a^2 / 3$. More precisely, one obtains

$$\mathrm{Bo}_1 = \lambda_b\, \mathrm{Ca}_1, \quad \mathrm{Bo}_0 = \lambda_b\, \mathrm{Ca}_0. \tag{1.37}$$

As the bubble approaches and is slowed down by the free surface $U < U_\infty$, the dimensionless drag $\lambda_b > 1$ is of order unity. Moreover, at any time $\lambda_b \geq \mathcal{O}(1)$ implying that $\mathrm{Ca}_1 \leq \mathcal{O}(\mathrm{Bo}_1)$. Therefore, we will take in practice three dimensionless parameters: $\hat{\gamma}$, Bo_0 (on Ca_0) and Bo_1 (on Ca_1).

1.3 Boundary formulation and resulting relevant boundary -integral equation

Before describing the boundary and numerical method used in this work, a review of the various techniques to compute multiphase flows is presented below.

1.3.1 Numerical method to track a time-dependent interface

A large choice of numerical methods is available to perform a careful investigation in time of the bubble and fluid interface surfaces or more generally to simulate multiphase flows.

An interface motion is mostly characterized using either an explicit treatment as the so-called front-tracking method or an implicit method such as volume of fluid, level-set and phase field techniques.

(i) In the front-tracking method, a stationary grid is used for fluids while the interface is tracked by a separate grid. In addition, this technique treats the two phases as the whole.

This scheme introduced by Unverdi and Tryggvason in [25] is a powerful method which handles a large number of grid points [6] and therefore accurately deals with a complex geometry of the interface. In addition, the explicit treatment of the boundary ensures that spurious current, non physical interface motion which are usually observed in the implicit method during the interface reconstruction steps, do not appear and implies the front-tracking to be a quite robust method.

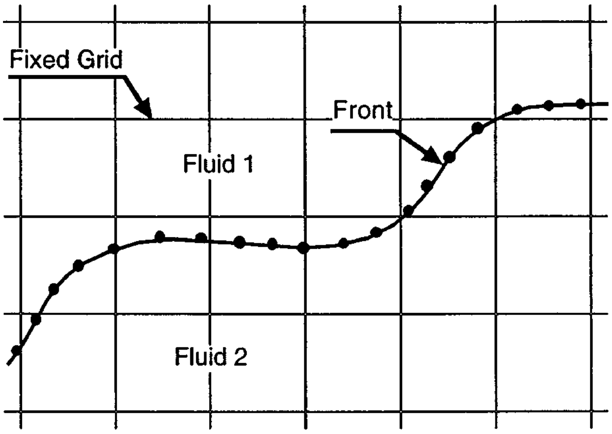

Figure 1.4: Front tracking for a two-phase flow problem on a fixed grid and a phase boundary where the moving interface consists of connected marker points [25].

Nevertheless, the continuous interaction between the stationary grid and the interface grid requires dynamical remeshing of the interface grid (as the computation proceeds) and therefore increases the computation time. Moreover, the explicit treatment of the interface does not handle topological changes such as coalescence or break up of the boundary [24]-[22].

In contrast, implicit methods do not require to rebuild the interface at each time step as is needed for the front-tracking method. These techniques represent indeed the boundary with a marker function.

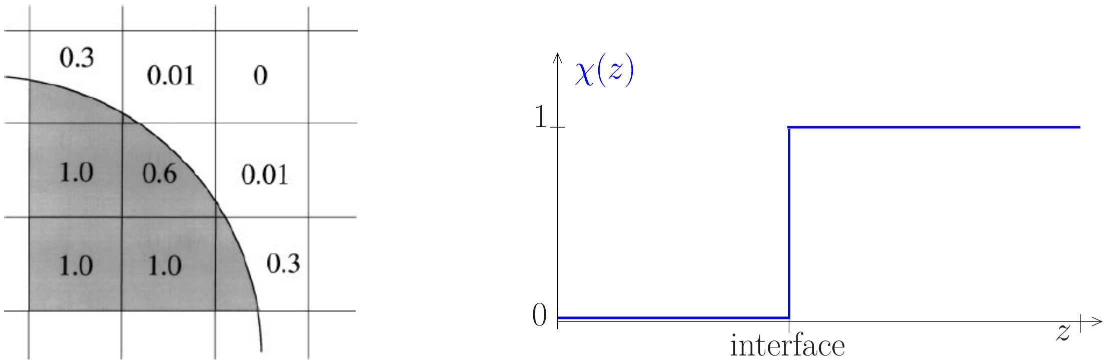

(a) The exact volume-of-fluid color function for a smooth circular arc over a square grid [21].

(b) The indicator function $\chi(x, y, z, t)$ versus z at an interface.

Figure 1.5: Volume-of-fluid method.

(ii) Volume of fluid method considers indeed an indicator function $\chi(x, y, z, t)$ which equals one in phase and zero in phase 2. Taking $h(x, y, t)$ a height function such as $z = h(x, y, t)$ the indicator function then reads $\chi(x, y, z, t) = H[z - h(x, y, t)]$ where H is the Heaviside step function, so that $z < h$ corresponds to phase 1 and $z > h$ relates to phase 2 as illustrated in Figure 1.5b (b). The front is directly captured on a stationary grid and the interface motion then reads

$$\frac{\partial \chi}{\partial t} = -\mathbf{u} \cdot \nabla \chi. \tag{1.38}$$

A sharp profile of the boundaries is given by calculating the volume fraction function C on each cell which discretizes the domain as illustrated in Figure 1.5.

Then, an interface reconstruction step is employed from the knowledge of the liquid fluid distribution which is equivalent to the determination of the unit normal vector $\mathbf{n} = (\boldsymbol{\nabla} C)/|\boldsymbol{\nabla} C|$ of each interface element [21]. Easy to implement [25], the volume of fluid method does not require mesh reconnection at each time steps. Moreover, this method presents an inherent mass conservation property: the volume fraction field boundaries are enforced by a conservative discretization and this ensures an exact mass conservation. Furthermore, 3D remeshing when the grid encounters strong deformation is avoided by the use of a fixed grid method [8].

However, non-physical behaviors such as spurious currents are observed by Lafauri [13]. In addition, using the volume fraction to rebuild the interface is a non trivial task and leads to low accuracy of geometrical parameter calculation (curvature) since the indicator function presents a strong discontinuity at the interface [4]. Nevertheless, this technique has been highly improved the ten past years, specially when combining with the level-set method [4] or by either smoothing the indicator function so that the derivatives are easy to implement [1] or by appealing to other methods to calculate the derivatives [15].

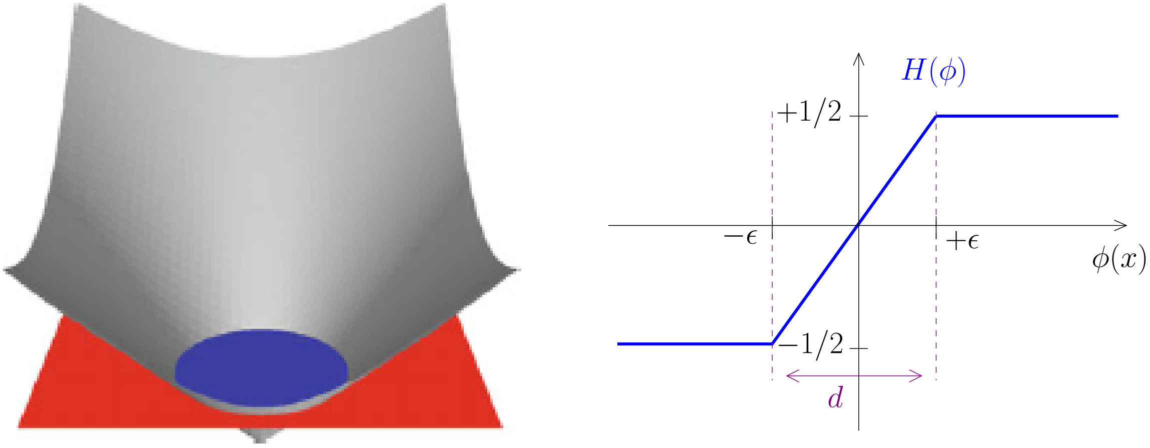

(a) 2D example of an initial level set function ϕ_0 which equals a signed distance function given in [7].

(b) The Heaviside function $H(\phi)$ versus the indicator function ϕ at an interface.

Figure 1.6: Level set method.

(iii) The level-set method relies on an implicit representation of the interface by an iso-surface of a smooth level-set function ϕ. The motion equation of the interface is numerically approximated using schemes based on hyperbolic-conservativ laws with an Eulerian grid which, in the absence of mass transfer, writes

$$\frac{\partial \phi}{\partial t} + F|\boldsymbol{\nabla}\phi| = 0. \tag{1.39}$$

with F the speed function. Taking $\phi < 0$ in phase 1 whereas $\phi > 0$ in phase 2, the function ϕ is here a continuum surface force which approximates the boundary as a volume force and can give the unit normal ($\mathbf{n} = \nabla\phi/||\nabla\phi||$) or the curvature terms ($\kappa = -\nabla \cdot (\nabla\phi/||\nabla\phi||)$). The interface thickness is also defined using the zero level-set function $\phi(x, t = 0) = \pm\epsilon$ where ϵ is the signed distance to the interface. The constant density fluid in each side of the interface can be express as $\rho = \rho_g + (\rho_l - \rho_g)H(\phi)$ where the Heaviside function $H(\phi)$ is displayed in Figure 1.6b. Finally, to enforce a uniform front thickness, i.e using the so-called Eikonal equation $||\nabla\phi|| = 1$ when $||\phi|| \leq \epsilon$, one requires to reinitialize ϕ frequently without affecting the location of the $\phi = 0$ surface.

The main advantage of the level-set method is to easily handle topological changes since the set does not need to be a single curve and can break or merge as t evolves [4]. No redistribution of the surface grid is required and therefore no reconnecting of the interfaces is needed, for a 3D problem the numerical operations reach $\mathcal{O}(N^3\epsilon)$, with ϵ the interface thickness, reducing thus considerably the computation time comparing to an explicit method.

Moreover geometric quantities such as curvature are easily computed (ϕ is a smooth function) using level-set method and the conversion from 2D to 3D is quick [23]. However, the mass conservation property is not inherent to this formulation, the fluid mass gain or lost being defined by a positive or a negative curvature regions [4].

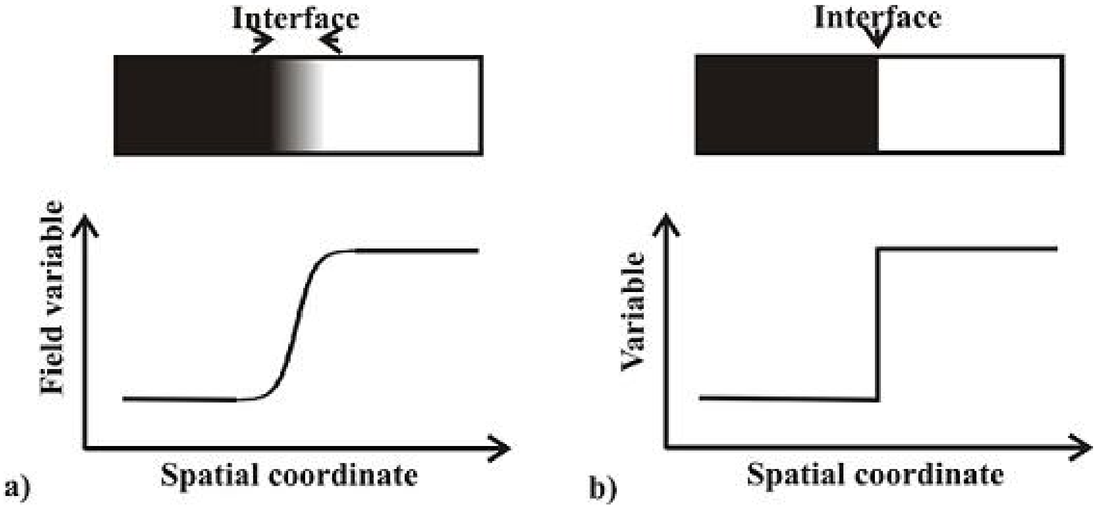

Figure 1.7: Scheme of the phase field method given by [5].

(iv) The phase field technique is prescribed for continuous problem with two distinct densities in each phase and a smooth change between both values in the zone surrounding a diffuse interface as sketched by Moelans and Blanpain [5] in Figure 1.7.

The density difference between the two phases of the boundary are described by a physical function Ψ which plays here the role of an order parameter. The correct interface dynamics is recovered in the limit of infinitesimal interface width. Based on a phase transition theory, the state of the system can be described by the function Ψ at each time step. When the system is not in equilibrium, the mixing between the two phases occurring at the thin interfacial region induces energy change, namely for the free energy or surface energy which is expressed as follows

$$F(\Psi) = \int_{\Omega} \left[f(\Psi(\mathbf{x})) + \frac{1}{2} k |\nabla \Psi(\mathbf{x})|^2 \right] dx, \tag{1.40}$$

where the terms $\frac{1}{2}k|\nabla\Psi(\mathbf{x})|^2$ is the surface energy, Ω the considered domain, k a constant and $f(\Psi(\mathbf{x}))$ is the bulk density energy which presents two stable uniform solutions $\Psi = \pm c$ representing the coexisting bulk phases and a meta-stable solution found by Van der waals [26]. Then, introducing the chemical potential μ as

$$\mu(\Psi) = \frac{\partial F(\Psi)}{\partial \Psi(\mathbf{x})} = f'(\Psi(\mathbf{x})) - k\nabla^2\Psi(\mathbf{x}), \tag{1.41}$$

one obtains the equilibrium profile solving $\mu(\Psi) = 0$, i.e by minimizing the free energy $F(\Psi)$ as the function Ψ changes.

Similarly to the level-set method, the phase field formulation is a powerful technique to handle topological changes. No refinement at each time step is requested resulting in a minimal cost and this technique offers a high stability [2]. In addition, the phase field method is relevant when examining special problems such as Stefan problem [29] or binary alloys [27].

Nevertheless, the phase function changes quickly near the interface and this requires an accurate calculation by taking a larger interface width.

As the width of the interface increases, the interfacial energy and mobility is affected and some spurious effects occur and though a lot of progress has been made to accurately control the interfacial profile, non-equilibrium effects remain [5]. Moreover, this technique is based on a non-trivial asymptotic analysis which links the phase field model and the sharp interface model.

One summarizes the advantages and drawbacks of each numerical method in the comparative Table 1.1.

	Advantages	**Drawbacks**
Front-tracking	- highly accurate - no spurious effect occurrence - complex interfaces geometry	- no topological change - time consuming method - remeshing requirement at regular time
Volume of fluid	- robust method -inherent mass conservation property - easy to implement - fixed grid, hence no 3D remeshing	- spurious effects occurs - non trivial reconstruction of the interface - low accuracy of physical quantities
Level-set	- handle topological changes - fast conversion 2D to 3D - smooth function - no remeshing	- spurious effects due to the non connected interface - poor mass conservation property
Phase-field	- handle topological changes - smooth function - computation time saving - relevant for special problem	- large grid point requested - non-trivial asymptotic analysis - spurious effect occurring

Table 1.1: Comparative table of the aforementioned numerical techniques.

In the present problem, the break up or coalescence of the interface are not taken in account, we then employ the front-tracking method to follow in time the interface boundaries.

1.3.2 Suitability of the boundary integral formulation

One here appeals to the Boundary Element Method (BEM) (see as an example Figure 1.8b) which is a global method (the node contains the information of all the other node in the meshing domain) whereas the finite element method (see for instance Figure 1.8a) FEM, hp-FEM or XFEM are local method (the node are connected only with their neighbors).

Stokes flow problems or potential problem being linear, one therefore applies the relevant boundary-integral formulation to solve the Stokes equations.

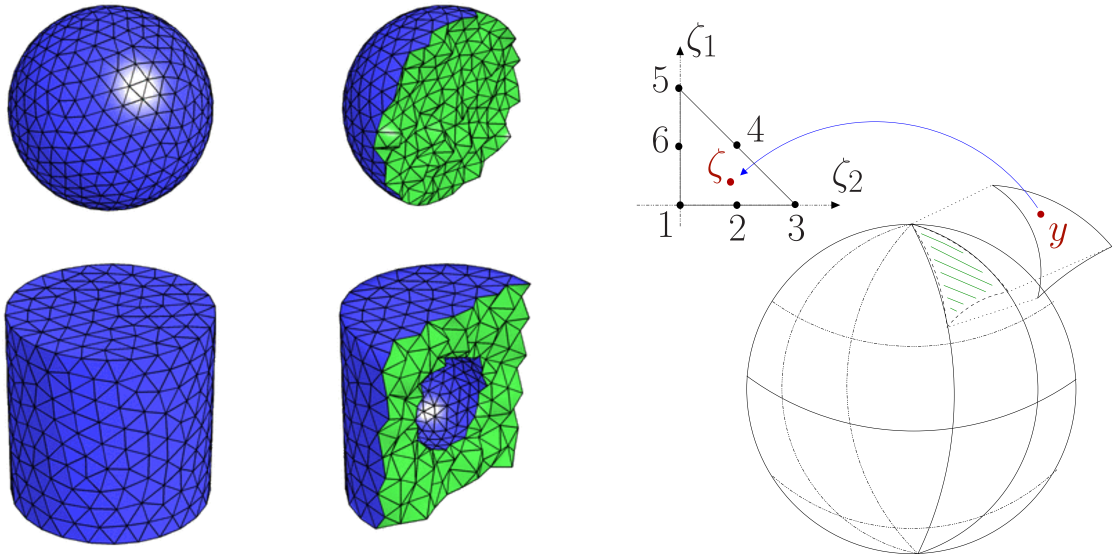

(a) Example of FEM 3D mesh obtain by *distmesh* taken from [17].

(b) Example of BEM 3D curve mesh.

Figure 1.8: Example of FEM 3D mesh (a) and a BEM 3D curve mesh (b).

The boundary element method (BEM) is a numerical technique for solving boundary-integral equations for which the unknown quantities are only surface quantities. It has been extensively exploited in various problems with deformable interface and 3D body problems [28]. This semi-analytic method appeals to the calculation of a free space solution, the so-called Green tensor and the use of the reciprocity relation [16], to offer indeed a high accuracy in problems dealing with discontinuity in stress across an interface. Moreover, the dimension reduction of the problem induces a fast mesh generation and this method can be coupled with other numerical techniques where no analytic solution is available [14]. Besides, this method is well suited for problems in unbounded domain and is able to deal with both 2D and 3D systems [28]. Furthermore, this technique makes it possible to precisely examine a particular internal region and to simplify the treatment of symmetrical problems (the discretization in the plane of symmetry is avoided).

However, BEM ends up with fully-populated matrices and leads to the growth of the storage requirement and computation time as the square of the problem size $\mathcal{O}(N^2)$[3]. New BEM methods improved the computation time saving by reducing the operation to $\mathcal{O}(N)$ [14]. Moreover, this approach requests the quick evaluation of a Green tensor, therefore reducing in practice its application to some linear problem. Nevertheless, the Fast multipole method deals with the non-homogeneous media and make it possible to solve non-linear problems [14] too.

To derive the boundary integral formulation, one first presents the Green solution and, using the reciprocity relation, then writes the integral representation of the velocity in the case of a steady Stokes flow.

1.3.3 Free-space Green tensor and relevant velocity integral representation

A Green tensor is a fundamental solution of the (linear) Stokes equations.

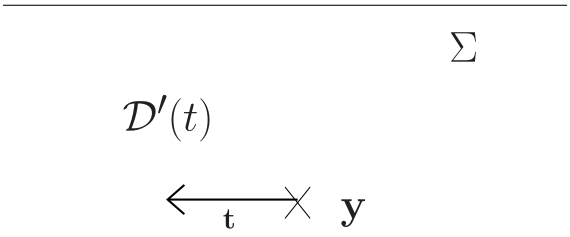

Figure 1.9: Point force with intensity **t** located at the pole **y** in the liquid domain $\mathcal{D}'$ near a surface Σ.

As illustrated in Figure 1.9, a point force with intensity **t** located at the pole **y** in the liquid domain $\mathcal{D}'$ induces a steady and so-called fundamental Stokes flow $(\mathbf{v}, q)$ which obeys the following equations

$$\mu \boldsymbol{\nabla}^2 \mathbf{v} = \boldsymbol{\nabla} q - \delta_{3d}(\mathbf{x} - \mathbf{y})\mathbf{t}, \quad \boldsymbol{\nabla} \cdot \mathbf{v} = 0 \quad \text{in } I\!R^3 \setminus \{\mathbf{y}\} \tag{1.42}$$

where $\delta_{3d}(\mathbf{x} - \mathbf{y}) = \delta_d(x_1 - y_1)\delta_d(x_2 - y_2)\delta_d(x_3 - y_3)$ if $x_i = \mathbf{x} \cdot \mathbf{e}_i$, $y_i = \mathbf{y} \cdot \mathbf{e}_i$ and δ_d, the Dirac pseudo-function.

The associated flow $(\mathbf{v}, q)$ is not unique. One indeed selects a solution, linearly depending upon the vector **t**, by adding a far-field behavior. Adopting the usual tensor summation convention, the solution and its associated stress tensor $\boldsymbol{\sigma}$ give the Green pressure vector **P**, the second-rank Green velocity tensor **G** and the third-rank stress tensor **T** with Cartesian components P_j, G_{ij} and T_{ijk} such that

$$q(\mathbf{x}) = \frac{P_j(\mathbf{x}, \mathbf{y})t_j}{8\pi}, \quad \mathbf{v}(\mathbf{x}) \cdot \mathbf{e}_i = v_i(\mathbf{x}) = \frac{G_{ij}(\mathbf{x}, \mathbf{y})t_j}{8\pi\mu}, \tag{1.43}$$

$$\mathbf{e}_i \cdot \boldsymbol{\sigma}(\mathbf{x}) \cdot \mathbf{e}_k = \sigma_{ik}(\mathbf{x}) = \frac{T_{ijk}(\mathbf{x}, \mathbf{y})t_j}{8\pi}. \tag{1.44}$$

Requiring the fundamental flow $(\mathbf{v}, q)$ to vanish far from the pole **y**, we then obtain the following free-space Oseen-Burger [19] solution

$$P_j(\mathbf{x}, \mathbf{y}) = \frac{2(x_j - y_j)}{||\mathbf{x} - \mathbf{y}||^3}, \qquad G_{ij}(\mathbf{x}, \mathbf{y}) = \frac{\delta_{ij}}{||\mathbf{x} - \mathbf{y}||} + \frac{(x_i - y_i)(x_j - y_j)}{||\mathbf{x} - \mathbf{y}||^3}, \tag{1.45}$$

$$T_{ijk}(\mathbf{x}, \mathbf{y}) = -6\frac{(x_i - y_i)(x_j - y_j)(x_k - y_k)}{||\mathbf{x} - \mathbf{y}||^5}. \tag{1.46}$$

Note that the pressure, velocity and stress tensor are *singular* as **x** tends to **y**. Moreover, the following basic symmetry properties hold (see (1.45))

$$G_{ij}(\mathbf{x}, \mathbf{y}) = G_{ij}(\mathbf{y}, \mathbf{x}), \quad G_{ij}(\mathbf{x}, \mathbf{y}) = G_{ji}(\mathbf{x}, \mathbf{y}) \quad \text{for any pair } (i, j). \tag{1.47}$$

As the reader may check, the flow $\mathbf{v}(\mathbf{x}) = T_{ijk}(\mathbf{x},\mathbf{y})\,\mathbf{e}_k$ is a steady Stokes flow with pressure $Q_{ik}(\mathbf{x},\mathbf{y})$ given by

$$Q_{ik}(\mathbf{x},\mathbf{y}) = 4\left\{\frac{3(x_i-y_i)(x_k-y_k)}{||\mathbf{x}-\mathbf{y}||^5} + \frac{\delta_{ik}}{||\mathbf{x}-\mathbf{y}||^3}\right\}. \tag{1.48}$$

Introducing the normal vector $\mathbf{n} = n_k\mathbf{e}_k$ directed into the liquid domain $\mathcal{D}$, the following key integral representation of the velocity field $\mathbf{u}$ in the entire liquid domain given by [19] holds [3]

$$\begin{aligned} u_j(\mathbf{x}) = &-\frac{1}{8\pi\mu}\int_{\partial\mathcal{D}} G_{ij}(\mathbf{y},\mathbf{x})f_i(\mathbf{y})dS(\mathbf{y}) \\ &+\frac{1}{8\pi}\int_{\partial\mathcal{D}} u_i(\mathbf{y})T_{ijk}(\mathbf{y},\mathbf{x})n_k(\mathbf{y})dS(\mathbf{y}) \text{ for } j=1,2,3 \text{ and } \mathbf{x} \text{ in } \mathcal{D}. \end{aligned} \tag{1.49}$$

Clearly, the relation (1.49) shows that the knowledge of solely two physical quantities, the velocity $\mathbf{u}$ and the surface traction $\mathbf{f}$ on the entire liquid boundary $\partial\mathcal{D}$ are sufficient to obtain the unknown velocity field $\mathbf{u}$ in the liquid domain. The traction $\mathbf{f}$ on the boundary appears in the first integral on the right-hand side of (1.49), which is termed the single-layer integral. On its side, the velocity $\mathbf{u}$ on $\partial\mathcal{D}$ is involved through the second and so-called double-layer integral on the right-hand side of (1.49). The single-layer integral is a Stokes flow produced by a distribution of point forces with intensity $-\mathbf{f}$ at the boundary $\partial\mathcal{D}$. In addition, the double-layer term is also a Stokes flow as previously noticed (see remark above (1.49)). For the case of one bubble near a free surface, we deals with $\partial\mathcal{D} = S_0 \cup S_1$ and the stress jump boundary condition on $\partial\mathcal{D}$ provides the surface traction $\boldsymbol{\sigma}\cdot\mathbf{n}$ on the surface $S_0 \cup S_1$ whereas the surface velocity $\mathbf{u}$ is the unknown surface quantity.

1.3.4 Boundary integral equation

By letting the point $\mathbf{x}$ tend onto $\partial\mathcal{D} = S_0 \cup S_1$ in the relation (1.49), one establishes a relevant boundary-integral equation for the unknown velocity $\mathbf{u}$ on the entire surface $\partial\mathcal{D} = S_0 \cup S_1$. Such a limit process exhibits quite different behaviors for the single-layer or the double-layer contributions. Indeed, the single-layer term experiences a regular limit since the kernel $\mathbf{G}$ behaves as $1/r$ with $r = \|\mathbf{x}-\mathbf{y}\|$ vanishing as $\mathbf{x}$ tends to $\partial\mathcal{D}$. In contrast, the double-layer term behaves as $1/r^2$ and therefore presents a weakly singular behavior requiring a careful attention. As shown in [19], one gets

$$\lim_{\mathbf{x}\to\partial\mathcal{D}}\int_{\partial\mathcal{D}} u_i(\mathbf{y})T_{ijk}(\mathbf{y},\mathbf{x})n_k(\mathbf{y})dS(\mathbf{y}) = 4\pi u_j(\mathbf{x}) + \fint_{\partial\mathcal{D}} u_i(\mathbf{y})T_{ijk}(\mathbf{y},\mathbf{x})n_k(\mathbf{y})dS(\mathbf{y}) \tag{1.50}$$

where the symbol $\fint$ means a weakly-singular integration in the principal value sense of Cauchy [10] when the point $\mathbf{x}$ is right on $\partial\mathcal{D}$. Therefore, one obtains the following boundary-integral equation for the unknown velocity $\mathbf{u}$ on the liquid boundary $\partial\mathcal{D}$

$$u_j(\mathbf{x}) = -\frac{1}{4\pi\mu}\int_{\partial\mathcal{D}} G_{ij}(\mathbf{y},\mathbf{x})f_i(\mathbf{y})dS(\mathbf{y}) + \frac{1}{4\pi}\fint_{\partial\mathcal{D}} u_i(\mathbf{y})T_{ijk}(\mathbf{y},\mathbf{x})n_k(\mathbf{y})dS(\mathbf{y}) \tag{1.51}$$

for $j = 1, 2, 3$ and $\mathbf{x}$ on $\partial\mathcal{D}$.

---

[3] Adopting henceforth the usual tensor summation convention.

Combining (1.51) with the relation (1.9) for the surface traction $\mathbf{f} = \boldsymbol{\sigma} \cdot \mathbf{n}$, the boundary integral equation for the case of a bubble ascending toward a free surface reads

$$\mathbf{u}(\mathbf{x}) - \frac{1}{4\pi} \fint_{\partial \mathcal{D}} \mathbf{u}(\mathbf{y}) \cdot \mathbf{T}(\mathbf{y}, \mathbf{x}) \cdot \mathbf{n}(\mathbf{y}) dS = -\frac{1}{4\pi\mu} \int_{S_0} [(\rho_l \mathbf{g} \cdot \mathbf{y} + \gamma_0 \nabla_S \cdot \mathbf{n})\mathbf{n}](\mathbf{y}) \cdot \mathbf{G}(\mathbf{y}, \mathbf{x}) dS$$
$$- \frac{1}{4\pi\mu} \int_{S_1} [(\rho_l \mathbf{g} \cdot \mathbf{y} + \gamma_1 \nabla_S \cdot \mathbf{n})\mathbf{n}](\mathbf{y}) \cdot \mathbf{G}(\mathbf{y}, \mathbf{x}) dS \quad \text{for } \mathbf{x} \text{ on } \partial \mathcal{D}, \tag{1.52}$$

with δ_{ij} the Kronecker symbol and $\partial \mathcal{D} = S_0 \cup S_1$ the entire surface with S_0 and S_1 the free surface and bubble surface, respectively. Another equivalent and regularized boundary-integral equation will be also given in Chapter 6 for a cluster involving several particles (bubbles and/or solid bodies).

1.4 Summary step to track in time the entire liquid boundary

In the previous section, the addressed problem has been presented together with the adopted assumptions. In addition, the governing equations were established and handled at a given time by appealing to the boundary-integral formulations. Henceforth, one investigates the evolution in time of the entire boundary $\partial \mathcal{D} = S_0 \cup S_1$ when the bubble rises toward the free surface.

This task is performed by running at each time t the following steps :

Step 1: From the knowledge at time t of the liquid domain $\mathcal{D}(t)$, one first computes the quantity $\boldsymbol{\nabla}_S \cdot \mathbf{n}$ (see the relation (1.9)) on each surface $S_m(t)$.

Step 2: One then solves, at time t, equations (1.6)-(1.7), (1.9) and (1.17) to get the unknown fluid velocity $\mathbf{u}$ on each surface $S_m(t)$.

Step 3: The liquid boundary $\mathcal{D}(t + dt)$ at time $t + dt$ is obtained by moving at the material velocity $\mathbf{V}$ between times t and $t + dt$ each surface S_m by exploiting the relation (1.16).

Note that for such a procedure the following issues are of the utmost importance:

(i) Accurate computation of the local average curvature $(\boldsymbol{\nabla}_S \cdot \mathbf{n})/2$ on each surface S_m in Step 1.

(ii) Accurately and efficiently solving the Stokes equations (1.6)-(1.7), (1.9) and (1.17) in Step 2.

(iii) Adequately select a time step in Step 3.

Chapter 2 introduces a suitable treatment to cope with the previous issues (i)-(iii).

Bibliography

[1] S. Afkhami and M. Bussmann. Height functions for applying contact angles to 2d vof simulations. *Int. J. Numer. Meth. Fluids*, 57(4):453–472, 2008.

[2] V. E. Badalassi, H. D. Ceniceros, and S. Banerjee. Computation of multiphase systems with phase field models. *J. Comput. Phys.*, 190(2):371–397, September 2003.

[3] M. Bonnet. Regularized direct and indirect symmetric variational BIE formulations for three-dimensional elasticity. *Engineering Analysis with Boundary Elements*, 15(1):93 – 102, 1995.

[4] V. Le Chenadec and H. Pitsch. A 3d unsplit forward/backward volume-of-fluid approach and coupling to the level set method. *J. Comp. Phys.*, 233(0):10 – 33, 2013.

[5] N. Moelans et al. An introduction to phase-field modeling of microstructure evolution. *Computer Coupling of Phase Diagrams and Thermochemistry*, 32:268–294, 2008.

[6] J. Glimm, J. Grove, X. Li, K. Shyue, Y. Zeng, and Q. Zhang. Three-dimensional front tracking. *SIAM Journal on Scientific Computing*, 19(3):703–727, 1998.

[7] S. Gross and A. Reusken. *Numerical Methods for Two-phase Incompressible Flows*, volume 40. Springer Berlin Heidelberg Series in Computational Mathematics, Berlin Heidelberg, 2011.

[8] D. Gueyffier, J. Li, A. Nadim, R. Scardovelli, and S. Zaleski. Volume-of-fluid interface tracking with smoothed surface stress methods for three-dimensional flows. *Journal of Computational Physics*, 152(2):423 – 456, 1999.

[9] J. Hadamard. Mouvement permanent lent d'une sphère liquide et visqueuse dans un liquide visqueux. *C. R. Acad. Sci. Paris*, 152:1735–1738, 1911.

[10] J. Hadamard. *Lecture on Cauchy's problem in linear differential equations.* Dover Publications, Inc., New York, 1932.

[11] Daniel D. Joseph and Yuriko Y. Renardy. *Fundamentals of two-fluid dynamics.* Springer, New York, 1993.

[12] H. Kočárková. *Stabilité des mousses de verre: Expériences à l'échelle d'une bulle ou d'un film vertical.* PhD thesis, Université Paris-Est, 2011.

[13] B. Lafaurie, C. Nardone, R. Scardovelli, S. Zaleski, and G. Zanetti. Modelling merging and fragmentation in multiphase flows with SURFER. *J. Comput. Phys.*, 113(1):134 – 147, 1994.

[14] Y. J. Liu. *Fast Multipole Boundary Element Method - Theory and Applications in Engineering.* Cambridge University Press, Cambridge, 2009.

[15] M. Meier, G. Yadigaroglu, and B. L. Smith. A novel technique for including surface tension in PLIC-VOF methods. *Eur. J. Mech.-B/Fluids*, 21(1):61–73, 2002.

[16] F. K. G. Odqvist. Über die Randwertaufgaben der Hydrodynamik zäher Flüssigkeiten. *Mathematische Zeitschrift*, 32:329–375, 1930.

[17] O.Persson and G. Strang. A simple mesh generator in MATLAB. *Siam Rev.*, 49:329–345, 2004.

[18] F. Pigeonneau and F. Feuillebois. Collision of drops with inertia effects in strongly sheared linear flow fields. *Journal of Fluid Mechanics*, 455:359–386, 3 2002.

[19] C. Pozrikidis. *Boundary integral and singularity methods for linearized viscous flow.* Cambridge University Press, Cambridge, 1992.

[20] W. Rybczynski. Uber die fortschreitende bewegun einer flussingen kugel in einem zaben medium. *Bull. de l'Acad. des Sci. de Cracovie*, pages 40–46, 1911.

[21] R. Scardovelli and S. Zaleski. Direct numerical simulation of free-surface and interfacial flow. *Annu. Rev. Fluid Mech.*, 31(1):567–603, 1999.

[22] J. A. Sethian and P. Smereka. Level set methods for fluid interfaces. *Annu. Rev. Fluid Mech.*, 35:341–371, 2003.

[23] J.A. Sethian. *Level Set Methods and Fast Marching Methods.* Cambridge University Press, New York, 1999.

[24] G. Tryggvason, B. Bunner, A. Esmaeeli, D. Juric, N. Al-Rawahi, W. Tauber, J. Han, S. Nas, and Y.-J. Jan. A front-tracking method for the computations of multiphase flow. *J. Comput. Phy.*, 169(2):708 – 759, 2001.

[25] A. O. Unverdi and G. Tryggvason. A front-tracking method for viscous, incompressible, multi-fluid flows. *J. Comput. Phys.*, 100:25–37, 1992.

[26] J.D. van der Waals. The thermodynamic theory of capillarity flow under the hypothesis of a continuous variation of density (in dutch). *Verhandel/Konink. Akad. Weten. Amsterdam*, 1(8), 1893.

[27] J.A. Warren and W.J. Boettinger. Prediction of dendritic growth and microsegregation patterns in a binary alloy using the phase-field method. *Acta Metallurgica et Materiali*, 43(2):689 – 703, 1995.

[28] S Weinbaum, P Ganatos, and Z Yan. Numerical multipole and boundary integral equation techniques in Stokes flow. *Annu. Rev. Fluid Mech.*, 22(1):275–316, 1990.

[29] A.A. Wheeler, B.T. Murray, and R.J. Schaefer. Computation of dendrites using a phase field model. *Physica D: Nonlinear Phenomena*, 66(1 2):243 – 262, 1993.

Chapter 2

Numerical implementation and benchmark tests

Contents

The adopted numerical procedure is presented in this chapter. Discretized equations are first expressed in 2d-axisymmetric configuration for one bubble ascending toward a free surface. The mesh is then built using a collocation method in which an isoparametric interpolation approximates the flow components on each boundary element. Benchmark tests are thereafter performed to select the geometric parameters related to our problem in conjunction with reducing the computational time.

This chapter briefly introduces the numerical procedure based on a collocation method and a discrete Wielandt deflation technique while the reader is directed to [7] for further details. Numerical results obtained for one bubble interacting with a free surface will be presented and discussed later in Chapter 3. As a consequence, the present Chapter may be skipped in a first reading.

2.1 Boundary-integral formulation in 2d-axisymmetric configuration

Since we restrict our analysis to the axisymmetric configuration depicted in Figure 1.1, we adopt cylindrical coordinates (r, ϕ, z) with $r = \sqrt{x^2 + y^2}$, $z = x_3$ and ϕ the azimuthal angle in the range $[0, 2\pi]$. The boundary-integral equation (1.52) is then reduced to a one-dimensional boundary-integral equation over the entire contour $\mathcal{L} = \mathcal{L}_0 \cup \mathcal{L}_1$ of the boundaries in the azimuthal plane ($\mathcal{L}_0$ and $\mathcal{L}_1$ being the contour of the free surface and the bubble, respectively). Therefore, the boundary-integral equation (1.52) for the unknown velocity $\mathbf{u}$ on the liquid boundary is expressed in our 2d-axisymmetric configuration as

$$4\pi u_\alpha(\mathbf{x}_0) - \fint_{\mathcal{L}} C_{\alpha\beta}(\mathbf{x}, \mathbf{x}_0) u_\beta(\mathbf{x}) dl(\mathbf{x}) = -\frac{1}{\mu} \int_{\mathcal{L}_0} B_{\alpha\beta}(\mathbf{x}, \mathbf{x}_0)[-\rho_l g z + \gamma_0 \nabla_S \cdot \mathbf{n}] n_\beta(\mathbf{x}) dl(\mathbf{x})$$
$$- \frac{1}{\mu} \int_{\mathcal{L}_1} B_{\alpha\beta}(\mathbf{x}, \mathbf{x}_0)[-\rho_l g z + \gamma_1 \nabla_S \cdot \mathbf{n}] n_\beta(\mathbf{x}) dl(\mathbf{x}) \quad \text{for } \mathbf{x}_0 \text{ on } \mathcal{L} \tag{2.1}$$

where α, β are either r or z (the radial or axial components) and dl denotes the differential arc length in the $\phi = 0$ plane. By performing an exact integration of the velocity Green tensor $\mathbf{G}$ and the stress Green tensor $\mathbf{T}$ (see §1.4.2) over the azimuthal angle ϕ, one obtains the single-layer and double-layer 2×2 square matrices $B_{\alpha\beta}(\mathbf{x}, \mathbf{x}_0)$ and $C_{\alpha\beta}(\mathbf{x}, \mathbf{x}_0)$ given in Pozrikidis [9] and recalled in Appendix A. As outlined in this latter Appendix, all the components of those matrices are solely expressed in terms of the following complete elliptic integrals of the first $E(k)$ and second kind $F(k)$

$$F(k) = \int_0^{\pi/2} \frac{d\phi}{(1 - k^2 \cos^2 \phi)^{1/2}}, \qquad E(k) = \int_0^{\pi/2} (1 - k^2 \cos^2 \phi)^{1/2} d\phi \tag{2.2}$$

where, $\mathbf{x}_0$ and $\mathbf{x}$ having cylindrical coordinates (r_0, z_0) and (r, z) respectively,

$$k^2 = \frac{4 r r_0}{\hat{z}^2 + (r + r_0)^2}, \quad \hat{z} = z - z_0. \tag{2.3}$$

2.2 Numerical implementation

Three main numerical techniques are used to solved the previous boundary-integral equation such as Galerkin formulation [5]-[2], spectral techniques [13]-[6] and the collocation method [10]-[3] -[8]. In the present problem, the boundary-integral equation is numerically inverted appealing to the well-known and easy to implement collocation point method.

2.2.1 Mesh and collocation method

In implementing the boundary element method, only the entire truncated boundary contour is discretized into N_e curved boundary elements Δ_e, as shown in Figure 2.1. Indeed, the flow far-field behavior allow us to take a truncated contour of the free surface (the flow vanishing far from the bubble-free surface interaction). In 2d-axisymmetric configuration, our contour shows the $x \to -x$ axis symmetry. Each boundary element has two ends points and N_c collocation points spread by a Gauss or a uniform distribution.

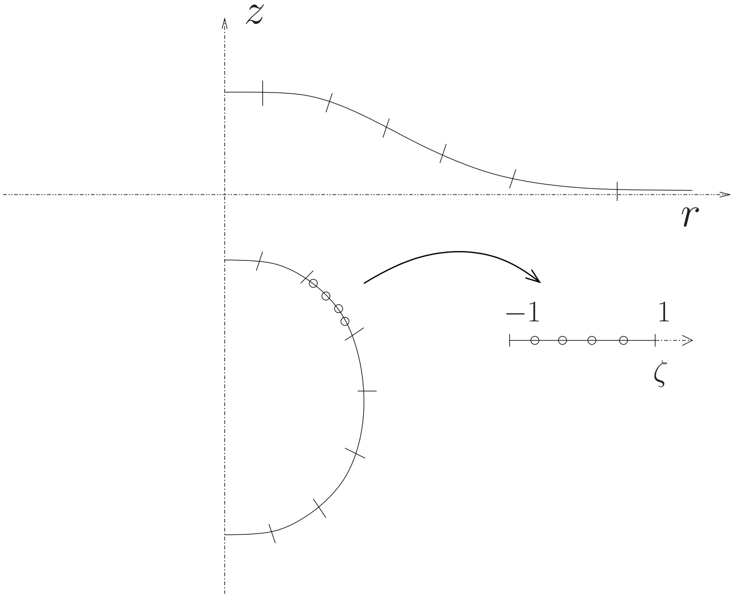

Figure 2.1: Discretization of the contours $\mathcal{L}_0$ and $\mathcal{L}_1$ associated with the axisymetric truncated free surface and bubble surface. Mapping of one boundary element Δ_e onto the domain $[-1, 1]$ where collocation points are indicated by circles.

Each element i_e has N_c nodes $\mathbf{x}_{i_c}^{i_e}$ and we then end up with $N_e N_c$ nodal points spread on the bubble contour $\mathcal{L}_1$ and free surface truncated contour $\mathcal{L}_0$.

2.2.2 Isoparametric interpolation

In the present problem, one needs to determine the velocity $\mathbf{u}$ on each boundary element whereas the traction $\mathbf{f} = \boldsymbol{\sigma} \cdot \mathbf{n}$ is known on the contours $\mathcal{L}_0$ and $\mathcal{L}_1$. Therefore, an approximation of vectors $\mathbf{u}$ and $\mathbf{f} = \boldsymbol{\sigma} \cdot \mathbf{n}$ is performed on each boundary element. This is here achieved using an isoparametric interpolation. Taking the $(N_c - 1)$-order Lagrangian interpolate polynomial function L_{i_c}, we express the location of a point $\mathbf{x}^{i_e}$ associated on the element i_e as follows

$$\mathbf{x}^{i_e} = \sum_{i_c=1}^{N_c} L_{i_c}(\zeta)\mathbf{x}_{i_c}^{i_e} \tag{2.4}$$

with ζ the variable belonging to the segment $[-1, 1]$ onto which each boundary element is mapped. In addition, the approximated vectors $\mathbf{u}(\mathbf{x}^{i_e})$ and $\mathbf{f}(\mathbf{x}^{i_e})$ at the point $\mathbf{x}^{i_e}$ read, in a similar way

$$\mathbf{u}(\mathbf{x}^{i_e}) = \sum_{i_c=1}^{N_c} L_{i_c}(\zeta)\mathbf{u}_{i_c}^{i_e}, \quad \mathbf{f}(\mathbf{x}^{i_e}) = \sum_{i_c=1}^{N_c} L_{i_c}(\zeta)\mathbf{f}_{i_c}^{i_e}. \tag{2.5}$$

Then, the coupled boundary-integral equations in 2d-axisymmetric configuration (2.1) when enforced at the nodal points $\mathbf{x}_{i_c}^{i_e}$ on the i_e element write

$$\begin{aligned} 4\pi u_\alpha(\mathbf{x}_{i_c}^{i_e}) = & \fint_{\mathcal{L}} C_{\alpha\beta}(\mathbf{x}, \mathbf{x}_{i_c}^{i_e}) u_\beta(\mathbf{x}) dl(\mathbf{x}) \\ & - \frac{1}{\mu} \int_{\mathcal{L}} B_{\alpha\beta}(\mathbf{x}, \mathbf{x}_{i_c}^{i_e}) f_\beta(\mathbf{x}) n_\beta(\mathbf{x}) dl(\mathbf{x}) \quad \text{for } \mathbf{x}_{i_c}^{i_e} \text{ on } \mathcal{L}_{i_c} \end{aligned} \tag{2.6}$$

2.2.3 Discretized boundary-integral equation

At the $N_e N_c$ nodal points we introduce the components of the velocity $\mathbf{u} \cdot \mathbf{e}_\alpha$ and of the surface traction $\mathbf{f} \cdot \mathbf{e}_\alpha$. We then end up with two given $2N_eN_c$ stress vector $\mathbf{F}(\mathbf{f}_r, \mathbf{f}_z)$ and $2N_eN_c$ unknown velocity vectors $\mathbf{U}(\mathbf{u}_r, \mathbf{u}_z)$. Discretizing the boundary-integral equation (2.6) then shows that these vectors satisfy a $2N_eN_c$-equations linear system

$$\mathbf{U} - \mathbf{C}.\mathbf{U} = \mathbf{B}.\mathbf{F} \tag{2.7}$$

with matrices $\mathbf{B}$ and $\mathbf{C}$ having components expressed as integrals over the segment $[-1, 1]$ of the quantities $B_{\alpha\beta}$ and $C_{\alpha\beta}$ detailed below:

By injecting (2.5) in (2.6), one obtains

$$\begin{aligned} 4\pi u_\alpha(\mathbf{x}^{i_e}_{i_c}) = & \sum_{j_e=1}^{N_e} \fint_{\mathcal{L}_{j_e}} C_{\alpha\beta}(\mathbf{x}^{j_e}, \mathbf{x}^{i_e}_{i_c}) u_\beta(\mathbf{x}^{j_e}) dl(\mathbf{x}^{j_e}) \\ & - \frac{1}{\mu} \sum_{j_e=1}^{N_e} \int_{\mathcal{L}_{j_e}} B_{\alpha\beta}(\mathbf{x}^{j_e}, \mathbf{x}^{i_e}_{i_c}) f_\beta(\mathbf{x}^{j_e}) n_\beta(\mathbf{x}^{j_e}) dl(\mathbf{x}^{j_e}) \quad \text{for } \mathbf{x}^{i_e}_{i_c} \text{ on } \mathcal{L}_{i_e}. \end{aligned} \tag{2.8}$$

In addition, one enforces (2.5) at the N_c collocation points in (2.8) and arrives at

$$\begin{aligned} 4\pi u^{i_e}_{\alpha,i_c} = & \sum_{j_e=1}^{N_e} \fint_{\mathcal{L}_{j_e}} C_{\alpha\beta}(\mathbf{x}^{j_e}, \mathbf{x}^{i_e}_{i_c}) \sum_{j_c=1}^{N_c} L_{j_c}(\zeta) u^{j_e}_{\beta,j_c} dl(\mathbf{x}^{j_e}) \\ & - \frac{1}{\mu} \sum_{j_e=1}^{N_e} \int_{\mathcal{L}_{j_e}} B_{\alpha\beta}(\mathbf{x}^{j_e}, \mathbf{x}^{i_e}_{i_c}) \sum_{j_c=1}^{N_c} L_{j_c}(\zeta) f^{j_e}_{\beta,j_c} n_\beta(\mathbf{x}^{j_e}) dl(\mathbf{x}^{j_e}) \quad \text{for } \mathbf{x}^{i_e}_{i_c} \text{ on } \mathcal{L}_{i_e} \end{aligned} \tag{2.9}$$

where $u^{j_e}_{\beta,j_c} dl(\mathbf{x}^{j_e})$ and $f^{j_e}_{\beta,j_c} n_\beta(\mathbf{x}^{j_e})$ the velocity and traction component at the nodal point $\mathbf{x}^{j_e}$ on the element $j_e \neq i_e$.

At the nodal point $\mathbf{x}^{j_e}$ with coordinate ζ in the segment $[-1, 1]$, one defines the corresponding differential arc length $dl(\mathbf{x}^{j_e})/d\zeta = \sqrt{(dr^{j_e}/d\zeta)^2 + (dz^{j_e}/d\zeta)^2}$. We then get the following discretized boundary-integral equation evaluated at each collocation point $\mathbf{x}^{i_e}_{i_c}$ as a function of the ζ coordinate

$$4\pi u^{i_e}_{\alpha,i_c} = \sum_{j_e=1}^{N_e} \sum_{j_c=1}^{N_c} C^{i_e j_e}_{\alpha\beta;i_c j_c} u^{j_e}_{\beta,j_c} - \frac{1}{\mu} \sum_{j_e=1}^{N_e} \sum_{j_c=1}^{N_c} B^{i_e j_e}_{\alpha\beta;i_c j_c} f^{j_e}_{\beta,j_c} n_\beta(\mathbf{x}^{j_e}) \quad \text{for } \mathbf{x}^{i_e}_{i_c} \text{ on } \mathcal{L}_{i_e} \tag{2.10}$$

where the quantities

$$B^{i_e j_e}_{\alpha\beta;i_c j_c} = -\int_{-1}^{1} B_{\alpha\beta}(\mathbf{x}^{j_e}, \mathbf{x}^{i_e}_{i_c}) L_{j_c}(\zeta) dl_{j_e}(\zeta) d\zeta, \tag{2.11}$$

$$C^{i_e j_e}_{\alpha\beta;i_c j_c} = \int_{-1}^{1} C_{\alpha\beta}(\mathbf{x}^{j_e}, \mathbf{x}^{i_e}_{i_c}) \sum_{j_c=1}^{N_c} L_{j_c}(\zeta) dl_{j_e}(\zeta) d\zeta \qquad \text{for } i_e \neq j_e, \tag{2.12}$$

$$C^{i_e i_e}_{\alpha\beta;i_c j_c} = \fint_{-1}^{1} C_{\alpha\beta}(\mathbf{x}^{j_e}, \mathbf{x}^{i_e}_{i_c}) \sum_{j_c=1}^{N_c} L_{j_c}(\zeta) dl_{j_e}(\zeta) d\zeta\,, \tag{2.13}$$

are the coefficients of the matrices $\mathbf{B}$ and $\mathbf{C}$.

Since we enforce the discretized boundary equation (2.10) at each node on the N_e boundary elements, one needs to accurately calculate these coefficients. Moreover, computing these coefficients requires a careful attention knowing that (2.11) is indeed weakly *singular* when the collocation point $\mathbf{x}_{i_c}^{i_e}$ is located on the selected boundary element j_e. Henceforth, the free surface contour $\mathcal{L}_0$ will be truncated to perform our numerical computations.

2.2.4 Regular and weakly singular integrals

A polynomial approximation given in [1] of the complete elliptic integrals of the first and second kind $E(k)$ and $F(k)$ (see (2.2)) allows one to accurately compute the matrices $\mathbf{B}$ and $\mathbf{C}$. As $\mathbf{x}(r,z)$ tends onto $\mathbf{x}_0$, k tends to unity and $F(k)$ therefore takes an infinite value. Recall (see (2.2)) that

$$F(k)=\int_0^{\pi/2}\frac{d\phi}{(1-k^2\cos^2\phi)^{1/2}},\qquad E(k)=\int_0^{\pi/2}(1-k^2\cos^2\phi)^{1/2}d\phi. \tag{2.14}$$

with $\hat{r}=r-r_0$ and $k^2=4rr_0/(\hat{r}^2+(z+z_0)^2)$.

The behavior of the matrices $\mathbf{B}$ and $\mathbf{C}$ as $k\to 1$ in §2.2.3 are then handled by asymptotically expanding the complete elliptic integrals as

$$F(k)\simeq \ln\frac{4}{(1-k^2)^2}+\cdots\sim -\ln\hat{r}+\cdots\,,\qquad E(k)\simeq 1+\cdots\,. \tag{2.15}$$

One then ends up with regular integral for $E(k)$ whereas the integral $F(k)$ is a weakly singular integral. Computing the integrals in (2.11)-(2.13) at the nodes $\mathbf{x}_0$ requires to distinguish different cases depending on the location of the node $\mathbf{x}_0$:

1) The node $\mathbf{x}_0$ belongs to a boundary element different from the selected one, as sketched in Figure 2.2.

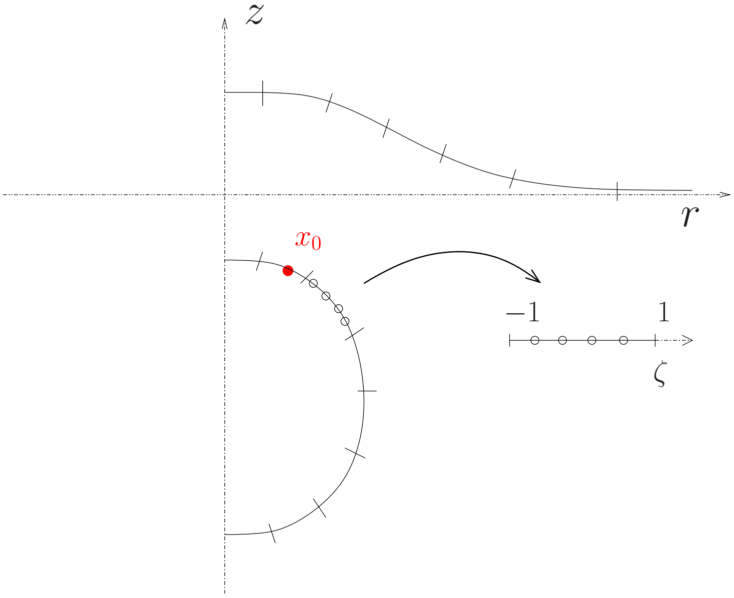

Figure 2.2: Case of a regular integral when the node $\mathbf{x}_0$ belongs to a boundary element different from the selected one bearing the o symbols.

As a result, each integral is regular and numerically calculated by dividing the segment $[-1, 1]$ into equal or unequal sub-segments using the Voutsinas and Bergeles [12] procedure.

2) The node $\mathbf{x}_0$ is located on the selected boundary element, as shown in Figure 2.3.

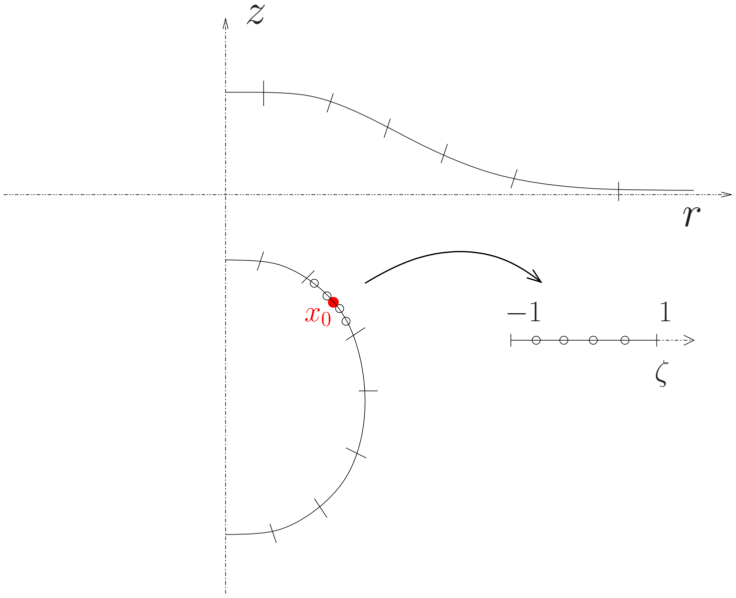

Figure 2.3: Case of a node $\mathbf{x}_0$ located on the selected boundary element.

In this case, one encounters both regular and singular integrals. Indeed, for $\mathbf{x}_0 = \mathbf{x}_{ic}^{ie}$ with coordinate ζ_{i_c} in the segment $[-1, 1]$ located on the boundary element i_e, the off-diagonal components, $B_{rz}(\mathbf{x}^{j_e}, \mathbf{x}_{i_c}^{i_e})$ and $B_{zr}(\mathbf{x}^{j_e}, \mathbf{x}_{i_c}^{i_e})$ tend to a finite value [9] being *regular integrals*. Moreover, as $\zeta \to \zeta_{i_c}$, the components of the matrix $\mathbf{C}$ (see Appendix A) read

$$C_{zz}(\mathbf{x}^{i_e}, \mathbf{x}_{i_c}^{i_e}) = -\frac{8z_{i_e}'^2(\zeta_{i_c})}{l_{i_e}'^2(\zeta_{i_c})} \frac{z_{i_e}'(\zeta_{i_c})n_z + r_{i_e}'(\zeta_{i_c})n_r}{\zeta - \zeta_{i_c}}, \tag{2.16}$$

$$C_{zr}(\mathbf{x}^{i_e}, \mathbf{x}_{i_c}^{i_e}) = C_{rz} = -\frac{8z_{i_e}'(\zeta_{i_c})r_{i_e}'(\zeta_{i_c})}{l_{i_e}'^2(\zeta_{i_c})} \frac{z_{i_e}'(\zeta_{i_c})n_z + r_{i_e}'(\zeta_{i_c})n_r}{\zeta - \zeta_{i_c}}, \tag{2.17}$$

$$C_{rr}(\mathbf{x}^{i_e}, \mathbf{x}_{i_c}^{i_e}) = -\frac{8r_{i_e}'^2(\zeta_{i_c})}{l_{i_e}'^2(\zeta_{i_c})} \frac{z_{i_e}'(\zeta_{i_c})n_z + r_{i_e}'(\zeta_{i_c})n_r}{\zeta - \zeta_{i_c}}, \tag{2.18}$$

where the normal components at the node $\mathbf{x}^{i_e}$ writes

$$n_z(\mathbf{x}^{i_e}) = -\frac{dr_{i_e}(\zeta)/d\zeta}{dl_{i_e}(\zeta)/d\zeta}, \qquad n_r(\mathbf{x}^{i_e}) = -\frac{dz_{i_e}(\zeta)/d\zeta}{dl_{i_e}(\zeta)/d\zeta}. \tag{2.19}$$

Therefore, as $\zeta \to \zeta_{i_c}$, (2.19) immediately yields

$$z_{i_e}'(\zeta_{i_c})n_z + r_{i_e}'(\zeta_{i_c})n_r = \frac{z_{i_e}'(\zeta_{i_c})r_{i_e}'(\zeta_{i_c})}{l_{i_e}'(\zeta_{i_c})} \left[\frac{z_{i_e}''(\zeta_{i_c})}{z_{i_e}'(\zeta_{i_c})} - \frac{r_{i_e}''(\zeta_{i_c})}{r_{i_e}'(\zeta_{i_c})}\right] (\zeta - \zeta_{i_c}). \tag{2.20}$$

Accordingly, each function $C_{\alpha\beta}(\mathbf{x}^{i_e}, \mathbf{x}^{i_e}_{i_c})$ turns out to be regular as $\mathbf{x}^{i_e}$ approaches $\mathbf{x}^{i_e}_{i_c}$. The case of weakly singular integrals appears only for integrals (2.11) when $\alpha = \beta$. The diagonals components of (2.11), as $\zeta \to \zeta_{i_c}$, then become

$$B_{rr}(\mathbf{x}^{i_e}, \mathbf{x}^{i_e}_{i_c}) \sim B_{zz}(\mathbf{x}^{i_e}, \mathbf{x}^{i_e}_{i_c}) \sim= 2 \ln \left[\frac{8 r_{i_e}(\zeta_{i_c}) r'_{i_e}(\zeta_{i_c})}{l'_{i_e}(\zeta_{i_c}) \| \zeta - \zeta_{i_c} \|} \right] \tag{2.21}$$

One arrives at two analytic expressions of the regular integrals B_{rr} and B_{zz} on the $[-1, \zeta_{i_c}]$ and $[\zeta_{i_c}, 1]$ segments which are solved using an iterative scheme. Following a procedure defined by [12], a non-uniform refinement of the $[-1, \zeta_{i_c}]$ and $[\zeta_{i_c}, 1]$ segments near the collocation point ζ_{i_c} is performed as illustrated in Figure 2.4.

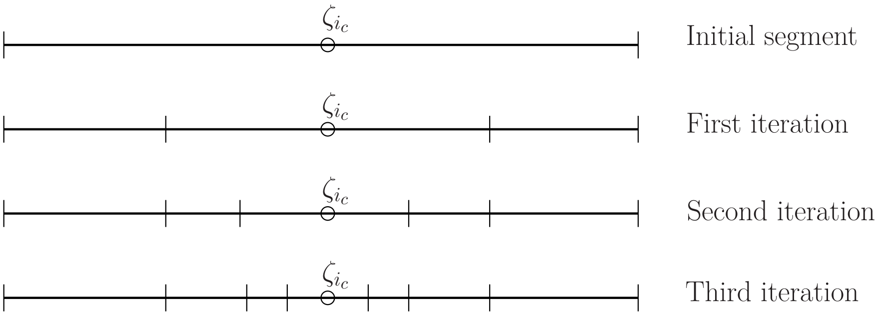

Figure 2.4: Non-uniform refinement on the segment [-1,1] near the collocation point ζ_{i_c}.

This self-adaptive method gives us a high precision of the localization ζ_{i_c}, then the accumulated errors when calculating the integrals B_{rr} and B_{zz} are small.

2.2.5 Wielandt deflation

Recalling the $2N_eN_c$-equation linear system (2.7) $\mathbf{U} - \mathbf{C} \cdot \mathbf{U} = \mathbf{B} \cdot \mathbf{F}$, Pozrikidis [9] shows that the corresponding homogeneous equations $\mathbf{U} - \mathbf{C}.\mathbf{U} = \mathbf{0}$ has only real eigenvalues ω with $\|\omega\| \geq 1$ where $\omega = 1$ are the marginal eigenvalue (the equation presents either no solution or an infinity of solution).

By removing this marginal eigenvalue in the homogeneous equations, one are able to solve the linear system (2.7). Such a task (see Kim and Karrila [4]) is indeed achieved by redefining the kernel of (2.7) while its solution remains unchanged using the Wielandt's deflation technique. Therefore, appealing to a QR method [11], n_{λ_1} eigenvalues close to unity are selected and one obtains a new matrix $\mathbf{C}'$ as explained in [9]

$$\mathbf{C}' = \mathbf{C} - \sum_{n=1}^{n_{\lambda_1}} \lambda_n \mathbf{Z}_n \mathbf{V}_n, \quad \mathbf{Z}_n = \mathbf{V}_n / ||\mathbf{V}_n||^2, \tag{2.22}$$

where $\mathbf{V}_n$ is the eigenvector of the adjoint matrix of $\mathbf{C}$ with its associated eigenvalue λ_n and its discrete norm $||\mathbf{V}_n||^2$ calculated on the entire surface $S = \cup_{m=0}^{N} S_n$. The vector $\mathbf{V}_n$ is collinear on S to the normal vector $\mathbf{n}$ and therefore the scalar product $\mathbf{V}_n \cdot (\mathbf{B} \cdot \mathbf{F})$ is almost equal to zero.

Accordingly, on obtains the new well-posed equation

$$\mathbf{U} - \mathbf{C}' \cdot \mathbf{U} = \mathbf{B} \cdot \mathbf{F} \tag{2.23}$$

to calculate the unknown velocity vector $\mathbf{U}$.

The Wielandt methods is indeed a key steps for the calculations of the relation (2.7). Considering a spherical bubble distant from a free surface, the eigenvalues λ_n of the matrix $\mathbf{C}$ has been predicted by Kim and Karrila [4] using the Lamb's solution such as

$$\lambda_n^- = \frac{-3}{(2n-1)(2n+1)}, \quad n = 1, 2, \cdots \tag{2.24}$$

$$\lambda_n^+ = \frac{3}{(2n+1)(2n+3)}, \quad n = 1, 2, \cdots \tag{2.25}$$

In Figure 2.5 obtained by Pigeonneau and Sellier [7], the computed values of λ_n are then compared with the eigenvalues obtains from (2.24)-(2.25) for different meshes. One clearly sees that for a given mesh, only one eigenvalue locates close to unity. Indeed, this eigenvalue w is built on the bubble and since the unit normal $\mathbf{n}$ and the gravity field $\mathbf{g}$ on the bubble are not collinear, one has $w = 1$ and therfore the Wielandt technique is not required here.

However, for a bubble close to a free surface also considered by Pigeonneau and Sellier [7] in Figure 2.6, the eigenvalues accumulate around the critical point -1 and $+1$ as the distance h between the bubble and the free surface decreases. Moreover, this behavior occurs both for deformed (square marker) and undeformed (diamond marker) free surfaces and one therefore requires the Wielandt method to remove the eigenvalues too close to unity.

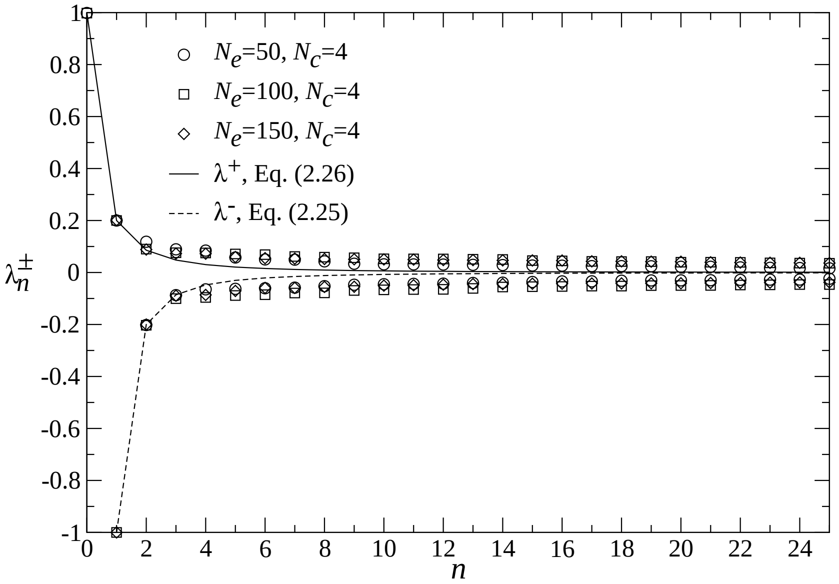

Figure 2.5: Computed eigenvalues and analytical predictions (2.24)-(2.25) for a spherical bubble immersed in an unbounded liquid.

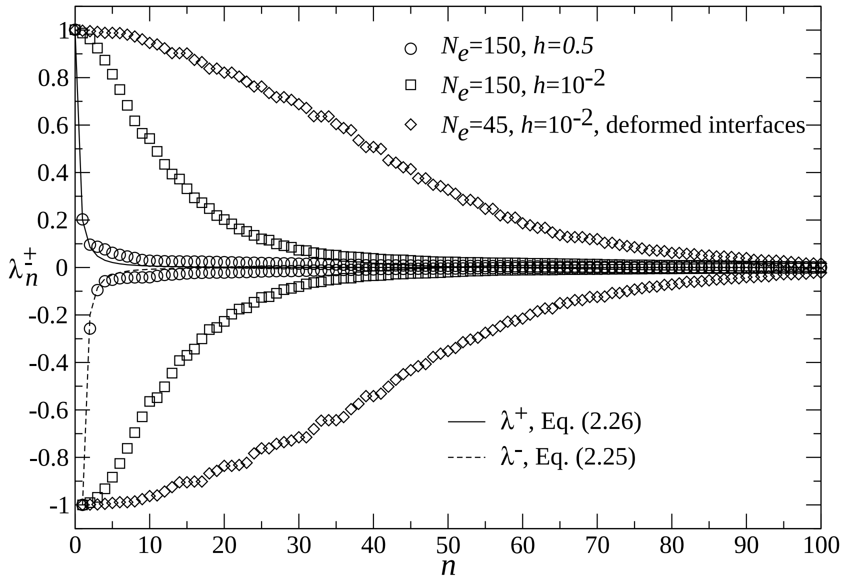

Figure 2.6: Computed eigenvalues for a spherical or non spherical bubble close to a free surface and comparisons with equations (2.24)-(2.25) for a spherical bubble immersed in an unbounded liquid.

Bubble-free surface interface tracking

The shape of each surface S_m is tracked in time using the boundary condition (1.16). Knowing the fluid velocity $\mathbf{u}$ at each nodal point $x_{i_c}^{i_e}$ allows us to move each nodal point $x_{i_c}^{i_e}$ on the boundary between times t and $t + dt$ by solving the equation

$$\frac{d\mathbf{x}_{i_c}^{i_e}}{dt} = \mathbf{u}(\mathbf{x}_{i_c}^{i_e}, t). \tag{2.26}$$

A Runge-Kutta-Fehlberg method performs this task using a time-step selected by controlling the errors for the second and third-order schemes. When the two schemes are in close agreement, the time-step is then accepted. In contrast, if the two schemes do not match to a specified accuracy, the time step is reduced. Once the second-order and third-order schemes are in agreement beyond the prescribed accuracy level, the step size is increased. The "optimal" new time step dt_{new} is therefore calculated from the current time step as follows

$$dt_{new} = dt \sqrt[3]{3 \, \frac{\epsilon}{\|\mathbf{x}_{i_c}^{\alpha}(t+dt) - \mathbf{x}_{i_c}^{\beta}(t+dt)\|}}, \tag{2.27}$$

with the computed position at the second and third order, $\mathbf{x}_{i_c}^{\alpha}(t+dt)$ and $\mathbf{x}_{i_c}^{\beta}(t+dt)$, respectively and a prescribed accuracy $\epsilon > 0$. These Runge-Kutta-Fehlberg schemes require special coefficients taken from the book of Stoer and Burlisch [11]. Regarding the bubble-free surface interaction, it is found that the time step is large and nearly constant between two time iterations when the bubble is far from the surface. On the contrary, when the bubble is closed to the free surface, the prescribed accuracy defined for the Runge-Kutta-Fehlberg method requires the time step to be decreased. Numerical computations are stopped as soon as the film thickness reaches the value of order 10^{-3} or whenever the adjusted time step becomes too small (in practice less than 10^{-5}).

One key issue for the present work is to precisely calculate the quantity $\nabla_S \cdot \mathbf{n}$ on each discretized surface S_m. An adequate approximation of this quantity indeed dictates the accuracy to which the velocity $\mathbf{u}$ is obtained solving (2.1) on the fluid boundary. This is achieved by putting enough nodes on each boundary element.

2.3 Benchmark tests

This section examines the numerical results sensitivity to relevant parameters such as the number of boundary elements on the interfaces, the initial bubble location and the free surface truncature. Indeed, the number of elements on each surface, the initial location of the bubble and the truncature of the free surface are initial parameters that might affect each computed interface shape and/or the film drainage.

2.3.1 Sensitivity to the number of boundary elements on the bubble contour

Numerical simulations have been performed for a bubble and a free surface having identical surface tensions $\gamma_1 = \gamma_0$, therefore the considered Bond number in the present test is $\mathrm{Bo}_1 = \mathrm{Bo}_0 = 1$. The initial (normalized by the bubble diameter) distance between the spherical bubble and the plane undeformed free surface is $h = 0.5$.

We first investigate the sensitivity to the number of boundary elements on the bubble by running simulations for different numbers N_{eb} of elements on the bubble taking $N_{eb} = 5, 10, 15$ and 20 with a given truncated free surface extending over 5 bubble diameters and meshed using 25 boundary elements. Moreover, 4 collocation points are uniformly spread on each boundary element and the smallest element on the free surface therefore presents a typical length of 1/5 in bubble diameter.

In the same manner, at initial normalized time $t = 6\mu/(\rho_l g a)$, the smallest boundary element length on the bubble surface are $\pi/10$, $\pi/20$, $\pi/30$ and $\pi/40$ for $N_{eb} = 5, 10, 15, 20$, respectively.

In the case of a distant bubble shown in Figure 2.7 (a), the bubble shapes nicely gather on the same curve. We further call “error” the difference between two solutions obtained respectively using a low number of element and a large number of element. The biggest error appears between the shapes obtained for $N_{eb} = 10$ and $N_{eb} = 20$ and corresponds to an error of 1% in bubble diameter.

In contrast, Figure 2.7 (b) shows a strong sensitivity of both the bubble and the free surface shapes to the number of boundary elements on a close bubble. This sensitivity decreases when the number of boundary element increases. Focusing on the upper part of the bubble shape along the $z = 0$ axis, a difference of $\Delta h_b = 3.8\,10^{-2}$ is observed (h_b is the height of the bubble) with shapes obtained for $N_{eb} = 5$ and $N_{eb} = 20$ corresponding then to an error of 3.8% in bubble diameter while the comparison between the case $N_{eb} = 10$ and $N_{eb} = 20$ exhibits a variation of 0.6% in bubble diameter.

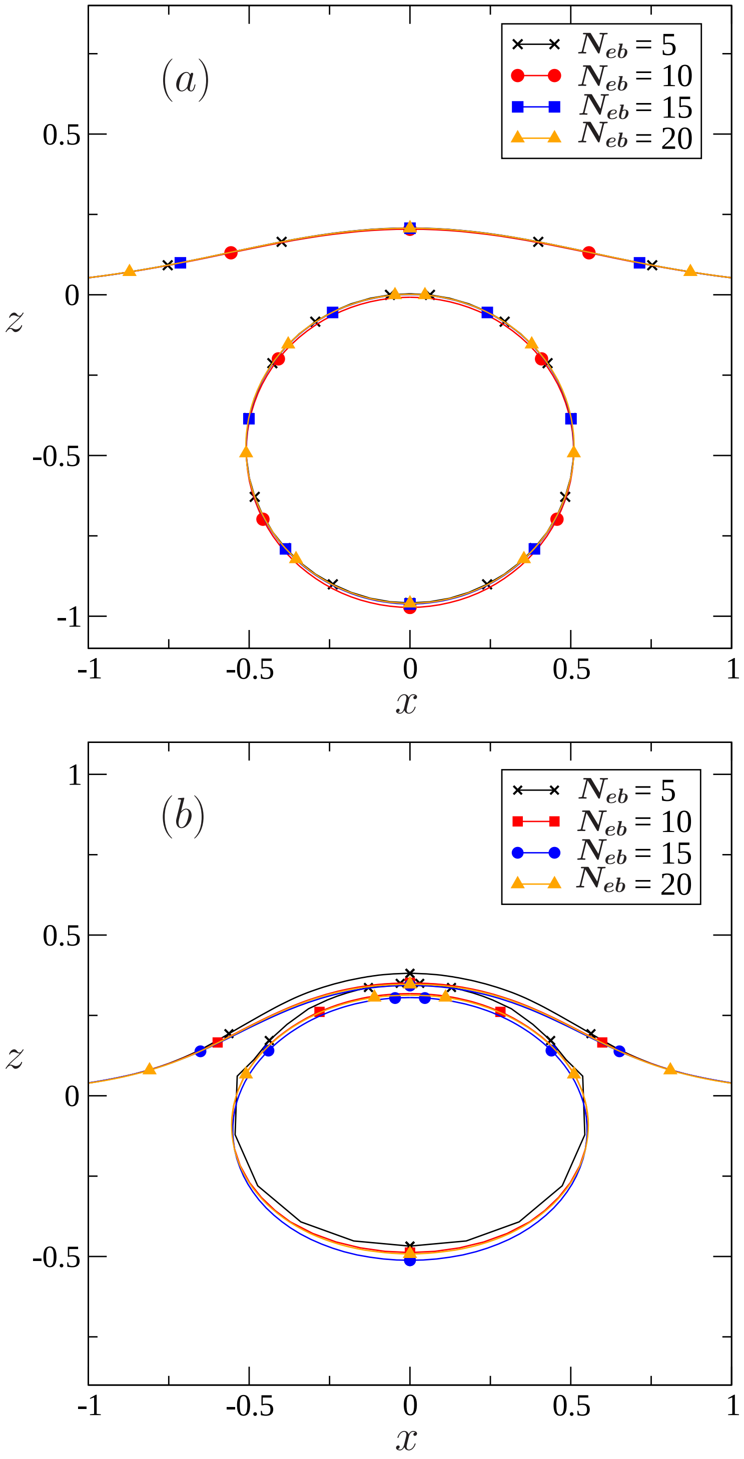

Figure 2.7: Bubble and truncated free surface shapes sensitivity to the number of boundary elements N_{eb} spread on the bubble surface. These computed shapes are obtained for $\mathrm{Bo}_1 = 1$ with equal surface tensions on the surfaces ($\gamma_0 = \gamma_1$) at normalized time (a) $t_a = 0.602$ and (b) $t_b = 1.486$.

The lower part of the bubble reveals, for $N_{eb} = 5$ and $N_e = 20$, a smaller difference of order of $\Delta h_b = 2.5\,10^{-2}$, i.e. 2.5% in bubble diameter.

Not surprisingly, more collocation points near the bubble-free surface interaction are required to obtain a better resolution. Moreover, the free surface shape is also affected by the number of boundary elements that are distributed on the bubble. In accordance with the previous results for the bubble shape, the free surface shape sensitivity to N_e reduces as the number N_{eb} of elements increases.

Comparing the case $N_{eb} = 5$ and $N_{eb} = 20$ one gains an error of $\Delta h_s = 3.5\,10^{-2}$ (h_s is the height of the free surface), i.e. of 3.5% in bubble diameter whereas the difference between $N_{eb} = 15$ and $N_{eb} = 20$ shows an error of $\Delta h_s = 6.10^{-3}$, i.e. of 0.6% in bubble diameter. Henceforth, 20 boundary elements on the bubble surface seems enough to accurately compute both the bubble and free surface shapes. Finally, introducing a relative error $\epsilon_b = \Delta h_b/h_b$ for the bubble shapes and $\epsilon_s = \Delta h_s/h_s$ for the free surface shapes, we consider then $\epsilon_b = 3.1\,10^{-2}$ and $\epsilon_s = 1.5\,10^{-2}$ being acceptable errors.

2.3.2 Sensitivity to the number of boundary elements on the free surface

Similarly to the previous test, the bubble and free surface shapes sensitivity to the number of boundary elements, N_{ef}, spread on the *free surface* for $\mathrm{Bo}_1 = 1$ and a spherical bubble initially distant of one radius from the free surface have been examined. Those shapes are computed for a bubble surface consisting of 20 boundary elements and a truncated free surface extending over 5 bubble diameters with different numbers $N_{ef} = 5, 10, 20, 25$ of boundary elements.

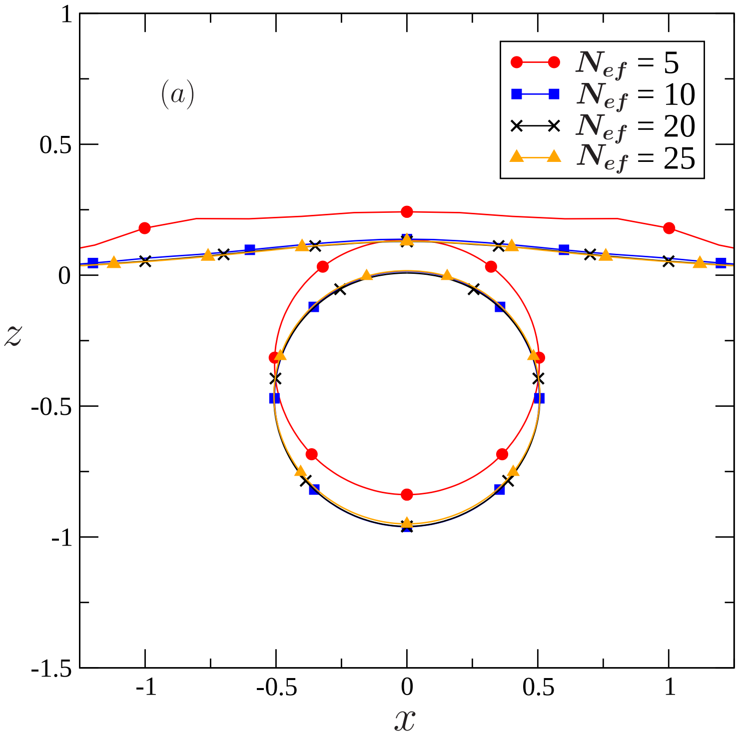

Figure 2.8: Bubble and free surface shapes sensitivity to the number of boundary elements N_{ef} spread on the free surface. The computed shapes are obtained at normalized time $t = 0.8005$ for $\mathrm{Bo}_1 = 1$ and equal surface tensions ($\gamma_0 = \gamma_1$).

Each boundary element has 4 collocation points and the smallest element on the bubble presents a typical length of $\pi/40$. Accordingly, at initial time, the smallest boundary element length on the free surface (which extend over 5 bubble diameters) are 1, 1/2, 1/4 and 1/5 for $N_{ef} = 5, 10, 20, 25$, respectively.

As expected, Figure 2.8 shows that the number of boundary elements on the free surface clearly affects the computed shapes. Once the number of boundary elements exceeds 5, the predicted free surface shapes gather nicely on the same curve. Differences with the shapes obtained for $N_{ef} = 5$ and $N_{ef} = 25$ are indeed of order of $\Delta h_s = 0.11$ (h_s is the free surface height taken at $x = 0$) which correspond to an error of 11% in bubble diameter whereas comparing the case of $N_{ef} = 10$ with $N_{ef} = 20$, one finds an error of $\Delta h_s = 9.10^{-3}$, i.e. 1% in bubble diameter. In addition, by increasing the number N_{ef} of boundary elements to 25, an suitable error of $\Delta h_s = 2.10^{-3}$ on the free surface shape (0.2% in bubble diameter) is reached. Hence, a number of $N_{ef} = 25$ boundary elements on the free surface is required to accurately calculate our free surface shapes.

Furthermore, one remarks that not only the free surface shape but also the bubble shape is sensitive to the number of boundary elements distributed on the free surface. Similarly to the free surface shape, as soon as the number of boundary elements exceeds 5, all the bubble shapes gather on the same curve with a minimal reasonable error of $\Delta h_b \sim 9.10^{-3}$ (h_b is the bubble height).

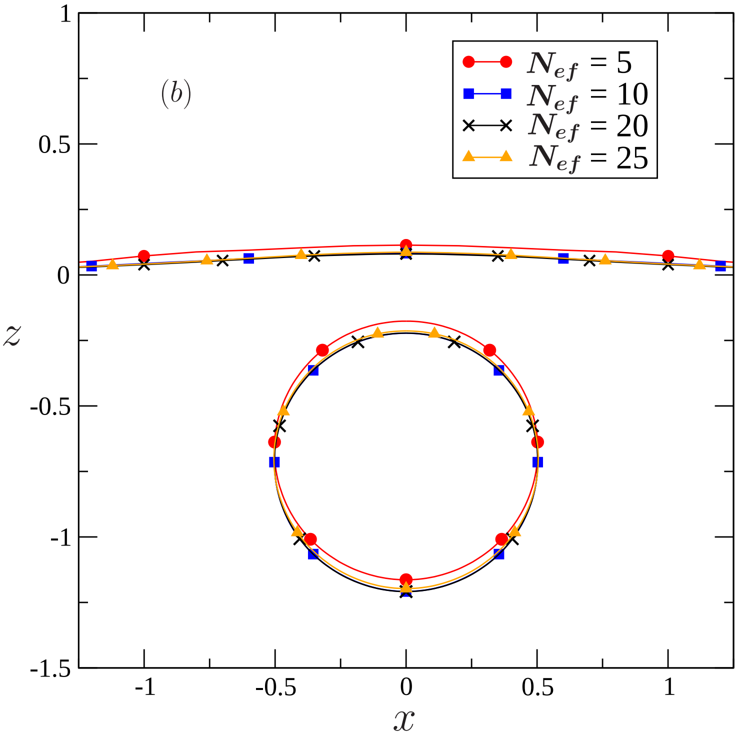

Figure 2.9: Bubble and free surface shapes sensitivity to the number of boundary elements N_{ef} distributed on the free surface. The computed shapes are obtained at normalized time $t = 0.680$ for $\mathrm{Bo}_1 = 1$ and equal surface tensions ($\gamma_0 = \gamma_1$).

Not surprisingly, the sensitivity to the number of boundary elements used on the free surface decreases for a distant bubble. Figure 2.9 depicts at small time $t = 0.680$ bubble and free surface shapes. By comparison with Figure 2.8, both the bubble and the free surface shapes obtained for $N_{ef} = 5$ show differences $\Delta h_s = \Delta h_b = 3.10^{-3}$ with the two errors calculated for $N_{ef} = 25$.

2.3.3 Sensitivity to the bubble initial location

Numerical simulations have also been achieved for five different initial bubble locations l_i below the fluid interface. The free surface is truncated over 5 bubble diameters and the number of boundary elements are $N_{eb} = 20$ and $N_{ef} = 25$ on the bubble and the free surface interfaces, respectively. Moreover, four collocation points on each boundary element are used. First, this test is performed for $\mathrm{Bo}_1 = 1$ with the bubble and the free surfaces having the same surface tension. In a second stage, extreme values for the Bond number and of the surface tension ratio $\hat{\gamma}$ are examined.

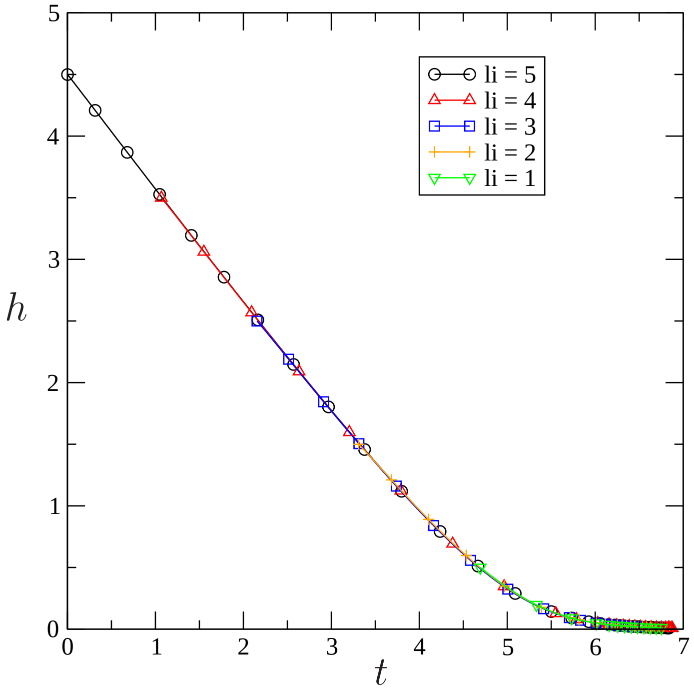

Figure 2.10: Film thickness $h(t)$ versus time for different initial bubble locations $l_i = 1, 2, 3, 4, 5$ and $\mathrm{Bo}_1 = 1$. Moreover $\gamma_0 = \gamma_1$.

Figure 2.10 plots versus time the film drainage $h(t)$ for one bubble with different initial bubble locations l_i, with l_i the bubble center distance to the flat undisturbed free surface ($z = 0$ plane). Accordingly $h(0) = l_i - 1/2$, i.e. for $l_i = 2$ the corresponding initial film thickness is $h(0) = 1.5$. Furthermore, the surface tensions are taken identical on the bubble and the free surface with $\mathrm{Bo}_1 = 1$. In all cases, the film drainage shows the same trend whatever the selected bubble location l_i.

Figure 2.11 depicts the corresponding interface shapes for different initial bubble locations l_i when $h = 0.5$. One observes as soon as $l_i \geq 1$, the bubble and free surface shapes gather on the same curve whereas the bubble and interface shapes for $l_i = 1$ present a clear difference.

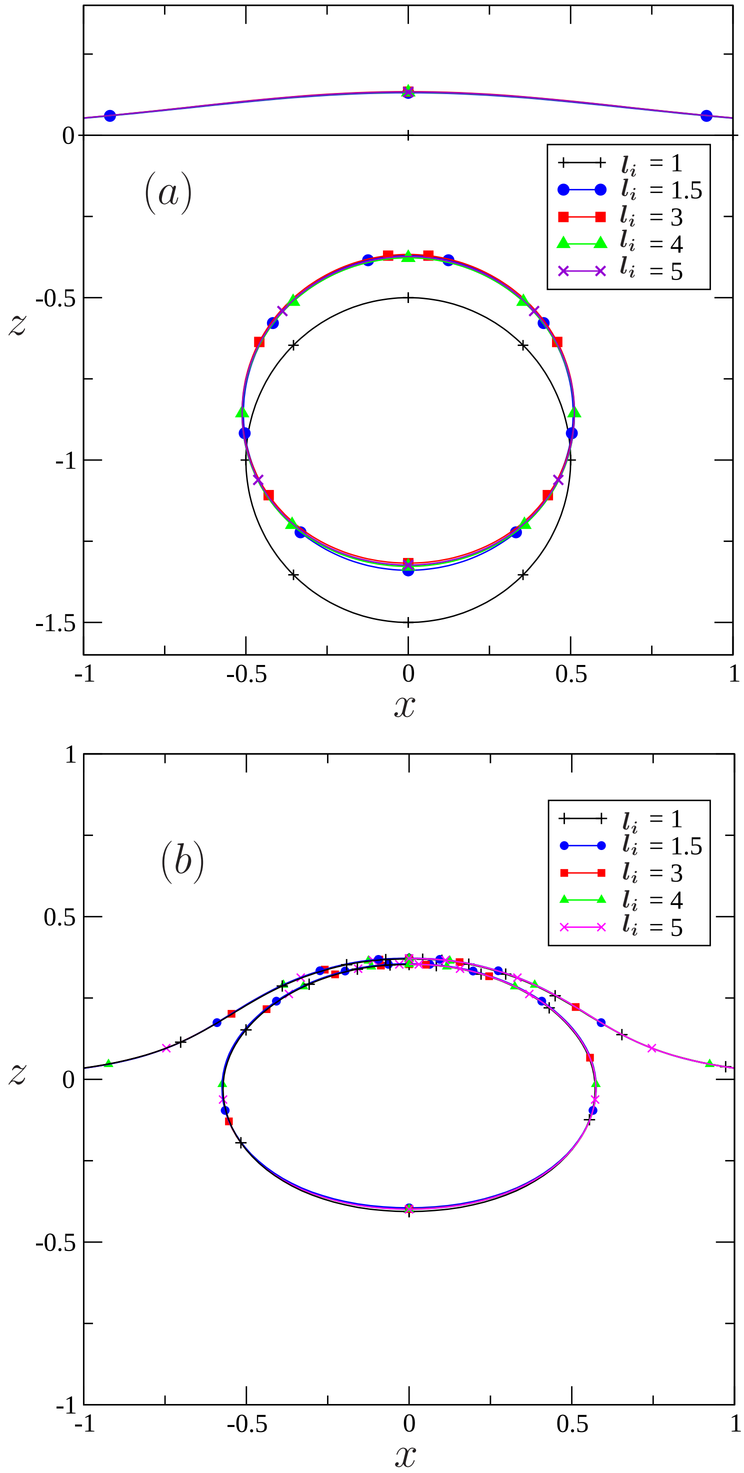

Figure 2.11: Bubble and free surface shapes for different initial bubble locations $l_i = 1, 1.5, 3, 4, 5$ and $\mathrm{Bo}_1 = 1$ ($\gamma_0 = \gamma_1$) as computed for (a) $h = 0.5$ and (b) $h = 1.77 \times 10^{-2}$.

Since the numerical simulation starts with a spherical bubble and a flat free surface, the first stage of the bubble ascension is indeed not yet stabilized in the earlier regime and a transition period is required to obtain the real deformed bubble and interface shapes corresponding to the distance $h = 0.5$. Therefore, the bubble shapes which start moving with $h(0) \geq 0.5$ are beyond the transition period and fit nicely together.

Nevertheless, when the bubble is close to the surface, all the interface shapes match at the same distance $h = 1.77 \times 10^{-2}$ as shown in Figure 2.11. The final drainage study of the film thickness $h(t)$ is then independent of the initial bubble location. However, the first drainage period should be examined with an initial bubble distance of $l_i = 1.5$.

When investigating the film drainage sensitivity to the surface tension, additional tests have been performed for a surface tension ratio $\hat{\gamma} = 0.2, 5$ and Bond numbers $\mathrm{Bo}_1 = \rho_l g a^2/(3\gamma_1) = 0.3, 1$ and 5. Figure 2.12 depicts, for $\mathrm{Bo}_1 = 1$, the film drainage sensitivity to the surface tension ratio $\hat{\gamma}$.

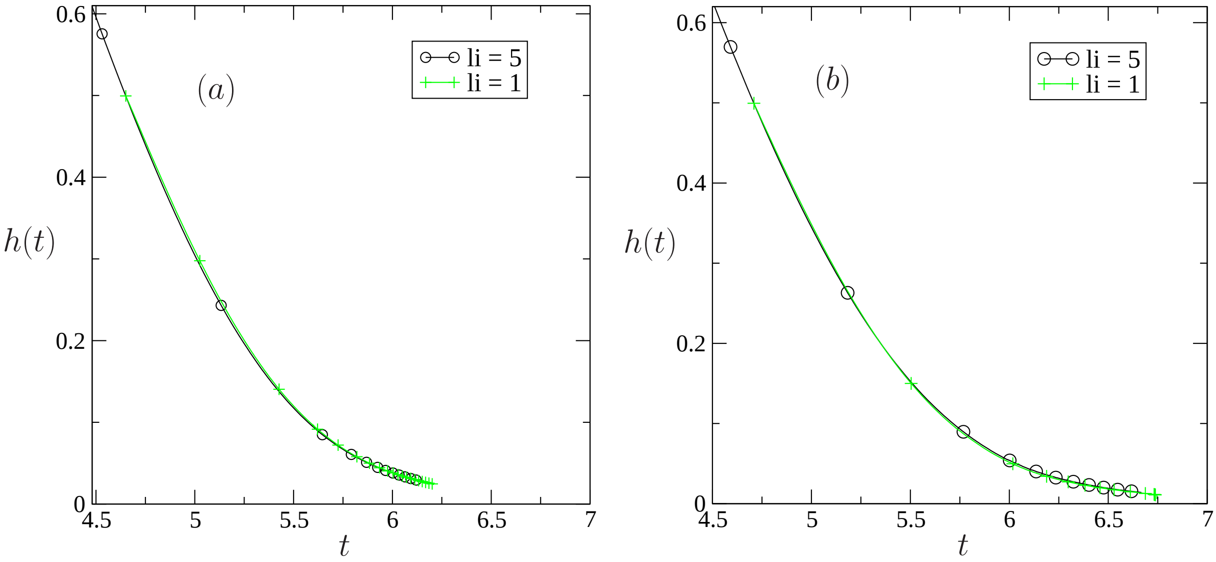

Figure 2.12: Film thickness $h(t)$ versus time for different initial bubble locations $l_i = 1$ (green cross line) and $l_i = 5$ (black circle line) at $\mathrm{Bo}_1 = 1$ for two different surface tension values: (a) $\hat{\gamma} = 5$ and (b) $\hat{\gamma} = 0.2$.

Clearly, for $\mathrm{Bo}_1 = 1$, the film drainage remains unaffected by the bubble initial location for both small and large given values of the surface tension ratio $\hat{\gamma}$.

The case of small and large Bond numbers has been also examined and the results are displayed in Figure 2.13 where the upper graphs correspond to $\mathrm{Bo}_1 = 5$ and the lower graphs are for $\mathrm{Bo}_1 = 0.3$. In contrast with the case of $\mathrm{Bo}_1 = 1$, the film drainage history is slightly different when the bubble starts rising at $l = 5$ than when starting at $l = 1$ for both $\hat{\gamma} = 5$ and $\hat{\gamma} = 0.2$ whatever the Bond number.

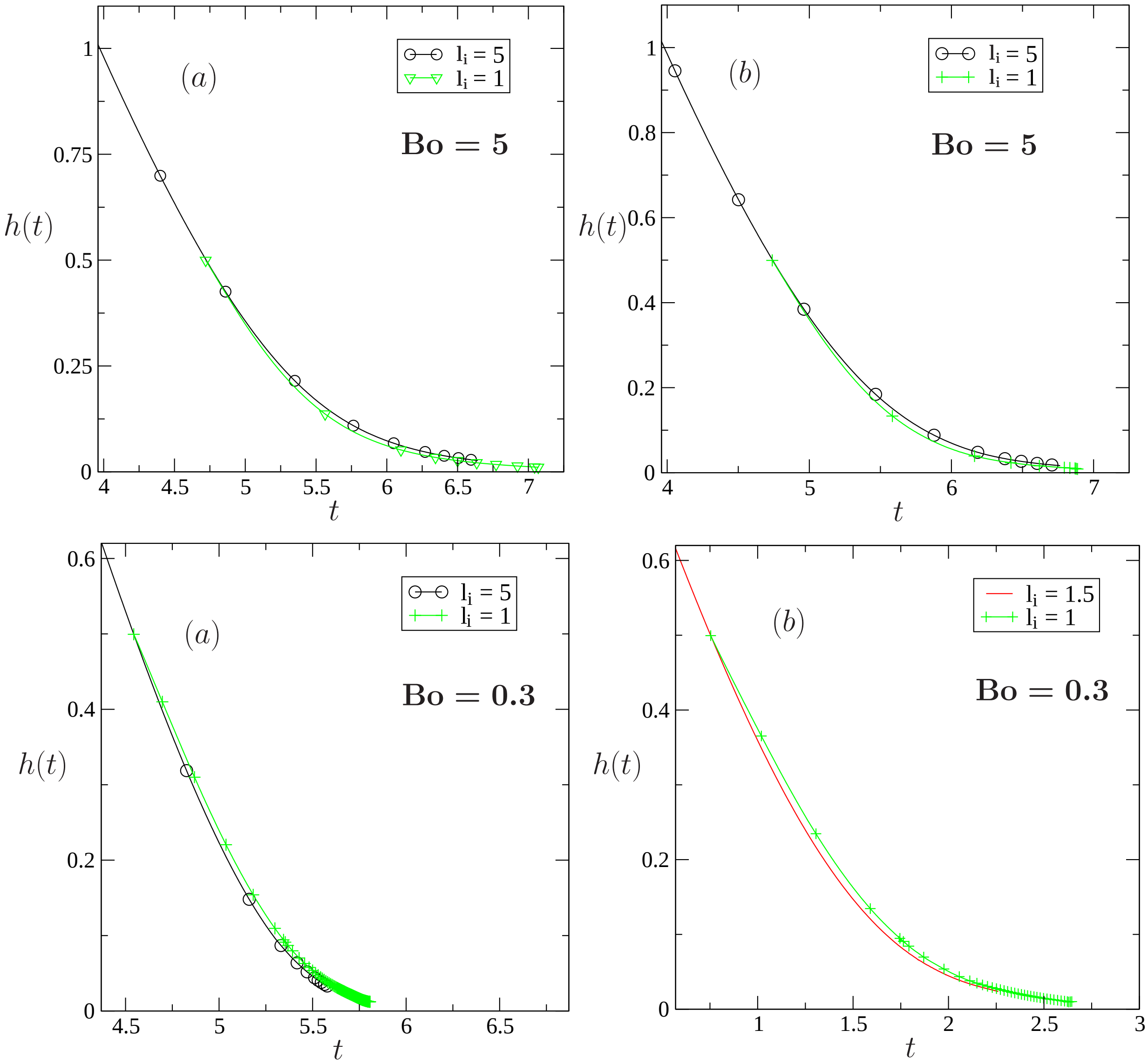

Figure 2.13: Film thickness $h(t)$ versus time for different initial bubble locations $l_i = 1$ (green cross line) and $l_i = 5$ (black circle line) at $\mathrm{Bo}_1 = 5$ (upper graphs) and $\mathrm{Bo}_1 = 0.3$ (lower figures) for two different surface tension values: (a) $\hat{\gamma} = 5$ and (b) $\hat{\gamma} = 0.2$.

Nevertheless, the curves for $l_i = 1$ and $l_i = 5$ exhibit similar trends and this discrepancy vanishes for $\mathrm{Bo}_1 = 5$ as soon as the initial location is equal to $l_i = 1.5$ (see Figure 2.14).

At small Bond number $\mathrm{Bo}_1 = 0.3$, the differences between the curves for $l_i = 1$ and $l_i = 5$ remain as shown in Figure 2.15. However for $\hat{\gamma} = 5$, this small difference holds constant in time implying that the drainage rate is identical for both initial bubble locations whereas the small discrepancy for $\hat{\gamma} = 0.2$ changes in time.

In summary, the initial bubble location affects the numerical results at the beginning of the computation as illustrated in Figure 2.11. This effect vanishes when the bubble motion starts at $l_i = 1.5$. The sensitivity of the film drainage to the initial bubble location is weak and occurs only for extreme values of the Bond number and surface tension ratio (see Figures 2.13-2.14).

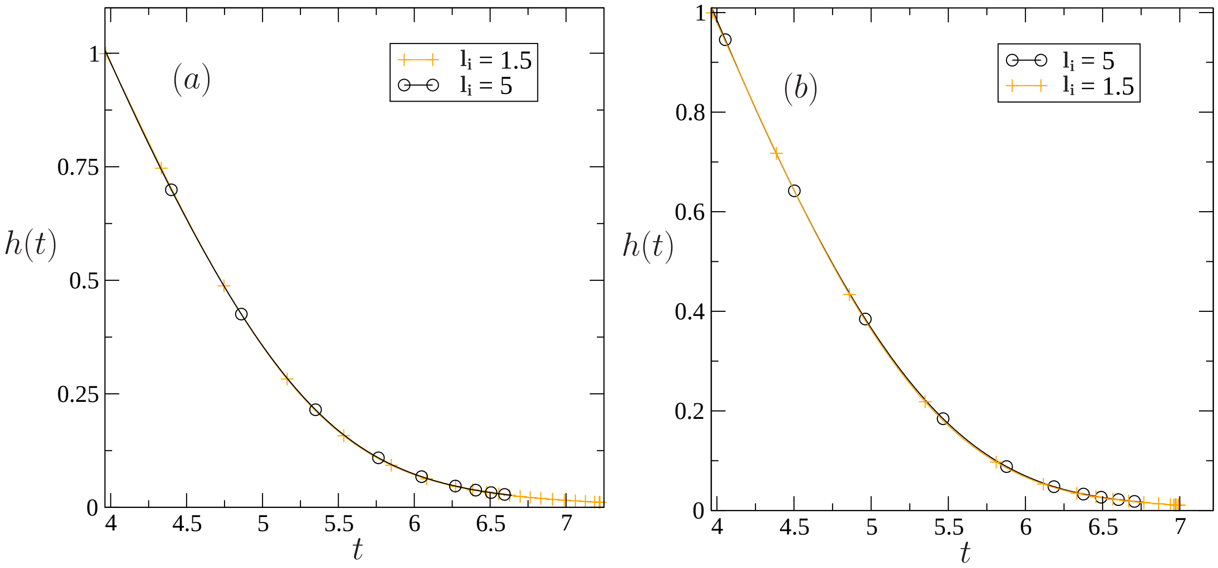

Figure 2.14: Film thickness $h(t)$ versus time for different initial bubble locations $l_i = 1.5$ (yellow cross line) and $l_i = 5$ (black circle line) at $\mathrm{Bo}_1 = 5$ for two different surface tension ratio: (a) $\hat{\gamma} = 5$ and (b) $\hat{\gamma} = 0.2$.

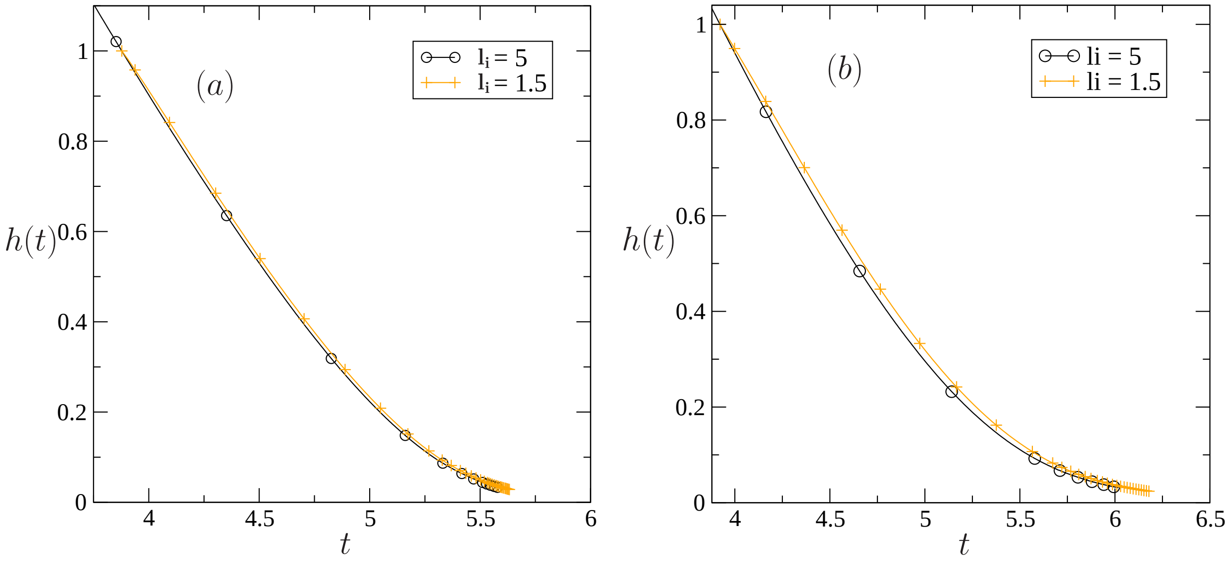

Figure 2.15: Film thickness $h(t)$ versus time for different initial bubble locations $l_i = 1.5$ (yellow cross line) and $l_i = 5$ (black circle line) at $\mathrm{Bo}_1 = 0.3$ for two different surface tension ratio: (a) $\hat{\gamma} = 5$ and (b) $\hat{\gamma} = 0.2$.

Furthermore, the discrepancy appearing between the two locations $l_i = 1$ and $l_i = 5$ vanishes when the bubble start its motion at $l_i = 1.5$ for $\mathrm{Bo}_1 = 5$. However, the case of small Bond number $\mathrm{Bo}_1 = 0.3$ has to be carefully handled since the difference remains even at the final computation step (see Figure 2.15).

2.3.4 Sensitivity to the free surface truncature

As explained in §I.2.2.1, the numerical treatment of the prescribed bubble-free surface interaction problem is achieved using a truncated free surface.

The size of such a truncated free surface directly dictates the computational time cost since one requires to supplement or to remove boundary elements from the surface to keep the typical length of those elements constant at initial time. For instance, boundary elements with typical length of 1/5 correspond to either a free surface extending over 5 bubble diameters and composed of $N_{ef} = 25$ boundary elements or a 10 bubble diameters free surface with $N_{ef} = 50$ boundary elements.

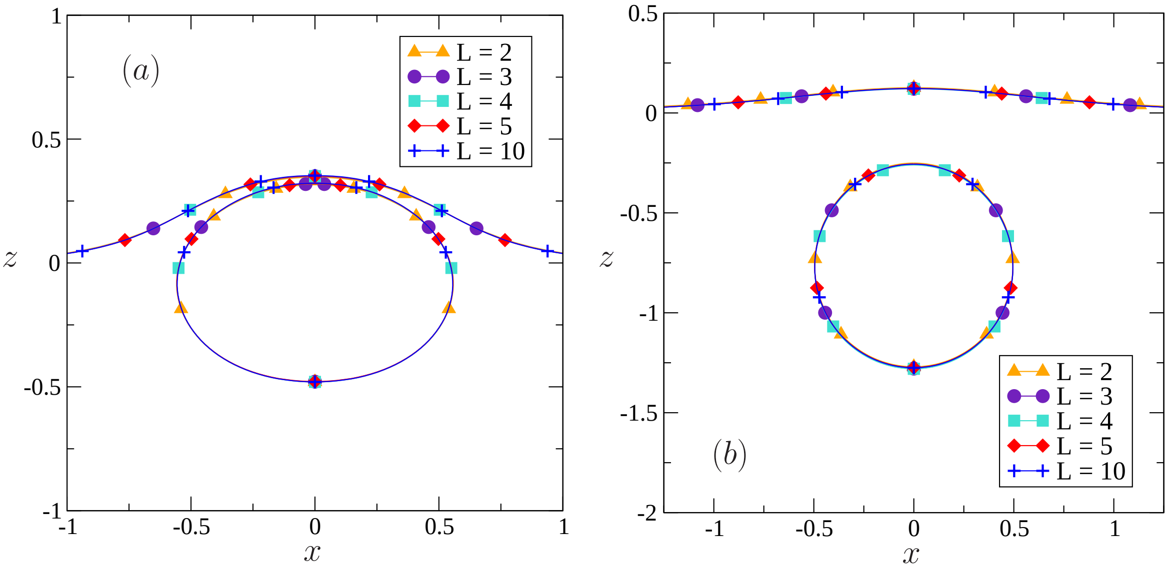

Figure 2.16: Bubble and free surface shapes at different times for different truncation distances $L = 2, 3, 4, 5, 10$ for the free surface with $\mathrm{Bo}_1 = 1$ and $\gamma_0 = \gamma_1$. (a) $t = 0.602$ and (b) $t = 0.221$.

One aims then at reducing the computational time cost by investigating the sensitivity of the bubble and truncated free surface to the distance L of truncation for the free surface.

As for the previous benchmark tests, the bubble is initially distant of one bubble diameter, the surface tensions are identical on the bubble and the free surface and $\mathrm{Bo}_1 = 1$.The number of boundary elements spread on the bubble and free surfaces are equal to $N_{eb} = 20$ and $N_{ef} = 25$, respectively and the computations are performed for various truncation distances $L = 2, 3, 4, 5, 10$ (in bubble diameters) with $N_{ef} = 10, 15, 20, 25, 50$ boundary elements spread on the free surface. The number of elements N_{ef} has been selected to keep the typical length (1/5) of the smallest element on the free surface constant as the distance L increases.

As seen in Figure 2.16(a), the bubble and the free surface shapes are unaffected by changing truncation. The difference with the shapes obtained for $L = 2, N_e = 10$ and $L = 5, N_e = 25$ is of order of $\Delta h = 4.5\,10^{-3}$. Denoting by $\epsilon = \Delta h/h$ the relative error on the free surface height at the $z = 0$ axis, on gets $\epsilon = 1.3\,10^{-2}$ in the present case which therefore corresponds to a suitable error of 1.3% in bubble diameter.

The case of a weakly deformed free surface for a distant bubble has also been considered. Similarly to the previous results, Figure 2.16(b) reveals that the bubble and the free surface shapes are slightly subjected to the truncation distance L of the free surface. The error for the cases of $L = 2, N_e = 10$ and $L = 5, N_e = 25$ is $\Delta h_s = 3.9\,10^{-3}$ (h_s is the free surface height taken at $x = 0$). Nevertheless, one finds a larger relative error $\epsilon = 3.2\,10^{-2}$ since the free surface is less deformed.

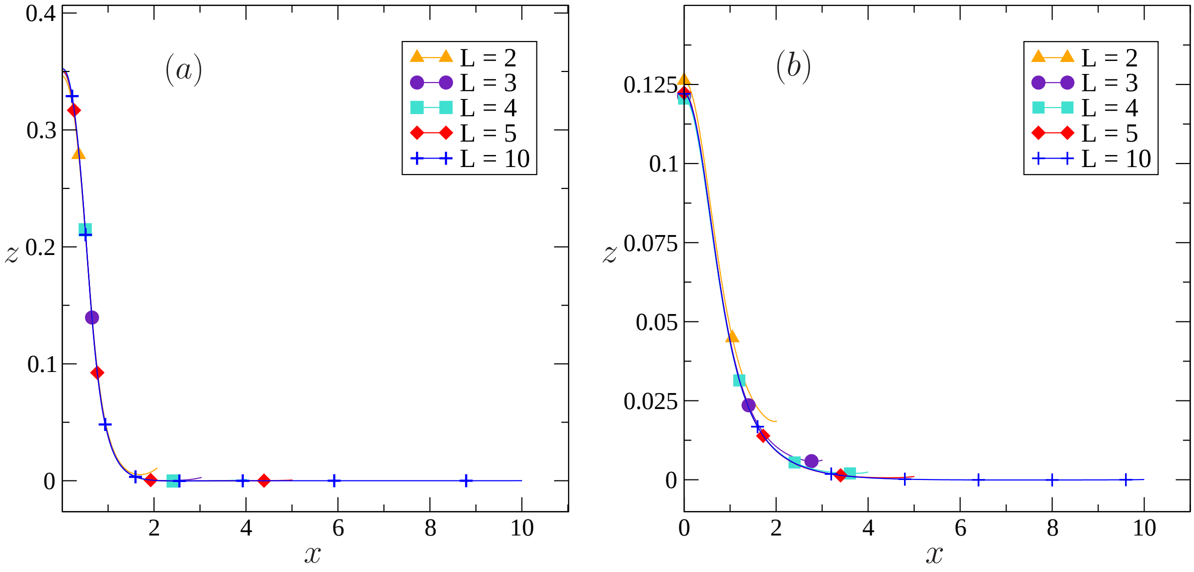

Figure 2.17: Free surface shapes at several normalized times for different truncation distances $L = 2, 3, 4, 5, 10$ for the free surface with $\mathrm{Bo}_1 = 1$ and $\gamma_0 = \gamma_1$. (a) $t = 0.602$ and (b) $t = 0.221$.

Finally, the tail of the free surface shape has been carefully examined in Figures 2.17(a) and 2.17(b). Surprisingly, the computed free surface shapes show different behaviors far from the z-axis. As shown in Figures 2.17(a), the free surface is highly deformed and its shapes meet on an identical curve for a truncation beyond the distance $L = 4$ bubble diameters.

For a distant bubble, the free surface is then weakly deformed and one requires a truncation at least at $L = 10$ bubble diameters distance to accurately impose the far-field behavior, i.e. a $z = 0$ free surface as $x \to \infty$.

Consequently, adopting a truncated free surface at $L = 5$ bubble diameters is a relevant choice in case of strong deformation. Nevertheless, as soon as the deformation becomes small, one needs a larger truncated free surface. Such a case of weakly deformed free surface is also encountered in the asymptotic analysis developed in Chapter 4.

Bibliography

[1] M. Abramowitz and I. A. Stegun. *Handbook of mathematical functions*. Dover Publications, Inc., New York, 1965.

[2] D. N. Arnold and W. L.Wendland. On the asymptotic convergence of collocation methods. *Math. of Comput.*, 41:349–381, 1983.

[3] Y. Iso and K. Onishi. On the stability of the boundary element collocation method applied to the linear heat equation. *J. Comput. Appl. Math.*, 38(1-3):201 – 209, 1991.

[4] S. Kim and S. J. Karrila. *Microhydrodynamics. Principles and selected applications.* Butterworth-Heinemann, Boston, 1991.

[5] P. Parreira and M. Guiggiani. On the implementation of the Galerkin approach in the boundary element method. *Comput. Struct.*, 33:269–279, 1989.

[6] A. P. Peirce and J. A. L. Napier. A spectral multipole method for efficient solution of large-scale boundary element models in elastostatics. *Int. J. Num. Methods Eng.*, 38(23):4009–4034, 1995.

[7] F. Pigeonneau and A. Sellier. Low-Reynolds-Number gravity-driven migration and deformation of bubbles near a free surface. *Phys. Fluids*, 23:092302, 2011.

[8] A. Portela, M. H. Aliabadi, and D. P. Rooke. The dual boundary element method: Effective implementation for crack problems. *Int. J. Num. Methods Eng.*, 33(6):1269–1287, 1992.

[9] C. Pozrikidis. *Boundary integral and singularity methods for linearized viscous flow.* Cambridge University Press, Cambridge, 1992.

[10] S. Sirtori. General stress analysis method by means of integral equation and boundary elements. *Meccanica*, 14:210–218, 1979.

[11] J. Stoer and R. Bulirsch. *Introduction to numerical analysis.* Springer-Verlag, New York, 1993.

[12] S. Voutsinas and G. Bergeles. Numerical calculation of singular integrals appearing in three-dimensional potential flow problems. *Appl. Math. Modelling*, 14:618–629, 1990.

[13] Y. Wang and P. Dimitrakopoulos. A three-dimensional spectral boundary element algorithm for interfacial dynamics in stokes flow. *Phys. Fluids*, 18(8):–, 2006.

Chapter 3

Numerical Results: surface tension effects

Contents

This chapter presents the numerical results obtained for a bubble rising toward a free surface in 2d-axisymmetric configuration. The surface tension effect is carefully investigated. The interface morphology and the drainage of the liquid film between the bubble and the free surface will be investigated.

The surface tension $\gamma_1 > 0$ on the bubble may be different from the surface tension of the free surface γ_0. Therefore, a surface tension ratio $\hat{\gamma} = \gamma_0/\gamma_1$ is introduced. Adopting a typical length based on the bubble diameter $2a$, a typical velocity $U_\infty = \rho_l g a^2/(3\mu)$ and a normalized time $t = \rho_l \mu/ga$, we introduce dimensionless numbers as the Bond number $\mathrm{Bo}_1 = \rho_l g a^2/(3\gamma_1)$ and Capillary number $\mathrm{Ca}_1 = \mu U/\gamma_1$. Henceforth, the computation are run taking $L_t = 5$ (free surface cut off), $N_{eb} = 20$ boundary elements on the bubble with center initially located at $l/2a = 1$ and $N_e = 25$ boundary elements on the truncated free surface.

3.1 Bubble and free surface shapes evolution in time

3.1.1 Sensitivity to the surface tension

The present work extends the experimental study of Kočárková [6] on the drainage of a nitrogen (N_2) bubble in molten glass.

During the glass melting process, raw materials, mainly composed of silica SiO_2, calcium carbonate $CaCO_3$ and sodium carbonate Na_2CO_3, are introduced in the glass furnaces. Once these materials start to melt (around 800°C), chemical reactions occurs the global reaction occur according to relation (3.1). In reality, the chemical paths are more complex depending on heating rate and granulometry of raw material [3]. The release of CO_2 leads to a huge amount of bubbles by nucleation process [16].

$$\mathrm{SiO_2 + Na_2CO_3 + CaCO_3 \to SiO_2 \cdot Na_2O \cdot CaO + CO_2}. \tag{3.1}$$

To help the bubble removal, fining agents such as sulfate (Na_2SO_4) are generally added in the raw materials, releasing SO_2 and O_2 bubbles at 1450°C and therefore increasing the bubbles sizes thanks to the mass transfer [6]-[16].

One should mention that the characteristic time for mass transfer is three order of magnitude smaller than the time scale for the bubble radius variation [11], due, for instance, to the weak solubility of the CO_2 and N_2 gases. The removal of bubbles is driven by the buoyancy forces. Since the terminal velocity of bubbles is proportional to the square of bubble radius, the larger is the radius, the faster is the removal. Sometimes, the source of bubbles coming from the bulk is sufficiently large to create of foam [13]. In fact, the occurence of foam is a balance of bubble source coming from the bulk and the bubble bursting at the top of the bath. This explains why it so important to know the lifetime of bubbles at the free surface.

The dynamic viscosity changes conjointly with temperature in molten glass, however, the present study is investigated for a given temperature of 1200°C (glass is in a liquid state) and therefore the viscosity is constant with a value $\mu = 72\ Pa.s$ [6]. A typical value of the surface tension in a molten glass at 1200°C is around 300 $\mathrm{mN.m^{-1}}$. Experimental measurements of the surface tension in the molten glass being ardeous tasks, the study of a nitrogen bubble near a free surface performed by Kočárková [6] has therefore not examined the surface tension effect on the bubble-free surface interacting system.

The surface tension indeed depends on the gas nature and the atmosphere effect on the surface tension of the glass has been examined for decades [10]. The change of surface tension in the molten glass dependings on the gas nature has been also studied by Nizhenko and Smironov [9] as illustrated in Figure 3.1.

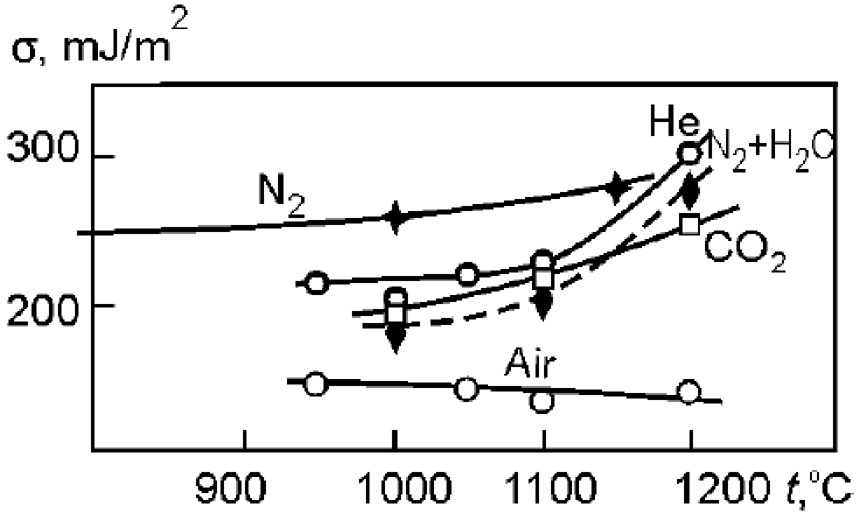

Figure 3.1: Sensitivity of the surface tension to the gas nature in the molten glass. Figure taken from [9] where $mJ/m^2 = mN/m$.

Recalling then the case of a nitrogen bubble near a free surface in [6] and using Figure 3.1, the surface tension in the case of N_2 is indeed twice more important than the value of the surface tension for air, i.e. $\gamma_{air}/\gamma_{N_2} = 0.56$ which may involve an effect on the dynamics of the bubble drainage. Denoting by $\hat{\gamma}$ the surface tension ratio comparing the free surface tension γ_0 to the bubble tension γ_1 such as

$$\hat{\gamma} = \frac{\gamma_0}{\gamma_1} \tag{3.2}$$

different cases of bubble-free surface interaction might therefore occur in molten glass depending on $\hat{\gamma}$.

Three cases are illustrated in Figure 3.2.

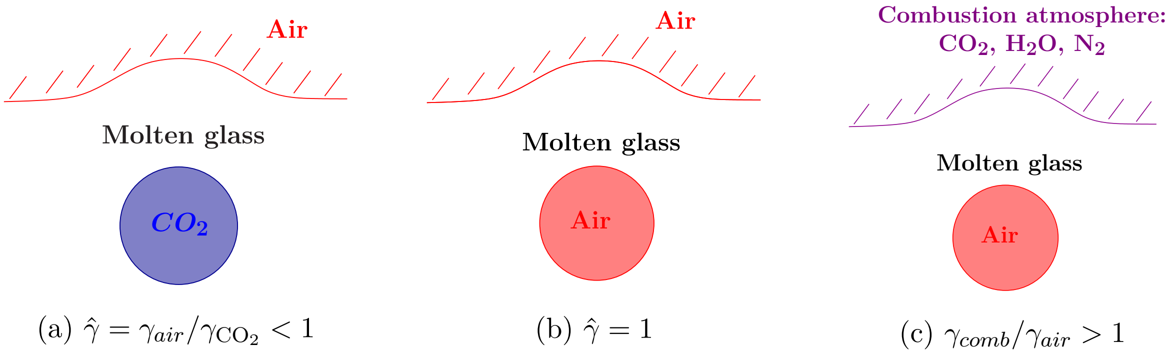

(a) $\hat{\gamma} = \gamma_{air}/\gamma_{CO_2} < 1$ (b) $\hat{\gamma} = 1$ (c) $\gamma_{comb}/\gamma_{air} > 1$

Figure 3.2: Sketch of three cases in which $\hat{\gamma} \leq 1$ or $\hat{\gamma} \geq 1$ in the molten glass: (a) ambient air above a bubble made of CO_2 or (b) ambient air above a air bubble or (c) combustion atmosphere (H_2O, N_2, CO_2) above an air bubble.

The gas above the molten glass is composed of various gas species such as water-vapor, ambient air, CO_2 and sulfur dioxide SO_2 [10].

Accordingly, the case of similar surface tension between the bubble and the free surface as sketched in Figure 3.2 (b) is quite uncommon and one should rather observe surface tension ratio $\hat{\gamma}$ values different of unity. For instance, taking a bubble of CO_2 gas under a free surface of ambient air (as sketched in Figure 3.2 (a)) from the Figure 3.1, the surface tension ratio equals $\hat{\gamma} = 0.56 < 1$ at 1200°C. In contrast, if we now consider a combustion atmosphere above the free surface constituted of H_2O, N_2 and CO_2 (as illustrated in Figure 3.2 (c)), one may obtain $\hat{\gamma} > 1$. Allowing different surface tension is therefore relevant when studying the bubble dynamics near a free surface in a viscous liquid.

The surface tension ratio $\hat{\gamma}$ supplements the Bond number Bo_1 (i.e. based on the bubble surface tension γ_1) to adequately describe all encountered cases. For instance, both for γ_0 and γ_1 having the same either large value or small value, the surface tension ratio is $\hat{\gamma} = 1$ while the Bond number, based on the bubble surface tension γ_1 shows different values. Combining the two dimensionless parameters (Bo_1, $\hat{\gamma}$) permits then one to cover the entire range of possible cases when paying attention to one bubble migrating near the free surface.

For each case (Bo_1, $\hat{\gamma}$), one first examines the bubble and free surface time-dependent shapes and then the liquid film thickness between the bubble and the free surface evolution in time (i.e. the so-called drainage).

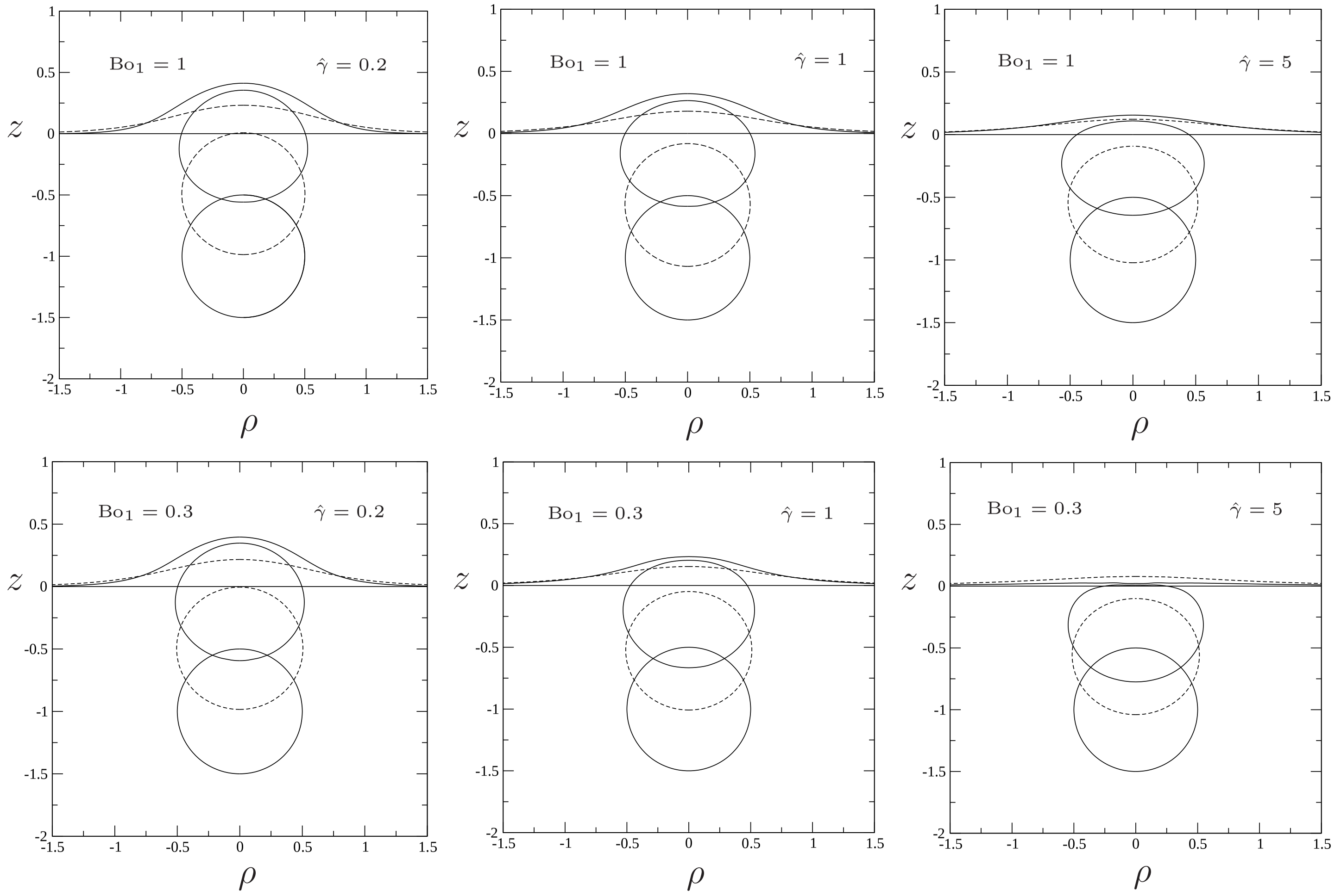

Figure 3.3: Bubble and free surface shapes at normalized times $t_0 = 0$, $t_1 = 0.590$ (dashed lines) and $t_f = 1.264$ for $\hat{\gamma} = 0.2, 1, 5$. The upper figures correspond to $\mathrm{Bo}_1 = 1$ whereas the lower figures are obtained for $\mathrm{Bo}_1 = 0.3$. In the reported cases one actually keeps g and γ_1 constant and changes γ_0.

The upper plots in Figure 3.3 depict the bubble and free surface shapes at three different normalized times (initial time $t_0 = 0$, time $t_1 = 0.590$ and a (long) final time $t_f = 1.264$) for three values of the surface tension ratio $\hat{\gamma} = 0.2, 1$ and 5 at the Bond number $\mathrm{Bo}_1 = 1$. The gravity field g and the initial bubble radius a are given values, moreover since $\mathrm{Bo}_1 = 1$ value is fixed, one also gets a constant bubble surface tension γ_1. Therefore, $\hat{\gamma}$ is modified by only changing the free surface tension γ_0. We expect then different cases of the free surface shape behaviors, some cases when the free surface resists to the pushing bubble and others where the free surface is strongly disturbed by the bubble ascent.

As revealed by the computed shapes, surface tension ratio $\hat{\gamma}$ clearly affects the free surface shapes. As $\hat{\gamma}$ increases (i.e. here γ_0 increases when γ_1 is constant), the free surface deformation decreases and the bubble rising is stopped earlier (the bubble is stuck by the free surface). Moreover, the bubble deformation increases (though γ_1 is constant) as the free surface resistance increases. Trapped under the resisting free surface while being pushed by the buoyancy force, the bubble is indeed forced to change its spherical shape into a lens shape.

When the surface tension ratio $\hat{\gamma}$ is less than one ($\hat{\gamma} = 0.2$), the surface tension of the free surface γ_0 being smaller than the given one of the bubble γ_1, the free surface is then more deformed than the bubble. On the contrary, for $\hat{\gamma} \geq 1$, $\gamma_0 > \gamma_1$ and the free surface strongly resists to the bubble rising. In one case, at $\hat{\gamma} = 5$ the free surface is deformed in a first stage (between times $t = 0$ and t_1) and nearly motionless at time t_f, as the bubble further ascends and expands away from the $z = 0$ axis. Furthermore, at the same time $t_1 = 0.590$ (dashed line), the bubble location is different for values of $\hat{\gamma}$ thereby revealing that the bubble velocity reduces as the surface tension ratio $\hat{\gamma}$ increases.

By decreasing the Bond number, surface tension effect is enhanced (see the lower plots in Figure 3.3). At small Bond number, the surface tension force dominates the gravity force and a high sensitivity to the surface tension ratio in this case is expected. Indeed, for $\hat{\gamma} = 0.2$ (see the case $(\mathrm{Bo}_1, \hat{\gamma}) = (0.3; 0.2)$ in Figure 3.3), the bubble is nearly spherical and the free surface is highly deformed, whereas for $\hat{\gamma} = 5$ (see the case $(\mathrm{Bo}_1, \hat{\gamma}) = (0.3; 5)$ in Figure 3.3), the free surface remains flat and the bubble adopts an ellipsoid shape with a flat border at the upper part.

In a similar fashion, the bubble and free surface shapes are plotted in Figure 3.4 for two different Bond numbers: $\mathrm{Bo}_1 = 1$ (the upper figures) and $\mathrm{Bo}_1 = 5$ (the lower figures) at three normalized times $t_0 = 0$, $t_1 = 0.590$ and $t_f = 1.747$ for three values of the surface tension ratio $\hat{\gamma} = 0.2, 1$ and 5. For large Bond number, $\mathrm{Bo}_1 = 5$, both the bubble and the free surface are strongly deformed whatever the $\hat{\gamma}$ value with the bubble shapes showing a flat border on the lower part. Nevertheless, the free surface deformation is enhanced for small surface tension $\hat{\gamma}$ as shown on the plotted shapes in Figure 3.4 when the bubble shape tends to an hemispherical form.

Moreover, the bubble velocity sensitivity to the surface tension ratio $\hat{\gamma}$ is reduced when the Bond number is large ($\mathrm{Bo}_1 = 5$), the bubble location being almost identical for each $\hat{\gamma}$ at the same time $t_1 = 0.590$ (dashed line). For large Bo_1, the gravity force dominates the surface tension force, therefore though the free surface strongly resists to the bubble pushing at large $\hat{\gamma} = 5$, the gravity force plays an important part in the bubble rising which is, as a result, less sensitive to the surface tension ratio.

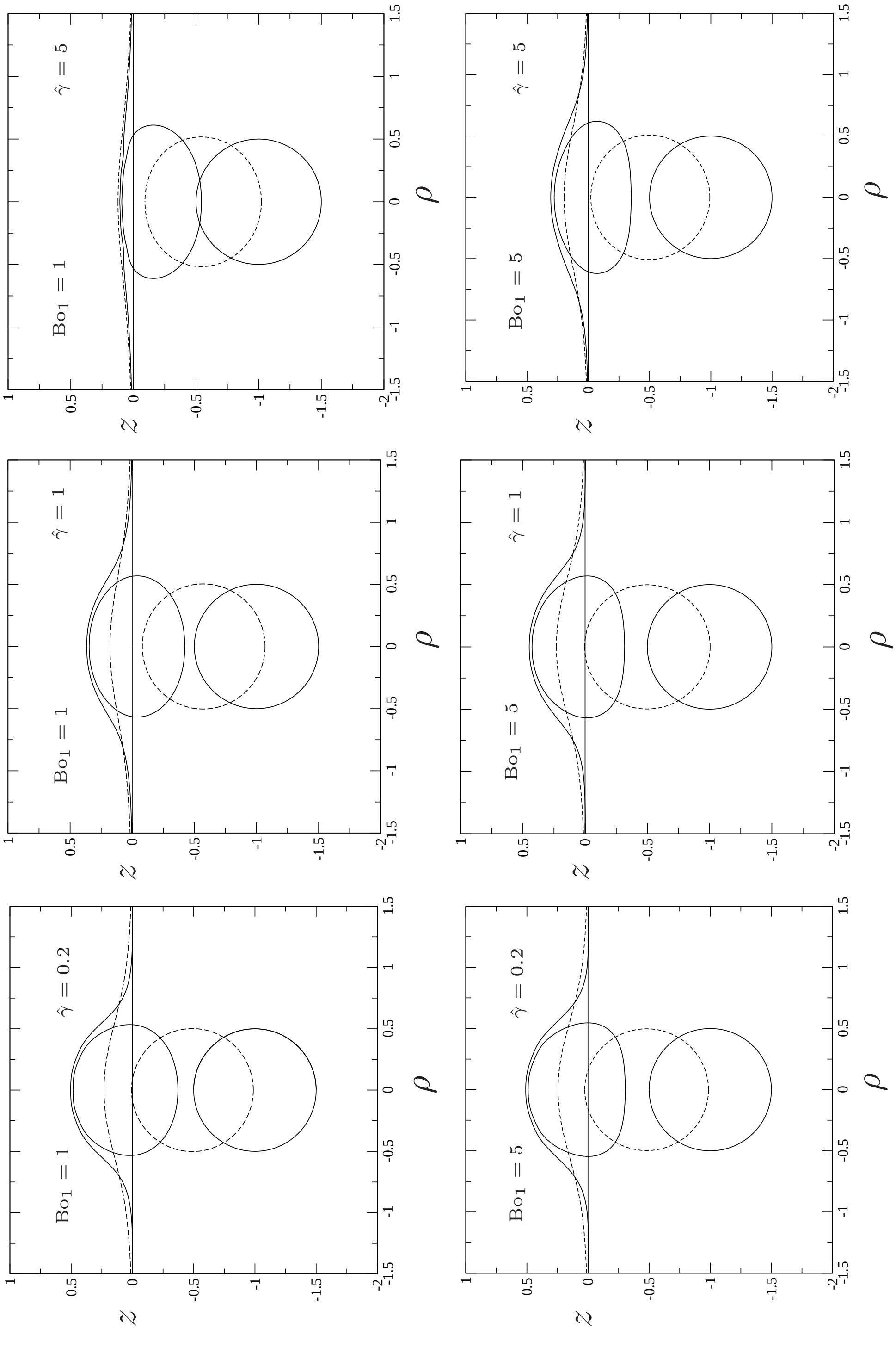

Figure 3.4: Bubble and free surface shapes at normalized times $t_0 = 0$, $t_1 = 0.590$ (dashed lines) and $t_f = 1.747$ for $\hat{\gamma} = 0.2, 1, 5$. The upper figures correspond to $\mathrm{Bo}_1 = 1$ whereas the lower figures are obtained for $\mathrm{Bo}_1 = 5$. In the reported cases one actually keeps g and γ_1 constant and changes γ_0.

A summary diagram of the computed bubble and free surface shapes when the drainage is almost finished is given in Figure 3.1.1 for different Bond numbers Bo_1 and surface tension ratios $\hat{\gamma}$. Shapes for $\hat{\gamma} \geq 1$ are indicated in blue while the ones for $\hat{\gamma} \leq 1$ are indicated in red. In addition, shapes for identical surface tension $\hat{\gamma} = 1$ are illustrated in maroon.

For identical surface tensions on the bubble and free surfaces, both the bubble and free surface shapes are strongly disturbed when the Bond number increases as was observed in [12] and in a recent experimental study of Nguyen and Chen [8]. For $\hat{\gamma} \leq 1$, the free surfaces are more deformed than the bubbles whereas for $\hat{\gamma} \geq 1$, the free surfaces are weakly disturbed while the bubbles shapes show strong deformations.

As previously described, at small Bond number $\mathrm{Bo}_1 = 0.3$, the surface tension ratio effects is clearly enhanced. The bubble is indeed nearly spherical with the highly disturbed free surface for the $(0.3, 0.2)$ computed shapes while the $(0.3, 5)$ computed shapes exhibit a flat free surface with a bubble shape strongly deformed on the top. Note that no expansion away of the z-axis is observed for the bubble in the $(0.3, 5)$ case.

At large Bond number, all the final bubble shapes present flat lower part and for $\hat{\gamma} > 3$, the bubble strongly expands away of the z-axis. Furthermore, the contact area between the bubble and the free surface reduces as $\hat{\gamma}$ increases or as the Bond number decreases.

Nevertheless, the computation is stopped when the minimum film thickness h reaches the value 10^{-3} or whenever the code encounters difficulties in accurately evaluating the curvature term. Therefore, for the plotted shapes in Figure 3.1.1, the bubble is never in contact with the free surface, i.e. one never reaches the “contact” regime.

When the liquid film reaches a small thickness, the integrals employed in the BEM are hard to compute due to the quasi-singularity of kernels (see Chapter 2, §2.2). In this limit, the free surface and the bubble interfaces are in the quasi-steady state whereas the liquid continues to drain.

According to previous work of Hartland [4] and Slattery [7] or see recently Howell [5], a lubrification model seems more appropriate to follow the drainage for which at very small scale, attractive forces like van der Waals force permit the film rupture. This step is usually steady by assuming a given steady shape of the bubble at the free surface.

As stated by Princen [14] for a one-phase problem and extend to a two-phases problem by Princen and Mason [15], the bubble shape can be obtained by using the hydrostatic balance. Here, the computed long-time bubbles shapes are compared with the Princen's model in the next section.

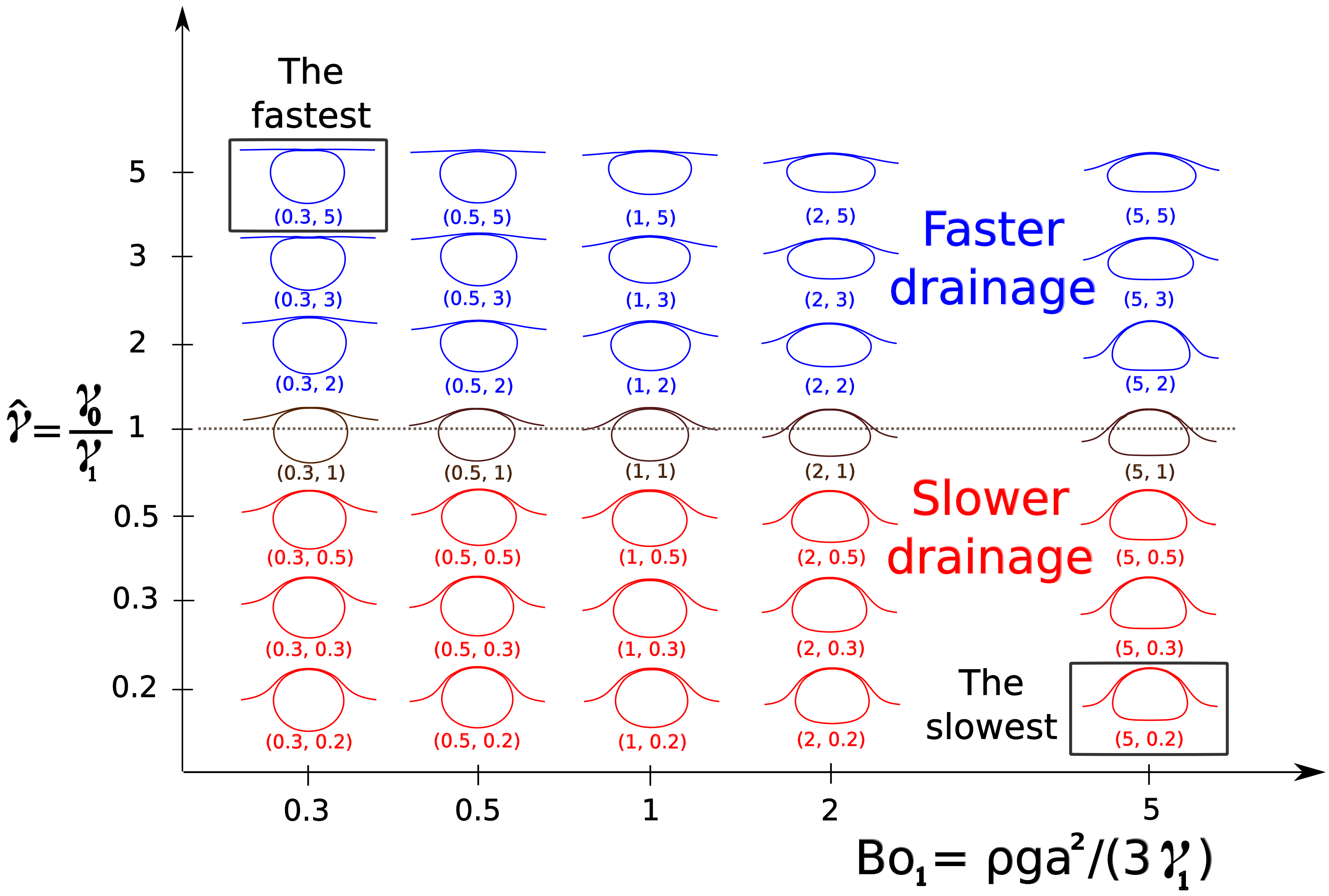

Figure 3.5: “Final” computed bubble and free surface shapes (i.e. when stopping the computation as soon as the minimum film thickness h reaches the value 10^{-3} or for larger value of h when the code encounters difficulties in accurately evaluating the curvature term (see Chapter 2 for details)). The handled different Bond number Bo_1 and surface tension are indicates by the pair $(\mathrm{Bo}_1, \hat{\gamma})$ in the Figure 3.1.1.

3.1.2 Princen shapes

Static form theory

Discarding the case of broken free surface and/or bubble, we expect to reach a final stage for which the liquid is at rest and each surface shape stationary. Using the simple model developed first by Princen [14] and extended by Princen and Manson [15], permits one to predict the final (long time) bubble and free surface shapes assuming a contact between the free surface and the bubble. The method has been implemented in the present work and this section introduces the main steps while further details are available in Appendix B.

As sketched in Figure 3.6, we consider a gas bubble (phase 1) immerged in a fluid (phase 3) both being separated from an ambient gas (phase 2) by a fluid interface. The configuration is 2d-axisymmetric and the origin of the coordinate system is the lowest point of the bubble. The bubble and the free surface shapes are described by the function $z(\rho)$. At any point (ρ, z) located on the free surface, the angle between the normal to the free surface and the negative z-direction is ϕ . All interfaces meet at a contact point (ρ_c, z_c) with a common slope $\tan\phi_c$.

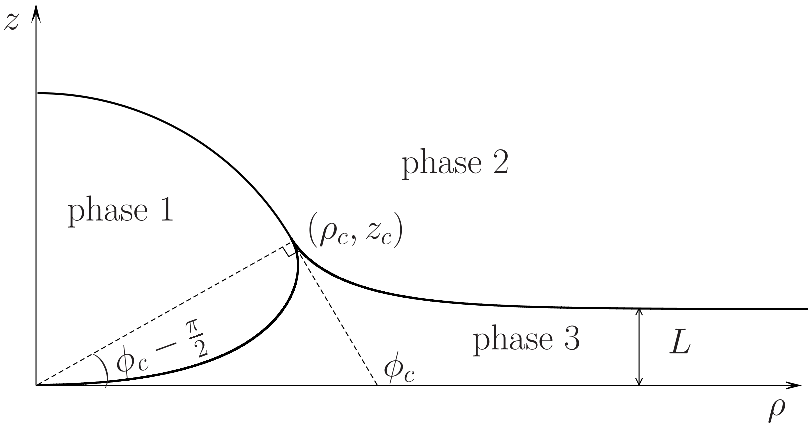

Figure 3.6: Cylindrical coordinate system adopted to describe the bubble and free surface shapes for a three-phase and axisymmetric system.

Three distinct interactions take place in the considered 3-phase system:

1) Bubble-liquid interface ($z < z_c$ and $\rho < \rho_c$)

2) Bubble-free surface interface ($z > z_c$ and $\rho < \rho_c$)

2) Liquid-ambient gas interface (further called the tail) ($\rho > \rho_c$)

When ρ becomes large, the tail asymptotes the straight line $z = L$.

It is assumed that the film thickness is negligible compared to the bubble length scale and that the surface tension γ_1 and γ_0 on the bubble and free surface are uniform (but not necessarily equal). The bubble and bulk interface shapes have been obtained in [15] in terms of surface tensions γ_1, γ_0 and density difference between the phases by balancing the surface tension and gravity forces.

Taking the spherical bubble radius of curvature b at the bubble lowest (origin) as length scale and introducing the Bond number Bo_p as

$$\mathrm{Bo}_p = \frac{\rho g b^2}{\gamma_1}. \tag{3.3}$$

Princen and Mason [15] obtained a governing equation for the unknown shape functions $z = z(\rho)$ of the interacting interfaces. Those equations, detailed in Appendix B, read:

(1) *Bubble-liquid interface equation for $z < z_c$ and $\rho < \rho_c$:*

$$\frac{1}{R_1/b} + \frac{1}{R_2/b} = \frac{z}{b}\,\mathrm{Bo}_p + 2, \tag{3.4}$$

where R_1 and R_2 are the two principal radii of curvature

$$\frac{1}{R_1} = \frac{\dfrac{d^2z}{d\rho^2}}{\left[1+\left(\dfrac{dz}{d\rho}\right)^2\right]^{3/2}}, \qquad \frac{1}{R_2} = \frac{\dfrac{dz}{d\rho}}{\rho\left[1+\left(\dfrac{dz}{d\rho}\right)^2\right]^{1/2}} = \frac{\sin\phi}{\rho}. \tag{3.5}$$

(2) *Bubble-free surface or contact area equation for $z > z_c$ and $\rho < \rho_c$:*

$$\frac{2}{R} = \frac{1}{R_1} + \frac{1}{R_2}, \qquad \frac{1}{R_2/b} = \frac{\sin\phi_c}{\rho_c/b}. \tag{3.6}$$

(3) *Bulk interface (or namely tail) equation for $\rho > \rho_c$:*

$$\frac{b}{R_1} + \frac{b}{R_2} = \frac{\gamma_1}{\gamma_0}\,\mathrm{Bo}_p\,\frac{(z-L)}{b} \tag{3.7}$$

where L is the obtained asymptotic value for z as ρ becomes large. Boundary conditions supplementing (3.7) then read

$$\frac{d(z/b)}{d(\rho/b)} = \tan\phi_c \qquad \text{for } \rho = \rho_c\,, \tag{3.8}$$

$$z = L \qquad \text{as } \rho \to \infty \tag{3.9}$$

and also

$$\frac{L}{b} = \frac{2}{\mathrm{Bo}_p}\left[\frac{(1+\gamma_0/\gamma_1)}{R/b} - 1\right]. \tag{3.10}$$

As announced, each previous relation has been actually normalized using the length scale b and the dimensionless Bond number Bo.

We present here the method used in [15] to solve the aforementioned bubble-fluid interface shape equations. The contact point (ρ_c, z_c) and its associated angle ϕ_c are required to determine the bubble and the fluid interface shapes. The entire bubble surface is discretized from the bottom (origin) to the top in N_s curve-linear abscissa s changing the $\phi \in [0, \pi]$ angle.

At each s, one solves first (3.4)-(3.8) employing an explicit Rugge-Kutta method at the fourth-order to obtain the associated contact point (ρ, z), angle ϕ and the related tail shape with its value L. Since the bubble shape does not cope with the required boundary condition, one selects a contact angle ϕ_c in the previous data set using the formula $\phi_c = (\phi^A + \phi^B)/2$ where initially, $\phi^A = \phi_1$ is the angle value ϕ of the first curve-linear abscissa s_1 and $\phi^B = \phi_{N_s}$ is the angle value ϕ of the last curve-linear abscissa s_{N_s}. The bubble-liquid interface is calculated once again to obtain the new contact point coordinates (ρ, z) and the corresponding L value. This new L value is compared with the asymptotic value given by the relation (3.10) when enforcing the boundary condition (3.8)-(3.9). Once the required L is obtained, the correct bubble-liquid interface and also the correct contact area are calculated using the suitable contact angle ϕ_c, contact point coordinates (ρ_c, z_c) and L value.

Note that in this numerical resolution, one takes $b = 1$. The linear dimensions of the latter system are obtained by testing if the bubble radius $a = (3V_b/4\pi)^{1/3} = 1$, with the bubble volume $V_b = \pi{\rho_c}^2 z_c + 2\pi\rho_c[(\rho_c - \sin\phi_c)/\mathrm{Bo}_p + \pi {h_{cap}}^2(3R - h_{cap})/3]$.

Comparison with numerical results

We numerically solved the previous Princen's final shapes equations and compared the resulting final bubble and free surface shapes with the computed ones. In addition, one should also mention that shapes obtained with the Princen method have been shifted in the $\mathbf{e}_z$ direction to match the final bubble shapes predicted by the direct numerical simulation. The case of $\hat{\gamma} = 1$ has been already investigated in [12] for three Bond values.

In the present work, the results are displayed in Figure 3.7 (a)-(b) for the small surface tension ratio $\hat{\gamma} = 0.2$. For theses comparisons the computed shapes correspond to the case when the numerical code reaches a minimal film thickness value of $h = 10^{-3}$ or when the optimized time step becomes too small (the computation being stopped at a final time t_{fm}). We observe a good agreement between the Princen bubble shapes (dashed lines) and the computed ones (solid lines) for the two given Bond numbers $\mathrm{Bo}_1 = 0.3$ and $\mathrm{Bo}_1 = 5$. Note that the bubble is weakly deformed for small surface tension ratio $\hat{\gamma} = \gamma_0/\gamma_1$.

On the contrary, the free surface Princen shapes, shifted along the $-\mathbf{e}_z$ direction to match the final bubbles shapes are not retrieving the ones numerically calculated. This is because as time will further increases the computed free surface shape will still be pushed and disturbed along the $\mathbf{e}_z$ direction by the bubble while final computed bubble shape has been already reached.

For the large surface tension ratio $\hat{\gamma} = 5$, Figure 3.8 (c)-(d) compare, again at $\mathrm{Bo}_1 = 0.3$ and $\mathrm{Bo}_1 = 5$, the "final" computed bubble and fluid interface shapes against the ones obtained following Princen and Mason [15] approach.

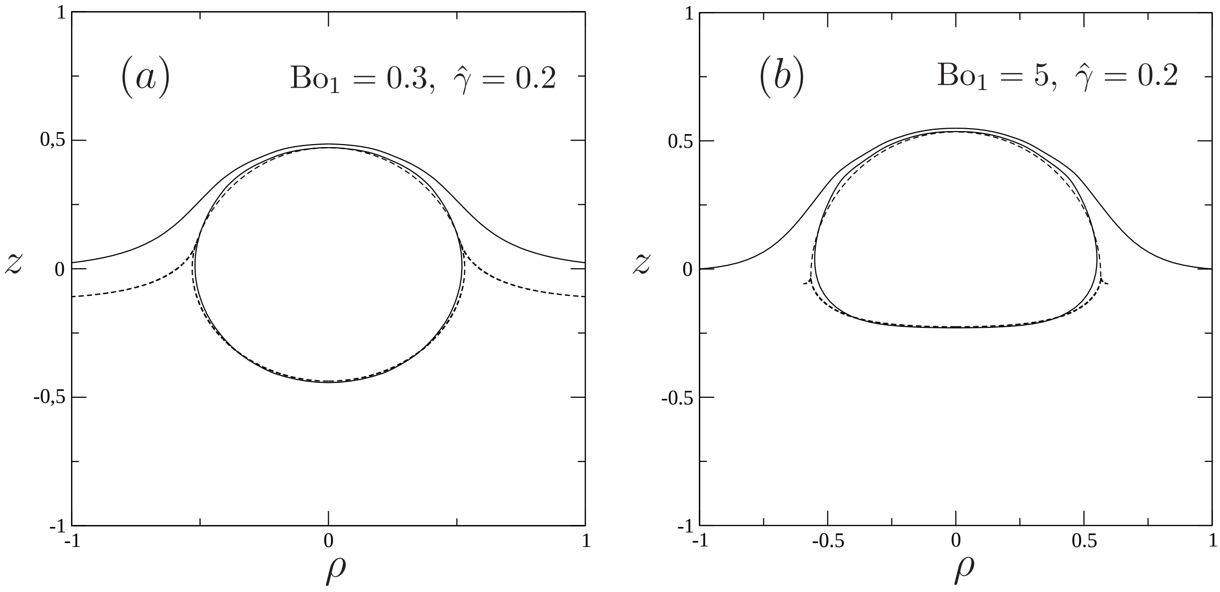

Figure 3.7: Comparisons between the computed *"final"* (t_{fm}) bubble shapes (solid line) and the bubble shapes (dashed lines) obtained by Princen and Mason [15] at $\hat{\gamma} = 0.2$ and at (a) $\mathrm{Bo}_1 = 0.3$ or (b) $\mathrm{Bo}_1 = 5$.

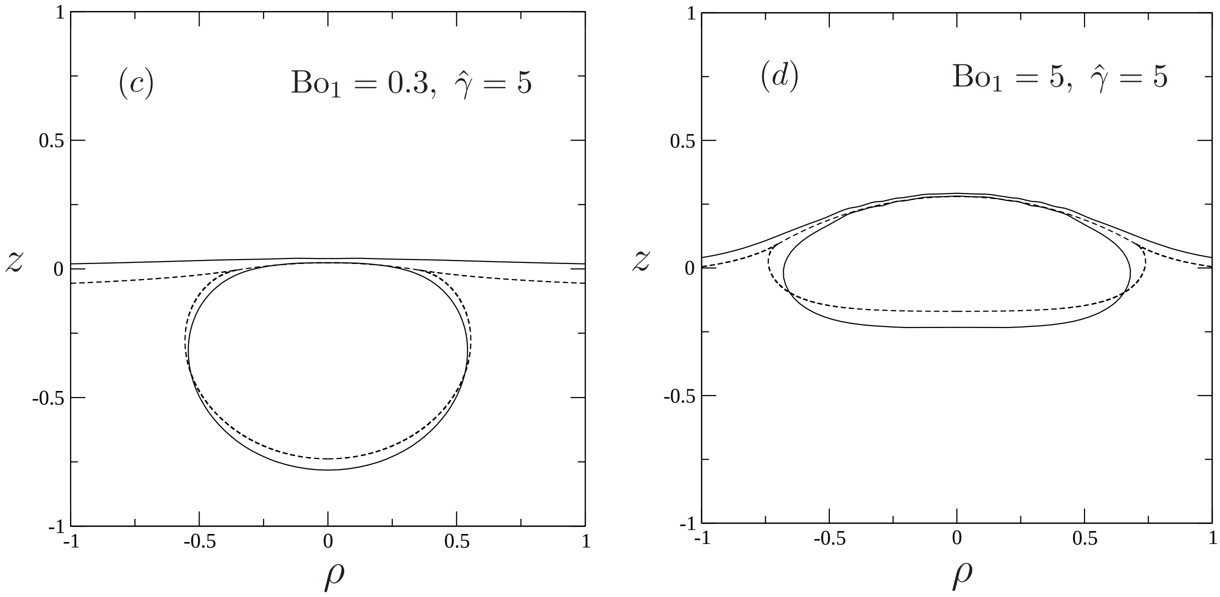

Figure 3.8: Comparisons between computed *"final"* (t_{fm}) bubble shapes (solid line) and the bubble shapes (dashed lines) obtained by Princen and Mason [15] at $\hat{\gamma} = 5$ and at (c) $\mathrm{Bo}_1 = 0.3$ or (d) $\mathrm{Bo}_1 = 5$.

By contrast with the previous figures, Princen bubble shapes and computational ones are different whereas the Princen free surface shapes show a similar trends with the numerically calculated ones though the Princen free surface has been shifted along the $\mathbf{e}_z$ direction to match the final bubbles shapes.

This indicates that the bubble final deformation is not reached and that as time evolves computed bubble shape will spread away from the $(0, \mathbf{e}_z)$ axis whilst is not any more able to further ascend (being now fully stopped by the quasi final interface). Actually, the bubble shapes obtained by the numerical code are less deformed than the Princen bubble shapes because the fluid is not yet at rest when the simulation is stopped (criterion $h = 10^{-3}$).

One further investigates the maximal free surface deformation δ_{max} (sketch in Figure 3.9), normalized by the bubble diameter $2a$, for the Princen shapes and the computed ones.

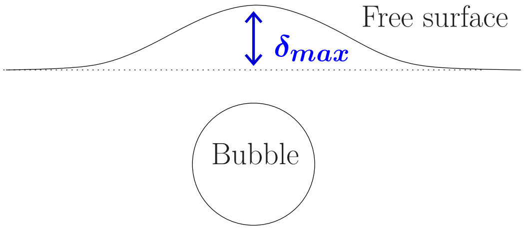

Figure 3.9: Sketch of the maximal free surface deformation δ_{max}.

Since the Princen shapes are shifted along the $-\mathbf{e}_z$ direction to match the bubbles location in the previous results Figure 3.7 (a)-(b) and Figure 3.8 (c)-(d), comparisons between the free surface Princen shapes and the computed ones are therefore arduous. Accordingly, we plot in Figure 3.9 the maximal free surface deformation δ_{max} for the Princen shapes and the computed ones versus the Bond number for two different surface tension ratio $\hat{\gamma} = 1$ and $\hat{\gamma} = 5$. In both Figure 3.10-(a) and Figure 3.10-(b), the computed maximal free surface deformation are obtained when the film thickness criterion, $h = 10^{-3}$, is reached or for the minimal values of h reached by the computation.

As shown in Figure 3.10, the maximal free surface deformation quickly increases with the ratio Bo_1 and then reaches a threshold value for large Bo_1. In addition, the threshold value of the maximal free surface deformation is larger for the static shapes since the computed shapes have not fully reached the equilibrium state of the free surface.

Indeed, the Princen static shapes are obtained for a zero liquid film thickness (contact between the bubble and the free surface) between the bubble and the free surface. As h tends to zero, the direct numerical code is limited due to a less accurate evaluation of the elliptic integrals (see Chapter 2 and Appendix A for further details). Then, the free surface and the bubble meshes becoming too close, the computation is therefore stopped to avoid numerical errors.

Furthermore, as the surface tension ratio $\hat{\gamma}$ decreases, the discrepancy between the Princen results and the numerical ones increases. In case of $\mathrm{Bo}_1 = 1$, the difference between the Princen and the numerical result at $\hat{\gamma} = 1$ (see Figure 3.10-(a)) is of order $\Delta\delta_{max}/\delta_{max} = 0.24$ whereas at $\hat{\gamma} = 5$ (see Figure 3.10-(b)), the numerical result matches the Princen one. Moreover, at large Bond number $\mathrm{Bo}_1 = 5$, discrepancy of $\Delta\delta_{max}/\delta_{max} = 0.18$ is observed at $\hat{\gamma} = 5$ while the difference between the result and the Princen one is of order $\Delta\delta_{max}/\delta_{max} = 0.42$ at $\hat{\gamma} = 1$.

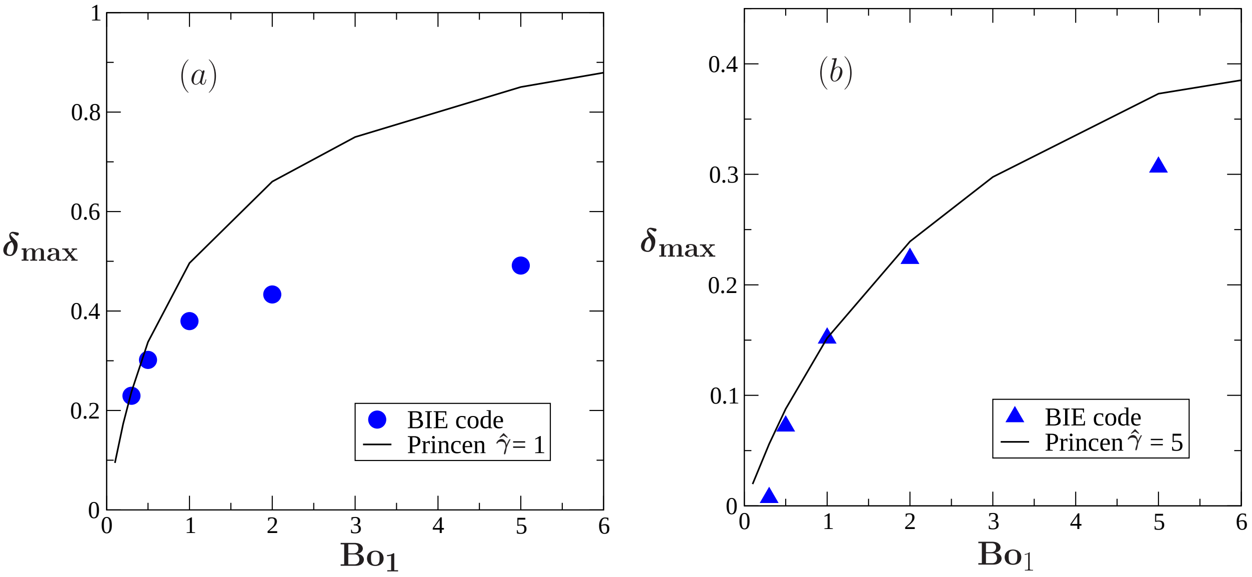

Figure 3.10: Normalized maximal free surface deformation δ_{max} versus Bo_1. Comparison between the Princen results (black curve) and the computed results (blue marker) for (a) $\hat{\gamma} = 1$ (triangle marker) (b) $\hat{\gamma} = 5$ (circle marker).

In the case of small $\hat{\gamma}$, the bubble remains indeed nearly spherical and reaches its equilibrium shapes faster than the free surface which keeps deforming under the bubble action. However, in this case, the bubble is too close to the free surface and the computation is stopped before the free surface reaches its equilibrium shape. In contrast, for large $\hat{\gamma}$, the computed bubble shapes do not match with the static ones. Clearly, the bubble is going to keep deforming especially far from the $\rho = 0$-axis of revolution, i.e. the reported computed shapes are obtained with a liquid experiencing a small flow. The obtained computed free surface shape for large $\hat{\gamma}$ has here reached its equilibrium shape or is closed to the equilibrium shape and then implies that its maximal deformation δ_{max} shows a smaller difference with the Princen results in Figure 3.10-(b).

In summary, one observes a good agreement between the final bubble shapes following Princen method once the surface tension ratio $\hat{\gamma}$ is small whereas the final free surface shapes exhibit different behavior. In contrast, the free surface shapes present a similar trend with the computed ones for large $\hat{\gamma}$ while the Princen bubble shapes mismatch the computed ones. Indeed, in the second case the computed bubble shapes are stopped before reaching their equilibrium shapes. Moreover, the maximal free surface deformation δ_{max} has been examined for both the Princen shapes and the computed ones at different values of the Bond number and two different surface tension ratio values.

Comparing δ_{max} obtained with the Princen shapes with the computed shapes, the numerical results are in good agreement at small Bo_1, the discrepancy observed at large Bond number Bo_1 decreasing as the surface tension ratio $\hat{\gamma}$ increases. Therefore, in addition to the bubble and free surface shapes, the time dependence of the film thickness $h(t)$ between the bubble and the free surface has been also investigated.

3.2 Time evolution of the film thickness between the bubble and the free surface

As a bubble approaches a free surface, the liquid film between both surfaces is evacuated and its thickness decreases with time. The film thickness evolution in time or so-called film drainage is caused by the bubble rising and depends upon the bubble velocity. This drainage has been studied here for a large range of Bond number and surface tension ratio.

3.2.1 Sensitivity to the Bond number

Drainage sensitivity to the Bond number, Bo_1, has been studied in [12] for $\hat{\gamma} = 1$, i.e. for free surface and bubble having identical surface tensions. The resulting plot of h versus time is give in Figure 3.11.

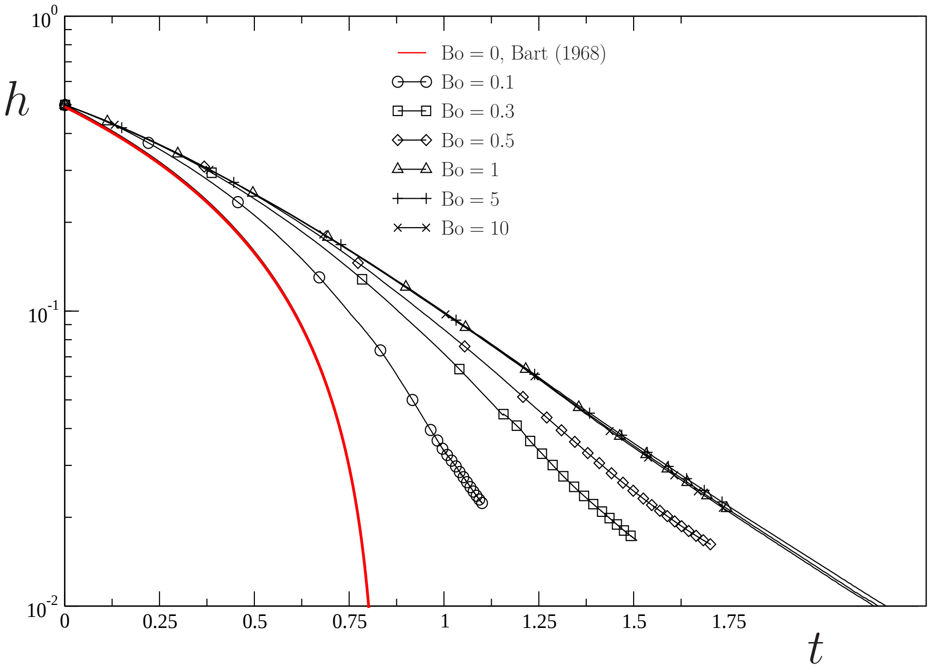

Figure 3.11: Film thickness h (logarithmic scale) versus time t at $\mathrm{Bo}_1 = 0.1, 0.3, 0.5, 1, 5, 10$. The solution at $\mathrm{Bo}_1 = 0$ (red curve) is obtained using the bipolar coordinates method developed in [1].

Each plotted curve corresponds to a given Bond number while the red solid curve is the solution obtained using the lubrification force calculated by Bart [1] at $\mathrm{Bo}_1 = 0$ (i.e. when there is no surface deformation). The film thickness shows a long-time exponential decay [11]-[2]

$$h(t) \sim h\, e^{-At} \tag{3.11}$$

with $A > 0$ the film thinning rate. Moreover, Figure 3.11 reveals a typical threshold $\mathrm{Bo}_1 = 1$ for the drainage sensitivity to the Bond number: for $\mathrm{Bo}_1 < 1$ the drainage rate increases as the Bond number decreases whereas as soon $\mathrm{Bo}_1 \geq 1$ a constant drainage rate takes place. In summary, at small Bond number and for equivalent surface tension on the bubble and the free surface ($\hat{\gamma} = 1$), the drainage is enhanced. One should mention that numerical restrictions appear for $\mathrm{Bo}_1 < 0.1$ because the normalization of our boundary conditions (see (1.31) in Chapter 1). In practice, one has $\mathcal{O}(\mathrm{Bo}_1) \simeq \mathcal{O}(\mathrm{Ca})$ in our numerical code and (1.31) the surface traction $\mathbf{f} = \boldsymbol{\sigma} \cdot \mathbf{n}$ then writes

$$\mathbf{f} = \left(-12\, z + \frac{\hat{\gamma} \boldsymbol{\nabla}_S \cdot \mathbf{n}}{\mathrm{Bo}_1} \right) \cdot \mathbf{n} \tag{3.12}$$

on the free surface.

The curvature term, denoted by $\boldsymbol{\nabla}_S \cdot \mathbf{n}$ is indeed ardeous to calculate with accuracy and the numerical errors, accumulated during the computation process, are amplified by the $(\boldsymbol{\nabla}_S \cdot \mathbf{n})/\mathrm{Bo}_1$ ratio being large when Bo_1 becomes less than one.

3.2.2 Sensitivity to the surface tension

As observed in the previous subsection, the liquid film is drained faster at small Bond number. In this section, we carefully investigate the film drainage sensitivity to the surface tension ratio $\hat{\gamma}$ for two given Bond numbers. First, we examine the case $\mathrm{Bo}_1 = 1$ for which the surface tension force is of the same order than the buoyancy force. Then, the interesting case of the small Bond number $\mathrm{Bo}_1 = 0.3$, for which the surface tension force this time dominates the gravity force, is investigated.

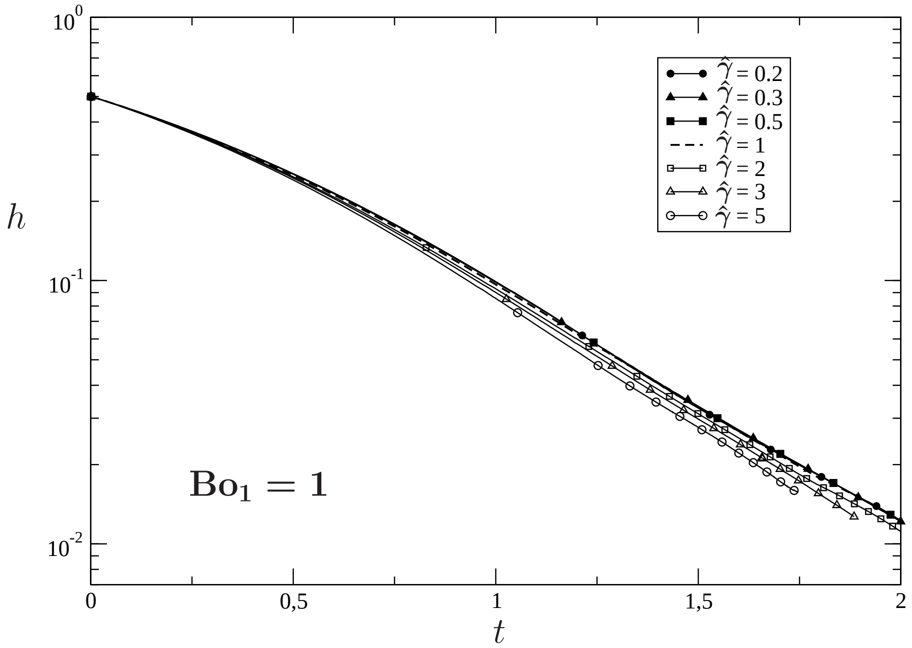

Figure 3.12: Film thickness h versus time t at $\hat{\gamma} = 0.2, 0.3, 0.5, 1, 2, 5$ for the unit Bond number $\mathrm{Bo}_1 = 1$.

Figure 3.12 and Figure 3.13 show the film thickness evolution in time for two given Bond numbers and different values of $\hat{\gamma}$. Clearly, the drainage is strongly affected by a change of surface tension ratio $\hat{\gamma}$ at small Bond number while it becomes weakly dependent upon $\hat{\gamma}$ at $\mathrm{Bo}_1 = 1$.

Furthermore, two different regimes occur in Figure 3.12 and Figure 3.13: a fast drainage regime for $\hat{\gamma} > 1$ and a slower drainage regime for $\hat{\gamma} < 1$. Indeed, for $\hat{\gamma} > 1$ the free surface tension is larger than the bubble surface tension and the free surface consequently resists to the bubble action. The squeezing of the liquid film then increases and therefore the liquid evacuates faster. On the contrary, for $\hat{\gamma} < 1$ the bubble pushes the fluid toward a deformed free surface and this consequently delays the squeezing time of the liquid film.

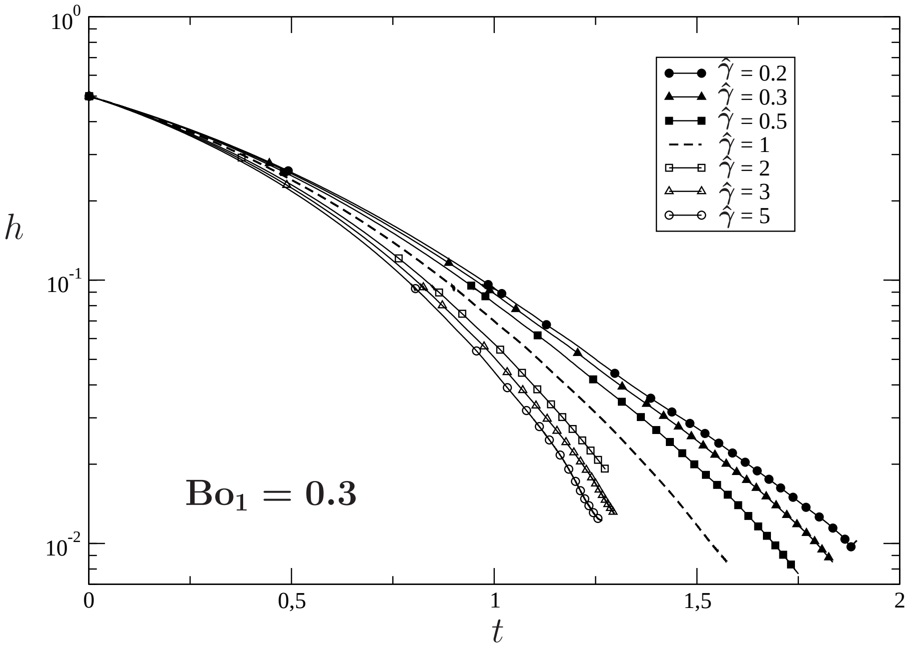

Figure 3.13: Film thickness h versus time t at $\hat{\gamma} = 0.2, 0.3, 0.5, 1, 2, 5$ for the weak Bond number $\mathrm{Bo}_1 = 0.3$.

Furthermore, one calculates the film thinning rate A for the final step of the bubble-free surface interaction. The results are depicted in Figure 3.14 for different Bond numbers and surface tension ratio values. The thinning rate is seen to decrease as the Bond number increases. At small Bond number ($\mathrm{Bo}_1 \simeq 0.1$), the drainage is clearly affected by the change of the surface tension ratio $\hat{\gamma}$ as was previously observed in Figure 3.13. In addition, the thinning rate A exhibits a quasi constant value for $\mathrm{Bo}_1 > 1$ since the gravity term indeed prevails over the surface tension term. Furthermore, in this Bond number range, the thinning rate is weakly sensitive to the surface tension ratio $\hat{\gamma}$.

The long-time thinning rates computationally gained are then compared with experimental results obtained in molten glass by Kočárková [6] and depict in Figure 3.15. In Figure 3.15, all the experimental results exhibit a similar trends than the numerical ones, their thinning rate decreases as the Bond number increases. Moreover, the experimental results for the glass composed of 1% of boron at 1228°C meet nicely with the numerical results at the large surface tension ratio $\hat{\gamma} = 5$.

Pointing out that the experimental data has been obtained for a large range of parameters such as the temperature, the viscosity and the glass composition, the numerical results are in good agreement with the experimental ones suggesting that the surface tension plays a role in the bubble-free surface dynamics.

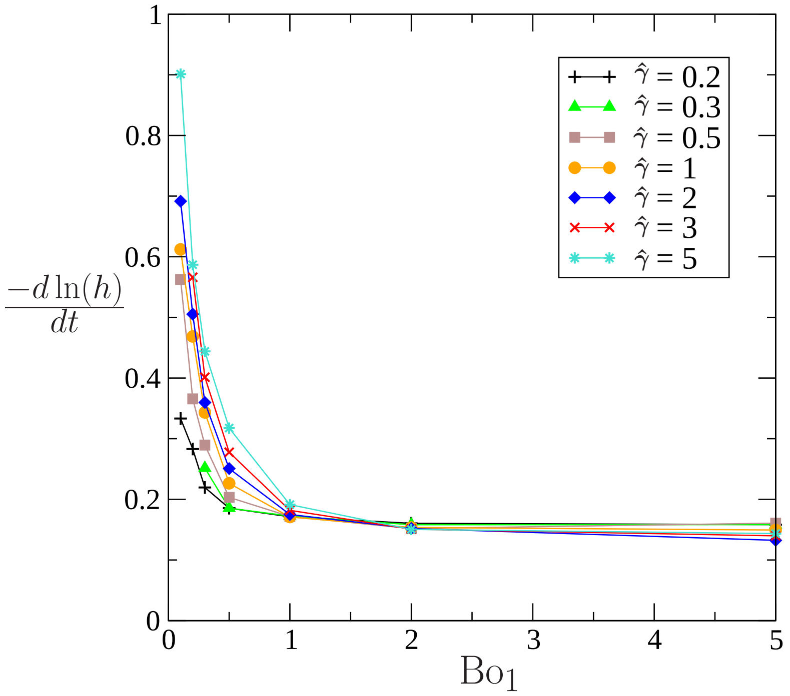

Figure 3.14: Long-time thinning rate $A = -d\ln(h)/dt$ versus different values of Bo_1 and $\hat{\gamma}$.

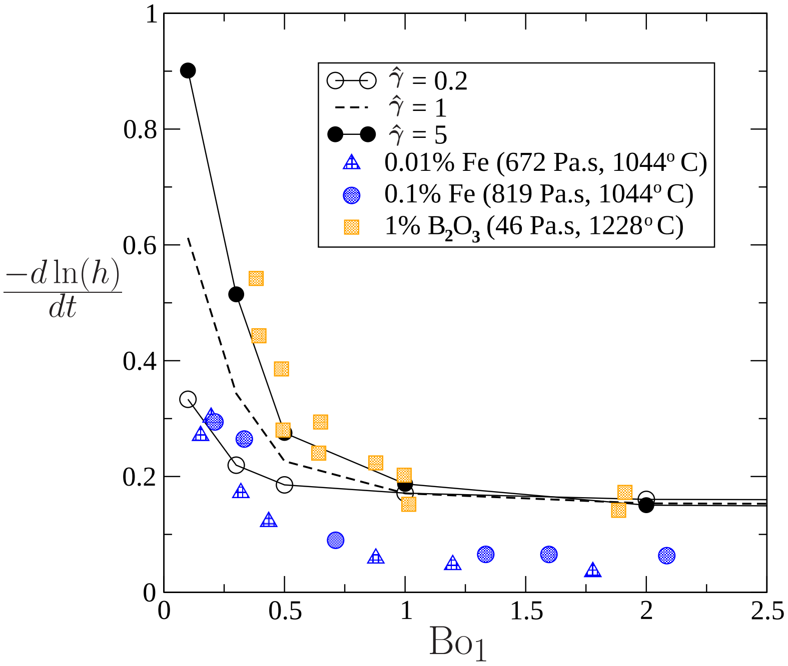

Figure 3.15: Long-time thinning rate $A = -d\ln(h)/dt$ versus different values of Bo_1 and $\hat{\gamma}$. Comparison with experimental results obtained by Kočárková [6].

A simple model developed in [6] permits one to compare the previous results with the one obtained by the Princen's theory. As the bubble rises under gravity to the resisting free surface, the liquid film h between the top of the bubble and the free surface is squeezed and therefore the film thinning results of both the buoyancy force exerted by the bubble and the capillary forces which push the interface downward.

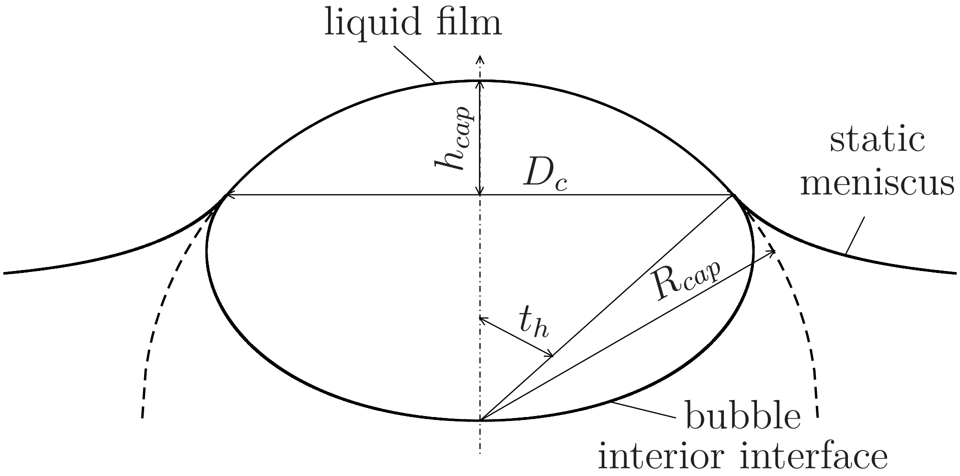

Figure 3.16: Bubble shape at a free surface for $\mathrm{Bo}_1 = 1$.

The film thickness being small compare to the bubble radius and, for axisymmetric reasons, the tangential and azimuthal stress are neglected compare to the radial stress and the film can then be approximated by a squeeze between two discs with area $Scap = 2R_{cap}h_{cap}$ where R_{cap} and S_{cap} are given in Figure 3.16.

The interfaces are assumed fully mobile and the flow is radially advected with a tensile stress written as

$$\sigma_T = 6\mu\frac{d\varepsilon}{dt}, \tag{3.13}$$

where the extensional rate of strain $d\varepsilon/dt$ reads

$$\frac{d\varepsilon}{dt} = -\frac{1}{2h}\frac{dh}{dt} \tag{3.14}$$

Moreover, the tensile stress is opposed to the pressure exerted by the gravity-driven bubble on the cap area and therefore one has

$$3\mu\frac{1}{h}\frac{dh}{dt} = \frac{\rho g 4\pi/3(D/2)^3}{S_{cap}} \tag{3.15}$$

where D is the diameter of the initial spherical bubble.

From (3.15), one obtains the thinning rate expression given in [6] as a function of the bubble size and S_{cap}

$$A \simeq \frac{2\pi}{9}\frac{(D/2)^2}{S_{cap}} \tag{3.16}$$

Appealing to the relation (3.16), the thinning rate of the film thickness h determined using the relation (3.16) conjointly with the Princen and Mason theory [15] is compared with the computed results in Figure 3.17.

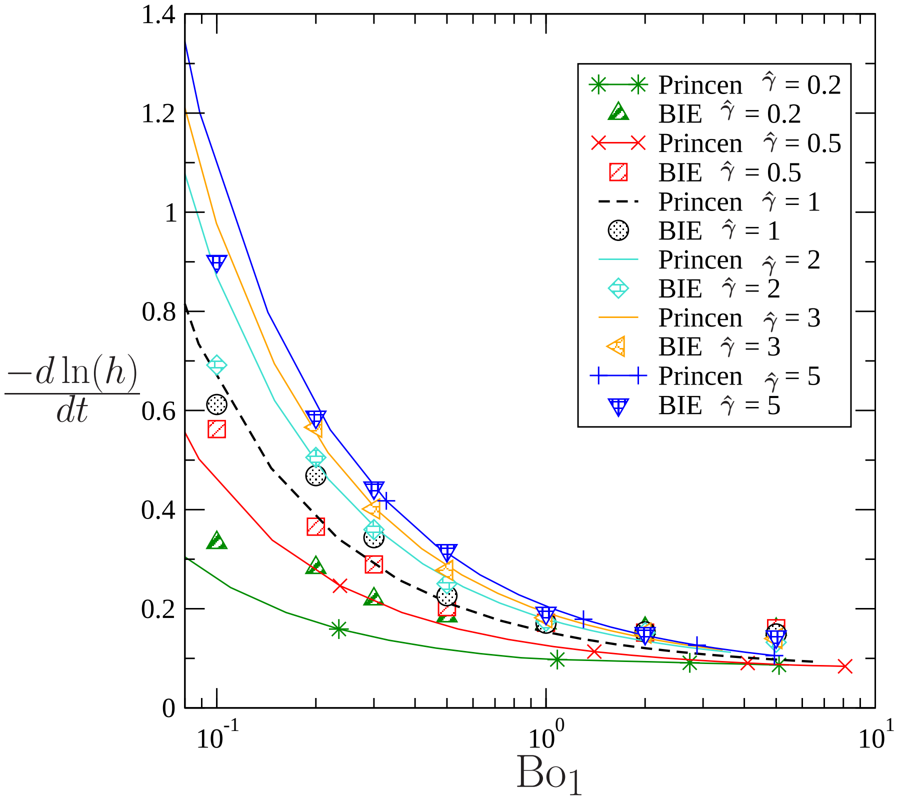

Figure 3.17: Long-time thinning rate $A = -d\ln(h)/dt$ versus different values of Bo_1 and $\hat{\gamma}$. Comparison with the Princen model [15] (solid line) and the computed results (marker).

All the results obtained with the Princen and Mason theory, represented by solid and dashed line, show a similar decay with the computed ones (indicated by symbols). For large surface tension ratio, i. e. $\hat{\gamma} > 1$, the Princen's results and the computed ones coincid nicely whereas for small surface tension ratio i. e. $\hat{\gamma} < 1$, the computed results exhibit larger thinning rate than the Prince results.

As mentionned is §3.1, at $\hat{\gamma} > 1$ the bubble keeps expending away along the ρ axis whereas the computed free surface has already reached is "final" shape. The interface therefore is almost motionless involving that a constant value of the film thinning rate has been attained. The computed film thinning rate thus agrees well with the one obtained using the relation (3.16). In contrast, the free surface is highly deformable at small surface tension ratio ($\hat{\gamma} < 1$) and is still continuously disturbed by the bubble for which the "final" shape has been reached.

At $\hat{\gamma} > 1$, the computed free surface has reached is "final" shape whereas the bubble keeps expending away along the ρ axis and is closed to the Princen free surface shapes. As the interface still evolves, the film thinning rate is therefore changing and this results in the difference observed between the computed thinning rate and the one obtained with the Princen and Mason theory for which the bubble and free surface gap equals zero and the interface is at rest.

For small Bond number, all the computed thinning rates differ from the ones obtained with (3.16) whenever $\hat{\gamma} \neq 1$. The film thickness is indeed sensitive to the initial distance of the bubble as previously noticed in Chapter 2, section §2.3.3 at small Bond number for $\hat{\gamma} \neq 1$. This may explain the large difference observed whenever $\hat{\gamma} \neq 1$ whereas for a surface tension ratio of $\hat{\gamma} = 1$, the computed thinning rate is in good agreement with the one prescribed by the Princen and Mason theory.

3.3 Conclusion

We performed a numerical study of one bubble ascending toward a free surface. The sensitivity of the bubble and free surface shapes and of the film drainage to the surface tension ratio $\hat{\gamma}$ between the free surface and the bubble has been investigated for a large range of Bond number and surface tension ratio values. Bubble and free surface shapes have been classified in a summary diagram and related to the drainage regimes. The shapes deformation increase with the Bond number and, at small Bond number, the change of surface tension strongly affects both the shape deformation and the film drainage. Moreover, the drainage is enhanced when the surface tension of the free surface is larger than the bubble one. A relation between the bubble-free surface contact area and the thinning rate has been extended to deal with the change of surface tension and successfully compared with computed results for a large range of Bond number and surface tension ratio.

However, the numerical code accuracy is spoiled as soon as the liquid film thickness value becomes too small and the bubble is actually never in real contact with the interacting free surface. In addition, numerical restrictions appear for $\text{Bo}_1 < 0.1$ due to the normalization of our boundary condition. In fact, accurately computing the mean curvature on the bubble and the (truncated) free surface is difficult (and as time evolves, numerical errors cumulates). Since the curvature term is multiplied with the ratio $1/\text{Bo}_1$, errors emerging from the mean curvature terms become large as the Bond number tends to zero and the numerical computation is then stopped.

To complete the numerical drainage study at small Bond number, an asymptotic analysis is developed for small deformations, i.e. at small Bond and capillary numbers. Such an analysis, developed in Chapter 4 and 5, will hold for the small Bond number domain presented in Figure 9 and is expected to match in an overlapping domain the numerical predictions at small Bond numbers.

Bibliography

[1] E. Bart. The slow unsteady settling of a fluid sphere toward a flat fluid interface. *Chem. Eng. Sci.*, 23:193–210, 1968.

[2] G. Debrégeas, P.-G. de Gennes, and F. Brochard-Wyart. The life and death of “bare” viscous bubbles. *Science*, 279:1704–1707, 1998.

[3] E. Gouillart, M. J. Toplis, J. Grynberg, M.-H. Chopinet, E. Søndergård, L. Salvo, M. Suéry, M. Di Michiel, and G. Varoquaux. In situ synchrotron microtomography reveals multiple reaction pathways during soda-lime glass synthesis. *J. Amer. Cer. Soc.*, 95(5):1504–1507, 2012.

[4] S. Hartland. The coalescence of a liquid drop at a liquid-liquid interface. Part II: Film thickness. *Trans. Instn Chem. Engrs*, 45:T102–T108, 1967.

[5] P. D. Howell. The draining of a two-dimensional bubble. *Journal of Engineering Mathematics*, 35:251–272, 1999.

[6] H. Kočárková. *Stabilité des mousses de verre: Expériences à l'échelle d'une bulle ou d'un film vertical.* PhD thesis, Université Paris-Est, 2011.

[7] C.-Y. Lin and J.C. Slattery. Thinning of a liquid film as a small drop or bubble approaches a solid plane. *AIChE J.*, 28(1):147–156, 1982.

[8] C. T. Nguyen, H. M. Gonnermann, Y. Chen, C. Huber, A. A. Maiorano, A. Gouldstone, and J. Dufek. Film drainage and the lifetime of bubbles. *Geochemistry, Geophysics, Geosystems*, 14(9):3616–3631, 2013.

[9] V. I. Nizhenko and Yu. I. Smirnov. Surface phenomena and interfacial interaction at the glass-liquid tin-gas phase interface. *Powder Metallurgy and Metal Ceramics*, 42(3-4):171–179, 2003.

[10] N. M. Parikh. Effect of atmosphere on surface tension of glass. *J. Amer. Cer. Soc.*, 41(1):18–22, 1958.

[11] F. Pigeonneau, D. Martin, and O. Mario. Shrinkage of oxygen bubble rising in a molten glass. *Chem. Eng. Sci.*, 65:3158–3168, 2010.

[12] F. Pigeonneau and A. Sellier. Low-Reynolds-Number gravity-driven migration and deformation of bubbles near a free surface. *Phys. Fluids*, 23:092302, 2011.

[13] Laurent Pilon. *Foams in Glass Manufacturing*, pages 355–409. John Wiley & Sons, Ltd, 2012.

[14] H. M. Princen. Shape of a fluid drop at a liquid-liquid interface. *J. Colloid Interface Sci.*, 18:178–195, 1963.

[15] H. M. Princen and S.G. Mason. Shape of a fluid drop at a liquid-liquid interface. I. Extension and test of two-phase theory. *J. Colloid Interface Sci.*, 20(2):156–172, 1965.

[16] J. E. Shelby. *Introduction to Glass Science and Technology.* The Royal Society of Chemistry, Cambridge, 1997.

Chapter 4

Asymptotic analysis at small Bond number for a bubble or a solid particle near a free surface in 2D-axisymmetric configuration

Contents

As outlined in the previous Chapter 3, the numerical code experiences losses in accuracy as the Bond number becomes small. In such circumstances, the free surface and the bubble surface are weakly disturbed (i.e. close to the $z = 0$ plane and to a spherical shape, respectively) and these properties suggest developing an asymptotic analysis at vanishing Bond number. Such a task is theoretically performed in the present Chapter while the Chapter 5 is devoted to the numerical implementation, benchmark tests and results of the derived asymptotic theory. In this Chapter, we successively address the following points: we first expand at small Bond number the flow thereby introducing two zeroth-order and first-order flow problems, we then show how the zeroth-order flow may be accurately solved employing the bipolar coordinates and we finally provide the governing problems for the first-order free surface and bubble surface shapes.

Note that the proposed approach to get the free surface disturbed shape holds either for the case of a nearly-spherical bubble or the case of a solid sphere.

4.1 Governing equations and resulting zeroth-order and first-order flows

As the Bond number vanishes, each interface (free surface or bubble boundary if any) is weakly disturbed and the liquid flow is nearly the one obtained for rigid free surface and particle (rigid spherical bubble or solid sphere). This first section provides the suitable first-order flow decomposition versus the small Capillary number.

4.1.1 Axisymmetric problem and assumptions. Flow expansion

At a given time t, the particle (bubble or solid sphere) *center-of-volume* is located at a distance l from the free surface. As seen in Chapter 1, the liquid flow $(\mathbf{u}, p)$ obeys the steady Stokes equations

$$\boldsymbol{\nabla} \cdot \mathbf{u} = 0, \quad \nabla p = \mu \nabla^2 \mathbf{u} \text{ in } \mathcal{D}(t), \tag{4.1}$$

with $\mathcal{D}(t)$ the liquid domain and also the far-field behavior

$$(\mathbf{u}, p) \to (\mathbf{0}, 0) \text{as } ||\mathbf{x}|| \to \infty. \tag{4.2}$$

Here p denotes the dynamic pressure while the total pressure in the liquid reads $p + \rho_l \mathbf{g}.\mathbf{x}$. The problem (4.1)-(4.2) is supplemented with proper boundary conditions on the particle boundary and on the free surface S_0. If the particle is solid with surface Σ and experiences the translational velocity $U\mathbf{e}_z$ (no rotation for symmetry reasons) one prescribes the usual no-slip boundary condition

$$\mathbf{u} = U\mathbf{e}_z \text{ on } \Sigma. \tag{4.3}$$

In other words, the solid particle translates with velocity $U\mathbf{e}_z$ along the z-axis toward the free surface. Having unit outward normal $\mathbf{n}$ on the free surface S_0 and the bubble surface S_1 (when any), one also adds the following boundary conditions (recall (1.9) and (1.16))

$$\mathbf{u} \cdot \mathbf{n} = \mathbf{V} \cdot \mathbf{n} \quad \text{on } S_m \text{ for } m = 0, 1 \tag{4.4}$$

with $\mathbf{V}$ the material velocity on each surface and, denoting by $\boldsymbol{\sigma}$ the flow stress tensor, the condition

$$\boldsymbol{\sigma} \cdot \mathbf{n} = (\rho_l \mathbf{g}.\mathbf{x} + \gamma_0 \boldsymbol{\nabla}_S \cdot \mathbf{n})\, \mathbf{n} \quad \text{on } S_0 \tag{4.5}$$

on the free surface and in the case of the bubble, the condition

$$\boldsymbol{\sigma} \cdot \mathbf{n} = (\rho_l \mathbf{g}.\mathbf{x} - p_{1b} + \gamma_1 \boldsymbol{\nabla}_S \cdot \mathbf{n})\, \mathbf{n} \text{ on } S_1. \tag{4.6}$$

on the bubble surface with p_{1b} the constant pressure inside the bubble.

Of course, if the particle is solid, one solely takes (4.3) and (4.5) while for a bubble, one considers the relations (4.4)-(4.6). Denoting by U the typical magnitude of the particle velocity, the hydrodynamic force $\mathbf{F}$ exerted on a solid sphere with radius a ascending toward the free surface reads

$$\mathbf{F} = \int_{\Sigma} \boldsymbol{\sigma} \cdot \mathbf{n} \, d\Sigma = -6\pi\mu U a \lambda_s \, \mathbf{e}_z \tag{4.7}$$

where for a solid sphere rising through an unbounded liquid, the typical magnitude velocity reads $U = 2\rho_l g a^2/(9\mu)$ with λ_s the drag factor. In the case of a bubble, the typical magnitude velocity is $U = \rho_l g a^2/(3\mu)$ while the drag force writes $\mathbf{F} = -4\pi\mu U a \lambda_b \, \mathbf{e}_z$ with the associated drag factor λ_b (see (1.20)).

Neglecting the particle (solid sphere or bubble) inertia, one also requires the particle to be force-free (there is no torque for symmetry reasons). Such a requirement yields

$$6\pi\mu \, U \, a \, \lambda_s = \frac{4\pi(\rho_s - \rho_l) \, g a^3}{3}, \quad 4\pi\mu \, U \, a \, \lambda_b = \frac{4\pi\rho_l g a^3}{3}. \tag{4.8}$$

with ρ_s the uniform density of the solid sphere.

The problem consisting of (4.1)-(4.6) and (4.8) is linear for a given liquid domain $\mathcal{D}(t)$. It depends on the gravity field $\mathbf{g} = -g\mathbf{e}_z$, the bubble or sphere diameter $2a$, the surface tension of the free surface γ_0 and the bubble surface tension γ_1 (if any). If the particle is a solid sphere, one ends up with two dimensionless Bond and capillary numbers defined as

$$\mathrm{Bo}_0 = \frac{\rho_l g a^2}{3\gamma_0}, \ \mathrm{Ca}_0 = \frac{\mu U}{\gamma_0}, \tag{4.9}$$

and due to (4.8) such numbers are related as follows

$$\mathrm{Ca}_0 = \frac{2 \, \mathrm{Bo}_0}{3\lambda_s}. \tag{4.10}$$

If the particle is a bubble, two additionnal Bond number Bo_1 and capillary number Ca_1 are introduced as (see also Chapter 1)

$$\mathrm{Bo}_1 = \frac{\rho_l g a^2}{3\gamma_1}, \ \mathrm{Ca}_1 = \frac{\mu U}{\gamma_1}. \tag{4.11}$$

For the free-force bubble, one this time has the link

$$\mathrm{Ca}_1 = \frac{\mathrm{Bo}_1}{\lambda_b}. \tag{4.12}$$

As seen in Chapter 1, capillary numbers Ca_0, Ca_1 and Bond numbers Bo_0, Bo_1 are related through the surface tension ratio $\hat{\gamma} = \gamma_0/\gamma_1$. Note that both λ_s or λ_b are larger than unity and increase as the particle approaches the free surface. Hence, assuming in this Chapter that Bo_0 and Bo_1 are small compared to unity it appears that $\mathrm{Ca} = \mathrm{Ca}_0$ (for the solid sphere) and $\mathrm{Ca} = \max(\mathrm{Ca}_0, \mathrm{Ca}_1)$ (for the case of the bubble) is such that $\mathrm{Ca} \leq 1$. This latter property is the key assumption of the present Chapter. It permits one to develop an asymptotic treatment in terms of the small parameter Ca.

Accordingly, the flow $(\mathbf{u}, p)$ and its stress tensor $\boldsymbol{\sigma}$ are then expanded in terms of the small parameter Ca as follows

$$\mathbf{u} = \mathbf{u}_0 + \mathrm{Ca}\,\mathbf{u}_1 + \mathcal{O}(\mathrm{Ca}^2),\ \ p = p_0 + \mathrm{Ca}\,p_1 + \mathcal{O}(\mathrm{Ca}^2),\ \ \boldsymbol{\sigma} = \boldsymbol{\sigma}_0 + \mathrm{Ca}\,\boldsymbol{\sigma}_1 + \mathcal{O}(\mathrm{Ca}^2) \quad (4.13)$$

with $(\mathbf{u}_0, p_0)$ the Stokes flow about a rigid spherical bubble or solid sphere moving toward a rigid *flat* free surface.

The zeroth-order field $(\mathbf{u}_0, p_0)$ and $\boldsymbol{\sigma}_0$ correspond to the case of undisturbed flat free surface and spherical particle (bubble or solid sphere) obtained in the limit $\gamma_0 \to \infty$ (and for the bubble $\gamma_1 \to \infty$). The first-order flow $(\mathbf{u}_1, p_1)$ is determined for the weakly deformed surface(s). On each surface, the unit normal vector $\mathbf{n}$, directed into the liquid, is also developed as

$$\mathbf{n} = \mathbf{n_0} + \mathrm{Ca}\,\mathbf{n_1} + \mathcal{O}(\mathrm{Ca}^2) \quad (4.14)$$

with $\mathbf{n_0}$ the unit normal vector on the undisturbed boundary and $\mathbf{n_1}$ a vector which will be given later (see Chapter 4, §4.4.3). In a similar fashion, the velocity boundary conditions are expanded on each surface in terms of the small capillary number Ca. The material velocity $\mathbf{V}$ on S_0 and S_1 is then expanded versus Ca as

$$\mathbf{V} = \mathbf{V}_0 + \mathrm{Ca}\,\mathbf{V}_1 + \mathcal{O}(\mathrm{Ca}^2). \quad (4.15)$$

In our zeroth-order problem of rigid surfaces, we shall take $\mathbf{V}_0 = \mathbf{0}$ on S_0 and $\mathbf{V}_0 = U\mathbf{e}_z$ constant on S_1. The velocity boundary conditions thus write

$$[\mathbf{u}_0 + \mathrm{Ca}\,\mathbf{u}_1]\cdot[\mathbf{n}_0 + \mathrm{Ca}\,\mathbf{n}_1] = [\mathbf{V}_0 + \mathrm{Ca}\,\mathbf{V}_1]\cdot[\mathbf{n}_0 + \mathrm{Ca}\,\mathbf{n}_1] + \mathcal{O}(\mathrm{Ca}^2)\ \text{ on } S_0 \text{ or } S_1, \quad (4.16)$$

$$\mathbf{u}_0 + \mathrm{Ca}\,\mathbf{u}_1 + \mathcal{O}(\mathrm{Ca}^2) = U\mathbf{e}_z\ \text{ on } \Sigma \text{ (solid sphere)}. \quad (4.17)$$

Since we asymptotically expand each physical quantity up to the first-order in Ca, (4.16)-(4.17) then become

$$\begin{aligned}\mathbf{u}_0\cdot\mathbf{n}_0 + \mathrm{Ca}\,[\mathbf{u}_0\cdot\mathbf{n}_1 + \mathbf{u}_1\cdot\mathbf{n}_0] = \mathbf{V}_0\cdot\mathbf{n}_0 + \mathrm{Ca}\,[\mathbf{V}_0\cdot\mathbf{n}_1 + \mathbf{V}_1\cdot\mathbf{n}_0]&\\ + \mathcal{O}(\mathrm{Ca}^2)\ \text{ on } S_0 \text{ or } S_1,& \quad (4.18)\\ \mathbf{u}_0 + \mathrm{Ca}\,\mathbf{u}_1 + \mathcal{O}(\mathrm{Ca}^2) = U\mathbf{e}_z\ \text{ on } \Sigma \text{ (solid sphere)}.& \quad (4.19)\end{aligned}$$

As previously pointed out, for rigid flat free surface S_0' and particle (bubble or solid) we take $\mathbf{V}_0 = 0$ on S_0' and $\mathbf{V}_0 = U\mathbf{e}_z$ on S_1' (or Σ). Finally, the stress boundary condition has to be imposed on the bubble and free surfaces given by the relation (4.4)-(4.6). Each condition may be decomposed into two equivalent relations involving the normal stress and the tangential stress components as follows

$$\begin{aligned}\mathbf{n}\cdot\boldsymbol{\sigma}\cdot\mathbf{n} &= \rho_l\mathbf{g}\cdot\mathbf{x} + \gamma_0\boldsymbol{\nabla}_S\cdot\mathbf{n} \quad \text{on } S_0, && (4.20)\\ \mathbf{n}\cdot\boldsymbol{\sigma}\cdot\mathbf{n} &= \rho_l\mathbf{g}\cdot\mathbf{x} - p_{1b} + \gamma_1\boldsymbol{\nabla}_S\cdot\mathbf{n} \quad \text{on } S_1, && (4.21)\\ (\boldsymbol{\sigma}\cdot\mathbf{n})\wedge\mathbf{n} &= 0 \ \text{ on } S_m \text{ for } m = 0, 1. && (4.22)\end{aligned}$$

As will be shown later, (4.20)-(4.21) actually dictate each interface shape and will be then invoked latter to approximate the weakly disturbed bubble and free surface shapes. In contrast, the condition (4.22) of zero tangential traction on each interface is here expanded in terms of Ca as follows

$$\Big([\boldsymbol{\sigma}_0 + \mathrm{Ca}\,\boldsymbol{\sigma}_1]\cdot[\mathbf{n}_0 + \mathrm{Ca}\,\mathbf{n}_1]\Big)\wedge[\mathbf{n}_0 + \mathrm{Ca}\,\mathbf{n}_1] + \mathcal{O}(\mathrm{Ca}^2) = 0\text{on } S_0, S_1. \quad (4.23)$$

4.1.2 Zeroth-order flow and first-order flow problems

4.1.2.1 Zeroth-order flow

As illustrated in Figure 4.1, it is clear from the previous considerations that the flow $(\mathbf{u}_0, p_0)$ is the Stokes flow due to a *rigid* spherical bubble or a solid sphere translating at the velocity $U\mathbf{e}_z$ toward the flat (and rigid) $z = 0$ free surface S'_0. This flow fulfills the following Stokes equations and far-field behavior

$$\mu\boldsymbol{\nabla}^2\mathbf{u}_0 = \boldsymbol{\nabla}p_0, \;\; \boldsymbol{\nabla}\cdot\mathbf{u}_0 = 0 \;\text{ in } \mathcal{D}_0, \tag{4.24}$$

$$(\mathbf{u}_0, p_0) \to (\mathbf{0}, 0) \quad \text{as } |\mathbf{x}| \to \infty. \tag{4.25}$$

where of course $\mathcal{D}_0$ is the liquid domain bounded by the *undisturbed* surfaces S'_0 and S'_1 (or Σ). The equations (4.24) and (4.25) are supplemented with the zeroth-order boundary conditions obtained from (4.18)-(4.19) and (4.22)

$$\mathbf{u}_0\cdot\mathbf{n}_0 = 0 \;\text{ on } S'_0 \text{ (free surface)}, \tag{4.26}$$

$$\mathbf{u}_0\cdot\mathbf{n}_0 = U\mathbf{e}_z\cdot\mathbf{n}_0 \;\text{ on } S'_1 \text{ (bubble)}, \;\; \mathbf{u}_0 = U\mathbf{e}_z \text{ on } \Sigma \text{ (solid particle)}. \tag{4.27}$$

$$(\boldsymbol{\sigma}_0\cdot\mathbf{n}_0)\wedge\mathbf{n}_0 = 0 \quad \text{on } S'_0 \cup S'_1 \tag{4.28}$$

where the surfaces S'_0 and S'_1 are the $z = 0$ plane and rigid spherical bubble surface, respectively.

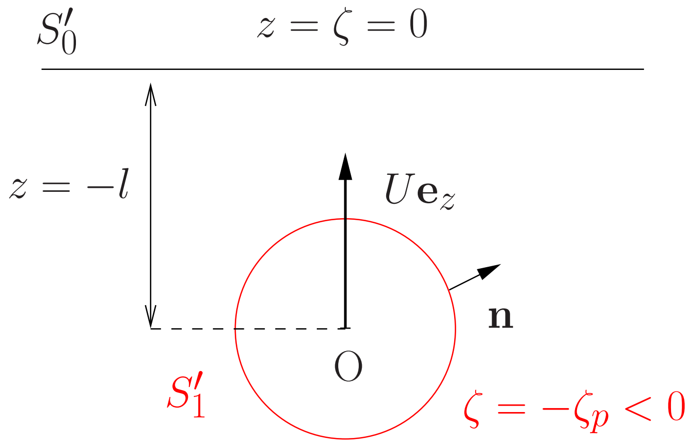

Figure 4.1: A rigid particle (spherical bubble or solid sphere) translating at the velocity $U\mathbf{e}_z$ toward the $z = 0$ flat free surface S'_0 in a liquid occupying the domain $\mathcal{D}_0$.

4.1.2.2 First-order flow

Retaining the $\mathcal{O}(\text{Ca})$ terms in the flow problem and associated boundary conditions, one arrives at the first-order flow problem

$$\mu\boldsymbol{\nabla}^2\mathbf{u}_1 = \boldsymbol{\nabla}p_1, \;\; \boldsymbol{\nabla}\cdot\mathbf{u}_1 = 0 \;\text{ in } \mathcal{D}_0, \tag{4.29}$$

$$(\mathbf{u}_1, p_1) \to (\mathbf{0}, 0) \quad \text{as } |\mathbf{x}| \to \infty \tag{4.30}$$

which is supplemented with the boundary conditions

$$\mathbf{u}_1 \cdot \mathbf{n}_0 = -\mathbf{u}_0 \cdot \mathbf{n}_1 + \mathbf{V}_1 \cdot \mathbf{n}_0 \ \text{ on } S_0', \tag{4.31}$$

$$\mathbf{u}_1 \cdot \mathbf{n}_0 = (U\mathbf{e}_z - \mathbf{u}_0) \cdot \mathbf{n}_1 + \mathbf{V}_1 \cdot \mathbf{n}_0 \ \text{ on } S_1', \tag{4.32}$$

$$\mathbf{u}_1 = \mathbf{0} \quad \text{on } \Sigma \text{ (solid particle)}, \tag{4.33}$$

while the first-order tangential stress on both the disturbed bubble and free surface writes

$$(\boldsymbol{\sigma}_1 \cdot \mathbf{n}_0) \wedge \mathbf{n}_0 = -(\boldsymbol{\sigma}_0 \cdot \mathbf{n}_0) \wedge \mathbf{n}_1 \ \text{ on } S_0' \cup S_1'. \tag{4.34}$$

Note that $\mathbf{V}_1 \cdot \mathbf{n}_0$ on one interface is actually obtained from this interface deformation which will be determined (see §4.3 and §4.4) using the zeroth-order flow.

4.2 Zeroth-order solution in bipolar coordinates

As it will be shown in §4.3.1 and §4.4.1, the *accurate* determination of the zeroth-order normal traction $\mathbf{n}_0 \cdot \boldsymbol{\sigma}_0 \cdot \mathbf{n}_0$ is needed on the undisturbed free surface S_0' and (if any) spherical bubble boundary S_1'. One can think about getting the traction $\boldsymbol{\sigma}_0 \cdot \mathbf{n}_0 = (\mathbf{n}_0 \cdot \boldsymbol{\sigma}_0 \cdot \mathbf{n}_0)\mathbf{n}_0$ on S_0' (and if needed on S_1') by employing a boundary approach (i.e. the usual BEM technique). However, such a method has accuracy of order 10^{-4} which is not sufficient for our analysis. Therefore, the zeroth-order flow is solved in the present work by appealing to the bipolar coordinates [8]-[6]. For instance, the case of a bubble near a free surface without buoyancy force has been treated by Meyyapan and Wilcox [7] using such coordinates. By linearity, we henceforth solve this flow setting $U = 1$.

4.2.1 Bipolar coordinates

The zeroth-order problem is solved using the bipolar coordinates $(\mathbf{e}_\zeta, \mathbf{e}_\eta, \mathbf{e}_\phi)$ defined in [6]. These coordinates are well adapted to deal with a liquid boundary consisting of a plane surface S_0' and a spherical surface (S_1' and Σ). In addition, this procedure allows us to accurately compute on each surface S_0' and S_1', the required traction $\boldsymbol{\sigma}_0 \cdot \mathbf{n}_0$ and therefore its normal components $\mathbf{n}_0 \cdot \boldsymbol{\sigma}_0 \cdot \mathbf{n}_0$.

The usual relations between the cylindrical coordinates (ρ, ϕ, z) and the bipolar coordinates are expressed as follows (see also Appendix C)

$$z = \frac{c \sinh \zeta}{\cosh \zeta - \cos \eta}, \qquad \rho = \frac{c \sin \eta}{\cosh \zeta - \cos \eta} \tag{4.35}$$

with $\zeta \leq 0$ and $\eta \in [0, \pi]$. The $z = 0$ plane is the $\zeta = 0$ surface while the $\zeta = -\zeta_p < 0$ surface is a sphere with radius $a = c/\sinh \zeta_p$ and center located at $z = -l$ with $l = c \coth \zeta_p$.

4.2.2 Stream function, pressure and resulting drag force

The zeroth-order incompressible axisymmetric velocity field $\mathbf{u}_0$ may be derived from a stream function $\psi(x, y)$. Here, it is convenient to introduce a stream function $\psi(\zeta, \chi)$ with $\chi = \cos \eta$.

Invoking the stress tensor general expression

$$\boldsymbol{\sigma}_0 = -p_0\mathbf{I} + \mu\left(\boldsymbol{\nabla}\mathbf{u}_0 + \boldsymbol{\nabla}\mathbf{u}_0^T\right) = -p_0\mathbf{I} + \boldsymbol{\tau}_0 \tag{4.36}$$

with the viscous stress denoted by $\boldsymbol{\tau}_0 = (\boldsymbol{\nabla}\mathbf{u}_0 + \boldsymbol{\nabla}\mathbf{u_0}^T)$, one casts the pressure gradient in terms of $\psi(\zeta, \eta)$ as follows

$$\frac{\partial p_0}{\partial \zeta} = -\frac{\mu(\cosh\zeta - \chi)}{c}\frac{\partial E^2(\psi)}{\partial \chi}\,, \tag{4.37}$$

$$\frac{\partial p_0}{\partial \eta} = -\frac{\mu(\cosh\zeta - \chi)}{c\sin\eta}\frac{\partial E^2(\psi)}{\partial \zeta} \tag{4.38}$$

where the harmonic operator E^2 is defined [7] as

$$E^2 = \frac{(\cosh\zeta - \chi)^2}{c^2}\left\{\frac{\partial^2}{\partial\zeta^2}\left[(\cosh\zeta - \chi)\frac{\partial}{\partial\zeta}\right] + (1-\chi^2)\frac{\partial}{\partial\chi}\left[(\cosh\zeta - \chi)\frac{\partial}{\partial\chi}\right]\right\}. \tag{4.39}$$

Note that $\psi(\zeta, \eta)$ obeys the biharmonic equation corresponding to the Stokes equations [9]

$$E^2[E^2(\psi)] = 0. \tag{4.40}$$

In a similar fashion, since the velocity vector in bipolar coordinates reads $\mathbf{u}_0 = u_{0\zeta}\mathbf{e}_\zeta + u_{0\eta}\mathbf{e}_\eta$, each velocity component in terms of $\psi(\zeta, \eta)$ is expressed as follows

$$u_{0\zeta} = -\frac{(\cosh(\zeta) - \chi)^2}{c^2}\frac{\partial\psi}{\partial\chi}, \tag{4.41}$$

$$u_{0\eta} = -\frac{(\cosh(\zeta) - \chi)^2}{c^2\sin(\eta)}\frac{\partial\psi}{\partial\zeta}. \tag{4.42}$$

Appealing to [8], the Stokes function ψ solution to (4.40) writes

$$\psi(\zeta, \chi) = \frac{1}{(\cosh(\zeta) - \chi)^{\frac{3}{2}}}\sum_{n=1}^{\infty} U_n(\zeta)\, V_n(\chi) \tag{4.43}$$

with $V_n(\chi) = P_{n-1}(\chi) - P_{n+1}(\chi)$, $P_n(\chi)$ the Legendre polynomial of order n and each function $U_n(\zeta)$ of the form

$$\begin{aligned} U_n(\zeta) =& A_n\cosh\left[\left(n - \frac{1}{2}\right)\,\zeta\right] + B_n\sinh\left[\left(n - \frac{1}{2}\right)\,\zeta\right] \\ &+ C_n\cosh\left[\left(n + \frac{3}{2}\right)\,\zeta\right] + D_n\sinh\left[\left(n + \frac{3}{2}\right)\,\zeta\right] \end{aligned} \tag{4.44}$$

with unknown coefficients A_n, B_n, C_n and D_n to be obtained from the boundary conditions (4.26)-(4.28). Recalling the zeroth-order flow boundary conditions for the velocity (4.26)-(4.28) on the $\zeta = 0$ free surface reduces to

$$u_{0\zeta}(0, \eta) = 0, \tag{4.45}$$

$$\sigma_{0\zeta\eta}(0, \eta) = \frac{\partial}{\partial\eta}\left(u_{0\zeta}\,h\right) + \frac{\partial}{\partial\zeta}\left(u_{0\eta}\,h\right) = 0 \tag{4.46}$$

with $h = c/(\cosh\zeta - \cos\eta)$ the scale factor (see (F.19) in Appendix F). Exploiting the decomposition of the unit vector $\mathbf{e}_z$

$$\mathbf{e}_z = \frac{1-\cos\eta\cosh\zeta}{\cosh\zeta-\cos\eta}\,\mathbf{e}_\zeta - \frac{\sin\eta\sinh\zeta}{\cosh\zeta-\cos\eta}\,\mathbf{e}_\eta, \tag{4.47}$$

the boundary condition on the bubble surface (4.27), where $\mathbf{n}_0 = \mathbf{e}_\zeta$, becomes

$$u_{0\zeta}(-\zeta_p,\eta) = \mathbf{e}_z\cdot\mathbf{e}_\zeta = \frac{1-\cos\eta\cosh\zeta_p}{\cosh\zeta_p-\cos\eta}. \tag{4.48}$$

On a solid sphere, the boundary condition (4.27) yields [1]

$$u_{0\zeta}(-\zeta_p,\eta) = \frac{1-\cos\eta\cosh\zeta_p}{\cosh\zeta_p-\cos\eta}, \tag{4.49}$$

$$u_{0\eta}(-\zeta_p,\eta) = \frac{\sin\eta\sinh\zeta_p}{\cosh\zeta_p-\cos\eta}. \tag{4.50}$$

Expressing (4.45)-(4.46) in terms of the Stokes function $\psi(\zeta,\eta)$ implies that

$$U_n(0) = 0 \quad \text{for } n\geq 1, \tag{4.51}$$

$$\frac{d^2U_n(0)}{d\zeta^2} = 0 \quad \text{for } n\geq 1. \tag{4.52}$$

These relations (4.51)-(4.52) easily ensure that $A_n = C_n = 0$ and therefore (4.44) becomes [2]

$$U_n(\zeta) = B_n\sinh\left[(n-\frac{1}{2})\,\zeta\right] + D_n\sinh\left[(n+\frac{3}{2})\,\zeta\right]. \tag{4.53}$$

The boundary condition (4.48) (or equivalently (4.49)) on the particle surface yields

$$U_n(\zeta_p) = -\frac{c^2(n+1)n}{\sqrt{2}(2n+1)}\left[\frac{e^{-(n-\frac{1}{2})\zeta_p}}{2n-1} - \frac{e^{-(n+\frac{3}{2})\zeta_p}}{2n+3}\right]. \tag{4.54}$$

In addition, for a solid sphere (4.50) adds the relation

$$\frac{dU_n(\zeta_p)}{d\zeta} = \frac{c^2(n+1)n\sinh\zeta_p}{\sqrt{2}(2n+1)}\,e^{(n+\frac{1}{2})\zeta_p} \tag{4.55}$$

whilst the condition (4.28) on the bubble ($\zeta = -\zeta_p$) which is

$$\sigma_{0\zeta\eta}(-\zeta_p,\eta) = \frac{\partial}{\partial\eta}\left(u_{0\zeta}\,h\right) + \frac{\partial}{\partial\zeta}\left(u_{0\eta}\,h\right) = 0, \tag{4.56}$$

takes the form

$$\sigma_{0\zeta\eta}(-\zeta_p,\eta) = \frac{(\cosh\zeta_p-\chi)^2}{(1-\chi)^{1/2}}\left\{(1-\chi^2)\left[(\cosh\zeta_p-\chi)\frac{\partial^2\psi}{\partial\chi^2} - 3\frac{\partial\psi}{\partial\chi}\right]\right.$$
$$\left. - \left[(\cosh\zeta_p-\chi)\frac{\partial^2\psi}{\partial\zeta^2} - 3\sinh\zeta\frac{\partial\psi}{\partial\zeta}\right]\right\}. \tag{4.57}$$

---

[1] Of course because $\mathbf{u}\cdot\mathbf{n} = \mathbf{e}_z\cdot\mathbf{n}$ on the particle surface whatever its nature. Note (4.48) and (4.49) turn out to be identical relations.

[2] Of course, the result (4.54) holds whatever the particle nature (bubble or solid sphere).

Taking (4.43) into account (4.57) becomes

$$\sigma_{0\zeta\eta}(-\zeta_p,\eta) = \frac{(\cosh\zeta_p-\chi)^{3/2}}{(1-\chi)^{1/2}}\sum_{n=1}^{\infty} V_n(\chi)\left\{\left[\frac{3}{4}-n(n+1)\right]U_n(\zeta_p)\right.$$
$$\left.+\frac{3\sinh\zeta_p}{(\cosh\zeta_p-\chi)^2}U_n(\zeta_p)-U_n''(\zeta_p)\right\}. \quad (4.58)$$

In summary, the stream function ψ is obtained by determining the unknown coefficients B_n and D_n (for $n>1$) from (4.54)-(4.55) for the solid sphere and from (4.54) and (4.58) for the bubble. For the solid sphere the coefficients B_n and D_n also given in [3], are

$$B_n = -\frac{(2n+3)\,k_n\left[(2n+1)e^{-2\zeta_p}+2e^{(2n+1)\zeta_p}-(2n-1)\right]}{2\sinh(2n+1)\zeta_p-(2n+1)\sinh 2\zeta_p}, \quad (4.60)$$

$$D_n = \frac{(2n-1)\,k_n\left[(2n+3)-(2n+1)e^{2\zeta_p}+2e^{(2n+1)\zeta_p}\right]}{2\sinh(2n+1)\zeta_p-(2n+1)\sinh 2\zeta_p} \quad (4.61)$$

with $k_n = c^2\,n(n+1)/[\sqrt{2}(2n+1)(2n+3)(2n-1)]$. For the bubble, one obtains [3]

$$B_n = \frac{(2n+3)\,k_n}{\cosh(2n+1)\zeta_p-\cosh 2\zeta_p}\left[e^{2\zeta_p}-e^{-(2n+1)\zeta_p}\right], \quad (4.62)$$

$$D_n = \frac{(2n-1)\,k_n}{\cosh(2n+1)\zeta_p-\cosh 2\zeta_p}\left[e^{-(2n+1)\zeta_p}-e^{-2\zeta_p}\right] \quad (4.63)$$

again with $k_n = c^2\,n(n+1)/[\sqrt{2}(2n+1)(2n+3)(2n-1)]$.

From the knowledge of the stream function ψ, the viscous stress $\boldsymbol{\tau}_0 = \mu(\boldsymbol{\nabla}\mathbf{u}_0+\boldsymbol{\nabla}\mathbf{u_0}^T)$ is then obtained using (4.41)-(4.42) and the relations (F.18)-(F.19) giving in Appendix F the components of $\boldsymbol{\tau}_0$ in terms of the velocity $\mathbf{u}_0$. However, the stress tensor $\boldsymbol{\sigma}_0 = -p_0\mathbf{I}+\boldsymbol{\tau}_0$ has to be considered in the present work. Therefore, one also needs to calculate the zeroth-order pressure p_0. This pressure p_0, obtained in [5] in bipolar coordinates, writes

$$p_0(\zeta,\chi) = \frac{(\cosh\zeta-\chi)^{1/2}}{c^3}\sum_{n=0}^{\infty}\alpha_n\cosh\left[(n+\frac{1}{2})\zeta\right]P_n(\chi)\,, \quad (4.64)$$

with coefficients α_n given by the following recursive relations

$$\alpha_n = \sum_{n=1}^{n-1}\frac{(2m+1)b_m}{m(m+1)}+\frac{(2n+1)b_n}{n}+\alpha_0 \quad \text{for } n\geq 1, \quad (4.65)$$

$$b_n = -(2n-1)B_n+\frac{2n(2n+3)}{2n+1}B_{n+1}$$
$$+(2n+3)D_n-\frac{2(n-1)(2n-1)}{2n+1}D_{n-1} \quad \text{for } n\geq 1. \quad (4.66)$$

Knowing the B_n and D_n coefficients it is thus sufficient to obtain the coeffficient α_0

$$\alpha_0 = -\lim_{n\to\infty}\left[\sum_{n=1}^{n-1}\frac{(2m+1)b_m}{m(m+1)}+\frac{(2n+1)b_n}{n}\right]. \quad (4.67)$$

---

[3] Correcting the misprint errors in [7].

Now we can evaluate the zeroth-order hydrodynamic force $\mathbf{F}_0$ exerted on the particle

$$\mathbf{F}_0 = \int_{S_1 \text{ or } \Sigma} \boldsymbol{\sigma}_0 \cdot \mathbf{n}_0 dS = -\int_{S_0} \boldsymbol{\sigma}_0 \cdot \mathbf{n}_0 dS \tag{4.68}$$

where the properties $\boldsymbol{\nabla} \cdot \boldsymbol{\sigma}_0 = 0$ has been invoked to obtain the second equality in (4.68). For symmetry reasons, one has $\mathbf{F}_0 = F_0 \mathbf{e}_z$. Moreover, as given in [3], the hydrodynamic force component writes

$$F_0 = \frac{2\pi U \mu \sqrt{2}}{c} \sum_{n=1}^{\infty} (2n+1)(B_n + D_n) \, . \tag{4.69}$$

4.3 First-order free surface deformation

In the present section, we look at the first-order asymptotic approximation of the weakly disturbed free surface shape. As previouly announced, the (accurate) determination of the normal zeroth-order traction $\mathbf{n}_0 \cdot \boldsymbol{\sigma}_0 \cdot \mathbf{n}_0$ on the undisturbed $z = 0$ free surface S_0' is needed in getting such a disturbed shape. We first derive the problem governing the approximated free surface shape in §4.3.1 and then give two different methods to solve this problem in §4.3.2 and §4.3.3.

4.3.1 Governing problem for the free surface shape

The free surface shape is actually dictated by the condition (4.20) giving the normal traction $\mathbf{n} \cdot \boldsymbol{\sigma} \cdot \mathbf{n}$ on the disturbed free surface S_0. Such a condition, which has been discarded so far, reads (since $\mathbf{g} = -g\mathbf{e}_z$)

$$\mathbf{n} \cdot \boldsymbol{\sigma} \cdot \mathbf{n} = -\rho_l g z + \gamma_0 \boldsymbol{\nabla}_S \cdot \mathbf{n} \quad \text{on } S_0 \tag{4.70}$$

where $\boldsymbol{\nabla}_S \cdot \mathbf{n}$ is the mean curvature. Adopting dimensionless variables (see Chapter 1, §1.2) such that $z = 2a\overline{z}$, $\boldsymbol{\sigma} = \mu U \overline{\boldsymbol{\sigma}}/\gamma_0, \boldsymbol{\nabla}_S \cdot \mathbf{n} = \overline{\boldsymbol{\nabla}}_S \cdot \mathbf{n}/d$ with $d = 2a$ the undisturbed particle diameter, one can rewrite (4.70) as

$$\mathbf{n} \cdot \overline{\boldsymbol{\sigma}} \cdot \mathbf{n} = \frac{1}{\mathrm{Ca}_0} \left(-12 \, \mathrm{Bo}_0 \, \overline{z} + \overline{\boldsymbol{\nabla}}_S \cdot \mathbf{n} \right) \quad \text{on } \overline{S}_0 \tag{4.71}$$

where the overlined quantities are dimensionless ones, $\mathrm{Bo}_0 = \rho_l g a^2/(3\gamma_0)$ and $\mathrm{Ca}_0 = \mu U/\gamma_0$. In (4.71) the surface $\overline{S}_0$ is the normalized disturbed free surface. Inspecting (4.71) and recalling that the undisturbed free surface obtained for $\mathrm{Ca}_0 = 0$ is the $z = 0$ plane, we further describe the disturbed (normalized) free surface by an unknown shape function f such that $\overline{z} = \mathrm{Ca}_0 f$ on the disturbed free surface. Omitting henceforth overlines, one obtains on the free surface

$$z = \mathrm{Ca}_0 f + \mathcal{O}(\mathrm{Ca}_0^2), \quad \mathbf{n} \sim \mathbf{n_0} + \mathrm{Ca}_0 \, \tilde{\mathbf{n}}_1 \tag{4.72}$$

with $\tilde{\mathbf{n}}_1$ a vector (a not-necessarily unit one) linearly depending upon shape function f. In (4.72) note that for a solid sphere $\tilde{\mathbf{n}}_1 = \mathbf{n}_1$ while for a bubble $\tilde{\mathbf{n}}_1 = \mathrm{Ca} \, \mathbf{n}_1/\mathrm{Ca}_0$ with $\mathrm{Ca} = Max(\mathrm{Ca}_0, \mathrm{Ca}_1)$. Since the free surface is undisturbed far from the $(z'Oz)$ axis while it exhibits (because of the axisymmetric configuration) an horizontal tangent on the $(z'Oz)$ axis, one imposes the following and simple boundary conditions

$$\frac{df}{d\rho} = 0 \text{ for } \rho = 0, \; f(\rho) = 0 \text{ as } \rho \to \infty, \tag{4.73}$$

where ρ is the usual cylindrical coordinates, i.e. the (normalized) distance to the $(z'Oz)$ axis.

Injecting the approximations (4.72) in (4.71), noting that $\mathbf{n}_0 = \mathbf{e}_z$ is constant and retaining only the leading terms yields the equation

$$\mathbf{n}_0 \cdot \boldsymbol{\sigma}_0 \cdot \mathbf{n}_0 = -12\,\mathrm{Bo}_0\, f + [\boldsymbol{\nabla}_S \cdot \mathbf{n}_1]\,(f) \text{ at } z = 0. \tag{4.74}$$

Actually, the first-order mean curvature $\boldsymbol{\nabla}_S \cdot \tilde{\mathbf{n}}_1$ linearly depends upon the shape function f and this property is here recalled by using the notation $[\boldsymbol{\nabla}_S \cdot \tilde{\mathbf{n}}_1](f)$ in (4.74). Consequently, (4.73)-(4.74) turn out to be a linear problem for the unknown shape function f for which the (small) Bond number Bo_0 is given.

The first-order free surface location $z = \mathrm{Ca}_0 f(\rho)$ then depends on $(\mathrm{Bo}_0, \mathrm{Ca}_0)$ and of the particle position and nature through the term $\mathbf{n}_0 \cdot \boldsymbol{\sigma}_0 \cdot \mathbf{n}_0$ (hence for a bubble it does not depend upon the bubble surface tension γ_1). Moreover, the normal traction $[\mathbf{n}_0 \cdot \boldsymbol{\sigma}_0 \cdot \mathbf{n}_0](z = 0)$ on the undisturbed $z = 0$ free surface is accurately known from the zeroth-order solution (here in bipolar coordinates) previously presented in §4.2. Two different methods are then described in §4.3.2 and §4.3.3 to solve the governing problem (4.73)-(4.74).

Whenever $\mathrm{Bo}_0 = \mathcal{O}(\mathrm{Ca}_0)$ is small, as noticed for a *force-free* particle, it turns out that it is possible to neglect the term $-12\,\mathrm{Bo}_0\, f$ on the right-hand side of (4.74). However, Berdan and Leal [2] also considered the case of a sphere not necessarily force-free but with an imposed velocity. In that case, the $\mathrm{Bo}_0 = \mathcal{O}(\mathrm{Ca}_0)$ relation is not always valid and those authors actually also examined the case $\mathrm{Bo}_0 = \mathcal{O}(1)$ and Ca_0 small. Since (see §4.3.2) it is moreover possible to solve (4.73)-(4.74) in close form we decided to keep the $-12\,\mathrm{Bo}_0\, f$ term in our analysis (therefore introducing a $\mathcal{O}(\mathrm{Ca}_0^2)$ error when Bo_0 becomes very small).

4.3.2 Solution in cylindrical coordinates

A problem similar to (4.73)-(4.74) has been actually handled in Berdan and Leal [2] using cylindrical coordinates for a *distant solid* sphere. In such a case, Berdan and Leal [2] resorted to an asymptotic approximation of the quantity $\mathbf{n}_0 \cdot \boldsymbol{\sigma}_0 \cdot \mathbf{n}_0$ solely valid when the solid sphere distance l to the $z = 0$ plane is large compared to the sphere radius a.

In the present subsection we extend the Berdan and Leal procedure to our case of a particle (i.e. either a bubble or a solid sphere) of *arbitrary* location (i.e. for which l is not necessarily large compared to a). Adopting usual cylindrical coordinates z and ρ (distance to the $(z'Oz)$ axis) the free surface location has equation $z = \mathrm{Ca}_0 f(\rho)$ and one gets the relation

$$[\boldsymbol{\nabla}_S \cdot \tilde{\mathbf{n}}_1](f) = \frac{d^2 f}{d\rho^2} + \frac{1}{\rho}\frac{df}{d\rho}. \tag{4.75}$$

Accordingly, one arrives at the well-posed problem

$$\rho \frac{d^2 f}{d\rho^2} + \frac{df}{d\rho} - t\rho f = \rho \left[\mathbf{n}_0 \cdot \boldsymbol{\sigma}_0 \cdot \mathbf{n}_0\right](z=0) \tag{4.76}$$

$$\frac{df}{d\rho} = 0 \ \text{ at } \rho = 0, \qquad f(\rho) = 0 \text{ as } \rho \to \infty \tag{4.77}$$

with parameter $t = 12\,\mathrm{Bo}_0$.

It turns out that (4.76)-(4.77) admit a solution in closed form. As detailed in Appendix D and noting that $\mathbf{n}_0 \cdot \boldsymbol{\sigma}_0 \cdot \mathbf{n}_0 = \sigma_{0\zeta\zeta}$ on the $z = 0$ plane, this solution writes

$$f(\rho) = \left\{ I_0(\sqrt{t}\rho) \int_\rho^\infty K_0(\sqrt{t}u)\, u\, \sigma_{0\zeta\zeta}(u) du - K_0(\sqrt{t}\rho) \int_0^\rho I_0(\sqrt{t}u)\, u\, \sigma_{0\zeta\zeta}(u) du \right\} \tag{4.78}$$

where I_0 and K_0 denote the usual modified Bessel functions of the first and second kind, respectively. Those functions are defined as (see [1])

$$I_0(x) = \frac{1}{\pi}\int_0^\pi \cosh(x\cos\theta) d\theta, \quad K_0(x) = \int_0^\infty \frac{\cos(tx)}{\sqrt{t^2+1}} dt. \tag{4.79}$$

By virtue of (4.79), one immediately gets $I_0(0) = 1$. The value of the shape function at the $(z'Oz)$ axis then becomes

$$f(0) = \int_0^\infty K_0(\sqrt{t}u)\, u\, \sigma_{0\zeta\zeta}(u) du. \tag{4.80}$$

Finally, appealing to the properties $I_0' = I_1$ and $K_0' = -K_1$, the free surface shape function has the following slope form

$$\frac{df}{d\rho} = \sqrt{t} \left\{ K_1(\sqrt{t}\rho) \int_0^\rho \sigma_{0\zeta\zeta}(u) u\, I_0(\sqrt{t}u) du - I_1(\sqrt{t}\rho) \int_\rho^\infty \sigma_{0\zeta\zeta}(u) u\, K_0(\sqrt{t}u) du \right\}. \tag{4.81}$$

Since $I_0(1) = 0$ such a slope vanishes at $\rho = 0$ and this property complies with the requested condition (4.77).

One should note that (4.81) holds whatever the particle nature: solid sphere or (spherical) bubble. One solely needs to accurately compute the required zeroth-order normal traction $\sigma_{0\zeta\zeta}(0,\eta) = [\mathbf{n}_0 \cdot \boldsymbol{\sigma}_0 \cdot \mathbf{n}_0](z = 0)$ on the flat $z = 0$ undisturbed free surface for each type of particle. This key step is in practice adequately achieved using the bipolar coordinates and the formula (F.22) expressing the quantity $\sigma_{0\zeta\zeta}(\rho) = \sigma_{0\zeta\zeta}(0,\eta)$ with the link $\rho = c\sin\eta/(1 - cos\eta)$ and $\eta \in [0,\pi]$.

4.3.3 Solution in bipolar coordinates

Using the well-adapted bipolar coordinates in §4.2 to obtain the zeroth-order flow might suggest also solving the problem (4.73)-(4.74) by appealing again to such unusual coordinates. Such a task has been actually performed by Chervenivanova and Zapryanov [5] to determine the first-order free surface shape at vanishing Bond number for a nearly-spherical droplet weakly interacting with a free surface. Although Chervenivanova and Zapryanov [5] handled the case of a *droplet* and a free surface with not-necessarily equal surface tensions, the achieved work amazingly does not require the disturbed free surface to admit an horizontal tangent on the $(z'Oz)$ axis.

Therefore, the obtained and computed free surface shapes for different values of the free surface and droplet surface tensions are not relevant. The present section develops a solution in bipolar coordinates for the shape function f which, in contrast, complies with the zero slope condition at the $(z'Oz)$ axis, i.e. with our boundary condition $df/d\rho = 0$ at $\rho = 0$.

Since the undisturbed free surface has equation $z = \zeta = 0$ one sets $\zeta = \mathrm{Ca}_0\, F(\eta)$. From (4.35) then on the disturbed free surface one has

$$z = \frac{c\,\mathrm{Ca}_0\, F(\eta)}{1-\cos\eta}, \quad f = \frac{c\, F(\eta)}{1-\cos\eta}. \tag{4.82}$$

From (4.35) it appears that $\rho \to \infty$ for $\eta \to 0$. Hence, the condition (4.73) for ρ large becomes

$$\lim_{\eta\to 0} \frac{F(\eta)}{1-\cos\eta} \to 0. \tag{4.83}$$

Using the relations

$$\frac{z}{c} = \frac{\sinh\zeta}{\cosh\zeta-\cos\eta}, \qquad \frac{\rho}{c} = \frac{\sin\eta}{\cosh\zeta-\cos\eta}, \tag{4.84}$$

it follows that

$$\frac{dz}{d\rho} = \frac{\mathrm{Ca}_0 F'[1-\cosh\zeta\cos\eta] - \sinh\zeta\sin\eta}{-1+\cos\eta\cosh\zeta - \mathrm{Ca}_0 F'\sinh\zeta\sin\eta}, \quad F' = \frac{dF}{d\eta}. \tag{4.85}$$

In enforcing the first condition (4.73) of zero slope in the $(z'Oz)$ axis, one set $\eta = \pi - \alpha$ where $\alpha > 0$ is small. Using the behaviors

$$\cos\eta = -\cos\alpha \sim -1 + \frac{\alpha^2}{2}, \quad \sin\eta = \sin\alpha \sim \alpha \tag{4.86}$$

the condition (4.86) becomes

$$\lim_{\eta\to\pi} \frac{dz}{d\rho} \sim -\mathrm{Ca}_0 \left[F' - \frac{\alpha}{2}F\right] \tag{4.87}$$

Setting $\chi = \cos\eta$ with $\chi \in [-1, 1]$, one has

$$\frac{dF}{d\eta} = -\sin\eta\,\frac{dF}{d\chi} \sim -\alpha\,\frac{dF}{d\chi}. \tag{4.88}$$

Finally, one arrives at the condition

$$\alpha\,\mathrm{Ca}_0 \left[2\frac{dF}{d\chi} + F\right] = 0 \qquad \text{for } \eta = \pi \ (\chi = -1). \tag{4.89}$$

For the surface $\zeta = \mathrm{Ca}_0 F(\eta)$, it is possible to establish that

$$[\boldsymbol{\nabla}\cdot\tilde{\mathbf{n}}_1] = -\frac{1}{c}\left[(1-\chi)^3\frac{\partial}{\partial\chi}\left\{\frac{1-\chi^2}{(1-\chi)^2}\frac{dF}{d\chi}\right\} + 2F\right]. \tag{4.90}$$

Injecting (4.90) into (4.74) one arrives at the governing problem

$$\mathrm{Ca}\,\sigma_{0\zeta\zeta}(0,\eta) = \frac{12\,\mathrm{Bo}\,c\,F(\eta)}{1-\chi} - \frac{1}{c}\left[(1-\chi)^3\frac{\partial}{\partial\chi}\left\{\frac{1-\chi^2}{(1-\chi)^2}\frac{dF}{d\chi}\right\} + 2\,F\right] \tag{4.91}$$

$$2\,\frac{dF}{d\chi} + F = 0 \;\text{ at } \chi = -1, \qquad \lim_{\chi\to 1}\frac{F(\chi)}{(1-\chi)} = 0 \quad \text{at } \chi \to 1 \tag{4.92}$$

for the unkown free surface new shape function F. The problem (4.91)-(4.92) is the counterpart for F in bipolar coordinates of the problem (4.76)-(4.77) for f in cylindrical coordinates. Note that (4.91) together with the second condition (4.92) have been proposed by Cherveninvanova and Zapryanov [4] in the case of a free surface weakly deformed by a nearly-spherical *droplet*. Moreover, those authors proposed to seek the shapes function F under the following form

$$F(\chi) = (1-\chi)^{3/2}\sum_{n=0}^{\infty} H_n P_n(\chi) \tag{4.93}$$

where it is recalled that P_n is the Legendre polynomial of order n (see definition of V_n right after (4.43)) and the coefficients H_n are unknown quantities. Enforcing the second condition (4.92) and injecting (4.93) into (4.91), Chervenivanova and Zapryanov [4] arrived at an infinite linear system for the coefficients H_n which has been numerically solved by truncation. Unfortunately, such an approach exhibits a slow rate of convergence and moreover the zero slope condition at $\rho = 0$ is not taken in account. For the present work, we retained the $(1-\chi)^{3/2}$ factor in (4.93) and thus introduce a new unknown function $h(\chi)$ such that

$$F(\chi) = (1-\chi)^{3/2} h(\chi). \tag{4.94}$$

After elementary manipulations, the differential equation (4.91) for F yields for h

$$\begin{aligned}(1+\chi)(1-\chi)^3\,h''(\chi) &+ [2(1-\chi)^2 - 3(1+\chi)(1-\chi)^2]\,h'(\chi) \\ &+ [\frac{3}{4}(1+\chi)(1-\chi) + 2(1-\chi) - 12\,c^2\mathrm{Bo}]\,h(\chi) = -c\,(1-\chi)^{-1/2}\,\sigma_{0\zeta\zeta}\end{aligned} \tag{4.95}$$

while the boundary conditions (4.92) become

$$4h'(\chi) - h(\chi) = 0 \;\text{ at } \chi = -1, \quad \lim_{\chi\to 1}\frac{h(\chi)}{(1-\chi)^{1/2}} \to 0 \quad \text{at } \chi \to 1. \tag{4.96}$$

4.4 First-order bubble shape

In this section, we now pay attention to the first-order shape of a weakly deformed bubble (the particle is a bubble).

4.4.1 Governing problem for the bubble shape

A similar problem has been handled using bipolar coordinates in Chervenivanova and Zapryanov [4] for a droplet weakly interacting with a free surface. As previously seen in §4.3 for the free surface shape and also from the procedure worked out in [4], it turns out that resorting to bipolar coordinates complicates the treatment. The undisturbed free surface is flat and in that case cylindrical coordinates have been found suitable. Since the undisturbed bubble is spherical we here use spherical coordinates centered on the undisturbed bubble center O'. Such a choice is illustrated in Figure 4.2.

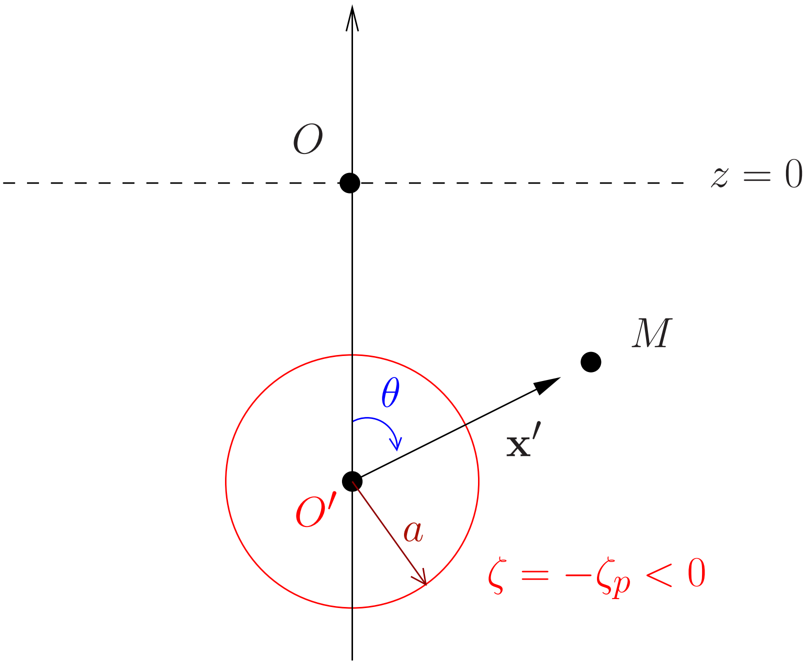

Figure 4.2: Adopted spherical coordinates (r', θ, ϕ) with $\mathbf{x}' = \mathbf{O'M}$, $r' = |\mathbf{x}'|$, $z' = \mathbf{O'M}.\mathbf{e}_z = r' \cos\theta$. O' is the bubble center-of-volume.

Since our problem is axisymmetric, the equation of the disturbed bubble surface is taken to be

$$r' = r'(\theta) = a[1 + \mathrm{Ca}_1\, \xi(\theta) + \mathcal{O}(\mathrm{Ca}_1^2)] \tag{4.97}$$

with ξ an unknown shape function. As pointed out in Chapter 1, the bubble volume V_b is requested to be constant. Such a condition immediately reads

$$\int_0^{2\pi} \left\{ \int_0^{\pi} \left[\int_0^{r'(\theta)} r'^2 dr' \right] \sin\theta d\theta \right\} d\phi = \frac{4\pi a^3}{3}. \tag{4.98}$$

Retaining in (4.98) the $\mathcal{O}(\mathrm{Ca}_1)$ term, it accordingly turns out that

$$\int_0^{\pi} \xi(\theta) \sin\theta d\theta = 0. \tag{4.99}$$

In addition, the point O' is the bubble center-of-volume. It is selected when following in time the bubble location and we require the disturbed bubble to have O' as center-of-volume. In other words, one also enforces the following additionnal center-of-volume conservation

$$\int_{\mathcal{B}_1} \mathbf{x}' \cdot \mathbf{e}_z d\Omega = 0 \tag{4.100}$$

where $\mathcal{B}_1$ denotes the disturbed bubble domain.

Because $\mathbf{x}' \cdot \mathbf{e}_z = r' \cos\theta$, (4.100) becomes

$$\int_0^{2\pi} \left\{ \int_0^{\pi} \left[\int_0^{r'(\theta)} r'^2 dr' \right] \sin\theta \cos\theta d\theta \right\} d\phi = 0. \tag{4.101}$$

Expanding (4.101) in terms of the capillary number Ca_1, one then arrives at the second relation

$$\int_0^{\pi} \xi(\theta) \sin\theta \cos\theta d\theta = 0. \tag{4.102}$$

Since $r' = r'(\theta)$, the unit vector $\mathbf{n}$ on the *disturbed* bubble surface (here directed into the liquid domain) writes

$$\mathbf{n} = \frac{r'\mathbf{e}_r - \dfrac{dr'}{d\theta}\mathbf{e}_\theta}{\sqrt{r'^2 + \left(\dfrac{dr'}{d\theta}\right)^2}} \tag{4.103}$$

with $\mathbf{e}_r = \mathbf{x}'/r'$ and $\mathbf{e}_\theta$ the usual unit vector in spherical coordinates. Requiring the bubble surface to admit (for axisymmetry reasons) an horizontal tangent at its two pole ($\theta = 0$ and $\theta = \pi$) on the $(z'Oz)$ axis then yields two additionnals conditions

$$\xi' = \frac{d\xi}{d\theta} = 0 \ \text{ at } \theta = 0, \qquad \zeta' = \frac{d\xi}{d\theta} = 0 \ \text{ at } \theta = \pi. \tag{4.104}$$

As for the free surface case, the differential equation for the shape function ξ' is dictated by the relation (4.21) for the normal traction $\mathbf{n}_0 \cdot \boldsymbol{\sigma}_0 \cdot \mathbf{n}_0$ on the disturbed bubble surface S_1. This equation reads

$$\mathbf{n} \cdot \boldsymbol{\sigma} \cdot \mathbf{n} = -\rho_l g z - p_{1b} + \gamma_1 \boldsymbol{\nabla}_S \cdot \mathbf{n} \quad \text{ on } S_1 \tag{4.105}$$

with p_{1b} the uniform pressure in the bubble. This pressure is now expanded versus the small capillary number Ca_1 as follows

$$p_{1b} = p_{1b}^0 + \mathrm{Ca}_1 p_{1b}^1 + \mathcal{O}(\mathrm{Ca}^2) \tag{4.106}$$

where constant pressure p_{1b}^0 and p_{1b}^1 are unknown quantities. Accordingly, one has to determine both the bubble shape function ξ and the pressures p_{1b}^0 and p_{1b}^1.

As introduced in Chapter 1, we normalize in (4.105) the quantities as follows (denoting by $d = 2a$ the undisturbed bubble diameter)

$$\boldsymbol{\sigma} \equiv \frac{\mu U}{d}\overline{\boldsymbol{\sigma}}\ , \qquad l = d\,\bar{l}, \qquad z = d\bar{z}\ , \qquad r' = d\bar{r}'\ , \qquad \boldsymbol{\nabla}_S \cdot \mathbf{n} = \overline{\boldsymbol{\nabla}}_S \cdot \mathbf{n}/d. \tag{4.107}$$

Recalling the definitions

$$\mathrm{Bo}_1 = \frac{\rho_l g a^2}{3\gamma_1}, \qquad \mathrm{Ca}_1 = \frac{\mu U}{\gamma_1} \tag{4.108}$$

and the relation $z = -l + r'\cos(\theta)$ on the bubble, (4.105) becomes

$$\mathbf{n} \cdot \boldsymbol{\sigma} \cdot \mathbf{n} = \frac{12\,\mathrm{Bo}_1}{\mathrm{Ca}_1}\,\bar{l} - \frac{d}{\gamma_1 \mathrm{Ca}_1} p_{1b} - \frac{12\,\mathrm{Bo}_1}{\mathrm{Ca}_1}\,\bar{r}'\cos\theta + \frac{1}{\mathrm{Ca}_1}\overline{\boldsymbol{\nabla}}_S \cdot \mathbf{n} \quad \text{ on } \overline{S}_1. \tag{4.109}$$

The next step consists in approximating (4.109) using the expansion (4.97) for $\overline{r}' = r'/d$, (4.106) for the constant bubble pressure p_{1b} and also the curvature expansion (which may be easily deduced from (4.97))

$$\overline{\boldsymbol{\nabla}}_s \cdot \mathbf{n} = d\boldsymbol{\nabla} \cdot \mathbf{n} = 2\left\{2 - \mathrm{Ca}_1 \left[2\xi + \frac{1}{\sin\theta}\frac{d}{d\theta}\left(\sin\theta\frac{d\xi}{d\theta}\right)\right]\right\} + \mathcal{O}(\mathrm{Ca}^2). \tag{4.110}$$

After elementary manipulations, one thus arrives at the approximated normal traction condition (dropping henceforth the overlines)

$$\mathbf{n}_0 \cdot \boldsymbol{\sigma}_0 \cdot \mathbf{n}_0 = \frac{1}{\mathrm{Ca}_1}\frac{d}{\gamma_1}\left[\frac{2\gamma_1}{a} - p^0_{1b}\right] + \frac{12\,\mathrm{Bo}_1}{\mathrm{Ca}_1}\,l - \frac{d}{\gamma_1}p^1_{1b} - \frac{6\,\mathrm{Bo}_1}{\mathrm{Ca}_1}\cos\theta \\ - 2\left[3\,\mathrm{Bo}_1\xi\cos\theta + L(\xi)\right] \tag{4.111}$$

where the quantity $\mathbf{n}_0 \cdot \boldsymbol{\sigma}_0 \cdot \mathbf{n}_0$ is to be taken on the *undisturbed* bubble ($r' = a$) therefore solely depending on $\theta \in [0, \pi]$ and the linear differential operator L is defined as

$$L(\xi) = 2\xi + \frac{1}{\sin\theta}\frac{d}{d\theta}\left[\sin\theta\frac{d\xi}{d\theta}\right]. \tag{4.112}$$

In the limit of vanishing capillary number Ca_1 (4.112) then immediately yields at order $\mathcal{O}(\mathrm{Ca}_1^{-1})$ the relation

$$p^0_{1b} = \frac{2\gamma_1}{a} \tag{4.113}$$

and at the $\mathcal{O}(1)$ order the key differential equation

$$3\,\mathrm{Bo}_1\xi\cos\theta + L(\xi) = R(\theta; p^1_{1b}) \tag{4.114}$$

where the right-hand side $R(\theta; p^1_{1b})$ depends upon the *undisturbed* pressure p^1_{1b} and is defined as

$$R(\theta; p^1_{1b}) = \frac{1}{2}\left\{\frac{12\,\mathrm{Bo}_1}{\mathrm{Ca}_1}\,l - \frac{d}{\gamma_1}p^1_{1b} - \frac{6\,\mathrm{Bo}_1}{\mathrm{Ca}_1}\cos\theta - [\mathbf{n}_0 \cdot \boldsymbol{\sigma}_0 \cdot \mathbf{n}_0](\theta)\right\}. \tag{4.115}$$

In summary, the first-order bubble disturbed shape ξ is gained by solving the following problem for the unknown function $\xi(\theta)$ and constant pressure p^1_{1b}

$$t\,\xi\cos\theta + L(\xi) = R(\theta; p^1_{1b}), \tag{4.116}$$

$$\int_0^\pi \xi(\theta)\sin\theta d\theta = 0, \tag{4.117}$$

$$\int_0^\pi \xi(\theta)\sin\theta\cos\theta d\theta = 0, \tag{4.118}$$

$$\xi' = \frac{d\xi}{d\theta} = 0 \;\text{ at }\; \theta = 0, \qquad \xi' = \frac{d\xi}{d\theta} = 0 \;\text{ at }\; \theta = \pi, \tag{4.119}$$

with $t = 3\mathrm{Bo}_1$. Combining (4.112) with (4.116) gives the relation

$$t\xi\sin\theta\cos\theta + 2\xi\sin\theta + \frac{d}{d\theta}\left[\sin\theta\frac{d\xi}{d\theta}\right] = R(\theta; p^1_{1b})\sin\theta \tag{4.120}$$

which, when integrated over θ in the range $[0,\pi]$, yields because of the requirements (4.117)-(4.118) the compatibility relation

$$\int_0^\pi R(\theta;p_{1b}^1)\sin\theta d\theta=0. \tag{4.121}$$

This latter condition actually provides the constant pressure p_{1b}^1 which then writes

$$p_{1b}^1=\frac{\gamma_1}{d}\left\{\frac{12\,\mathrm{Bo}_1}{\mathrm{Ca}_1}\,l-\frac{1}{2}\int_0^\pi[\mathbf{n}_0\cdot\boldsymbol{\sigma}_0\cdot\mathbf{n}_0](\theta)\sin\theta d\theta\right\}. \tag{4.122}$$

Using (4.122) permits one to reduce the linear problem for the shape function ξ to (4.116), (4.117)-(4.119). As seen before for a force-free bubble, one has $\mathrm{Bo}_1=\mathcal{O}(\mathrm{Ca}_1)$ and this suggests neglecting the term $t\,\xi\cos\theta$ on the left-hand side of (4.116) as soon as $\mathrm{Bo}_1\le 1$.

4.4.2 Solution in closed form

Our linear problems (4.116), (4.117)-(4.119) is the counterpart for the bubble shape of the linear problem (4.76)-(4.77) derived from the free surface shape. Unfortunately, it has not been possible to derive the bubble shape function ξ in closed form (as was achieved for the free surface, see result (4.78)). The parameter $t=3\mathrm{Bo}_1$ occurring in (4.116) vanishes with Bo_1. Therefore, at the retained first-order approximation, one may be tempted to ignore on the right-hand side of (4.116) the term $t\,\xi\cos\theta$. In the present work we therefore discard this term in (4.116). The bubble shape function ξ then obeys the problem

$$L(\xi)=R(\theta;p_{1b}^1)=S(\theta), \tag{4.123}$$

$$\int_0^\pi\xi(\theta)\sin\theta d\theta=\int_0^\pi\xi(\theta)\sin\theta\cos\theta d\theta=0, \tag{4.124}$$

$$\frac{d\xi}{d\theta}=0\ \text{ for }\theta=0\text{ and }\theta=\pi. \tag{4.125}$$

Contrary to the more tricky problem (4.116)-(4.119), the solution (4.123)-(4.125) has been obtained here in closed form. Adopting the technique used to write (4.120) it is first easy to prove that the first condition (4.124) holds if the following compatibility condition

$$\int_0^\pi S(\theta)\sin\theta d\theta=0, \tag{4.126}$$

is satisfied. Applying the above relation to (4.123) shows that the pressure p_{1b}^1 is again provided by (4.122). As also established in Appendix E, the linear problem (4.123)-(4.125) is actually well-posed under the two following compatibility conditions for the right-hand side $S(\theta)$ (the first one being (4.126))

$$\int_0^\pi S(\theta)\sin\theta d\theta=0,\int_0^\pi S(\theta)\sin\theta\cos\theta d\theta=0. \tag{4.127}$$

Under those conditions (4.127) the unique solution to (4.123)-(4.125) is (see details in Appendix E)

$$\xi(\theta)=-\frac{3}{2}\left[\int_0^\pi f(u)\sin(u)\cos(u)du\right]\cos\theta+f_S(\theta) \tag{4.128}$$

with function f_S depending upon the right-hand side as follows

$$f_S(\theta) = \int_0^\pi \Big\{[1+\cos\theta\log(\tan\frac{\pi}{2})]\cos(u) \\ -\cos\theta[1+\cos(u)\log(\tan\frac{u}{2})]\Big\}\, S(u)\sin(u)du. \qquad (4.129)$$

As previously noticed, the first condition (4.127) is satisfied for the problem (4.123)-(4.125). Let us now turn to the second condition (4.127). One thus has to check that

$$\int_0^\pi R(\theta, p_0)\sin\theta\cos\theta d\theta = 0. \qquad (4.130)$$

Recalling (4.118) the condition (4.115) is equivalent to the link

$$\int_0^\pi \left\{[\mathbf{n}_0\cdot\boldsymbol{\sigma}_0\cdot\mathbf{n}_0](\theta) + \frac{6\,\mathrm{Bo}_1}{\mathrm{Ca}_1}\cos\theta\right\}\cos\theta\sin\theta d\theta = 0, \qquad (4.131)$$

where $\int_0^\pi[\mathbf{n}_0\cdot\boldsymbol{\sigma}_0\cdot\mathbf{n}_0](\theta)\sin\theta d\theta$ is a constant and therefore vanishes when integrating over $\cos\theta\sin\theta d\theta$. At this point it is worth recalling the boundary condition for the traction $\boldsymbol{\sigma}\cdot\mathbf{n}$ on the bubble surface which reads

$$\boldsymbol{\sigma}\cdot\mathbf{n} = (-\rho_l gz - p_{1b} + \gamma_1\boldsymbol{\nabla}_s\cdot\mathbf{n})\mathbf{n} \quad \text{on } S_1. \qquad (4.132)$$

Integrating (4.132) over the bubble surface gives (no contribution of the mean curvature term $\boldsymbol{\nabla}_s\cdot\mathbf{n}$, as seen in Chapter 1)

$$\int_{S_1}[\boldsymbol{\sigma}\cdot\mathbf{n} + \rho_l gz\mathbf{n}]\,dS = 0. \qquad (4.133)$$

The relation (4.133) is expanded versus Ca_1 using the link $z = -l + \overline{r'}(\theta)$. Adopting dimensionless variable it thus yields, at order $\mathcal{O}(\mathrm{Ca}_1)$

$$\int_{S_{1_0}}\left[\boldsymbol{\sigma}_0\cdot\mathbf{n}_0 + 6\frac{\mathrm{Bo}_1}{\mathrm{Ca}_1}\mathbf{n}_0\right]dS = \mathbf{0} \qquad (4.134)$$

with S_{1_0} the spherical surface of the disturbed bubble. Since for the zeroth-order flow $(\mathbf{u}_0, p_0)$ one has the boundary condition $\boldsymbol{\sigma}_0\cdot\mathbf{n}_0 = [\mathbf{n}_0\cdot\boldsymbol{\sigma}_0\cdot\mathbf{n}_0]\mathbf{n}_0$, taking the z component (the only non-zero one for the addressed axisymmetric problem), one then arrives at the relation

$$\int_0^\pi\left[\mathbf{n}_0\cdot\boldsymbol{\sigma}_0\cdot\mathbf{n}_0 + \frac{6\mathrm{Bo}_1}{\mathrm{Ca}_1}\right](\mathbf{n}_0\cdot\mathbf{e}_z)\sin\theta d\theta = 0 \qquad (4.135)$$

which turns out to be the condition (4.131). Accordingly, the problem (4.123)-(4.125) is well-posed and its solution is given by (4.128)-(4.129).

Bibliography

[1] M. Abramowitz and I. A. Stegun. *Handbook of mathematical functions.* Dover Publications, Inc., New York, 1965.

[2] C. Berdan and L. G. Leal. Motion of a sphere in the presence of a deformation interface. I. Perturbation of the interface from flat: The effects on drag and torque. *J. Colloid Interface Sci.*, 87:62–80, 1982.

[3] Howard Brenner. The slow motion of a sphere through a viscous fluid towards a plane surface. *Chem. Eng. Sci.*, 16(3):242–251, 1961.

[4] E. Chervenivanova and Z. Zapryanov. On the deformation of two droplets in a quasisteady Stokes flow. *Int. J. Multiphase Flow*, 11:721–738, 1985.

[5] E. Chervenivanova and Z. Zapryanov. The slow motion of droplets perpendicular to a deformable flat fluid interface. *Q. J. Mechanics Appl. Math.*, 41(3):419–444, 1988.

[6] J. Happel and H. Brenner. *Low Reynolds number hydrodynamics.* Martinus Nijhoff Publishers, The Hague, 1983.

[7] R. Shankar Subramanian M. Meyyeppan, W. R. Wilcox. Thermocapillary migration of a bubble normal to a plane surface. *J. Colloid Interface Sci.*, 83:199–208, 1981.

[8] M. Stimson and G. B. Jeffery. The motion of two spheres in a viscous fluid. *Prod. R. Soc. London, Serie A*, 111:110–116, 1926.

[9] Z. Zapryanov and S. Tabakova. *Dynamics of bubbles, drops and rigid particles.* Kluwer academic publishers, Dordrecht, 1999.

Chapter 5

Asymptotic analysis: benchmark tests and results

Contents

In this Chapter, the asymptotic analysis described in Chapter 4 is implemented and tested. First, the zeroth-order flow $(\mathbf{u}_0, p_0)$ and the associated zeroth-order force $\mathbf{F}_0$ exerted on a spherical particle (solid sphere or bubble) interacting with a flat free surface are obtained and compared with the results given in [1]. Then, we determine the free surface shape when weakly disturbed using two different methods. The first technique appeals to the cylindrical coordinates to obtain the weakly deformed free surface shape, extending the results obtained in [2] whatever the particle location. In the second approach, the free surface is determined using the bipolar coordinates. Finally, the asymptotically obtained free surface shape is compared with the computed free surface (obtained with the BEM Code) for different Bond number and surface tension ratio $\hat{\gamma} = \gamma_0/\gamma_1$ where γ_0 and γ_1 are the free surface tension and the bubble surface tension, respectively.

5.1 Zeroth-order problem: results and validation

The bipolar method introduced in the previous Chapter 4 (see §4.2.1) is carefully tested against the literature. First, we determine the zeroth-order flow $(\mathbf{u}_0, p_0)$ either for a solid sphere or a bubble. We then compare the computed hydrodynamic force $\mathbf{F}_0$ exerted on the particle against the values given in [1].

For a solid sphere with radius a ascending in an unbounded fluid with viscosity μ at the velocity $U\mathbf{e}_z$, the Stokes law for the applied hydrodynamic force is $\mathbf{F}_\infty = -6\pi\mu\, a\, U\mathbf{e}_z$. In the case of a sphere interacting with a *rigid* free surface, one gets (for symmetry reasons)

$$\mathbf{F}_{0s} = -6\pi\mu\, a\, \lambda_{0s}\, U\mathbf{e}_z, \tag{5.1}$$

with $\lambda_{0s} > 0$ the drag coefficient. Similarly, the drag force $\mathbf{F}_{0b}$ on a bubble, which takes the value $-4\pi\mu\, a\, U\mathbf{e}_z$ in the unbounded liquid, here writes when iteracting with a *rigid* free surface

$$\mathbf{F}_{0b} = -4\pi\mu\, a\, \lambda_{0b}\, U\mathbf{e}_z, \tag{5.2}$$

with $\lambda_{0b} > 0$ the associated drag coefficient.

Recalling the results (4.68), the required drag coefficients λ_{0s} and λ_{0b} read

$$\lambda_{0s} = -\frac{\sqrt{2}}{3ac}\sum_{n=1}^{\infty}(2n+1)(B_n+D_n)\ \text{(solid particle)}\ , \tag{5.3}$$

$$\lambda_{0b} = -\frac{\sqrt{2}}{2ac}\sum_{n=1}^{\infty}(2n+1)(B_n+D_n)\ \text{(bubble)} \tag{5.4}$$

where coefficients B_n and D_n depend on the particle nature (solid sphere or spherical bubble) and are given in Chapter 4 (see §4.4.2).

The particle (solid or bubble) having a surface with equation $\zeta = -\zeta_p$ $(\zeta_p > 0)$ presents a center-of-volume located at $z = -l$ with $l = a\cosh\zeta_p$. The values of λ_{0s} and λ_{0b} are then computed from the relations (5.3) and (5.4) for a given particle location l/a, here normalized by the bubble radius a. Some numerical results are provided in Table 5.1 for comparison with Bart results given in [1].

l/a	ζ_p	λ_{0s} (Bart)[1]	λ_{0s}	λ_{0b}* (Bart)[1]	λ_{0b}
1.127626	0.5	3.986699	3.986699	2.049981	2.049981
1.543081	1.0	1.973681	1.973681	1.509456	1.509455
2.352410	1.5	1.463478	1.463478	1.2734500	1.2734499
3.762196	2.0	1.247126	1.247126	1.1536956	1.1536956
6.132289	2.5	1.138856	1.138856	1.0888266	1.0888266
10.067660	3.0	1.080376	1.080376	1.0522662	1.0522661

Table 5.1: Computed drag coefficients λ_{0s} and λ_{0b} versus l/a and ζ_p.

One should mention that the drag coefficient λ_{0b} given in [1] is obtained using the drag force relation (5.3) implying therefore a factor 2/3 when compare with our computed λ_{0b} values. One then calculates the Bart values using the relation (5.4), denoting the results by $\lambda_{0b}{}^*$ in Table 5.1. These results are obtained with a summation of the coefficients B_n and D_n with (5.3)-(5.4) (see the relation (4.68) in Chapter 4) truncated at $N_t = 20$ which is quite sufficient here for $l/a \geq 0.5$. These values are identical up to 6 digits to the results given in [1].

Furthermore, the knowledge of λ_{0s} and λ_{0b} permits one to check the accurate computation of the key zeroth-order normal traction either on the particle boundary by invoking (4.67) or on the flat undisturbed free surface. Indeed, the right-hand side of the free surface equation (4.95) requests the evaluation of $\sigma_{0\zeta\zeta}$ when determining the free surface shape for a given particle location. Note that we here both prescribe Bo_0 and Ca_0. This means that we impose the particle translational velocity $U\mathbf{e}_z$ with magnitude $U > 0$ given by the selected value of the Capillary number Ca_0. The integral achieved using spherical coordinates is given by

$$F_{0b} \cdot \mathbf{e}_z = F_{0_z} = 2\pi a^2 \int_0^\pi \sigma_{0\zeta\zeta} \cos\theta \sin\theta \, d\theta = -4\pi\mu\lambda_{0b} U. \tag{5.5}$$

One numerically tests the relations (5.4) using two integration methods. First, a trapezoidal rule for which the domain $[a, b]$ is discretized in N_x equal subdomains is applied using the following approximation

$$\int_a^b f(x)dx = \frac{(b-a)}{N_x}\left[\frac{f(a)+f(b)}{2} + \sum_{i=1}^{Nx-1} f\left(a + i\,\frac{(b-a)}{N_x}\right)\right] + \mathcal{O}\left[\left(\frac{b-a}{N_x}\right)^3\right]. \tag{5.6}$$

Second, one employs a 8-point Gauss-Legendre iterative quadrature scheme to approximate the integral up to a prescribed accuracy. Comparisons of the two methods for a bubble located at $l/a = 2$ are displayed in Table 5.2

Trapezoidal rule		Gaussian quadrature	
accuracy	λ_{0b}	accuracy	λ_{0b}
10^{-5}	1.3406980	10^{-5}	1.34105981445861345
10^{-6}	1.3410561	10^{-8}	1.3410598130782838
3.10^{-7}	1.3410589	10^{-14}	1.34105981307843105

Table 5.2: Comparison of two methods of integration (trapezoidal rule and iterative Gaussian quadrature) for the coefficients λ_{0b} computed from (5.5). Here $N_x = 2000$ for the trapezoidal rule.

The value obtained from (5.4) is $\lambda_b = 1.34105981307843$. As seen in Table 5.2, the trapezoidal rule shows an accuracy of order of 10^{-6} ($N_x = 2000$) while the iterative Gaussian quadrature reaches its prescribed 10^{-14} accuracy. One will further use the Gaussian iterative method to evaluate the integrals.

The problem (4.95)-(4.96) is solved using a second-order central finite-difference scheme.

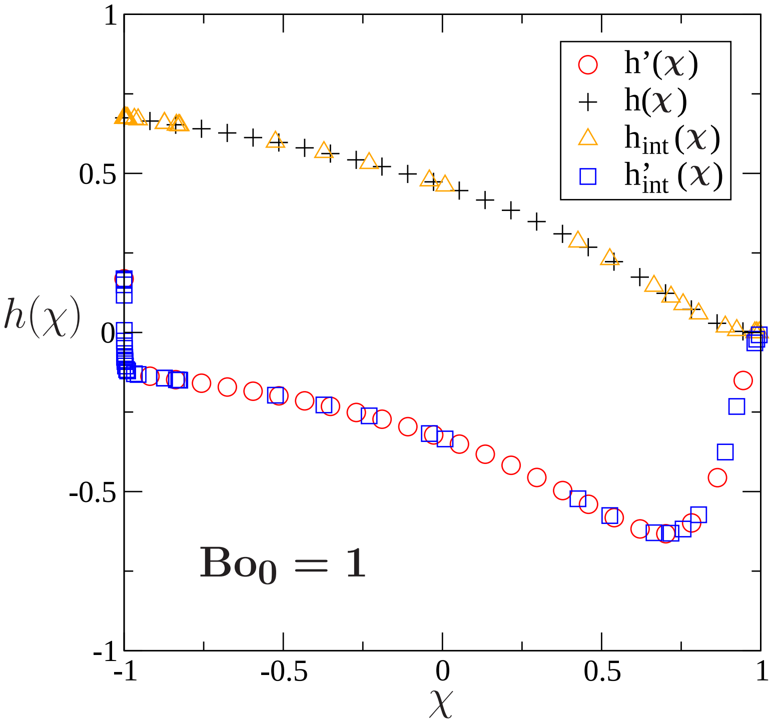

Figure 5.1: Comparisons between the functions $h(\chi)$ and $h'(\chi)$ with their associated interpolated function $h_{int}(\chi)$ and $h'_{int}(\chi)$ at $l/a = 6$ with $\mathrm{Bo}_0 = 1$ and $\mathrm{Ca}_0 = 0.2$

One may remarks that this method accuracy is of an order of $\mathcal{O}(h^2)$, nevertheless, Figure 5.1 depicts the function $h(\chi)$ obtained from the relation (4.96) and its derivative $h'(\chi)$ determined using a trapezoidal rule as well as the interpolated functions $h_{int}(\chi)$ and $h'_{int}(\chi)$. Here, $h_{int}(\chi)$ and $h'_{int}(\chi)$ were obtained appealing to a cubic spline interpolation. The interpolated functions $h_{int}(\chi)$ and $h'_{int}(\chi)$ gather nicely on the same curve as $h(\chi)$ and $h'(\chi)$ which suggests that the employed scheme gives a sufficient accuracy.

5.2 Numerical results for the disturbed free surface shape

5.2.1 Comparison of the two proposed methods: case of a solid sphere

One performs a Gaussian integration over the coordinate ρ with accuracy of 10^{-8} to numerically solve (4.78). The modified Bessel function I_0 and K_0 are called from the current *slatec* library [4] and the normal stress tensor $\sigma_{0\zeta\zeta}$ is obtained from the discretized bipolar expression (F.24) (see appendix F) with a size step of $h = 1/2000$ and further interpolated. Moreover, in the present work one restricts attention to the range $\rho \leq 10$.

Figure 5.2 (a) gives the free surface shape using the cylindrical coordinates (4.78) (green square dots) at $\mathrm{Bo}_0 = 1/3$ and $\mathrm{Ca}_0 = 0.2$ when the solid sphere is distant from the $z = 0$ plane of $l/a = 6$ sphere radius. Note that for such values of Bo_0 and Ca_0, the solid sphere is actually not force-free.

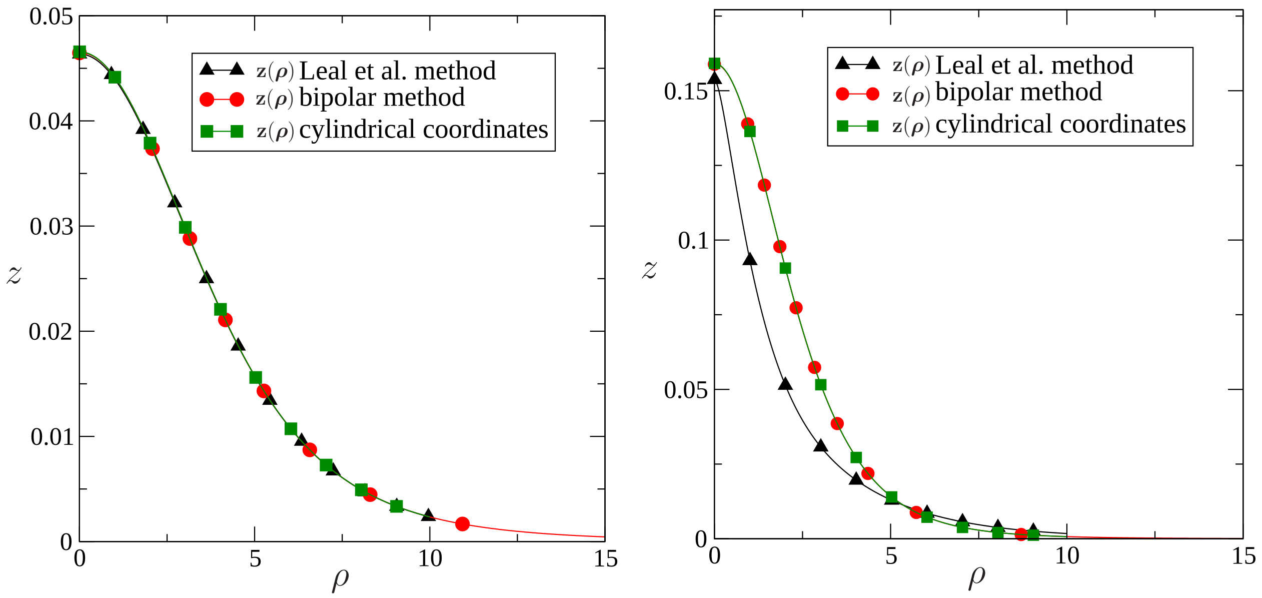

(a) Solid sphere with $l/a = 6$

(b) Solid sphere with $l/a = 3$

Figure 5.2: Computed free surface shapes $z = z(\rho)$. Comparison between the treatment in cylindrical coordinates and bipolar coordinates. The free surface deformation at $\mathrm{Bo}_0 = \rho_l g a^2/(3\gamma_0) = 1/3$ and $\mathrm{Ca}_0 = \mu U/\gamma_0 = 0.2$ is also compared with the results obtained in Berdan and Leal [2] for a distant sphere. Both analytical solutions are obtained using (4.74) with $z = \mathrm{Ca}_0\, f(\rho)$ in cylindrical coordinates and $z = c\,\mathrm{Ca}_0\, F(\eta)/(1-\chi)$ in bipolar coordinates.

The solution is compared with the free surface shape calculated by Berdan and Leal [2] (black triangle symbols) approximating in terms of a/l small the quantity $\sigma_{0\zeta\zeta}$ with accuracy of order $\mathcal{O}((a/l)^3)$. Therefore, one expects an error of 10^{-3} between the two computed solutions. Since the maximal difference is $\sim 2.8 \times 10^{-3}$ at $\rho = 0$ in Figure 5.2 (a), the two solutions nicely matched.

Moreover, one also plots the free surface shape obtained from the bipolar coordinates method (red filled circle symbols). The obtained curve nicely fits the previous analytical solutions. Our asymptotic analysis is therefore valid in the case of a distant solid sphere ($l/a = 6$). Not surprisingly, when the sphere is too close to the free surface (for instance for $l/a = 3$ as addressed in Figure 5.2 (b)), the analytical solution given by Leal [2] does not match any more the two other approaches. The far-field approximation of the stress tensor component $\boldsymbol{\sigma}_{0\zeta\zeta}$ employed in Leal [2] reaches its limit for $l/a = 3$.

Despite the similar results obtained using the cylindrical method and the bipolar one, the cpu time for the cylindrical technique increases with the calculation of the integrals. Moreover, the Bessel functions $I_0(\rho)$ diverges at large ρ and this property appears, in practice, as soon as $\rho > 10$. The bipolar method is therefore required to determine the tail of free surface shape.

5.2.2 Free surface shapes in the case of one bubble

In contrast to the previous case of a solid sphere, no result for a bubble is available for comparison purposes in the literature (at least to our very best knowledge). Indeed, Chervenivanova and Zapryanov [3] actually solely deal with a droplet and moreover give wrong results since obtaining a non-physical free surface exhibiting a cusp on the $(z'Oz)$ axis (non-zero slope of the free surface shape function).

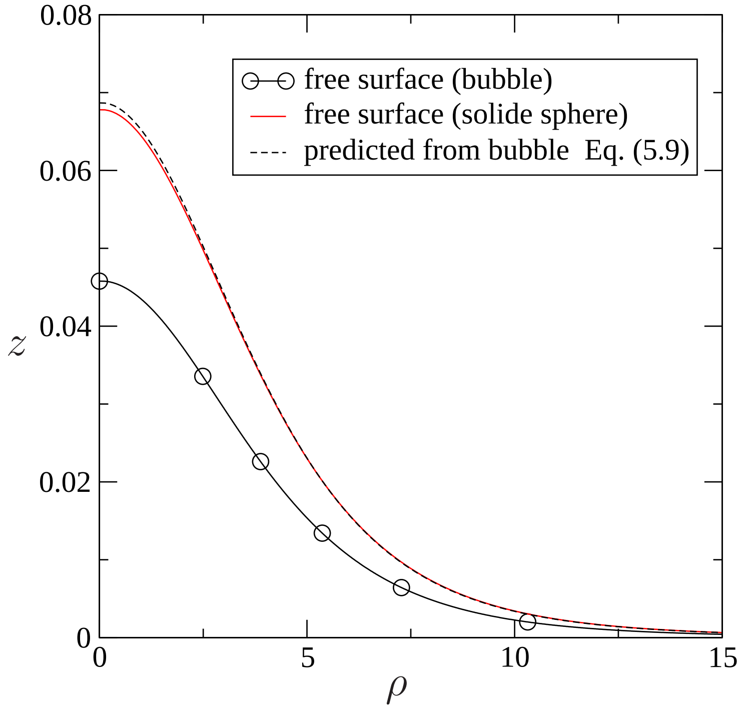

Figure 5.3: Free surface shapes for a bubble and (transformed and not transformed) for a solid sphere located at $l/a = 6$ at $\mathrm{Bo}_0 = 1/3$.

For comparison purposes, one then establishes a relation between the free surface shapes obtained either in the case of a solid sphere $h_s(\chi)$ or in the case of a bubble $h_b(\chi)$. For a *distant* particle (solid sphere or bubble), the free surface is, in first approximation, pushed by a point force (in presence of the motionless free surface where there is no tangential stress) with associated strength

$$\mathbf{F}_s = -6\pi\mu U \, a\lambda_s \mathbf{e}_z \tag{5.7}$$

for the solid sphere and

$$\mathbf{F}_b = -4\pi\mu U \, a\lambda_b \mathbf{e}_z \tag{5.8}$$

in the case of the bubble. The ratio of the strength $||\mathbf{F}_s||$ and $||\mathbf{F}_b||$ provides then a valuable homothetic transformation between the free surface shapes $h_s(\chi)$ and $h_b(\chi)$. Such a relation reads

$$\frac{h_s(\chi)}{h_b(\chi)} = \frac{||\mathbf{F}_s||}{||\mathbf{F}_b||} = \frac{2}{3}\frac{\lambda_s}{\lambda_b}, \tag{5.9}$$

and is actually valid at the leading order where both the solid sphere and the bubble are located at the same and *large enough* distance from the $z = 0$ plane. We apply the link of (5.9) to the deformation $h_b(\chi)$ predicted by a distant bubble located at $l/a = 6$ at

$\mathrm{Bo}_0 = 1/3$ in Figure 5.3 and compare the predicted shapes $h_s(\chi)$ with the one computed for the solid sphere.

The dashed line in Figure 5.3 corresponds to the homothetic transformation of the free surface shape $h_b(\chi)$ using the previous relation (5.9). It appears to nicely match the free surface shape for the solid sphere $h_s(\chi)$ depicted by the red line. Accordingly, the results for the free surface shape in presence of a distant bubble are consistent with the one for a solid sphere located at the same distance. Furthermore, note that the free surface is less disturbed by the bubble than by the solid sphere for a given Bond number Bo_0 (given gravity field and surface tension of the free surface γ_0). This is due to the different nature of the prescribed boundary conditions on the particle: no-slip condition for the solid sphere and allowed slip in the case of the bubble.

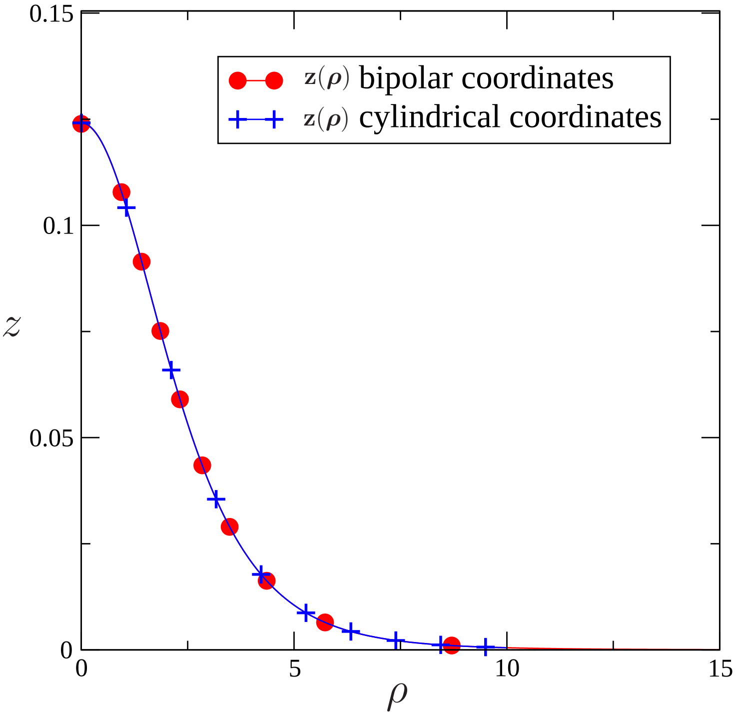

Figure 5.4: Comparison between the cylindrical method and the bipolar technique for the free surface deformation induced by a bubble distant of $l = 3a$, $\mathrm{Bo}_0 = 1/3$ and $\mathrm{Ca}_0 = 0.2$. Here $\gamma_0 = \gamma_1$ and $z = \mathrm{Ca}_0\, f(\rho)$ or $z = c\,\mathrm{Ca}_0\, F(\eta)/(1-\chi)$ for the cylindrical coordinates and the bipolar coordinates, respectively.

Finally, comparisons between the bipolar method and the cylindrical method for a rather close bubble are displayed in Figure 5.4. The bubble is located at $l = 3a$, $\mathrm{Bo}_0 = 1/3$ and $\mathrm{Ca}_0 = 0.2$ (again the bubble then not force-free since we separately selected Bo_0 and Ca_0). Both solutions nicely match.

The bipolar coordinates method has thus been validated both for the case of a distant bubble and the case of a distant solid sphere. In addition, for a bubble close to the surface, the bipolar method and the cylindrical method agree perfectly.

5.2.3 Comparisons with the BEM

The results predicted by the asymptotic analysis developed in Chapter 4 are now compared with the Boundary Element Method (BEM) numerical code presented in Chapter 2. Such comparisons are of course achieved at small Bond number.

The expected domain of validity of the asymptotic predictions concerns small values of the Bond number Bo_0 and capillary number Ca_0. The error made in the free surface location z is of order $\mathcal{O}(\mathrm{Ca}_0^2)$. Here the free surface shapes predicted by the BEM approach and the asymptotic technique are plotted in Figure 5.5 at $\mathrm{Bo}_1 = 0.1$ for a bubble location $l/a = 6$ and three values of $\hat{\gamma} = \gamma_0/\gamma_1$.

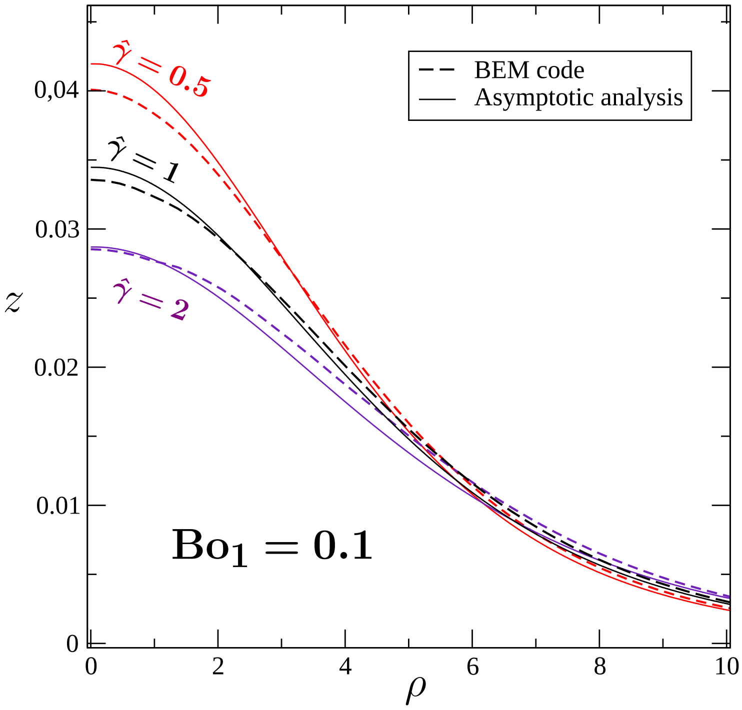

Figure 5.5: Free surface shapes at $\mathrm{Bo}_1 = 0.1$ as obtained from the BEM technique and the asymptotic approach in the case of a distant bubble located at $l/a = 6$ for $\hat{\gamma} = \gamma_0/\gamma_1 = 0.5, 1, 2$.

We denote by $z_a(\rho)$ and $z_{num}(\rho)$ the shapes obtained by the asymptotic analysis and the BEM computation, respectively. For comparisons, the relative error

$$\epsilon = \frac{|z_a(0) - z_{num}(0)|}{z_a(0) + z_{num}(0)} \tag{5.10}$$

is introduced (it then compares the free surface shapes on the $(z'Oz)$ axis). Recall that we need to extimate the Bond number $\mathrm{Bo}_0 = \mathrm{Bo}_1/\hat{\gamma}$ and the capillary number $\mathrm{Ca}_0 = \mathrm{Ca}_1/\hat{\gamma}$. For our force-free bubble at $\mathrm{Bo}_1 = 0.1$ it is here found that $\mathrm{Ca}_1 = 0.1375$ (the numbers Bo_1 and Ca_1 are related because the bubble is force-free). For the cases depicted in Figure 5.5, one gets the following results:

(1) For $\hat{\gamma} = 1$, then $\mathrm{Bo}_0 = \mathrm{Bo}_1 = 0.1$; $\mathrm{Ca}_0 = \mathrm{Ca}_1 = 0.1375$ and $\mathrm{Ca}_0^2 = 0.019$. Moreover, $\epsilon = 0.01$.

(2) For $\hat{\gamma} = 1/2$, then $\mathrm{Bo}_0 = 0.2$ and $\mathrm{Ca}_0 = 2\,\mathrm{Ca}_1$ so that $\mathrm{Ca}_0^2 = 0.072$. In addition, one has $\epsilon = 0.019$.

(3) For $\hat{\gamma} = 2$, then $\mathrm{Bo}_0 = 0.05$ and $\mathrm{Ca}_0 = \mathrm{Ca}_1/2$ so that $\mathrm{Ca}_0^2 = 0.048$. The value of ϵ is $\epsilon = 0.0029$.

Accordingly, for comparisons depicted in Figure 5.5 the relative error ϵ is at the most order of Ca_0^2. This trend validates the asymptotic analysis against the BEM code for the selected cases.

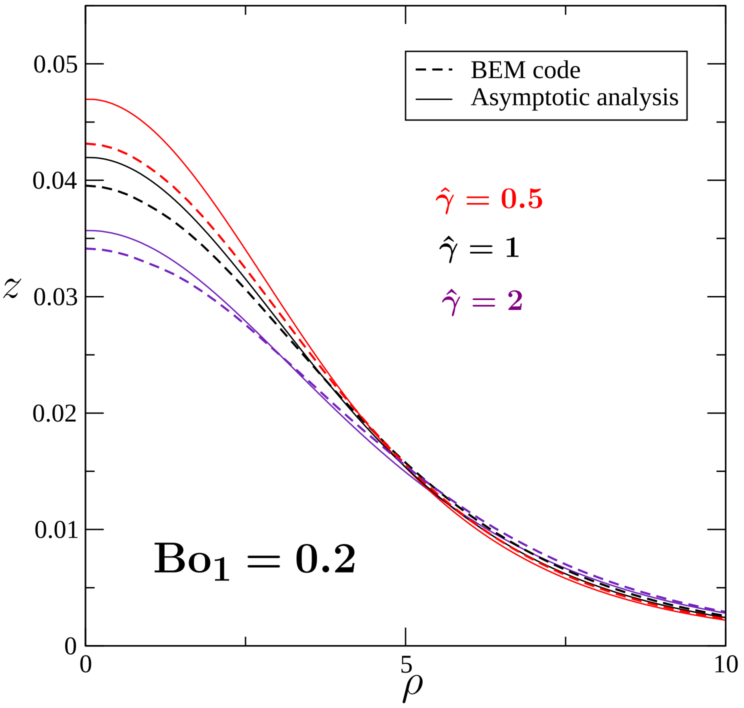

Figure 5.6: Free surface shapes at $\mathrm{Bo}_1 = 0.2$ both with the BEM technique and the asymptotic approach in the case of a distant bubble located at $l/a = 6$ and for $\hat{\gamma} = \gamma_0/\gamma_1 = 0.5, 1, 2$.

The free surface shapes has been also obtained again for a bubble located at $l = 6a$ and for $\hat{\gamma} = 0.5, 1, 2$ but at $\mathrm{Bo}_1 = 0.2$. The results are displayed in Figure 5.6. Here the capillary number one finds is $\mathrm{Ca}_1 = 0.0183$. As shown previously for $\mathrm{Bo}_1 = 0.1$, the three cases plotted in Figure 5.6 give the following results:

(1) For $\hat{\gamma} = 1$, then $\mathrm{Bo}_0 = \mathrm{Bo}_1 = 0.2$; $\mathrm{Ca}_0 = \mathrm{Ca}_1 = 0.1833$ and $\mathrm{Ca}_0^2 = 0.0335$. Moreover, the relative error previously defined for the case at $\mathrm{Bo}_1 = 0.1$ is $\epsilon = 0.030$.

(2) For $\hat{\gamma} = 1/2$, then $\mathrm{Bo}_0 = 0.4$ and $\mathrm{Ca}_0 = 2\,\mathrm{Ca}_1$ so that $\mathrm{Ca}_0^2 = 0.1344$. In addition one has $\epsilon = 0.0421$.

(3) For $\hat{\gamma} = 2$, then $\mathrm{Bo}_0 = 0.1$ and $\mathrm{Ca}_0 = \mathrm{Ca}_1/2$, hence $\mathrm{Ca}_0^2 = 0.0084$. Besides, the relative error reads $\epsilon = 0.022$.

Here, the relative error ϵ is either smaller or of order Ca_0^2 for $\hat{\gamma} = 0.5$ and 1. This suggests that the numerical results and the asymptotic one are in good agreement for these two $\hat{\gamma}$ values. However, the relative error ϵ being larger than $\mathcal{O}(\mathrm{Ca}_0^2)$ at $\hat{\gamma} = 2$, our asymptotic analysis is therefore not valid any more at $\mathrm{Bo}_1 = 0.2$.

5.2.4 Free surface shapes at small Bond number

As outlined when discussing the results shown in Figure 5.5, the asymptotic analysis is valid for Bo_0 at the most of order 10^{-1}. We present in Figure 5.7-5.8 the predicted free surface shape in this range for a few bubble locations ($l/a = 2, 4, 6$) and four sufficiently small values of Bo_0. Moreover we take $\gamma_0 = \gamma_1$.

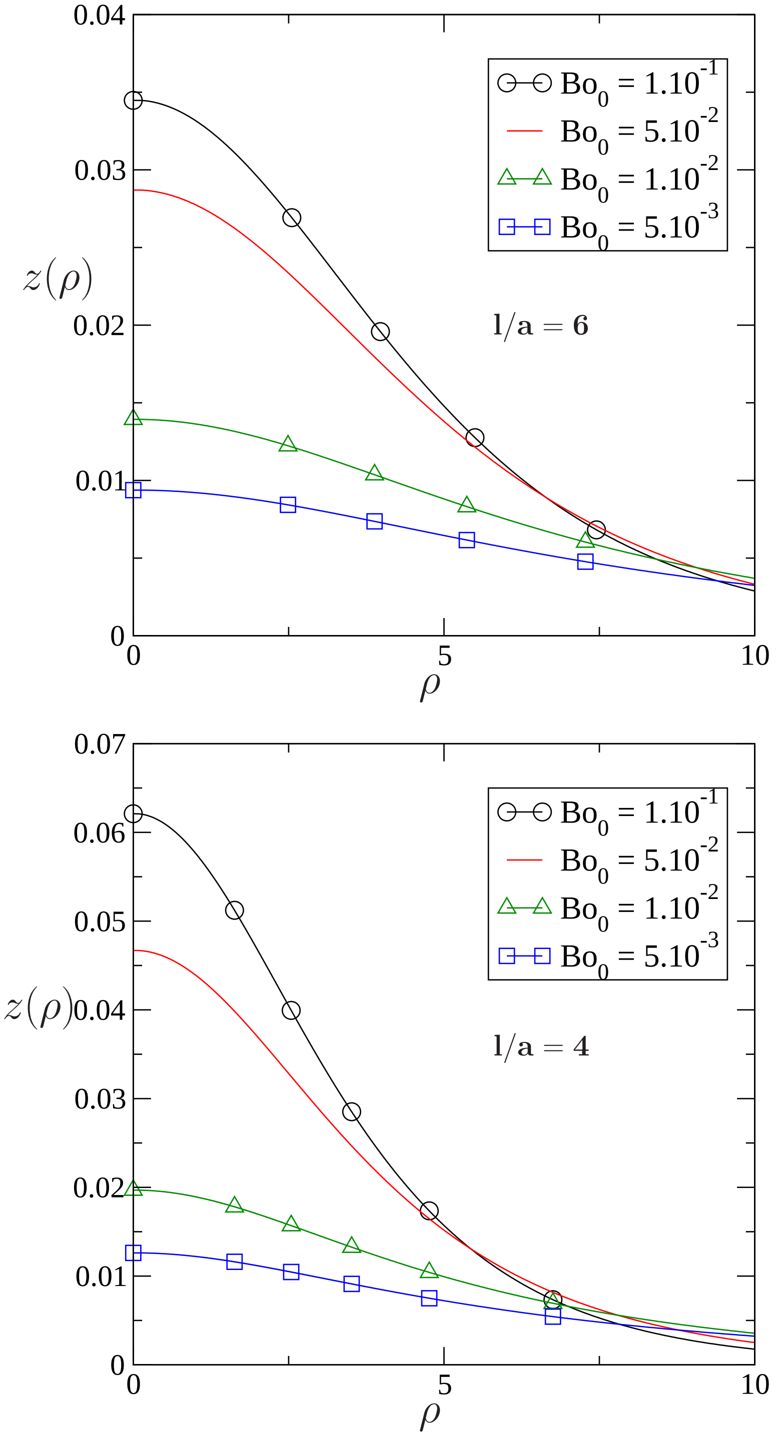

Figure 5.7: Free surface shapes for $\hat{\gamma} = 1$ and at different Bond number $\mathrm{Bo}_1 = \mathrm{Bo}_0$ for a bubble located at $l/a = 6$ and at $l/a = 4$.

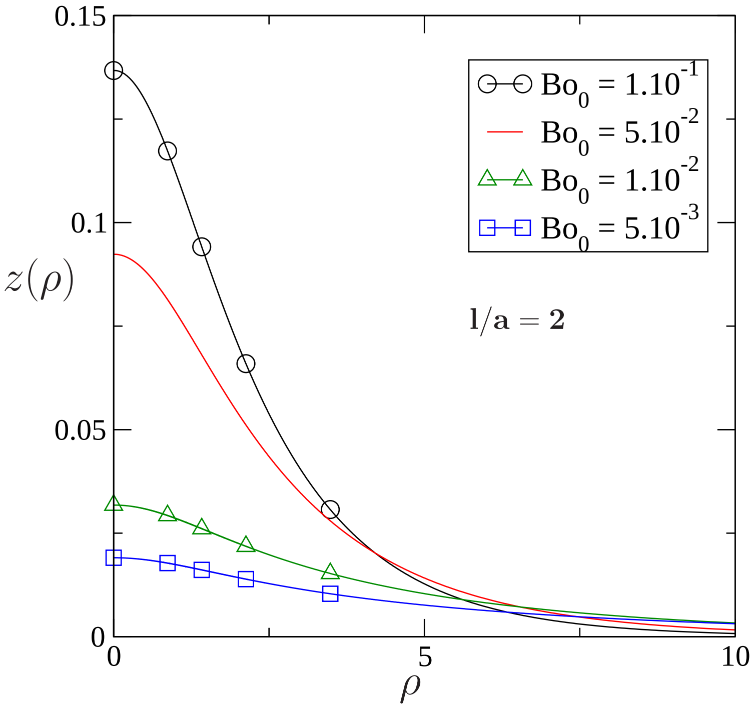

Figure 5.8: Free surface shapes for $\hat{\gamma} = 1$ at different Bond numbers $\mathrm{Bo}_1 = \mathrm{Bo}_0$. For a bubble located at $l/a = 2$.

As the distance l/a decreases, the free surface deformation increases. Indeed, when the bubble is located at $l/a = 2$, the free surface is five times more disturbed than for a bubble distant of $l/a = 6$ at $\mathrm{Bo}_0 = 0.1$. Moreover, as the Bond number drops from 0.1 to 5.10^{-3}, the free surface deformation strongly decreases as shown in each figure. This decay is the biggest when the bubble is close to the free surface ($l/a = 2$). The maximal deformation shown by the free surface at the $(z'Oz)$ axis is indeed nearly seven times smaller at $\mathrm{Bo}_0 = 5.10^{-3}$ than at $\mathrm{Bo}_0 = 0.1$. In contrast, when the bubble is distant ($l/a = 6$), the difference becomes four times smaller at $\mathrm{Bo}_0 = 5.10^{-3}$ than at $\mathrm{Bo}_0 = 0.1$.

5.2.5 Bubble shape: preliminary results

The first-order bubble shape has been obtained in Chapter 4 and the expecting domain of validity is this time for small values of $\mathrm{Bo}_1 = \rho_l g a^2/(3\gamma_1)$. The disturbed bubble shape has been computed using the results (4.129) putting the bubble center-of-volume at a prescribed location (given by the BEM Code). The expected error made in the bubble surface location z is of order $\mathcal{O}(\mathrm{Ca}_1^2)$.

The bubble shapes predicted by the BEM Code and the asymptotic approach are displayed in Figure 5.9 (a), 5.9 (b) and 5.10 at $\mathrm{Bo}_1 = 0.3$ (not so small Bond number) for different bubble center-of-volume locations. The undisturbed spherical bubble shape is also plotted (dashed red curve). Moreover, each figure is obtained for a bubble and a free surface having identical surface tensions ($\gamma_1 = \gamma_0$).

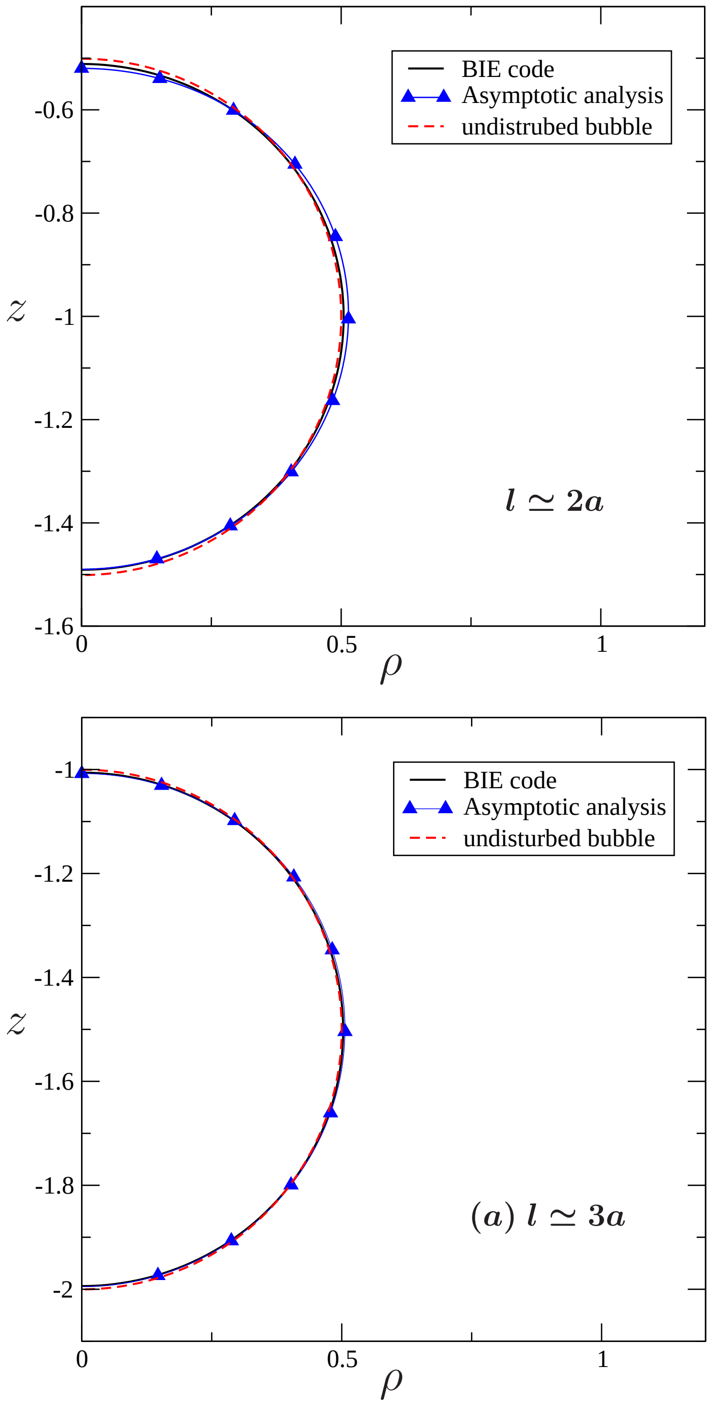

Figure 5.9: Half bubble surface shapes at $\mathrm{Bo}_1 = 0.3$ both with the BEM technique (blue curve) and the asymptotic approach for the bubble center of mass located at (a) $l/a \simeq 2.002$ and (b) $l/a \simeq 3.0004$. The undisturbed spherical bubble is represented by the dashed red curve.

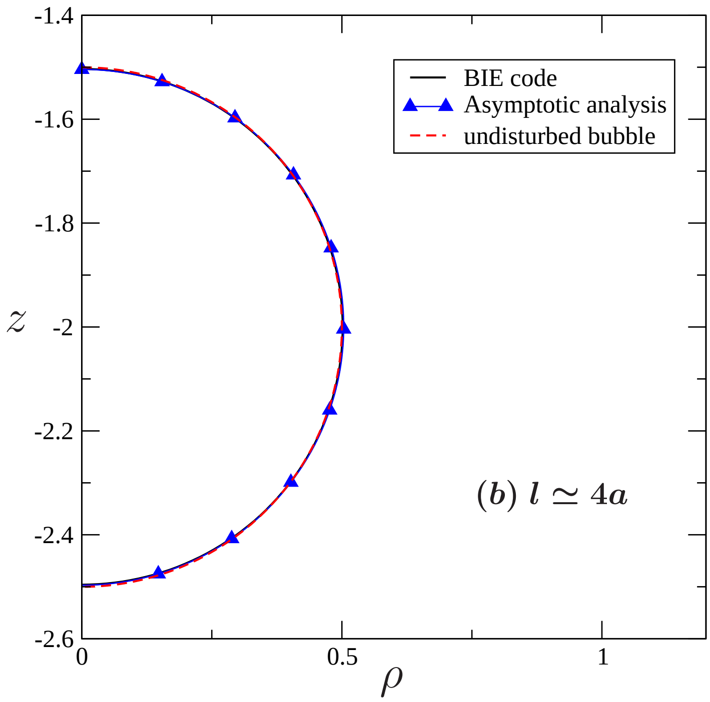

Figure 5.10: Half bubble surface shapes at $\mathrm{Bo}_1 = 0.3$ both with the BEM technique (blue curve) and the asymptotic approach for the bubble center-of-volume located at $l/a \simeq 4.0002$. The undisturbed spherical bubble is represented by the dashed red curve.

One denotes by $z_a^{(b)}(\rho)$ and $z_{num}^{(b)}(\rho)$ the bubble shapes obtained by the asymptotic analysis and the BEM computation, respectively. For comparisons, the relative error ϵ_b which compares the bubble surface shapes on the $(z'Oz)$ axis at the bubble top and bottom is introduced such as

$$\epsilon_b = \frac{\Delta z^b}{z_a(0)^{(b)} + z_{num}^{(b)}(0)} \tag{5.11}$$

where $\Delta z^b = |z_a^{(b)}(0) - z_{num}^{(b)}(0)|$ is the maximal difference comparing the errors obtained at the bubble top and bottom. In addition, the difference between the undisturbed spherical bubble and the computed one is denoted by ε and is based on the same calculation as the relative error ϵ_b. For a bubble close to the free surface, at $l \simeq 2$ (see in Figure 5.9 (a)), the relative error reads $\epsilon_b = 7.10^{-3}$ when $\varepsilon = 2.10^{-2}$. The capillary number being $\mathrm{Ca}_1 = 1.118\,10^{-1}$ (i.e. $\mathrm{Ca}_1^2 = 1.251\,10^{-2}$) the relative errors ϵ_b is therefore suitable regarding our asymptotic approach.

When the bubble is a bit farther to the free surface, at $l \simeq 3$ (see in Figure 5.9 (b)), the relative error reads $\epsilon_b = 1.7\,10^{-3}$ when $\varepsilon = 1.10^{-2}$. The capillary number is here $\mathrm{Ca}_1 = 1.248\,10^{-1}$ implying that the relative errors ϵ_b is small compared to $\mathrm{Ca}_1^2 = 1.559\,10^{-2}$ which therefore complies with our asymptotic approach. Nevertheless, note that ε is $\mathcal{O}(\mathrm{Ca}_1^2)$ and this suggests that the bubble is weakly deformed.

Finally, when the bubble is far from the free surface with a center of mass located at $l \simeq 4$, (see in Figure 5.10), one gets a relative error of $\epsilon_b = 7.10^{-4}$ whereas $\varepsilon = 8.10^{-3}$. The capillary number being $\mathrm{Ca}_1 = 1.312\,10^{-1}$ (i.e. $\mathrm{Ca}_1^2 = 1.721\,10^{-2}$) both ϵ_b and ε are suitable errors for our asymptotic approach. The bubble surface deformation is indeed too small to be separate from the undisturbed one. An asymptotic treatment at higher order whould be therefore required to adequately capture the weakly disturbed bubble surface.

5.3 Conclusions on the asymptotic analysis

The zeroth-order flow problem has been obtained and compared with a good agreement against the literature. The first-order free surface shapes have been determined using two different methods: a first one appealing to the cylindrical coordinates and a second one using the bipolar coordinates. The results obtained with both methods agree well with the ones given by Berdan and Leal [2] for a distant solid body. Moreover, the second asymptotic method has been checked for the free surface shape in the case of a distant bubble using an homothetic relation. Then, the first asymptotic method using the cylindrical coordinates has been compared with the second one when the bubble is close to the free surface and the results match perfectly. In addition, our asymptotic analysis results have been tested with the ones obtained using the BEM code in the case of a distant bubble at small Bond number and for different surface tension ratios. The comparisons are in good agreement for a sufficently small Bond number and therefore validate our asymptotic analysis for the free surface shape. New results have then been determined for a bubble and a free surface having the same surface tension at different small Bond numbers and for three bubble locations. The free surface shape deformation is clearly sensitive both to the Bond number and the bubble location. The free surface deformation decreases when the distance between the bubble and the free surface increases. In constrast, as the Bond number increases, the free surface is more disturbed. Finally, the disturbed bubble shape has been obtained using the asymptotic analysis and the preliminary results for a weakly disturbed bubble agree well with the ones computed using the BEM code.

Bibliography

[1] E. Bart. The slow unsteady settling of a fluid sphere toward a flat fluid interface. *Chem. Eng. Sci.*, 23:193–210, 1968.

[2] C. Berdan and L. G. Leal. Motion of a sphere in the presence of a deformation interface. I. Perturbation of the interface from flat: The effects on drag and torque. *J. Colloid Interface Sci.*, 87:62–80, 1982.

[3] E. Chervenivanova and Z. Zapryanov. The slow motion of droplets perpendicular to a deformable flat fluid interface. *Q. J. Mechanics Appl. Math.*, 41(3):419–444, 1988.

[4] W. Kirby, T.H. Jefferson, S. Tokihiko, and L. Walton. Guide to the slatec common mathematical library. netlib.org, 1993.

Part II

Clusters consisting in $M \geq 0$ bubble(s) and $N \geq 1$ solid particle(s) with $N + M \geq 2$.

Chapter 6

Gravity-driven migration of bubble(s) and/or solid particle(s) near a free surface

Contents

So far the previous Chapters have restricted attention to the case of a particle (bubble or solid sphere) interacting with a free surface under the action of the gravity. This has been achieved both numerically and asymptotically for sufficiently small Bond and Capillary numbers, within the creeping flow assumption and for axisymmetric cases.

As outlined in the present thesis introduction, one unfortunately also encounters during the glass process clusters made of bubble(s) and/or solid body(s). Tracking in time the location of the free surface and of each involved particle (bubble and solid body) then becomes a tremendously-involved task even within the Low-Reynolds-number flow framework because, in general, the cluster adopts a fully tridimensional geometry (i.e. the flow exhibits no symmetry of revolution parallel with the acting uniform gravity)!

For the sake of simplicity we shall however henceforth solely pay attention to axisymmetric cases while still resorting to the Stokes equations for the liquid flow. As shown in this Chapter, it is then possible to reduce the problem, at each time step, to the treatment of $N + 1$ boundary-integral equations on the liquid boundary consisting of the free surface and the entire cluster boundary assuming here that the cluster involves $N \geq 1$ solid particle(s). This Chapter also briefly presents the implementation. The numerical results obtained for different clusters either solely made of bubble(s) or made of both bubble(s) and solid particle(s) are subsequently presented and discussed in Chapter 7.

6.1 Governing general problem and advocated trick

This section presents the problem to solve at each time step for clusters consisting of bubble(s) and/or solid body(s) and gives a trick to calculate each solid particle velocity when at least one solid body is involved.

6.1.1 Governing equation and key remarks

As sketched in Figure 6.1 for a sphere-bubble cluster, we consider at time t a cluster consisting of $M \geq 1$ bubble(s) with surface $S_m(t)$ and $N \geq 0$ solid particle(s) $\mathcal{P}_n$ immersed in a Newtonian liquid with viscosity μ and density ρ_l. The liquid is bounded by a free surface $S_0(t)$ and both the cluster and the liquid are subject to a uniform gravity field $\mathbf{g} = -g\mathbf{e}_z$.

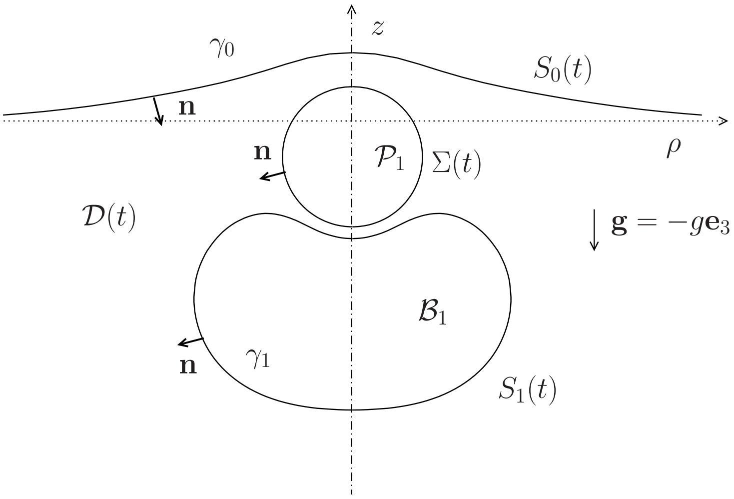

Figure 6.1: Axisymmetric migration of a bubble $\mathcal{B}_1$ and a solid sphere $\mathcal{P}_1$ ascending near the free surface S_0.The plotted shapes are the computed ones at normalized time $\bar{t} = (\rho_l g a)t/(6\mu) = 1.90$ for identical surface tension $\gamma_0 = \gamma_1$ and Bond number $\mathrm{Bo} = \rho g a^2/(3\gamma_1) = 2$ with a the initial bubble radius. The solid sphere has radius $a/2$.

Moreover, each surface $S_m(t)$ has uniform surface tension γ_m and we shall allow unequal surface tensions for the bubble(s) and the free surface. At initial time $t = 0$ the surfaces $S_m(t)$ and $\Sigma_n(t)$ are sufficiently separated so that the free surface $S_0(0)$ is the $z = 0$ plane and each bubble $\mathcal{B}_m$ is spherical with radius a_m. In addition, at time $t \geq 0$ all surfaces $S_m(t)$ and $\Sigma_n(t)$ admit the same axis of revolution $(O, \mathbf{e}_z)$ and each solid particle $\mathcal{P}_n$ translates (without rotating) at the velocity $U^{(n)}(t)\mathbf{e}_z$. This means that the center-of-mass of $\mathcal{P}_n$ is located on the $(O, \mathbf{e}_z)$ axis. In practice it is assumed that $\mathcal{P}_n$ has uniform and prescribed density ρ_n. The gas inside the bubble $\mathcal{B}_m$ has negligible mass and constant pressure p_m. Finally, we denote by $p_0 = 0$ the pressure above the free surface $S_0(t)$ far away from the cluster (far-field pressure).

We use Cartesian coordinates (O, x_1, x_2, x_3) with origin O located on the axis of revolution near the cluster. At each time t the liquid flow in the liquid domain $\mathcal{D}(t)$ has velocity $\mathbf{u}$ and pressure $p + \rho_l \mathbf{g}.\mathbf{x}$ (of course, here $\mathbf{x} = x_i \mathbf{e}_i$).

The velocity $\mathbf{u}$ has typical magnitude V and particles (bubbles and solid ones) have typical length a. Assuming that $\mathrm{Re} = \rho_l V a/\mu \ll 1$ we can neglect all inertial effects and the flow $(\mathbf{u}, p)$, with stress tensor $\boldsymbol{\sigma}$ obeys the following Stokes equations and far-field behavior

$$\boldsymbol{\nabla} \cdot \mathbf{u} = 0 \text{ and } \mu \boldsymbol{\nabla}^2 \mathbf{u} = \mathbf{grad} p \text{ in } \mathcal{D}(t), \ (\mathbf{u}, p) \to (\mathbf{0}, 0) \text{ as } ||\mathbf{x}|| \to \infty. \tag{6.1}$$

One of course supplements (6.1) with boundary conditions imposed on the free surface $S_0(t)$ and on each encountered bubble or solid particle surfaces. Recalling Chapter 1, those conditions read (since $p_0 = 0$)

$$\boldsymbol{\sigma} \cdot \mathbf{n} = (\rho_l \mathbf{g} \cdot \mathbf{x} + \gamma_0 \boldsymbol{\nabla}_S \cdot \mathbf{n})\, \mathbf{n} \text{ on } S_0(t) \tag{6.2}$$

$$\boldsymbol{\sigma} \cdot \mathbf{n} = (\rho_l \mathbf{g} \cdot \mathbf{x} - p_m + \gamma_m \boldsymbol{\nabla}_S \cdot \mathbf{n})\, \mathbf{n} \text{ on } S_m(t) \text{ for } m = 1, ..., M, \tag{6.3}$$

$$\mathbf{u} = U^{(n)}(t) \mathbf{e}_z \quad \text{on } \Sigma_n(t) \text{ for } n = 1, ..., N \text{ (if } N \geq 1) \tag{6.4}$$

where $\mathbf{n}$ denotes on each boundary the unit normal directed into the liquid and $\boldsymbol{\nabla}_S \cdot \mathbf{n}$ is the local mean curvature on each interface $S_l(t)$ with $l = 0, \cdots, M$.

The no-slip boundary condition (6.4) specifies that the fluid adopts on any solid body boundary the velocity of this body. For other parts $S_0(t), \cdots, S_M(t)$ of the liquid boundary $\partial\mathcal{D}(t)$ this is not the case. Indeed, denoting by $\mathbf{V}$ the material velocity of those interfaces one has this time the property

$$\mathbf{V} \cdot \mathbf{n} = \mathbf{u} \cdot \mathbf{n} \text{ on } S_l(t) \text{ for } l = 0, ..., M \tag{6.5}$$

because there is no liquid mass flux across such boundaries.

In our model each bubble is also assumed to have a time-independent volume. From the condition of gas incompressibility $\boldsymbol{\nabla} \cdot \mathbf{u} = 0$, this requirement gives the relations

$$\int_{S_m(t)} \mathbf{u} \cdot \mathbf{n} \, dS = 0 \quad \text{on } S_l(t) \text{ for } l = 0, ..., M. \tag{6.6}$$

Since $\boldsymbol{\nabla} \cdot \mathbf{u} = 0$ in $\mathcal{D}(t)$ by virtue of (6.1), such a property also holds for $S_0(t)$. At this stage, one thus has to solve the Stokes flow problem (6.1)-(6.4) together with the conditions (6.6).

Furthermore, one needs N additional relations to solve such a problem since each occurring solid body velocity component $U^{(n)}(t)$ is unknown. Assuming that each solid body $\mathcal{P}_n$ has negligible inertia one requires for our quasi-steady model each bubble and solid body to be force-free. Accordingly, for $N \geq 1$ we supplement (6.1)-(6.4) (cluster involving at least one solid body) with the conditions

$$\int_{\Sigma_n(t)} \mathbf{e}_z \cdot \boldsymbol{\sigma} \cdot \mathbf{n} dS = -(\rho_n - \rho_l) \mathcal{V}_n \, g \quad \text{for } n = 1, ..., N \text{ if } (N \geq 1) \tag{6.7}$$

where $\mathcal{V}_n$ designates the volume of the particle $\mathcal{P}_n$. As already pointed out in Chapter 1 in §1.2 for one bubble, the conditions of force-free bubble(s)

$$\left[\int_{S_m(t)} \left(\boldsymbol{\sigma} \cdot \mathbf{n} - \rho_l (\mathbf{g} \cdot \mathbf{x}) \mathbf{n} \right) dS \right] \cdot \mathbf{e}_z = 0 \text{ for } m = 1, \cdots, M \tag{6.8}$$

is automatically fulfilled by integrating on $S_m(t)$ the boundary conditions (6.3).

In summary, one has to solve for a cluster made of $M \geq 1$ bubble(s) and $N \geq 0$ solid body or bodies the problem (6.1)-(6.4), (6.6)-(6.7) for which the liquid domain $\mathcal{D}(t)$ and thus also the surfaces are prescribed together with the gravity field $\mathbf{g}$ and the surface tensions γ_l for $l = 0, ..., M$.

At that stage, such a challenging task deserves the following remarks:

1) It will be shown that it is not necessary to give the constant pressure p_m in the bubbles.

2) As already achieved for a bubble interacting with free surface, a numerical treatment is necessary. The accuracy of such a method also deeply depends on the way one carefully calculates on each interface $S_0(t), \cdots, S_M(t)$ the term $\boldsymbol{\nabla}_S \cdot \mathbf{n}$.

3) In order to track in time each surface shape and location it is necessary to accurately solve our problem at a reasonable CPU time cost.

4) For $N \geq 1$ one has also to determine the velocity $U^{(n)}(t)\mathbf{e}_z$ of each solid particle $\mathcal{P}_n$. At a first glance, one may think about getting those velocities by employing an iterative scheme based on the following sequence: put in (6.4) guessed values for the quantities $U^{(n)}(t)$, then solve (6.1)-(6.3) in conjunction with (6.6) through a FEM (Finite Element Method) after truncating the unbounded liquid domain $\mathcal{D}(t)$, compute on each solid particle surface the resulting traction $\boldsymbol{\sigma} \cdot \mathbf{n}$ and evaluate the integrals in the conditions (6.7).

For this approach, one finally ensures the condition (6.7) by iteratively changing the prescribed quantities $U^{(n)}(t)$. Unfortunately, such a procedure has two main drawbacks: it may be very CPU time consuming (since several calls to the FEM code are very likely to be needed) and one moreover needs to calculate on each surface $\Sigma_n(t)$ the stress tensor $\boldsymbol{\sigma}$, i.e. the derivatives of the velocity components.

This latter step results in a loss of accuracy which spoils the overall accuracy of the iterative approach.

Therefore, another approach free from the mentioned drawbacks is needed. As seen in Chapter 1, a BEM (Boundary Element Method) approach is suitable and possible when adequately solving (6.1)-(6.3) and (6.6). As it solely requires to mesh the liquid domain boundary (after, however, truncating the free surface $S_0(t)$) the boundary method turns out to be accurate enough and to reduce the task to the computation of a few surface quantities: the velocity $\mathbf{u}$ on $S_0(t), \cdots, S_M(t)$ and the surface traction $\mathbf{f} = \boldsymbol{\sigma} \cdot \mathbf{n}$ on each solid body surface $\Sigma_n(t)$ (for $N \geq 1$). The BEM might then be employed instead of the Finite Element Method in the previous iterative scheme to determine each solid body motion.

Unfortunately, again this method will also needs several iteration before giving the velocities $U^{(n)}(t)\mathbf{e}_z$.

6.1.2 Determination of each solid body velocity

As emphasized in the previous subsection, the key step consists in determining each solid body velocity when $N \geq 1$. In this subsection we show how it can be done without solving the problem for the liquid flow $(\mathbf{u}, p)$. The trick appeals to N auxiliary Stokes flows $(\mathbf{u}^{(n)}, p^{(n)})$, with stress tensor $\boldsymbol{\sigma}^{(n)}$, for $n = 1, ..., N$. More precisely, the Stokes flow $(\mathbf{u}^{(n)}, p^{(n)})$ is the one obtained when there is no traction on the surfaces $S_0(t), \cdots, S_M(t)$

and each solid body is at rest except the solid body $\mathcal{P}_n$ which moves at the velocity $\mathbf{e}_z$. In other words, one has

$$\boldsymbol{\nabla}\cdot\mathbf{u}^{(\mathbf{n})}=0 \text{ and } \mu\boldsymbol{\nabla}^2\mathbf{u}^{(n)}=\mathbf{grad}p^{(n)} \text{ in } \mathcal{D}(t),\ (\mathbf{u}^{(n)},p^{(n)})\to(\mathbf{0},0) \,\text{as}\, |\mathbf{x}|\to\infty, \tag{6.9}$$

and

$$\boldsymbol{\sigma}^{(n)}\cdot\mathbf{n}=\mathbf{0} \qquad \text{on } S_0(t),\cdots,S_M(t) \tag{6.10}$$

$$\mathbf{u}^{(n)}=\delta_{qn}\,\mathbf{e}_z \text{ on } \Sigma_q(t) \text{ for } q=1,\cdots,N, \tag{6.11}$$

$$\int_{S_m(t)}\mathbf{u}^{(n)}\cdot\mathbf{n}\,dS=0 \text{ on } S_m(t) \text{ for } m=0,...,M \tag{6.12}$$

with δ_{qn} the usual Kronecker symbol.

Solving (6.9)-(6.12) provides on each solid body surface $\Sigma_n(t)$ the surface traction $\boldsymbol{\sigma}^{(n)}\cdot\mathbf{n}$ and on the surfaces $S_0(t),\cdots,S_M(t)$ the velocity $\mathbf{u}^{(n)}$. The knowledge of those surface quantities permits one to recast the condition (6.7) for the solid body $\mathcal{P}_n$. This is achieved by applying to the Stokes flows $(\mathbf{u},p)$ and $(\mathbf{u}^{(n)},p^{(n)})$ the usual reciprocal identity. Denoting by $\partial\mathcal{D}(t)$ the liquid domain boundary (here made of surfaces $S_0(t),\cdots,S_M(t)$, $\Sigma_1(t),\cdots,\Sigma_n(t)$) this identity reads

$$\int_{\partial\mathcal{D}(t)}\mathbf{u}^{(n)}\cdot\boldsymbol{\sigma}\cdot\mathbf{n}\,dS=\int_{\partial\mathcal{D}(t)}\mathbf{u}\cdot\boldsymbol{\sigma}^{(n)}\cdot\mathbf{n}\,dS. \tag{6.13}$$

In exploiting (6.7), we first note that

$$\int_{\Sigma_n(t)}\mathbf{e}_z\cdot\boldsymbol{\sigma}\cdot\mathbf{n}\,dS=\int_{\Sigma_n(t)}\mathbf{u}^{(n)}\cdot\boldsymbol{\sigma}\cdot\mathbf{n}\,dS$$

$$\int_{\Sigma_n(t)}\mathbf{e}_z\cdot\boldsymbol{\sigma}\cdot\mathbf{n}\,dS=\int_{\partial\mathcal{D}}\mathbf{u}^{(n)}\cdot\boldsymbol{\sigma}\cdot\mathbf{n}\,dS-\sum_{m=0}^{M}\int_{S_m(t)}\mathbf{u}^{(n)}\cdot\boldsymbol{\sigma}\cdot\mathbf{n}\,dS \tag{6.14}$$

Using (6.13)-(6.7) then gives

$$(\rho_n-\rho)\mathcal{V}_n\,g=\int_{\partial\mathcal{D}}\mathbf{u}\cdot\boldsymbol{\sigma}^{(n)}\cdot\mathbf{n}\,dS-\sum_{m=0}^{M}\int_{S_m(t)}\mathbf{u}^{(n)}\cdot\boldsymbol{\sigma}\cdot\mathbf{n}\,dS. \tag{6.15}$$

By virtue of the boundary conditions satisfied on $\partial\mathcal{D}(t)$ by the flows $(\mathbf{u},p)$ and $(\mathbf{u}^{(n)},p^{(n)})$ it follows that (setting $p_0=0$)

$$\begin{aligned}(\rho_n-\rho_l)\mathcal{V}_n\,g=&\sum_{q=1}^{N}\left[\int_{\Sigma_q(t)}\mathbf{e}_z\cdot\boldsymbol{\sigma}^{(n)}\cdot\mathbf{n}\,dS\right]U^{(q)}(t)\\&-\sum_{m=0}^{M}\int_{S_m(t)}\mathbf{u}^{(n)}\cdot(\rho_l\mathbf{g}\cdot\mathbf{x}-p_m+\gamma_m\boldsymbol{\nabla}_S\cdot\mathbf{n})\,\mathbf{n}\,dS.\end{aligned} \tag{6.16}$$

Because p_m is constant over $S_m(t)$ and $(\mathbf{u}^{(n)},p^{(n)})$ satisfies (6.12) one finally arrives at the relation

$$\begin{aligned}\sum_{q=1}^{N}\Big(\int_{\Sigma_q(t)}\mathbf{e}_z\cdot\boldsymbol{\sigma}^{(n)}\cdot\mathbf{n}\,dS\Big)U^{(q)}(t)=&(\rho_n-\rho_l)\mathcal{V}_n\,g\\&+\sum_{m=0}^{M}\int_{S_m(t)}\mathbf{u}^{(n)}\cdot(\rho_l\mathbf{g}\cdot\mathbf{x}+\gamma_m\boldsymbol{\nabla}_S\cdot\mathbf{n})\,\mathbf{n}\,dS \text{ for } n=1,\cdots,N.\end{aligned} \tag{6.17}$$

Clearly, (6.17) is a N-equation linear system for the unknown velocities $U^{(1)}(t), \cdots, U^{(N)}(t)$. Its $N \times N$ matrix A has real valued coefficient A_{nq} defined as

$$A_{nq} = \int_{\Sigma_q(t)} \mathbf{e}_z \cdot \boldsymbol{\sigma}^{(n)} \cdot \mathbf{n} \, dS. \tag{6.18}$$

Invoking the boundary conditions for the flow $(\mathbf{u}^{(q)}, p^{(q)})$ and $(\mathbf{u}^{(n)}, p^{(n)})$, with stress tensors $\boldsymbol{\sigma}^{(q)}$ and $\boldsymbol{\sigma}^{(n)}$, and the reciprocal identity immediately shows that

$$A_{nq} = \int_{\Sigma_q(t)} \mathbf{u}^{(q)} \cdot \boldsymbol{\sigma}^{(n)} \cdot \mathbf{n} \, dS = \int_{\partial \mathcal{D}} \mathbf{u}^{(q)} \cdot \boldsymbol{\sigma}^{(n)} \cdot \mathbf{n} \, dS = \int_{\partial \mathcal{D}} \mathbf{u}^{(n)} \cdot \boldsymbol{\sigma}^{(q)} \cdot \mathbf{n} \, dS = A_{qn} \tag{6.19}$$

Setting $X = \left(U^{(1)}(t), \cdots, U^{(N)}(t)\right)$, we now consider the Stokes flow $(\mathbf{u}_X, p_X)$ obeying (6.9)-(6.10), (6.12) and the boundary conditions

$$\mathbf{u}_X = U^{(n)}(t) \qquad \text{on } \Sigma_n(t) \text{ for } n = 1, \cdots, N \tag{6.20}$$

Such a flow has stress tensor $\boldsymbol{\sigma}_X$ and we know that

$$E = \int_{\partial \mathcal{D}} \mathbf{u}_X \cdot \boldsymbol{\sigma}_X \cdot \mathbf{n} \, dS < 0 \quad \text{ if } X \neq (0, \cdots, 0) \tag{6.21}$$

while $E = 0$ for $U^{(1)}(t), \cdots, U^{(N)}(t) = 0$. Clearly,

$$E = \sum_{q=1}^{N} \int_{\partial \mathcal{D}} \mathbf{u}_X \cdot \boldsymbol{\sigma}_X \cdot \mathbf{n} \, dS = \sum_{q=1}^{N} \left[\int_{\Sigma_q(t)} \mathbf{e}_z \cdot \boldsymbol{\sigma}_X \cdot \mathbf{n} \, dS \right] U^{(q)}(t). \tag{6.22}$$

Moreover it turns out that $\boldsymbol{\sigma}_X = \sum_{n=1}^{N} U^{(n)}(t) \boldsymbol{\sigma}^{(n)}$. Therefore, one arrives at

$$E = \sum_{q=1}^{N} \sum_{n=1}^{N} A_{qn} U^{(n)}(t) U^{(q)}(t) < 0 \tag{6.23}$$

for any non-zero vector $X = \left(U^{(1)}(t), \cdots, U^{(N)}(t)\right)$. In view of its definition and its previous properties, the matrix A is real-valued, symmetric and negative definite. Accordingly, the linear system (6.17) admits a unique solution $(U^{(1)}(t), \cdots, U^{(N)}(t))$ whatever the addressed cluster (axisymmetric) geometry.

We then presented in this subsection a well-posed linear system to determine the solid bodies translational velocities $U^{(1)}(t)\mathbf{e}_z, \cdots, U^{(N)}(t)\mathbf{e}_z$ without obtaining the flow $(\mathbf{u}, p)$ about the cluster. Inspecting (6.17) also shows that such a linear system solely requires to determine a few surface quantities on the liquid domain boundary for N auxiliary Stokes flows $(\mathbf{u}^{(n)}, p^{(n)})$: the surface traction $\boldsymbol{\sigma}^{(n)} \cdot \mathbf{n}$ on the boundary of each solid body and the velocity $\mathbf{u}^{(n)}$ on the free surface $S_0(t)$ and on each bubble surface.

How those key surface quantities are efficiently obtained by inverting N boundary-integral equations on the liquid domain boundary $\partial \mathcal{D}(t)$ is explained in the next section §6.2.1.

6.2 Advocated boundary formulation

This section presents the boundary formulation adopted in this Chapter to efficiently solve $N + 1$ Stokes flow problems for $(\mathbf{u}, p)$ and (if $N \geq 1$) for the flows $(\mathbf{u}^{(n)}, p^{(n)})$.

6.2.1 Three dimensional velocity integral representation

Henceforth, we omit the time-dependence in the liquid domain ($\mathcal{D}$ instead of $\mathcal{D}(t)$) and surfaces $S_m(m = 0, \cdots, M)$ and (if $N \geq 1$). We shall also use the usual tensor summation notation with for instance $\mathbf{x} = x_i\mathbf{e}_i$. For any Stokes flow $(\mathbf{u}, p)$ fulfilling (6.1) and exerting on the liquid boundary $\partial\mathcal{D}$ the surface traction $\mathbf{f} = \boldsymbol{\sigma}\cdot\mathbf{n}$ one then obtains the key integral representation (which extends the property (1.48) given in Chapter 1)

$$\mathbf{u}(\mathbf{x}) = -\frac{1}{8\pi\mu}\int_{\partial\mathcal{D}}\mathbf{G}(\mathbf{y},\mathbf{x})\cdot\mathbf{f}(\mathbf{y})dS(\mathbf{y}) \\ + \frac{1}{8\pi}\int_{\partial\mathcal{D}}\mathbf{u}(\mathbf{y})\cdot\mathbf{T}(\mathbf{y},\mathbf{x})\cdot\mathbf{n}(\mathbf{y})dS(\mathbf{y}) \quad \text{for } \mathbf{x} \text{ in } \mathcal{D}. \tag{6.24}$$

If S designates an arbitrary closed surface or S_0, one also has the useful identities (whatever the indices i and j)

$$\int_S T_{ijk}(\mathbf{y},\mathbf{x})n_k(\mathbf{y})dS(\mathbf{y}) = 0 \quad \text{for } \mathbf{x} \text{ not on } S. \tag{6.25}$$

Combining (6.24) with (6.25) yields another equivalent integral representation

$$\mathbf{u}(\mathbf{x}) = -\frac{1}{8\pi\mu}\int_{\partial\mathcal{D}}\mathbf{G}(\mathbf{y},\mathbf{x})\cdot\mathbf{f}(\mathbf{y})dS(\mathbf{y}) + \frac{1}{8\pi}\int_{\partial\mathcal{D}\backslash S}\mathbf{u}(\mathbf{y})\cdot\mathbf{T}(\mathbf{y},\mathbf{x})\cdot\mathbf{n}(\mathbf{y})dS(\mathbf{y}) \\ + \frac{1}{8\pi}\int_{\partial\mathcal{D}}\Big[\mathbf{u}(\mathbf{y}) - \mathbf{u}(\mathbf{x})\Big]\cdot\mathbf{T}(\mathbf{y},\mathbf{x})\cdot\mathbf{n}(\mathbf{y})dS(\mathbf{y}) \quad \text{for } \mathbf{x} \text{ in } \mathcal{D} \tag{6.26}$$

where S is one of the surfaces $S_0, \cdots, S_M, \Sigma_1, \cdots, \Sigma_n$. The relation (6.26) also holds as $\mathbf{x}$ tends onto the selected surface S and one then arrives at the velocity boundary representation which actually holds for $\mathbf{x}$ in $\mathcal{D} \cup \mathcal{S}$.

Applying the previous results to the flow $(\mathbf{u}, p)$ obeying (6.1)-(6.4) then immediately provide coupled regularized boundary-integral equations for the unknown velocity $\mathbf{u}$ on each $S_m(m = 0, \cdots, M)$ and surface traction $\mathbf{f} = \boldsymbol{\sigma}\cdot\mathbf{n}$ and on each surface $\Sigma_n(n = 1, \cdots, N)$. Because of the property, for arbitrary located point $\mathbf{x}$,

$$\int_S G_{ij}(\mathbf{y},\mathbf{x})n_i(\mathbf{y})dS(\mathbf{y}) = 0 \tag{6.27}$$

the constant pressure(s) $p_m, \cdots, p_M$ inside the bubbles disappear from the obtained formulation. More precisely, one obtains the following boundary-integral equations (again using (6.25))

1) For a cluster made of M bubbles ($N = 0$)

$$8\mu\pi\mathbf{u}(\mathbf{x}) - \mu\int_{\partial\mathcal{D}}\Big[\mathbf{u}(\mathbf{y}) - \mathbf{u}(\mathbf{x})\Big]\cdot\mathbf{T}(\mathbf{y},\mathbf{x})\cdot\mathbf{n}(\mathbf{y})dS(\mathbf{y}) \\ - \mu\int_{\partial\mathcal{D}\backslash S_m}\mathbf{u}(\mathbf{y})\cdot\mathbf{T}(\mathbf{y},\mathbf{x})\cdot\mathbf{n}(\mathbf{y})dS(\mathbf{y}) = -\sum_{p=0}^{M}\int_{S_p}\mathbf{G}(\mathbf{y},\mathbf{x})\cdot\Big[\rho_l\mathbf{g}\cdot\mathbf{y} \\ + \gamma_p\boldsymbol{\nabla}_S\cdot\mathbf{n}\Big]n_\beta(\mathbf{y})dS(\mathbf{y}) \quad \text{for } \mathbf{x} \text{ on } S_m,\ m = 0, \cdots, M \tag{6.28}$$

2) For a cluster involving at least one solid body ($N \geq 1$)

$$8\mu\pi\mathbf{u}(\mathbf{x}) - \mu\int_{\partial\mathcal{D}\setminus S_m}\mathbf{u}(\mathbf{y})\cdot\mathbf{T}(\mathbf{y},\mathbf{x})\cdot\mathbf{n}(\mathbf{y})dS(\mathbf{y}) + \sum_{q=1}^{N}\int_{\Sigma_q}\mathbf{G}(\mathbf{y},\mathbf{x})\cdot[\boldsymbol{\sigma}\cdot\mathbf{n}](\mathbf{y})dS(\mathbf{y})$$
$$-\mu\int_{\partial\mathcal{D}}\Big[\mathbf{u}(\mathbf{y})-\mathbf{u}(\mathbf{x})\Big]\cdot\mathbf{T}(\mathbf{y},\mathbf{x})\cdot\mathbf{n}(\mathbf{y})dS(\mathbf{y}) = -\sum_{p=0}^{M}\int_{S_p}\mathbf{G}(\mathbf{y},\mathbf{x})\cdot[\rho_l\mathbf{g}\cdot\mathbf{y}$$
$$+\gamma_p\boldsymbol{\nabla}_S\cdot\mathbf{n}]\,n_\beta(\mathbf{y})dS(\mathbf{y}) \quad \text{for } \mathbf{x} \text{ on } S_m,\ m=0,\cdots,M \tag{6.29}$$

$$\mu\int_{\partial\mathcal{D}}\mathbf{u}(\mathbf{y})\cdot\mathbf{T}(\mathbf{y},\mathbf{x})\cdot\mathbf{n}(\mathbf{y})dS(\mathbf{y}) - \sum_{q=1}^{N}\int_{\Sigma_q}\mathbf{G}(\mathbf{y},\mathbf{x})\cdot[\boldsymbol{\sigma}\cdot\mathbf{n}](\mathbf{y})dS(\mathbf{y}) = 8\mu\pi U^{(n)}\mathbf{e}_z$$
$$-\sum_{p=0}^{M}\int_{S_p}\mathbf{G}(\mathbf{y},\mathbf{x})\cdot[\rho_l\mathbf{g}\cdot\mathbf{y}+\gamma_p\boldsymbol{\nabla}_S\cdot\mathbf{n}]\,n_\beta(\mathbf{y})dS(\mathbf{y}) \quad \text{for } \mathbf{x} \text{ on } \Sigma_n,\ n=1,\cdots,N. \tag{6.30}$$

The coupled boundary-integral equations (6.28) or (6.29)-(6.30) permit one to calculate on the liquid boundary $\mathcal{D}$ the unknown quantities (i.e. $\mathbf{u}$ on each S_p and $\mathbf{f}=\boldsymbol{\sigma}\cdot\mathbf{n}$ on each Σ_q). Moreover, as can easily be checked by the reader, the unknown velocity on the surfaces S_p governed by those integral equations automatically satisfies the conditions (6.6). Of course, when $N \geq 1$, one has first to get the velocities $U^{(n)}\mathbf{e}_z$ by solving the linear system obtained in §6.1.2. This is done by solving (6.29)-(6.30) for each auxiliary Stokes flow $(\mathbf{u}^{(p)}, p^{(p)})$ by replacing the quantity $\rho_l\mathbf{g}\cdot\mathbf{y}+\gamma_p\boldsymbol{\nabla}_S\cdot\mathbf{n}$ with zero on the right-hand sides of (6.29)-(6.30) and $U^{(n)}$ with δ_{np} on the right-hand side of (6.30). Because the cluster and the flow admit a symmetry of revolution about the $(z'Oz)$ axis, it is also useful to express the previous boundary-integral equations in cylindrical coordinates (ρ, z) (as was already done in Chapter 2).

6.2.2 Axisymmetric formulation

This subsection is an extension to the case of our cluster involving $M \geq 1$ bubbles and $N \geq 0$ solid bodies of the treatment proposed in Chapter 2 for one bubble. Since we restrict the analysis to the axisymmetric configuration depicted in Figure 6.1, we adopt cylindrical coordinates (r,ϕ,z) with $r=\sqrt{x^2+y^2}$, $z=x_3$ and ϕ the azimuthal angle in the range $[0,2\pi]$. We set $\mathbf{u}=u_r\mathbf{e}_r+u_z\mathbf{e}_z=u_\alpha\mathbf{e}_\alpha$ (with $\alpha=r,z$), $\mathbf{f}=\boldsymbol{\sigma}\cdot\mathbf{n}=f_r\mathbf{e}_r+f_z\mathbf{e}_z=f_\alpha\mathbf{e}_\alpha$ and $\mathbf{n}=n_r\mathbf{e}+n_z\mathbf{e}_z=n_\alpha\mathbf{e}_\alpha$ and introduce the traces $\mathcal{L}'_n$ of Σ_n and $\mathcal{L}_m$ of S_m in the $\phi=0$ half plane. We shall also denote by $\mathcal{L}$ the truncated contour associated with $\partial\mathcal{D}$.

Mimicking what has been done to obtain (2.1), we now proceed to rewrite the boundary-integral equations (6.28) or (6.29)-(6.30) in order to exploit the axisymmetry of the problem. First we replace $\mathbf{x}$ with $\mathbf{x}_0$ and also $\mathbf{y}$ by $\mathbf{x}$. Then, in absence of solid body ($N=0$) integrating over ϕ (6.28) easily yields the equivalent boundary-integral equations

$$4\pi\mu u_\alpha(\mathbf{x}_0) - \mu\int_{\mathcal{L}\setminus\mathcal{L}_m}C_{\alpha\beta}(\mathbf{x},\mathbf{x}_0)u_\beta(\mathbf{x})dl(\mathbf{x}) - \mu\int_{\mathcal{L}_m}C_{\alpha\beta}(\mathbf{x},\mathbf{x}_0)\Big[u_\beta(\mathbf{x})-u_\beta(\mathbf{x}_0)\Big]dl(\mathbf{x})$$
$$= -\sum_{p=0}^{M}\int_{\mathcal{L}_p}B_{\alpha\beta}(\mathbf{x},\mathbf{x}_0)[-\rho_l g z+\gamma_p\boldsymbol{\nabla}_S\cdot\mathbf{n}]\,n_\beta(\mathbf{x})dl(\mathbf{x}) \quad \text{for } \mathbf{x}_0 \text{ on } \mathcal{L}_m. \tag{6.31}$$

In a similar fashion (6.29)-(6.30) for a cluster involving at least one solid body becomes (by integrating over ϕ)

$$
\begin{aligned}
&4\pi\mu u_\alpha(\mathbf{x}_0) - \mu \int_{\mathcal{L}\setminus\mathcal{L}_m} C_{\alpha\beta}(\mathbf{x},\mathbf{x}_0) u_\beta(\mathbf{x}) dl(\mathbf{x}) - \mu \int_{\mathcal{L}_m} C_{\alpha\beta}(\mathbf{x},\mathbf{x}_0) \left[u_\beta(\mathbf{x}) - u_\beta(\mathbf{x}_0)\right] dl(\mathbf{x}) \\
&+ \sum_{q=1}^{N} \int_{\mathcal{L}'_q} B_{\alpha\beta}(\mathbf{x},\mathbf{x}_0) f_\beta(\mathbf{x}) dl(\mathbf{x}) = -\sum_{p=0}^{M} \int_{\mathcal{L}_p} B_{\alpha\beta}(\mathbf{x},\mathbf{x}_0)[-\rho_l g z + \gamma_p \boldsymbol{\nabla}_S \cdot \mathbf{n}]\, n_\beta(\mathbf{x}) dl(\mathbf{x}) \\
&\qquad\qquad \text{for } \mathbf{x}_0 \text{ on } \mathcal{L}_m,\ m = 0, \cdots, M
\end{aligned}
\tag{6.32}
$$

$$
\begin{aligned}
&\mu \sum_{m=0}^{M} \int_{\mathcal{L}_{\Updownarrow}} C_{\alpha\beta}(\mathbf{x},\mathbf{x}_0) u_\beta(\mathbf{x}) dl(\mathbf{x}) - \sum_{q=1}^{N} \int_{\mathcal{L}'_q} B_{\alpha\beta}(\mathbf{x},\mathbf{x}_0) f_\beta(\mathbf{x}) dl(\mathbf{x}) = 8\pi\mu U^{(n)} \delta_{z\alpha} \\
&+ \sum_{p=0}^{M} \int_{\mathcal{L}_p} B_{\alpha\beta}(\mathbf{x},\mathbf{x}_0)[-\rho_l g z + \gamma_p \boldsymbol{\nabla}_S \cdot \mathbf{n}]\, n_\beta(\mathbf{x}) dl(\mathbf{x}) \text{ for } \mathbf{x}_0 \text{ on } \mathcal{L}'_n,\ n = 0, \cdots, N.
\end{aligned}
\tag{6.33}
$$

For the auxiliary flow $(\mathbf{u}^{(p)}, p^{(p)})$ one has to replace $U^{(n)}$ with δ_{np} in (6.33) and to omit the integral on the right-hand side of (6.32)-(6.33). Note that it is straightforward to write the counterpart of (6.17) in cylindrical coordinates. Finally, the achieved numerical implementation closely follows the lines detailed in Chapter 2 (mesh and collocation method, isoparametric interpolation and Wielandt deflation technique).

6.3 Conclusion

In this theoretical Chapter, it has been shown how one can efficiently deals at a reasonable CPU time cost (by solely meshing contours) with the challenging case of clusters made of bubbles and/or solid particle(s) in axisymmetric configuration. For a cluster involving $N \geq 1$ solid body(ies) one needs to solve $N+1$ boundary-integral equations on the liquid domain (truncated) boundary (contour in our axisymmetric formulation). It should also be noted that for a given cluster geometry such an integral admits the same influence matrix when discretized. This nice property permits one to reduce a lot the CPU-time cost of the numerical implementation.

Chapter 7

Numerical results for several bubble(s) and/or solid particles

Contents

In this Chapter, we present and discuss the numerical results obtained by implementing the strategy proposed in Chapter 6. This is achieved for several types of clusters involving at least two particles (bubbles or solid body). The first section solely pays attention to the cluster made of bubbles whereas the challenging case of cluster involving at least one solid body is examined in a second section.

7.1 Cluster made of two bubbles

As announced in the introduction, we consider in this first section interacting bubbles. In this direction, one should note that Pigeonneau and Sellier [2] already addressed the case of bubbles having the same surface tension as the free surface. In our computations, different surface tensions are allowed and we restrict attention to a two-bubble cluster.

7.1.1 Comparison with the case of one bubble

The case of two bubbles ascending toward a free surface in axisymmetric configuration is investigated and compared with the case of one bubble rising near a free surface. Moreover, the surface tension γ_1 and γ_2 for the two bubbles are taken identical. Therefore the considered Bond number here is $\mathrm{Bo}_1 = \rho_l g a^2/(3\gamma_1)$. Each computation is performed using $N_{eb} = 20$ boundary elements on each bubble surface and $N_{ef} = 25$ boundary element on the truncated free surface while 4 collocation points are spread on each boundary element.

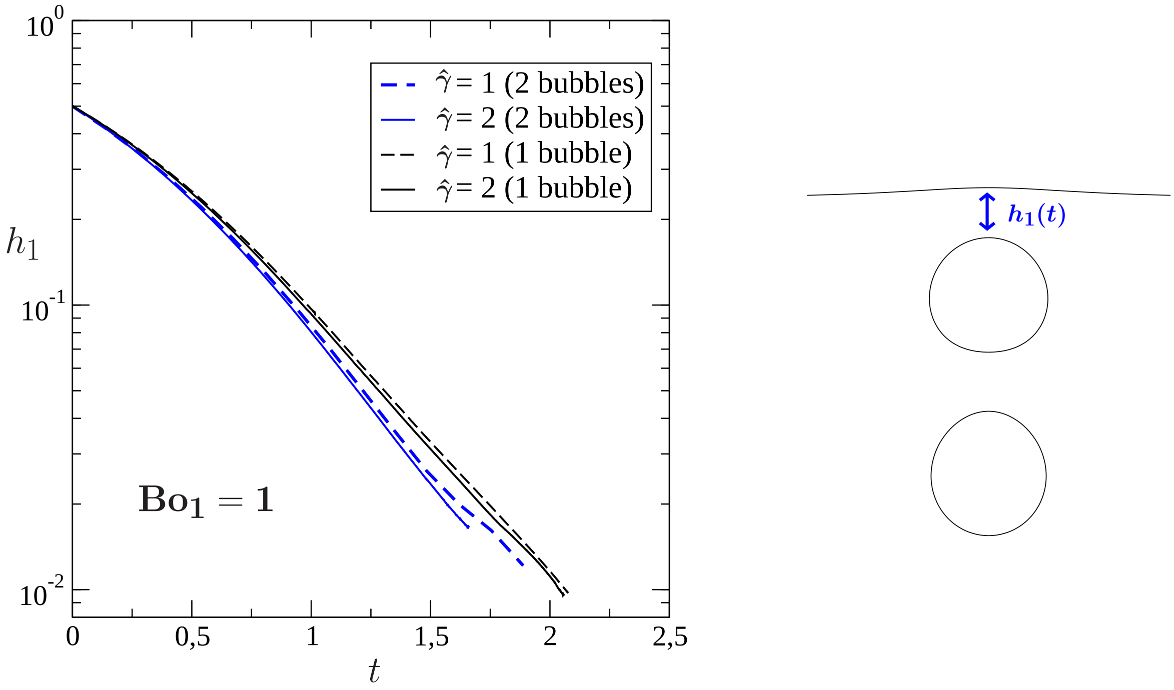

Figure 7.1: Normalized film thickness $h_1(t)$ time evolution for the Bond number $\mathrm{Bo}_1 = \rho g a^2/(3\gamma_1) = 1$ in the case of one bubble (black curves) and two bubbles (blue curves). The surface tension ratio equals $\hat{\gamma} = \gamma_0/\gamma_1 = 1$ (dashed line) or $\hat{\gamma} = 2$ (solid line).

Figure 7.1 shows the normalized time-dependent thickness $h_1(t)$ of the liquid film which takes place between the bubble and the free surface for one and two bubbles for $\mathrm{Bo}_1 = 1$. The blue curves indicate the two bubble case while the black curves correspond to the case of one bubble. Two different surface tension ratios $\hat{\gamma} = \gamma_0/\gamma_1$ are considered: the $\hat{\gamma} = 1$ case represented by dashed lines and the $\hat{\gamma} = 2$ case associated with the solid lines. The plotted curves exhibit a similar trend and that adding one bubble affects slightly the film thickness behavior in time. As seen in Chapter 3, the film thickness $h_1(t)$ shows a long-time exponential decay [2]-[1]

$$h(t) \sim h\, e^{-At} \tag{7.1}$$

with A the thinning rate.

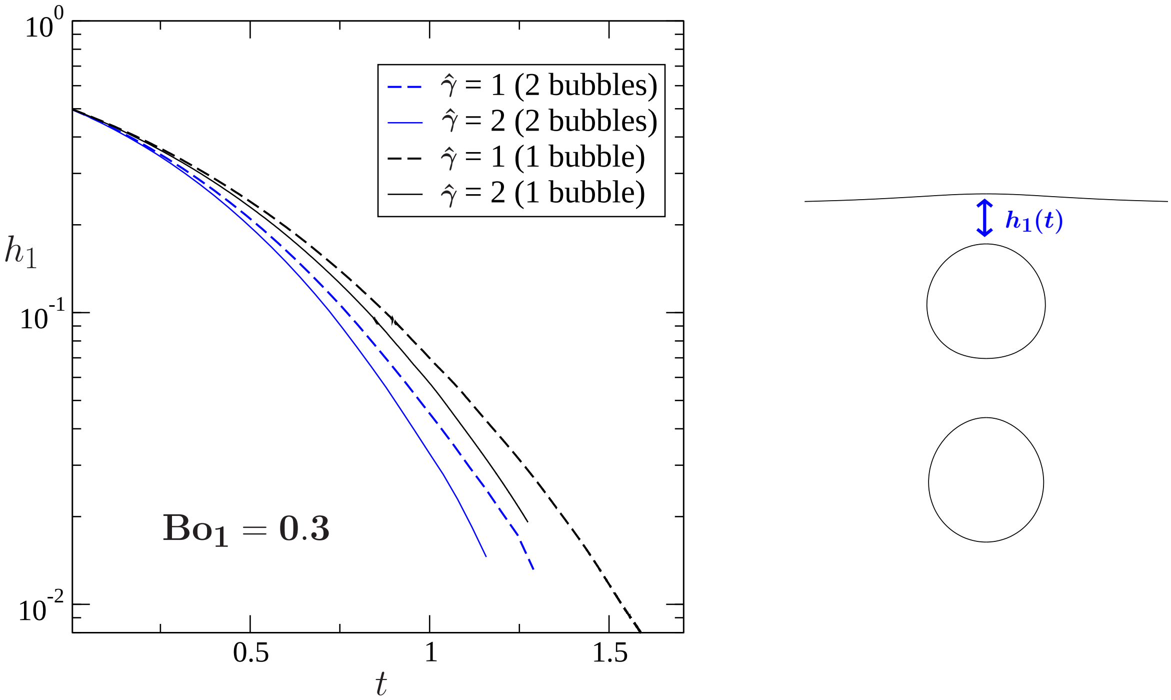

Figure 7.2: Normalized film thickness $h_1(t)$ time evolution for the Bond number $\mathrm{Bo}_1 = \rho g a^2/(3\gamma_1) = 0.3$ in the case of one bubble (black curves) and two bubbles (blue curves). The surface tension ratio equals $\hat{\gamma} = \gamma_0/\gamma_1 = 1$ (dashed line) or $\hat{\gamma} = 2$ (solid line).

In Figure 7.1, the thinning rate is found to be $A \sim 2.12$ for one bubble and $A \sim 2.42$ for two bubbles, agreeing well with the small sensitivity of $h_1(t)$ to the number of bubbles. Moreover, the drainage remains unaffected by the surface tension ratio $\hat{\gamma}$ either for one bubble or two bubbles.

Furthermore, the film drainage $h_1(t)$ has been computed at small Bond number $\mathrm{Bo}_1 = 0.3$ and plotted in Figure 7.2. In contrast with the previous results, the film drainage is here sensitive to both the number of bubbles and the surface tension ratio $\hat{\gamma}$.

For a given surface tension ratio $\hat{\gamma} = 1$, each curve exhibits the same "long-time" thinning rate $A \sim 3.89$ and this suggests that the drainage is solely delayed for the case of one bubble (black curve) when compared with the case of two bubbles (blue curve). In addition, comparing the drainage rate for $\hat{\gamma} = 1$ with the one for $\hat{\gamma} = 2$, a difference $\Delta A = |(A_{\hat{\gamma}=2} - A_{\hat{\gamma}=1})| = 0.17$ is obtained for one bubble while the two-bubble case shows a difference $\Delta A = 0.7$. The film thickness $h_1(t)$ sensitivity to the surface tension ratio is therefore slightly increased by the additional bubble in the two bubbles case.

7.1.2 Two bubbles with identical size and surface tension

7.1.2.1 Film thickness time evolution

The drainage sensitivity to the surface tension ratio $\hat{\gamma}$ in the case of two equals bubbles approaching a free surface is now carefully investigated. This case extends the preliminary results depicted in Figure 7.1 and Figure 7.2. Such a task is performed for two Bond numbers $\mathrm{Bo}_1 = 0.3$ and $\mathrm{Bo}_1 = 1$ and for a large range of surface tension ratio $\hat{\gamma} = 0.2, 0.5, 1, 2$ and 5. The obtained results are shown in Figure 7.3.

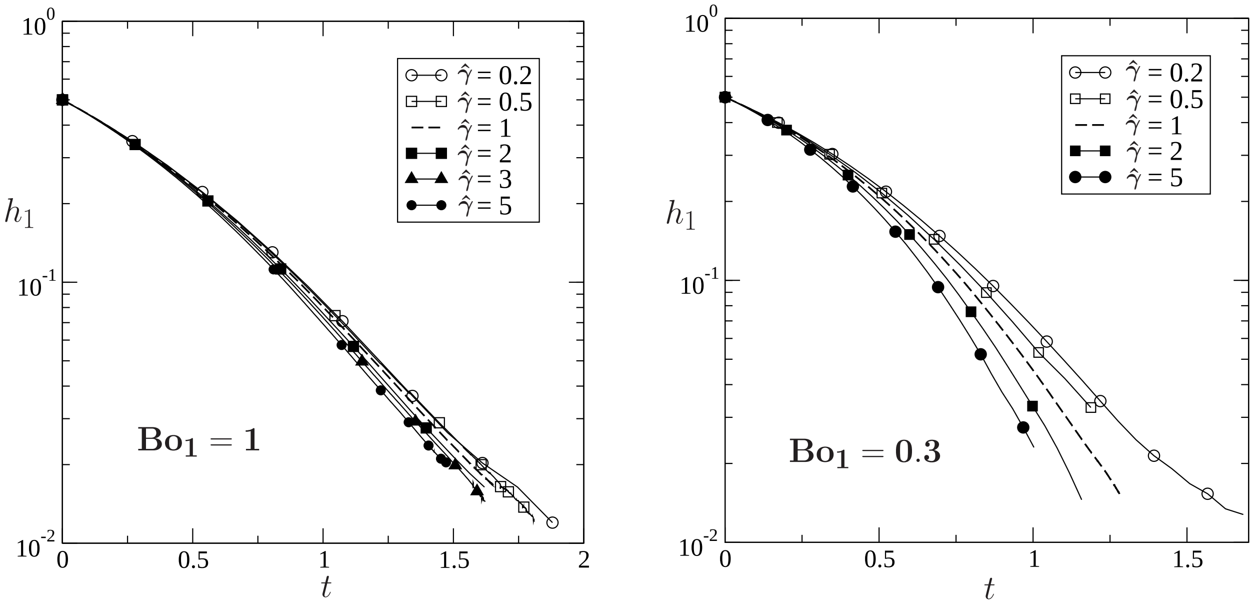

Figure 7.3: Normalized film thickness $h_1(t)$ time evolution for $\hat{\gamma} = 0.2, 0.3, 0.5, 1, 2, 5$ at $\mathrm{Bo}_1 = 1$ and $\mathrm{Bo}_1 = 0.3$.

As already noted, the film thickness $h_1(t)$ is weakly dependent on $\hat{\gamma}$ at a given Bond number $\mathrm{Bo}_1 = 1$ (see in Figure 7.3) whereas for small Bond number at $\mathrm{Bo}_1 = 0.3$ the time-dependent thickness $h_1(t)$ is clearly affected by the change of surface tension as illustrated in Figure 7.3. In Chapter 3, a threshold at which the drainage is unaffected by the surface tension ratio $\hat{\gamma}$ for $\mathrm{Bo}_1 = 1$ in the case of one bubble has been introduced. Such a threshold is indeed preserved for the two-bubble case.

At small Bond number, the drainage rate increases with the surface tension ratio $\hat{\gamma}$ and this behavior complies with the one observed in the case of one bubble (see §I.3.1.4). By adding one bubble, the film thickness sensitivity to the surface tension ratio is preserved at small Bond number and moderate Bond number although the drainage occurs earlier for the two bubbles case.

Furthermore, another film liquid occurs between the two bubbles (as sketched in Figure 7.4). Its time-dependent thickness $h_2(t)$ has been examined and compared to the time-dependent film thickness $h_1(t)$ in Figure 7.4 for $\mathrm{Bo}_1 = 1$ and $\hat{\gamma} = 1$.

The film drainage $h_1(t)$ is indicated by a blue solid line and the film drainage $h_2(t)$ is given by the red dashed line. The two plotted curves exhibit an exponential decay, although the drainage dynamics of the liquid film $h_2(t)$ take place later than the one for the liquid film $h_1(t)$ and its thinning rate is slightly smaller than $h_1(t)$. This suggests that the liquid film with thickness $h_1(t)$ is squeezed faster than the liquid film between the two bubbles $h_2(t)$.

Moreover, the drainage dynamic of $h_1(t)$ occurs immediately while $h_2(t)$ is nearly constant at small time (see Figure 7.4). This is explained by the identical bubble velocities (the two bubble having the same size) when distant from the free surface which keeps the distance h_2 constant at the beginning (as the two bubbles rise toward the free surface) while the gap h_1 decreases at once.

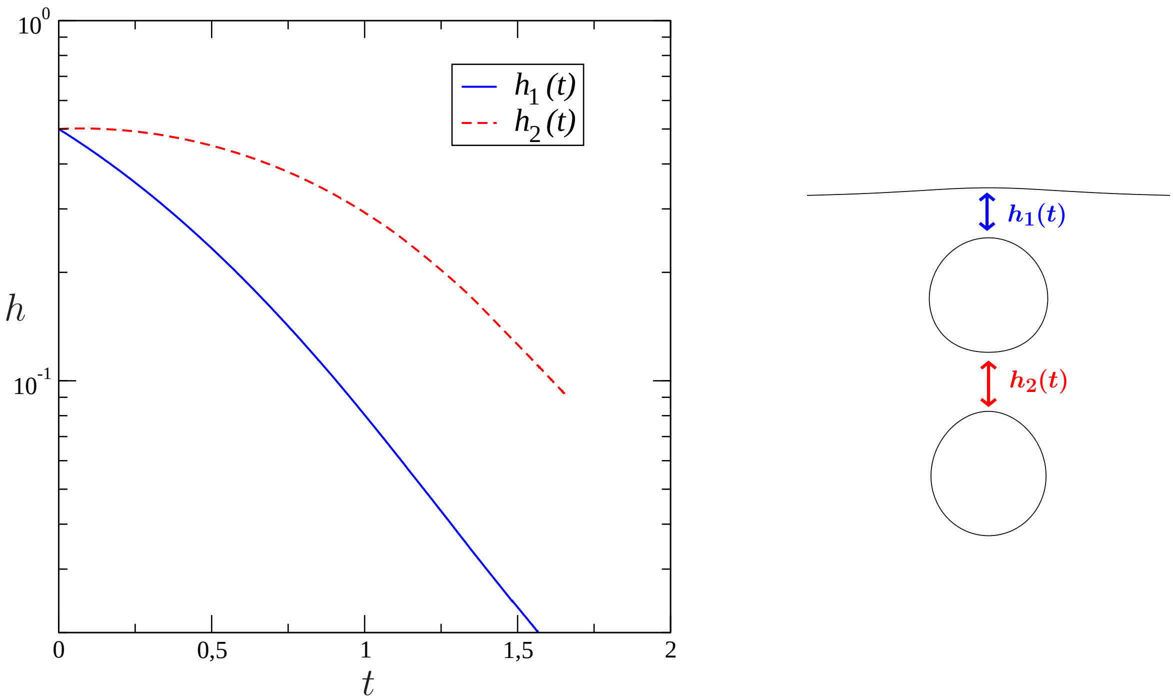

Figure 7.4: Normalized film thicknesses $h_1(t)$ (blue solid line) and $h_2(t)$(dashed red line) time evolution for $\hat{\gamma} = 1$ at $\mathrm{Bo}_1 = 1$ for the two bubbles case.

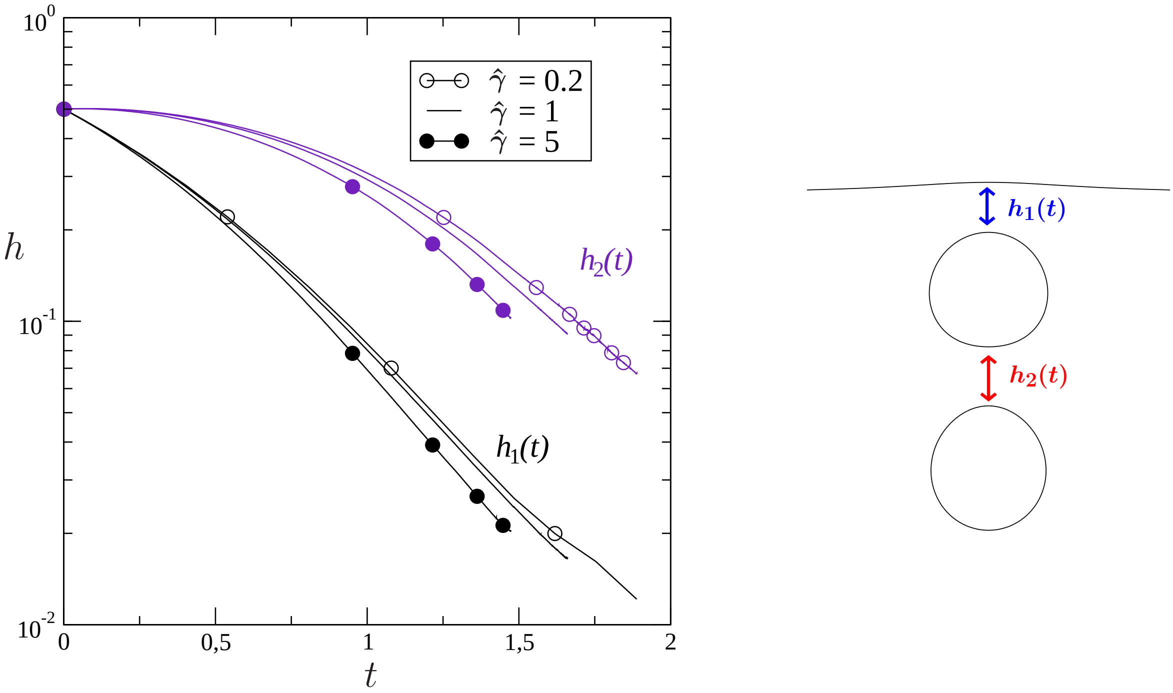

Figure 7.5: Normalized film thicknesses $h_1(t)$ (blue solid line) and $h_2(t)$(dashed red line) time evolution at $\mathrm{Bo}_1 = 1$ for $\hat{\gamma} = 0.2, 1, 5$ in the case of two equal bubbles.

In Figure 7.5, the sensitivity of the film drainage $h_1(t)$ (black curve) and $h_2(t)$(indigo curve) has been investigated at $\mathrm{Bo}_1 = 1$ for three different values of $\hat{\gamma} = 0.2, 1, 5$. The small surface tension ratio $\hat{\gamma} = 0.2$ is indicated by empty circles, the large surface tension ratio corresponds to the filled circles while the case of equal bubbles and free surface tension is plotted using a solid line.

Both $h_1(t)$ and $h_2(t)$ show a similar dependence to the surface tension ratio $\hat{\gamma}$, the thinning rate increasing with $\hat{\gamma}$. However, the sensitivity of the film drainage $h_2(t)$ to $\hat{\gamma}$ is stronger when compared with the film drainage $h_1(t)$.

Denoting by $\alpha = |\Delta A|/A'$ the "long-time" thinning rate relative difference where ΔA is the difference between the two considered thinning rate whereas A' is their summation, one gets $\alpha = 0.08$ between the $\hat{\gamma} = 1$ and $\hat{\gamma} = 5$ values for $h_1(t)$ while the film drainage $h_2(t)$ exhibits a difference of $\alpha = 0.12$. Similarly, between the $\hat{\gamma} = 1$ and $\hat{\gamma} = 0.3$ values, $h_2(t)$ shows a "long-time" thinning rate difference of $\alpha = 0.04$ whereas the film drainage $h_1(t)$ remains unaffected by the change of surface tension.

Indeed, at large $\hat{\gamma} = 5$ value, the free surface tension γ_0 is larger than the bubbles surface tension $\gamma_1 = \gamma_2$ and resists strongly to the first bubble action. The first bubble, stopped by the free surface, is then quickly caught up by the second bubble and as a result, the thickness h_2, being under the second bubble pressure and the stopped first bubble, decreases thus faster. In contrast, for small $\hat{\gamma}$ value, the free surface tension is weak compared to each bubble surface tension and therefore the free surface is strongly deformed by the pressure exerted by the first bubble. As the first bubble keeps rising toward the disturbed free surface, the thickness h_2 decreases then slower.

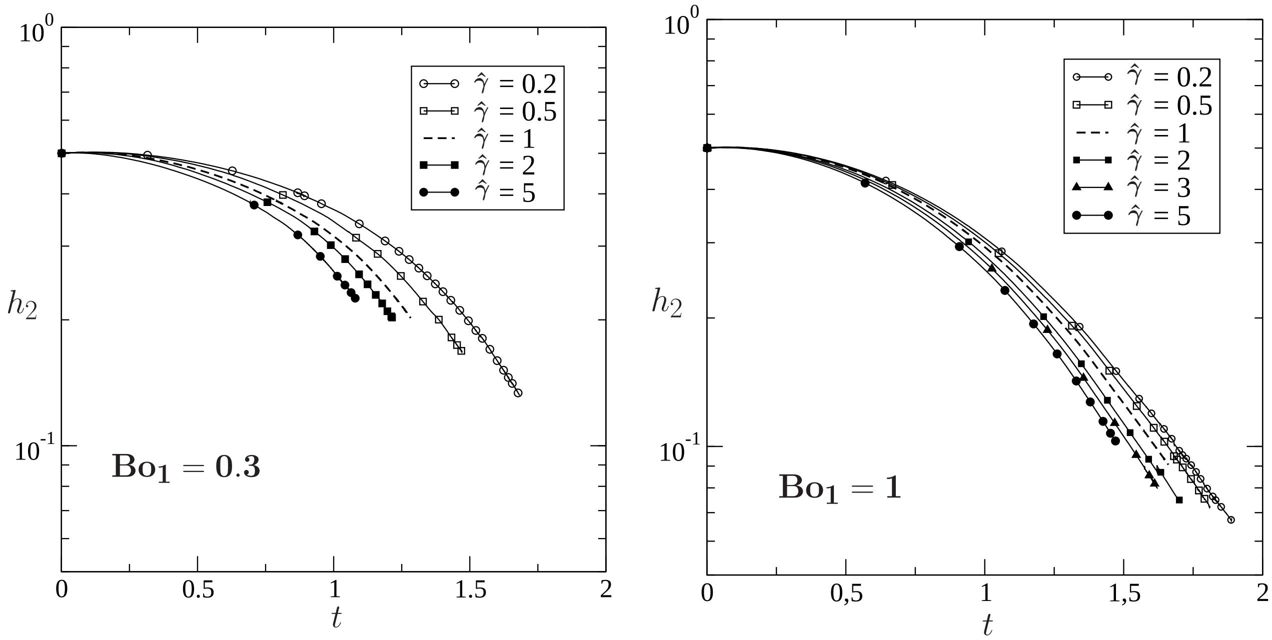

Figure 7.6: Normalized film thickness $h_2(t)$ time evolution for $\hat{\gamma} = 0.2, 0.5, 1, 2, 5$ at $\mathrm{Bo}_1 = 0.3$ and at $\mathrm{Bo}_1 = 1$.

The drainage sensitivity to the surface tension ratio $\hat{\gamma}$ for the film thickness h_2 has been also examined (similarly to h_1) for two given Bond numbers $\mathrm{Bo}_1 = 0.3$ and $\mathrm{Bo}_1 = 1$ and for a large range of surface tension ratio $\hat{\gamma} = 0.2, 0.5, 1, 2$ and 5. The obtained results are shown in Figure 7.6.

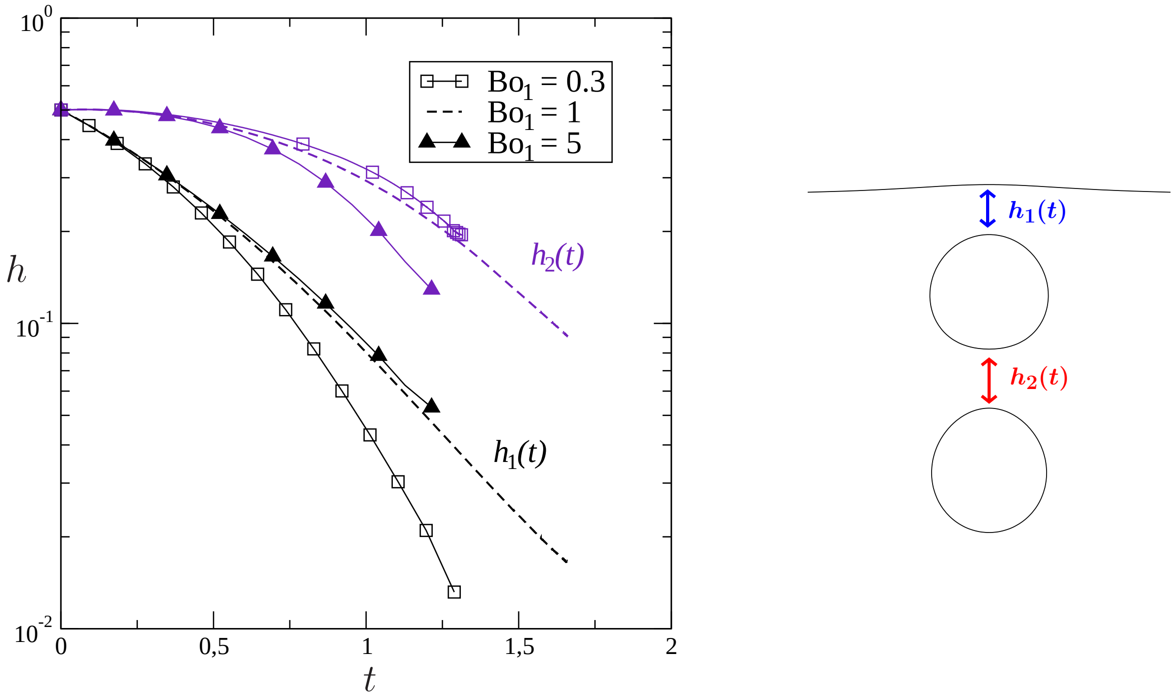

Figure 7.7: Normalized film thickness $h_1(t)$ (blue solid line) and $h_2(t)$(dashed red line) time evolution for $\hat{\gamma} = 1$ at $\mathrm{Bo}_1 = 0.3, 1$ and $\mathrm{Bo}_1 = 5$ for the two bubbles.

As seen in the previous results depicted in Figure 7.4, the film drainage $h_2(t)$ is clearly affected by the change of surface tension ratio at $\mathrm{Bo}_1 = 1$. The threshold at which the drainage is unaffected by the surface tension ratio $\hat{\gamma}$ for $\mathrm{Bo}_1 = 1$ in the case of two bubbles has been obtained for the film thickness h_1. Such a threshold is therefore shifted when compared to the thinning of the film h_2.

Moreover, at small Bond number ($\mathrm{Bo}_1 = 0.3$), the drainage sensitivity to the surface tension ratio is enhanced as shown in Figure 7.6. The thinning rate A increases with the surface tension ratio $\hat{\gamma}$ and one clearly remarks that the drainage is enhanced when the surface tension ratio exceeds unity. This result complies with the behavior observed for the film drainage $h_1(t)$ at $\mathrm{Bo}_1 = 0.3$ and in the case of one bubble (see in §I.3.1.4).

In addition, the film thickness h_2 is also affected by the change of Bond number. For a given surface tension ratio $\hat{\gamma}$ at small Bond number, the associated thinning rate A is smaller than for $\mathrm{Bo}_1 = 1$.

As depicted in Figure 7.7, the sensitivity of the film thickness h_1 (black curve) and h_2 (indigo curve) to the Bond number has been also investigated at a given surface tension ratio $\hat{\gamma} = 1$. The dashed line indicates the $\mathrm{Bo}_1 = 1$, the solid line with empty square symbols is for the $\mathrm{Bo}_1 = 0.3$ and the large Bond number $\mathrm{Bo}_1 = 5$ is plotted using filled triangles. Each film thickness shows a sensitivity to the Bond number. Nevertheless, while the drainage dynamics of h_1 is mostly affected at small Bond number and remains unaffected at large Bond number, h_2 exhibits a strong sensitivity at large Bond number and a weak sensitivity at small Bond number.

The behavior of h_1 has been already discussed in the case of one bubble. Such a behavior for two equal bubbles is now depicted in Figure 7.7. At large Bond number ($\mathrm{Bo}_1 = 5$), each surface is highly deformable and as the free surface is disturbed by the cluster action, the resulting gap h_1 decreases therefore slowly. In contrast, at small Bond number ($\mathrm{Bo}_1 = 0.3$), the free surface resists strongly to the cluster buoyancy force and therefore is weakly disturbed. Moreover, the two bubbles are also weakly disturbed, as a results, the thinning rate of h_1 is enhanced. In case of the film drainage h_2, since h_1 becomes small quickly at small Bond number, the distance h_2 between the two bubbles decreases slowly.

It is noteworthy that h_2 decreases faster and faster when the Bond number increases which is the inverse of the h_1. This means that the lubrication force is lesser between the two bubbles than between the free surface and the first bubble. As it is can be shown in the next subsection, the bottom of the first bubble is lesser deformed than the free surface. As we point out in the Chapter 3, the film drainage is strongly linked to the deformation of the first interface of the liquid film, i.e. the bottom part of the first bubble in the case of the second liquid film. Since the buoyancy increases with the Bond number, the dynamics of h_2 is then faster at large Bond number.

7.1.2.2 Bubble(s) and free surface shapes

As previously noticed, the film thickness sensitivity to the surface tension ratio is enhanced at small Bond number. Figure 7.8 depicts the corresponding computed shapes of the two bubbles and the free surface. For further convenience, one here actually selects three values of the surface tension ratio $\hat{\gamma} = 0.2, 1$ and 5 for the $\mathrm{Bo}_1 = 0.3, 1$.

The upper plots in Figure 7.8 depict the bubble and free surface shapes at two different normalized times (initial time $t_0 = 0$ and the final time $t_f = 1.079$) for $\mathrm{Bo}_1 = 1$. As seen on the computed shapes, the surface tension ratio $\hat{\gamma}$ clearly affects both the bubble and the free surface shapes. As $\hat{\gamma}$ increases, the free surface deformation not surprisingly decreases whereas the bubbles deformation increases more or less. More precisely, the upper bubble deformation to the free surface strongly depends upon $\hat{\gamma}$ while the lower bubble deformation is nearly unchanged.

Such trends are explained: the upon bubble interacts with a free surface whose shape deeply depends upon $\hat{\gamma}$ while the lower bubble mainly interacts with the bottom of the upper bubble and such a bottom is nearly independent of $\hat{\gamma}$ (as seen on the reported shapes).

For small surface tension ratio $(\mathrm{Bo}_1, \hat{\gamma}) = (1, 0.2)$ (i.e. a low free surface tension γ_0), each surface is highly deformed and the surface contact area between the upper bubble and the free surface is larger for $(\mathrm{Bo}_1, \hat{\gamma}) = (1, 1)$ or $(\mathrm{Bo}_1, \hat{\gamma}) = (1, 5)$. Since the contact area is large, the resulting drainage is weak and this prediction well agrees with the drainage rate given in Figure 7.3(b). On the contrary, the drainage is enhanced for $(\mathrm{Bo}_1, \hat{\gamma}) = (1, 5)$ because the contact surface shrinks and this feature complies with the results in Figure 7.3(b). Furthermore, at the final time $t_f = 1.079$, the two bubble locations evolve with the surface tension ratio $\hat{\gamma}$. Since the two bubbles with the same radius rise initially with the same initial velocity U, the different bubble location seen, for instance, at $(\mathrm{Bo}_1, \hat{\gamma}) = (1, 0.2)$ and $(\mathrm{Bo}_1, \hat{\gamma}) = (1, 5)$ in the Figure 7.3(b), implies therefore that the first bubble velocity reduces as $\hat{\gamma}$ increases. These results comply with the case of one bubble ascending toward a free surface shown in Chapter §3.1. Besides, the distance between the first bubble and the second one slightly shrinks as $\hat{\gamma}$ increases implying that the second bubble velocity keeps rising while the first bubble is stopped by the free surface and agrees with the behavior of the film thickness h_2 observed in Figure 7.4 (a)-(b).

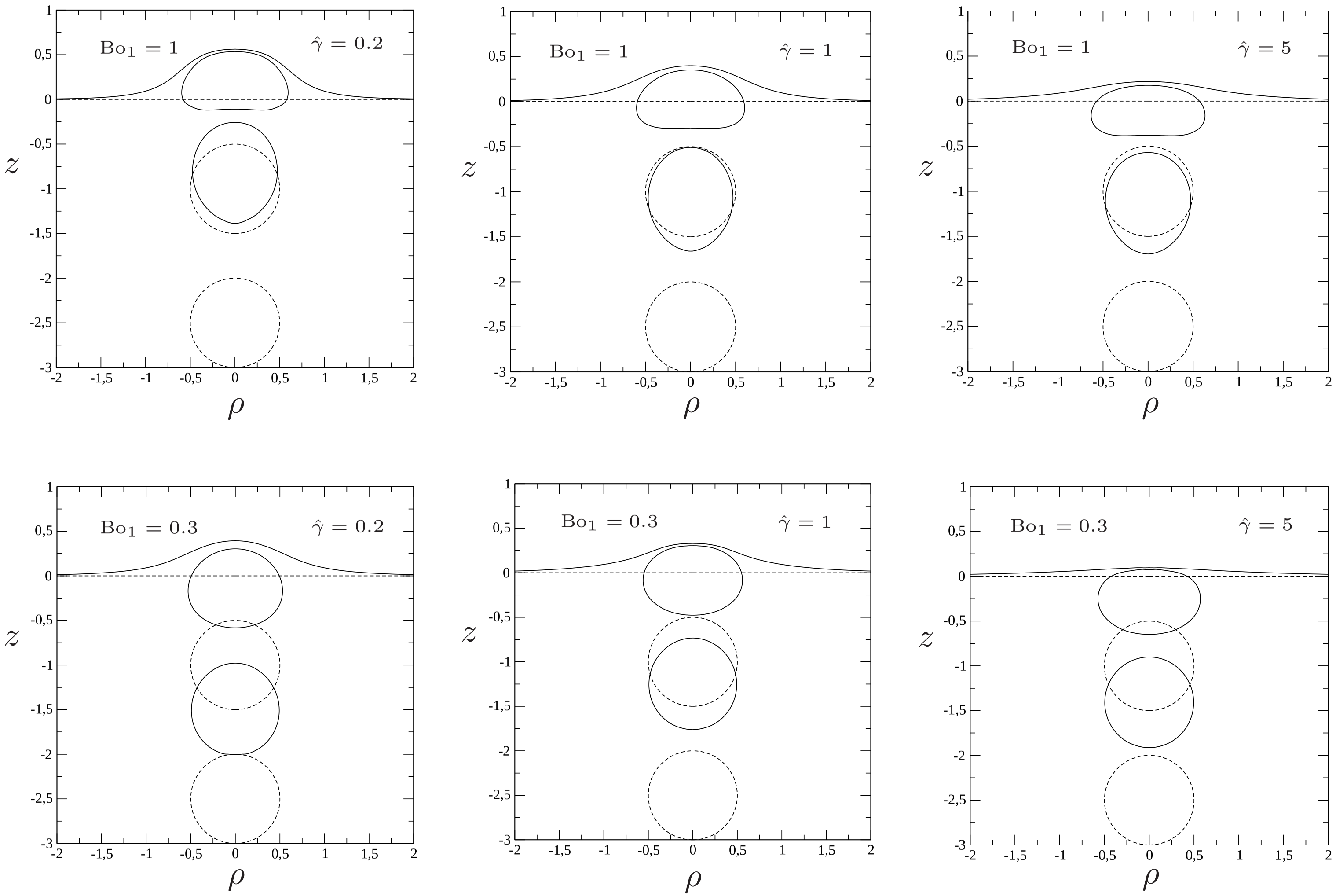

Figure 7.8: Computed bubbles and free surface shapes at normalized times $t_0 = 0$ (dashed lines) and final time $t_f = 1.079$ for $\hat{\gamma} = 0.2, 1, 5$. As indicated on each figure the upper and the lower plots correspond to $\mathrm{Bo}_1 = 1$ and $\mathrm{Bo}_1 = 0.3$, respectively. It is recalled that $\hat{\gamma} = \gamma_0/\gamma_1$ while $\mathrm{Bo}_1 = \rho g a^2/(3\gamma_1)$.

In addition, the first bubble shape exhibits a flat border at the lower part whatever the surface tension ratio $\hat{\gamma}$ value. In contrast with the case of one bubble interacting with a free surface for $\mathrm{Bo}_1 = 1$, here, the first bubble is pushed by the second bubble to the free surface and the force created by the second bubble adds therefore with the buoyancy force. The obtained computed shapes for the first bubble at $\mathrm{Bo}_1 = 1$ exhibit thus similar trends with the final bubble shapes in the case of one bubble at larger Bond number of $\mathrm{Bo}_1 = 5$.

For smaller Bond number of $\mathrm{Bo}_1 = 0.3$ (see in lower Figure 7.8), the two bubbles are less deformed, the first bubble still presenting a curve lower part and the second bubble remains nearly spherical whatever the surface tension ratio $\hat{\gamma}$. The bubble velocity sensitivity to $\hat{\gamma}$ is also observed, however opposing the case of $\mathrm{Bo}_1 = 1$, for small $\hat{\gamma}$ value ($\hat{\gamma} = 0.2$) at final time t_f, the two bubbles are closer to the initial position than at larger $\hat{\gamma} = 1$ value. Moreover, the distance between the first bubble and the second one remains the initial t_0 gap at $\hat{\gamma} = 0.2$. In fact, at small $\hat{\gamma}$, i.e. small free surface tension γ_0, the free surface is strongly disturbed and resists weakly to the first bubble which rises farther without being blocked. The two bubbles are still rising with the same initial velocity and therefore the initial gap between these two bubbles remains constant.

For large $\hat{\gamma}$ value ($\hat{\gamma} = 5$), the first bubble is stopped sooner by the free surface than at $\hat{\gamma} = 1$ and $\hat{\gamma} = 0.2$. Moreover, the initial distance between the two bubbles at final time t_f is slightly reduced compared to the surface tension value $\hat{\gamma} = 0.2$ and is similar to the one at $\hat{\gamma} = 1$. Since the surface tension force dominates the gravity force at $\mathrm{Bo}_1 = 0.3$, the free surface resistance variation therefore governs the bubble and free surface shapes behaviors.

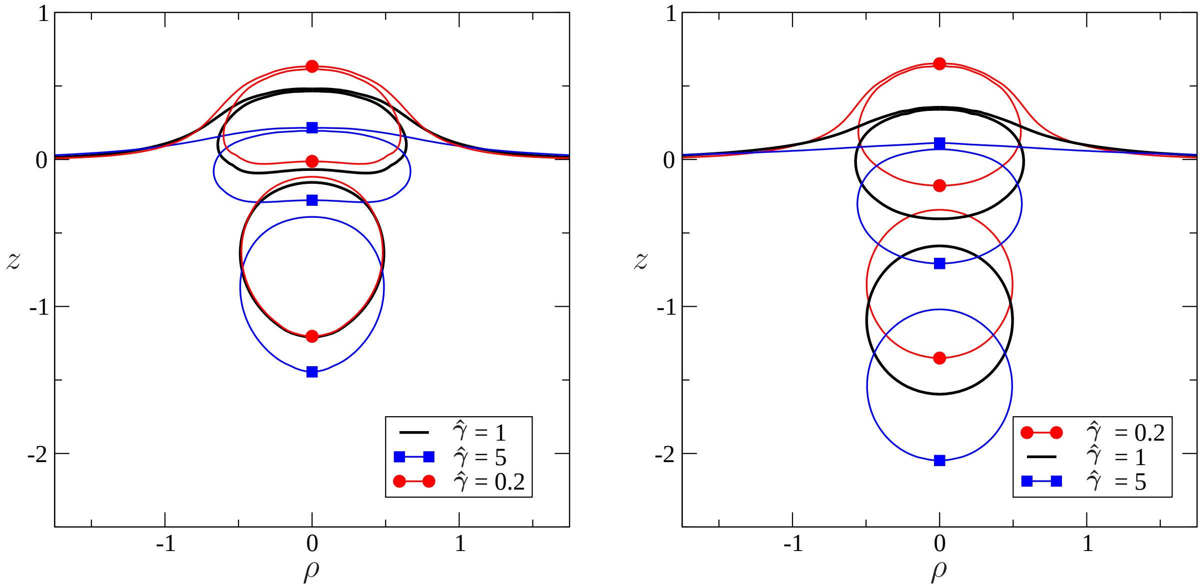

(a) Case $\mathrm{Bo}_1 = 1$ (b) Case $\mathrm{Bo}_1 = 0.3$

Figure 7.9: Compared bubbles "final" shapes obtained at normalized time t_f for $\hat{\gamma} = 0.2, 1, 5$. (a) Case $\mathrm{Bo}_1 = 1$. (b) Case $\mathrm{Bo}_1 = 0.3$.

Some computed shapes displayed at the same time t_f have not reached yet their "final" shapes. Then, the "final" computed shapes (plotted here for different final time t_f) are compared in Figure 7.9 for the three surface tension ratio values $\hat{\gamma} = 0.2, 1$ and 5 in the case of $\mathrm{Bo}_1 = 1$ with the case of $\mathrm{Bo}_1 = 0.3$. The final gap between the two bubbles is smaller for larger Bond number of $\mathrm{Bo}_1 = 1$. Moreover, at $\mathrm{Bo}_1 = 0.3$, the final gap between the two bubbles reduces with $\hat{\gamma}$. These last results are indeed obtained at different “final” time with different film thickness value as illustrated in Figure 7.6 at $\mathrm{Bo}_1 = 0.3$ and by extrapolating the curves for $\hat{\gamma} = 5$ in this latter Figure 7.6, the same value of h_2 may be reached sooner than for $\hat{\gamma} = 1$ and $\hat{\gamma} = 0.2$ since the film thinning rate increases with $\hat{\gamma}$.

Furthermore, the contact area is clearly sensitive to the surface tension ratio $\hat{\gamma}$ for both Bond number and suggests that the relation between the thinning rate and the contact area described in Chapter 3 (see §3.2) may be extend for the case of two bubbles.

7.1.3 Two bubbles different in size or in surface tension

Since our numerical BEM Code allows us to also consider bubbles of unequal surface tensions or sizes, we present in this section few results obtained for two bubbles different in size or surface tensions.

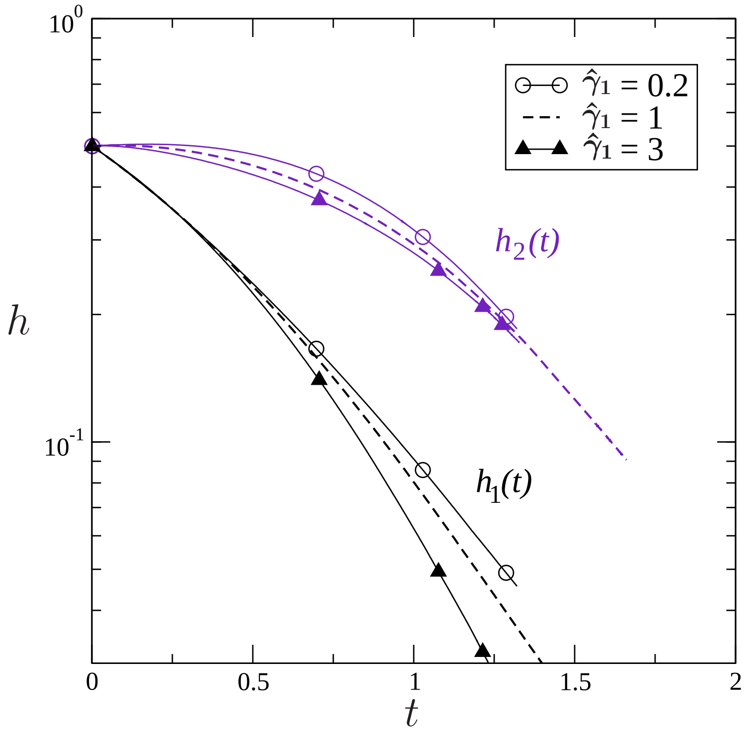

Figure 7.10: Normalized film thicknesses $h_1(t)$ (blue line) and $h_2(t)$ (indigo line) time evolution at $\mathrm{Bo}_2 = 1$ for the two equal bubbles with not-necessarily equal surface tensions: $\gamma_2 = 1$ and $\hat{\gamma}_1 = 0.2, 1, 3$.

First, the case of two equal bubbles with different surface tensions is addressed using the same mesh as for the previously shown cases. For this case, the lowest bubble and the free surface have the same surface tension, i.e $\gamma_0 = \gamma_2$, whereas the closest bubble surface tension is changing. A new surface tension ratio is then introduced

$$\hat{\gamma}_1 = \frac{\gamma_1}{\gamma_2} \tag{7.2}$$

Figure 7.10 displays the time-dependent film thickness $h_1(t)$ (blue line) and $h_2(t)$ (indigo line) at $\mathrm{Bo}_2 = \rho_l g a^2/(3\gamma_2) = 1$ (here based on the lowest bubble) for different surface tensions ratio $\hat{\gamma}_1 = 0.2, 1,\ 3$. Note that the Bond number $\mathrm{Bo}_0 = \mathrm{Bo}_2$ since $\gamma_0 = \gamma_2$.

The change of $\hat{\gamma}_1$ affects both the liquid film $h_1(t)$ and $h_2(t)$. For large surface tension $\hat{\gamma}_1 = 3$, the film drainage dynamics of $h_1(t)$ is enhanced while the film thickness $h_2(t)$ evolves slower although its drainage dynamics takes place earlier. At small surface tension $\hat{\gamma}_1 = 0.2$, the liquid film $h_1(t)$ drains slower while the film drainage dynamics of $h_2(t)$ remains the same when compared to the case of $\hat{\gamma}_1 = 1$.

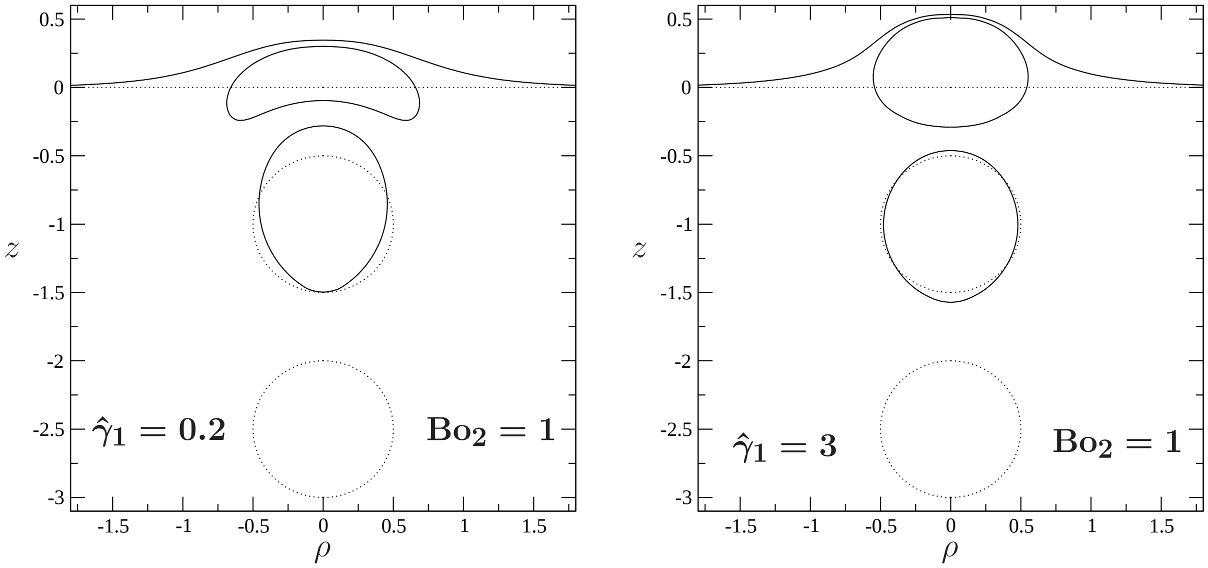

Figure 7.11: Computed bubbles (having the initial same size) and free surface shapes at normalized times $t_0 = 0$ (dashed lines) and final time $t_f = 1.327$ for $\mathrm{Bo}_2 = 1$ and $\hat{\gamma}_1 = 0.2, 3$.

The corresponding computed shapes at normalized initial time t_0 (dashed line) and "final" time $t_f = 1.327$ (solid line) are given in Figure 7.11 at $\mathrm{Bo}_2 = 1$ and for $\hat{\gamma}_1 = 0.2$ and 3. Clearly, the lower bubble shape is weakly sensitive to the change of surface tension $\hat{\gamma}_1$. Not surprisingly, the free surface and the upper bubble shapes are very different (at the same time t_f) for $\hat{\gamma}_1 = 0.2$ and $\hat{\gamma}_1 = 3$. For $\hat{\gamma}_1 = 3$ (case of a weakly disturbed upper bubble) the free surface is deeply affected and the liquid film between the upper bubble and the free surface, $h_1(t)$, is very thin. The drainage dynamics of the liquid film $h_1(t)$ is then enhanced.

For $\hat{\gamma}_1 = 0.2$, the upper bubble is easy to deform due to its interaction with both the free surface and the lower bubble. It is actually so much squeezed than it adopt the considered lens shape. The free surface is less affected by the upper bubble action and the liquid film $h_1(t)$ evolves then slowly. Moreover, as the upper bubble deforms by expanding away from the $(z'Oz)$ axis, the lower bubble catches up the upper bubble latter, which explains the decay of the liquid film drainage $h_2(t)$.

Now we turn to the interesting case of two unequal bubbles having identical surface tension $\gamma_1 = \gamma_2$. In that case, $\mathrm{Bo}_2 = \mathrm{Bo}_1$, and for further convenience, we will presently use Bo_1. The lower bubble has initial radius a while the upper one has initial radius $a/2$. We investigate the drainage dynamics of the liquid film $h_1(t)$ and $h_2(t)$ and the shapes sensitivity to both the surface tension ratio $\hat{\gamma} = \gamma_0/\gamma_1$ (at constant Bond number Bo_1)

and to the Bond number Bo_1 (for equal surface tension $\gamma_0 = \gamma_1 = \gamma_2$). The results are presented in Figure 7.12 and Figure 7.13.

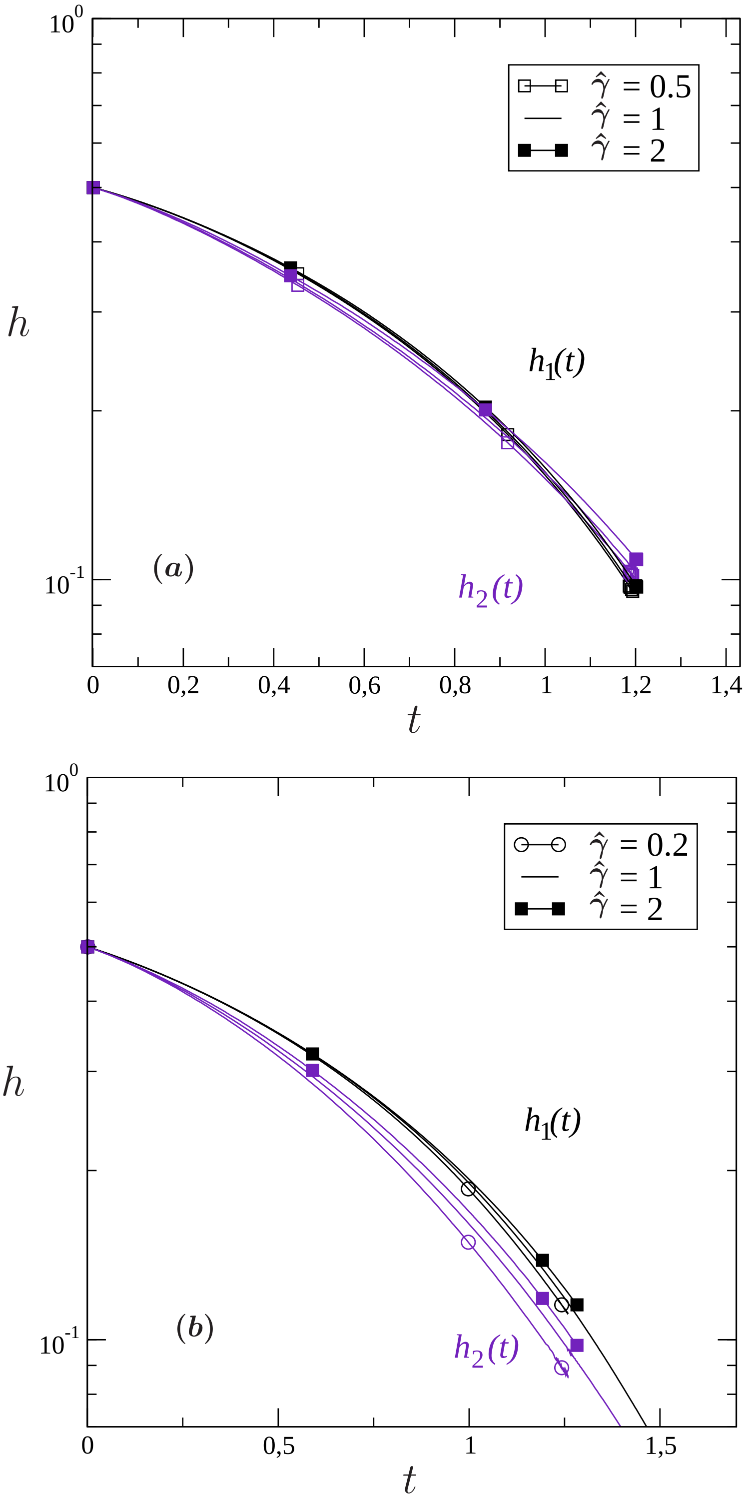

Figure 7.12: Normalized film thicknesses $h_1(t)$ (black solid line) and $h_2(t)$(indigo line) time evolution at $\hat{\gamma} = 0.5, 1, 2$ at $\mathrm{Bo}_1 = 0.5$ (a) and $\mathrm{Bo}_1 = 1$ (b) for two unequal bubbles $(a_1 = a/2,\ a_2 = a)$.

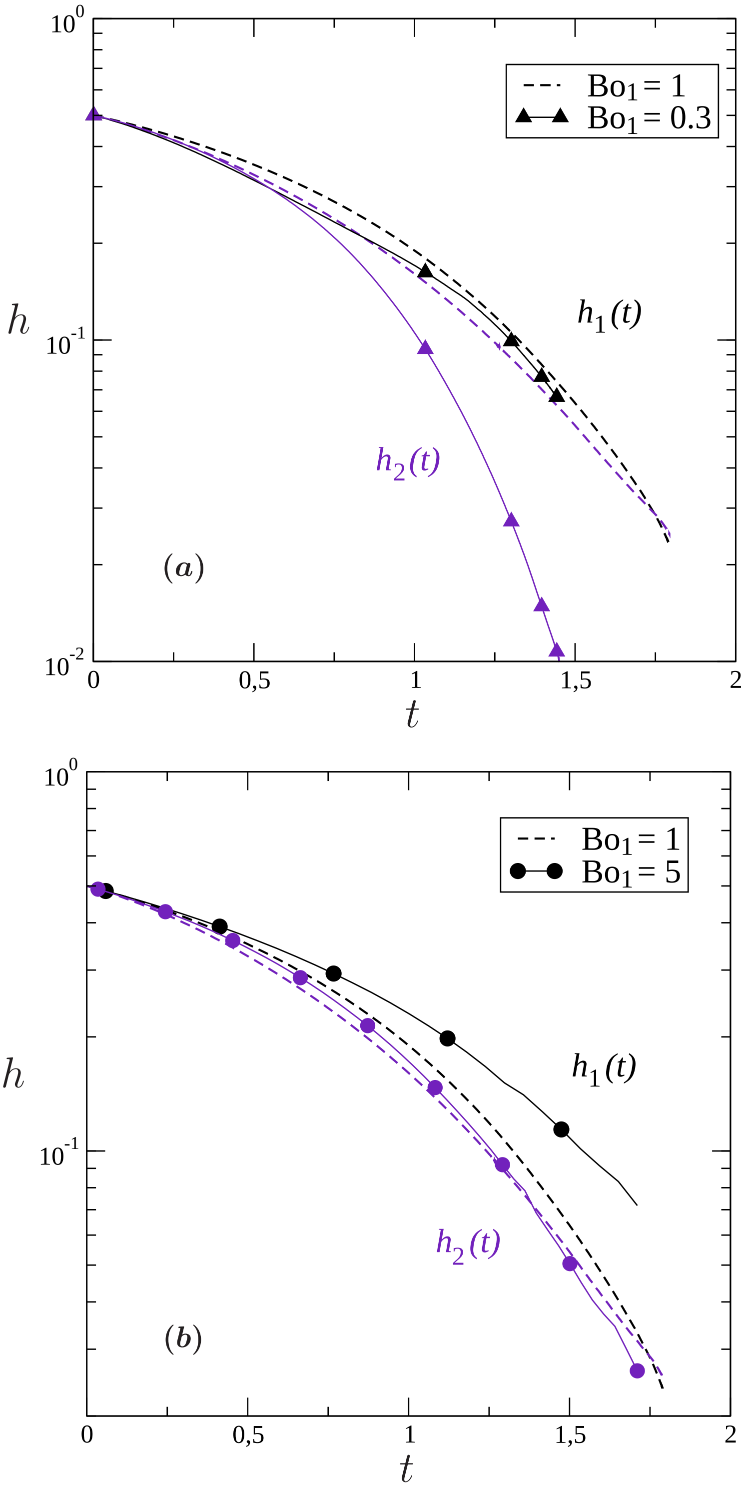

Figure 7.13: Normalized film thicknesses $h_1(t)$ (black solid line) and $h_2(t)$(indigo line) time evolution at $\hat{\gamma} = 1$ for $\mathrm{Bo}_1 = 0.3, 1$ (a) and $\mathrm{Bo}_1 = 1, 5$ (b) for two unequal bubbles $(a_1 = a/2,\ a_2 = a)$.

As seen in Figure 7.12, the drainage is more sensitive to $\hat{\gamma}$ at $\mathrm{Bo}_1 = 1$ than at $\mathrm{Bo}_1 = 0.5$. Moreover, note that the drainage dynamics of the liquid film $h_2(t)$ is more sensitive than the one for $h_1(t)$ at $\mathrm{Bo}_1 = 1$. In addition, at $\mathrm{Bo}_1 = 1$, the drainage dynamics of $h_2(t)$ takes place earlier than for $h_1(t)$. The lower bubble, being bigger than the upper bubble, rises then faster toward the small one and consequently, the liquid film $h_2(t)$ start to drain at once.

For $\gamma_0 = \gamma_1 = \gamma_2$, a strong change in the behaviors of $h_1(t)$ and $h_2(t)$ is observed in Figure 7.13 as Bo_1 drops from 5 to 0.3. At $\mathrm{Bo}_1 = 5$, $h_1(t)$ is the most affected while at $\mathrm{Bo}_1 = 0.3$ this is the case of $h_2(t)$. At small Bond number $\mathrm{Bo}_1 = 0.3$, each bubble and free surface shape is weakly disturbed and the upper bubble is strongly slowed down by the resisting free surface while the lower bubble keeps pushing up. The liquid film of thickness $h_2(t)$ decreases then faster.

In contrast, at large Bond number $\mathrm{Bo}_1 = 5$, the free surface is deeply affected by the cluster action and the upper bubble keeps rising. The gap h_2 between the two bubbles remains then nearly constant compared to $\mathrm{Bo}_1 = 1$. In addition, since the free surface deforms as the upper bubble approaches, the thickness h_1 decreases then slower than for the cases at $\mathrm{Bo}_1 = 1$.

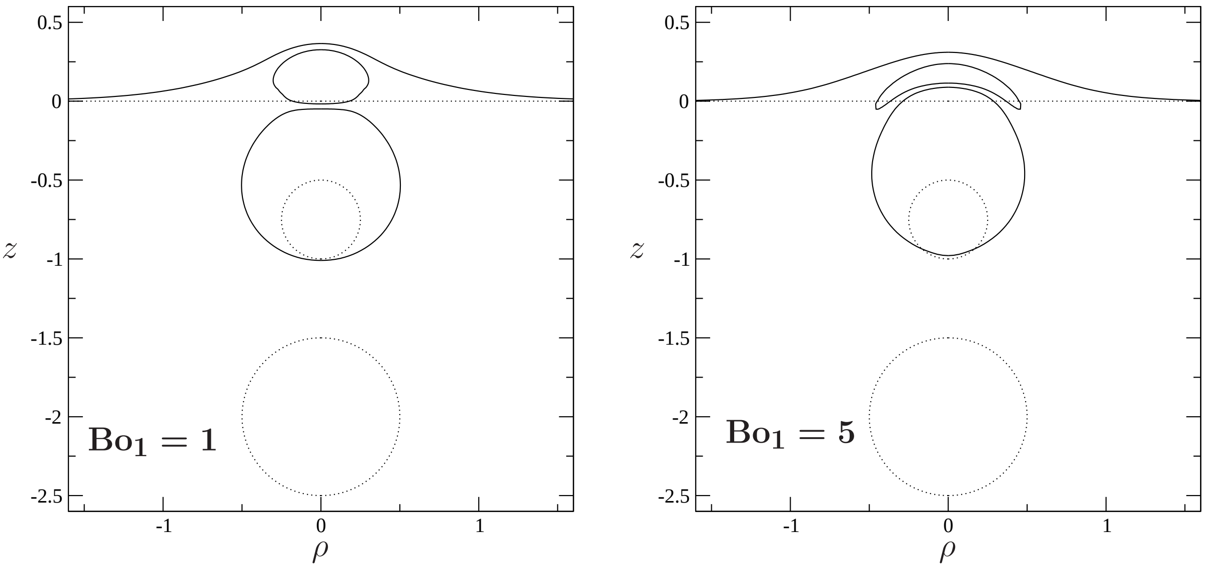

Figure 7.14: Computed bubbles and free surface shapes at normalized times $t_0 = 0$ (dashed lines) and final time $t_f = 1.71$ for $\hat{\gamma} = 1$ at $\mathrm{Bo}_1 = 5$ and $\mathrm{Bo}_1 = 1$.

The corresponding shapes of Figure 7.13 (b) at normalized time $t_f = 1.71$ are depicted in Figure 7.14. The biggest bubble has a buoyancy force four times larger than the one of the smallest bubble. The lowest bubble therefore pushes strongly the smallest bubble toward the free surface. Moreover, increasing Bo_1 (i.e. increasing the gravity since the surface tension is constant) result in increase of this force exerted by the large bubble on the small one. As a result, the small bubble is more squeezed between the free surface and the big bubble at $\mathrm{Bo}_1 = 5$ than at $\mathrm{Bo}_1 = 1$.

7.2 Cluster involving at least one solid body

In this section, we present numerical results for clusters made of one bubble and solid sphere(s) $\mathcal{P}_n$ with density ρ_n. Here we select $\rho_n/\rho_l = 0.94$, a typical density of unmolten silicate observed in the molten glass.

7.2.1 Bubble-sphere cluster

We further present numerical results for a solid sphere with uniform density ρ_n and radius a_s interacting with a bubble and a free surface of identical surface tensions $\gamma_1 = \gamma_0$.

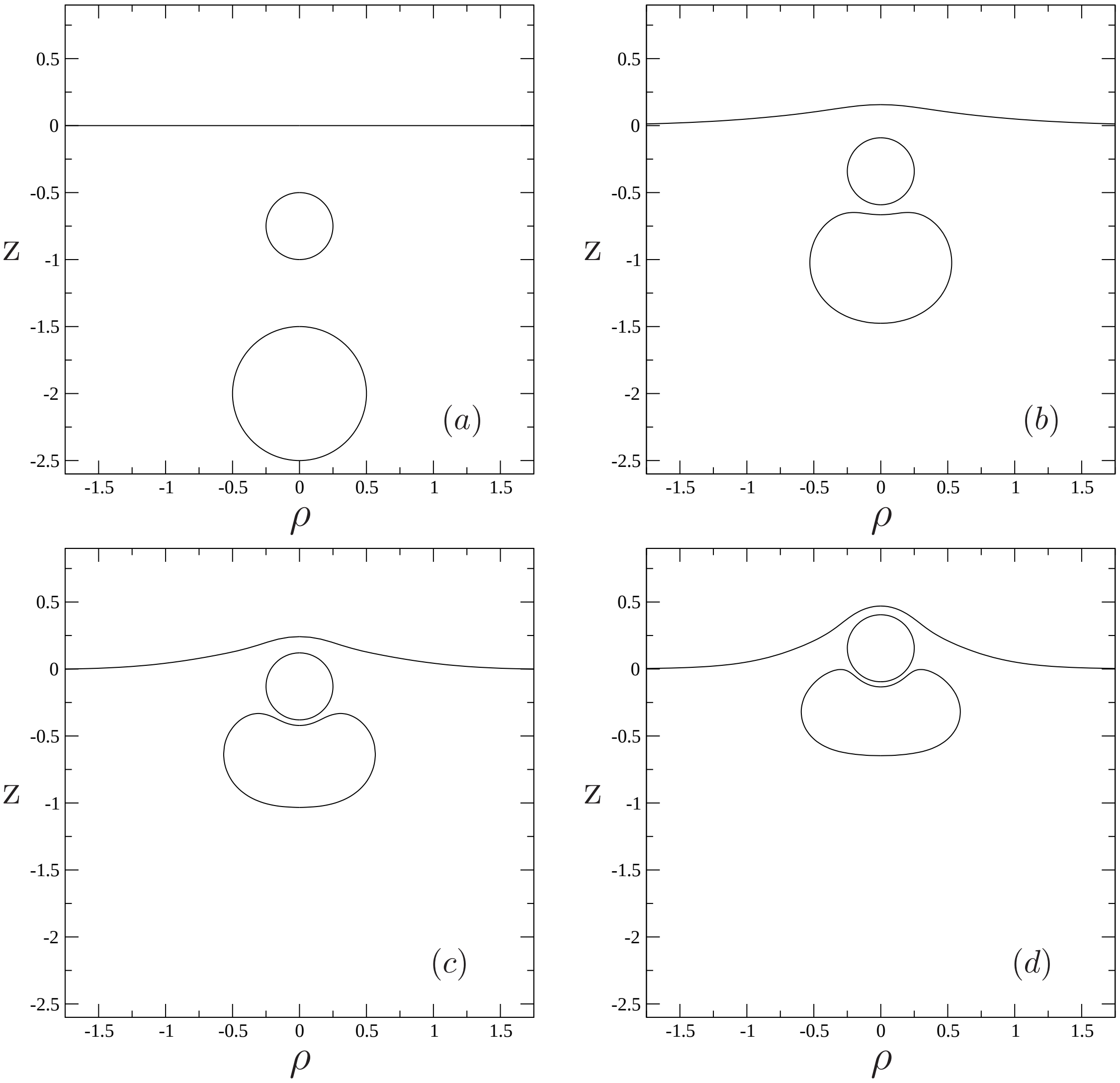

Figure 7.15: Computed free surface, bubble and solid sphere locations and shapes for $\mathrm{Bo}_1 = 2$ at different normalized times: $\bar{t} = 0\,(a), \bar{t} = 0.120\,(b), \bar{t} = 1.90\,(c)$ and $\bar{t} = 2.72\,(d)$.

Moreover, as it appears in liquid glass, the sphere is neutrally buoyant with $\rho_1 = \rho_n/\rho_l = 0.94$ (a value encountered in glass process).

When distant from the sphere and the free surface the bubble $\mathcal{B}$ is spherical with radius a and migrates at the velocity $V\mathbf{e}_3$ (the one obtained in an unbounded liquid) given by $V = \rho g a^2/(3\mu)$. Note that because its volume is preserved as time evolves, $\mathcal{B}$ has length scale a.

Henceforth, we take $2a$ and $2a/V$ as length and time scales, respectively. Therefore, the normalized time $\bar{t}$ is $\bar{t} = (\rho_l g a\, t)/(6\mu)$. Finally, the Bond number Bo_1 which compares at the bubble surface the "gravity" term $\rho \mathbf{g}.\mathbf{x}$ with the capillary "term" $\gamma_1 \boldsymbol{\nabla}_S \cdot \mathbf{n}$ is here defined as $\mathrm{Bo}_1 = \rho g a^2/(3\gamma_1)$.

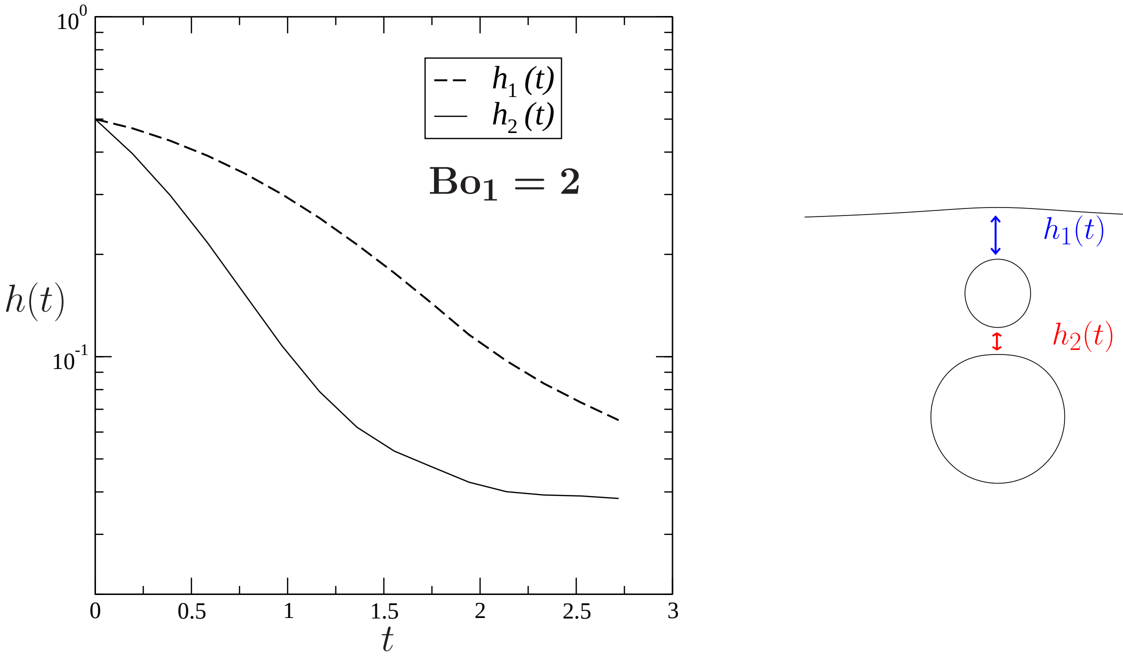

Figure 7.16: Film thickness evolution in time of $h_1(t)$ (dashed line) and $h_2(t)$ (solid line) at $\mathrm{Bo}_1 = 2$, $\gamma_1 = \gamma_0$ with the typical solid sphere density $\rho_1 = 0.94$ in molten glass.

Let us first take $a_s = a/2$ and $\mathrm{Bo} = 2$ and put at initial time $\bar{t} = 0$ the solid sphere between the spherical bubble and the undisturbed free surface, the initial gaps between the sphere and each other surface being equal to a.

As seen in Figure 7.15, two different regimes are found as time evolves. In a first "fast" regime the bubble ascends faster than the solid sphere and the sphere-bubble gap therefore decreases faster than the gap between the sphere and the free surface whereas the free surface is weakly deformed (compare Figure 2(a) with Figure 2(b)). In a second "slow" regime, illustrated in Figure 2(c) and Figure 2(d), the bubble and the sphere slowly migrate towards the free surface which now experiences a slight deformation due to the combined action of the sphere and the bubble. In this regime liquid films take place below and above the solid sphere with the film below being the thinner one.

The corresponding liquid film thickness $h_1(t)$ and $h_2(t)$ taking place between the solid sphere and the free surface and between the bubble and the solid sphere are depicted in Figure 7.16. As previously pointed out, the drainage dynamics of the film thickness $h_2(t)$ is faster than for $h_1(t)$ since the bubble rises faster than the solid sphere.

Moreover, at the final stage, $h_2(t)$ remains nearly constant while $h_1(t)$ keeps decreasing. The "fast" regime is then associated to the drainage dynamic of the film thickness $h_2(t)$ while $h_1(t)$ corresponds to the "slow" regime when the free surface is disturbed by the bubble-solid sphere cluster.

At the beginning, the thinning rate of $h_2(t)$ is $A \sim 1.21$ while the one for the liquid film $h_1(t)$ equals $A \sim 0.38$. The liquid film $h_2(t)$ then drains three times faster than $h_1(t)$. As soon as the bubble is stuck at the solid sphere, the drainage dynamic of $h_2(t)$ is slowed down and its associated thinning rate is small compared with the one of $h_1(t)$. Note that the two liquid films start to drain immediately.

Not surprisingly, the computed shapes in Figure 7.17 also depend upon the free-surface and bubble surface tensions $\gamma_1 = \gamma_0$. This is illustrated by plotting in this figure the obtained shapes for $\mathrm{Bo}_1 = 1, 2$ at different normalized times $\bar{t}$ starting with the same initial configuration.

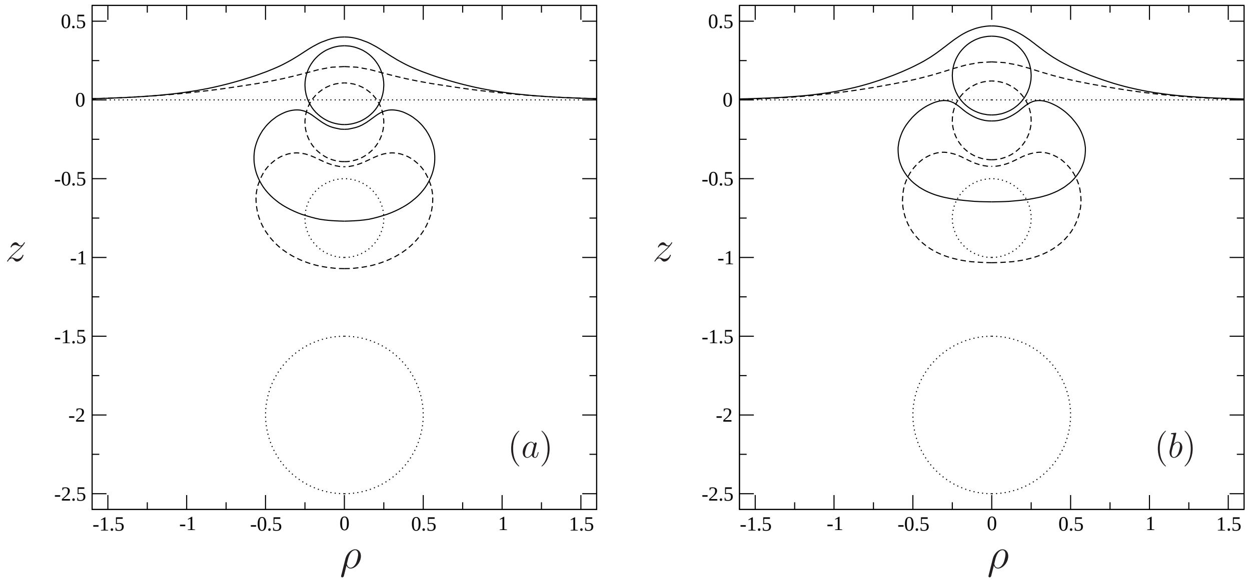

Figure 7.17: Compared shapes obtained at three different normalized times $\bar{t}_0 = 0, \bar{t}_1 = 1.19$ and $\bar{t}_2$ for $a_s = a/2$ at two different Bond numbers. (a) $\mathrm{Bo}_1 = 1$ and $\bar{t}_2 = 2.58$. (b) $\mathrm{Bo}_1 = 2$ and $\bar{t}_2 = 2.72$.

When the surface tension is weaker (case of $\mathrm{Bo}_1 = 1$ depicted in Figure 7.17 (a)) the bubble is less "flexible" and thus speeds up more the solid sphere (compare the sphere locations at time $\bar{t} = 1.20$ in Figure 7.17 (a) and Figure 7.17 (b)) during the previously-distinguished "fast" regime.

In addition, for this ratio $a_s = a/2$ the deformation of the free surface at $\bar{t} = 1.19$ appears to be larger for $\mathrm{Bo}_1 = 1$ than for $\mathrm{Bo}_1 = 2$ although the surface tension there is larger. Not surprisingly, during the second "slow" regime in which the drainage of both thin films really takes place the free surface deformation for $\mathrm{Bo}_1 = 2$ finally is more pronounced than for $\mathrm{Bo}_1 = 1$.

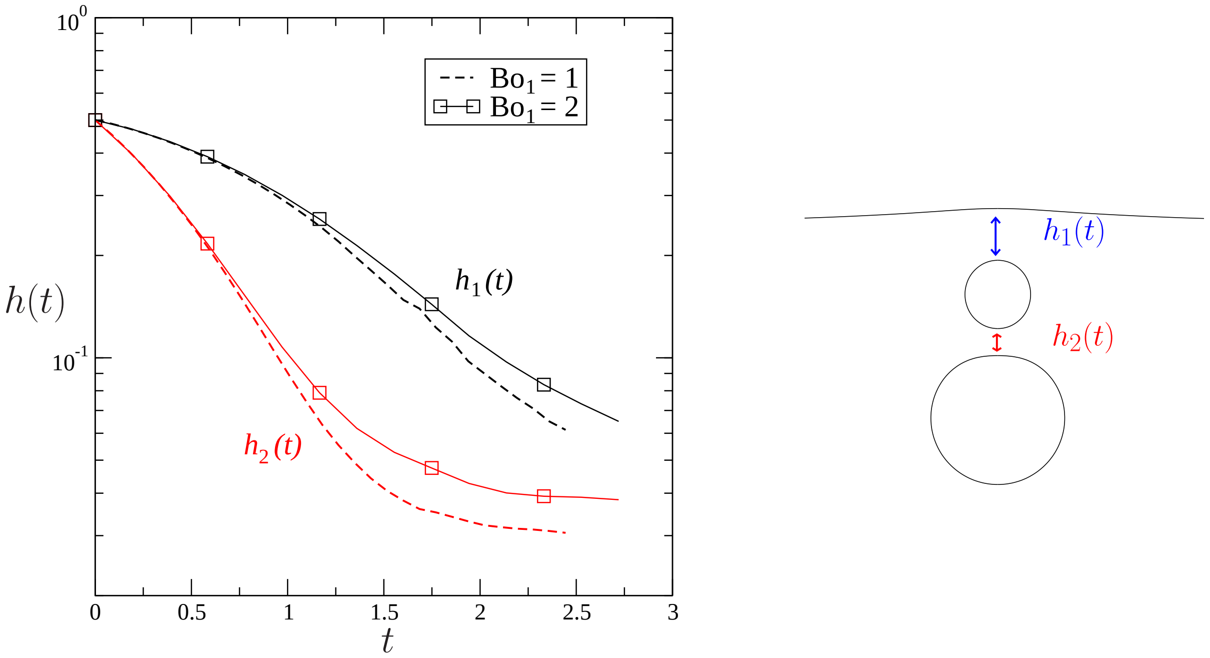

Figure 7.18: Film thickness evolution in time of $h_1(t)$ (dashed line) and $h_2(t)$ (solid line) at two Bond number $\mathrm{Bo}_1 = 2$ and $\mathrm{Bo}_1 = 1$, $\gamma_1 = \gamma_0$ with the typical solid sphere density $\rho_1 = 0.94$ in molten glass.

Figure 7.18 depicts the time-dependent film thickness $h_1(t)$ and $h_2(t)$ corresponding to the previous shapes in Figure 7.17. At the beginning, both $h_1(t)$ and $h_2(t)$ are unaffected by the change of Bond number. At a certain time $\bar{t} \sim 0.6$, $h_1(t)$ and $h_2(t)$ start to differ as the Bond number is changing. Indeed, as the Bond number decreases the drainage dynamics of $h_1(t)$ and $h_2(t)$ are enhanced.

In absence of sphere one would obtain (see [1]) a larger deformation of the free surface at each normalized time $\bar{t}$ for $\mathrm{Bo}_1 = 2$. This actually also occurs when the sphere is sufficiently small compared with the bubble. We illustrate this behaviour in Figure 7.19 for the case for $a_s = a/4$. In both $\mathrm{Bo}_1 = 1$ and 2, both the bubble and the free surface are strongly disturbed. Nevertheless, since the bubble at $\mathrm{Bo}_1 = 2$ has a larger buoyancy force than the one at $\mathrm{Bo}_1 = 1$, the cluster made of this bubble and the solid sphere exerts a larger force on the free surface which, therefore, is slightly more affected than at $\mathrm{Bo}_1 = 1$.

Comparisons for the film thickness $h_1(t)$ and $h_2(t)$ for a cluster made of one bubble and one solid sphere with size $a_s = a/2$ and with size $a_s = a/4$ have been made and displayed in Figure 7.20. At small time, the film thickness $h_1(t)$ and $h_2(t)$ remain unaffected by the solid sphere size.

When the cluster approaches the free surface, both $h_1(t)$ and $h_2(t)$ start to differs as the size of the solid sphere changes. Indeed, the drainage dynamics of the liquid films $h_1(t)$ and $h_2(t)$ is enhanced when the solid sphere is small. In addition, the liquid film $h_2(t)$ exhibits a thinner “final” thickness when the solid sphere is with $a_s = a/4$.

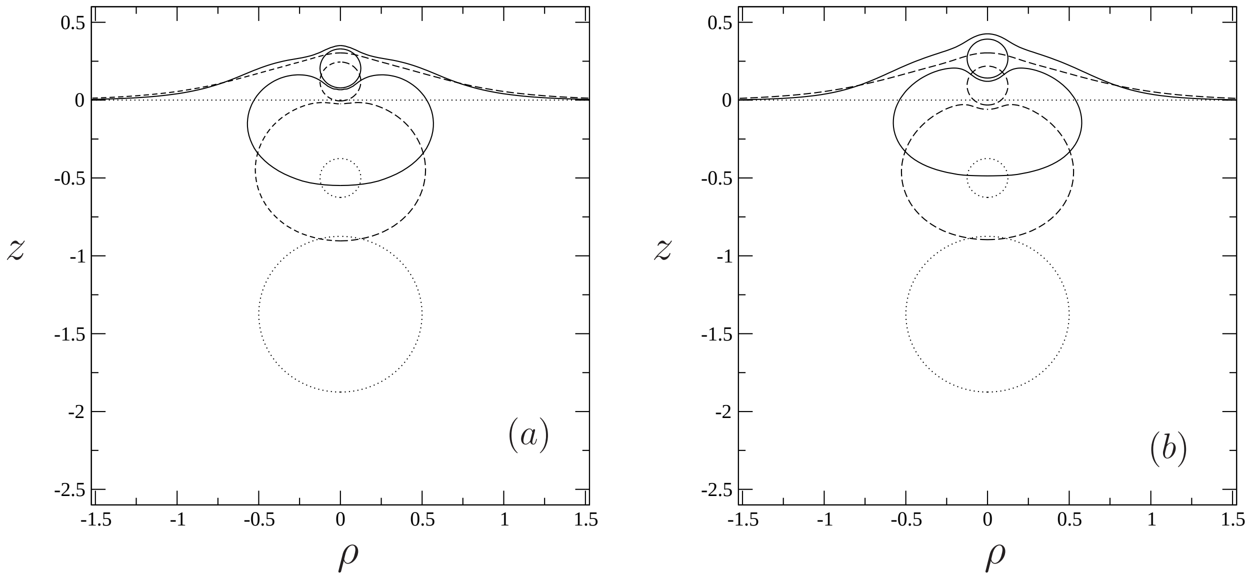

Figure 7.19: Compared shapes obtained at three different normalized times $\bar{t} = 0, \bar{t} = 1.19$ and $\bar{t} = 2.03$ for $a_s = a/4$ at two different Bond numbers. (a) $\text{Bo}_1 = 1$. (b) $\text{Bo}_1 = 2$.

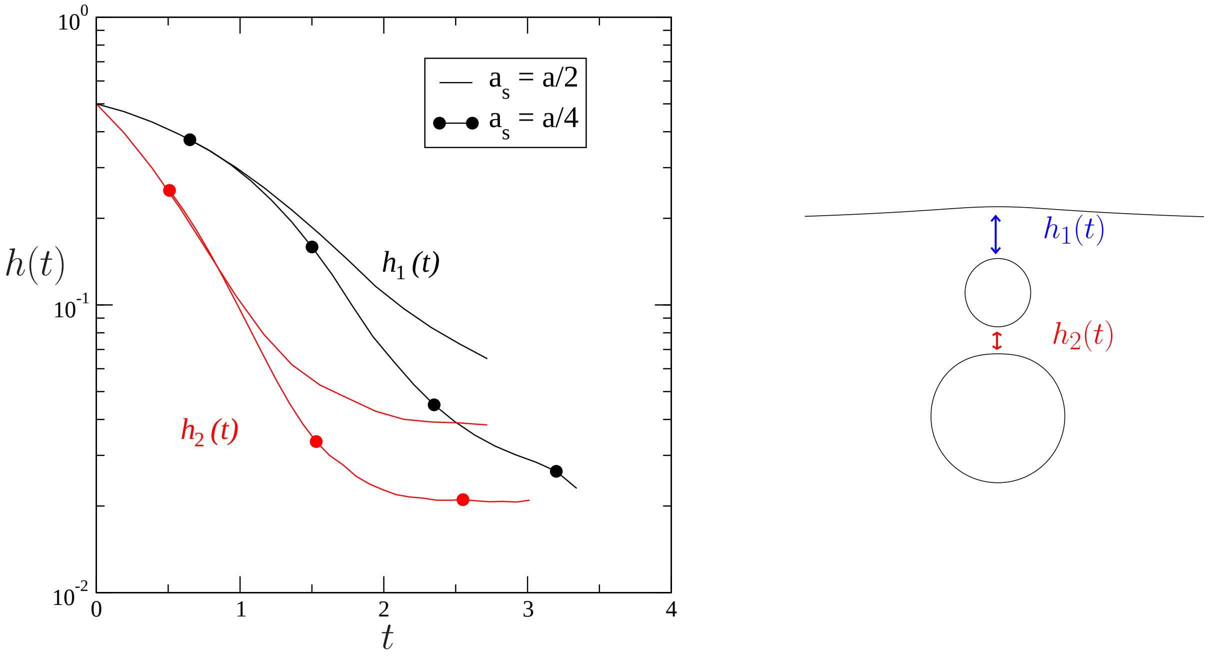

Figure 7.20: Film thickness in time of $h_1(t)$ (black curve) and $h_2(t)$ (red curve) at $\text{Bo}_1 = 2$ for two different solid sphere size: $a_s = a/2$ (solid line) and $a_s = a/4$ (filled circles).

As also observed in Figure 7.19, the bubble moves closer to the small sphere with radius $a_s = a/4$ than to the twice bigger sphere. Indeed, when the solid sphere is big, the contact area where the film drainage is taking place is larger which implies that the lubrication force distribution exerted on the liquid film is larger and therefore the film drains slower.

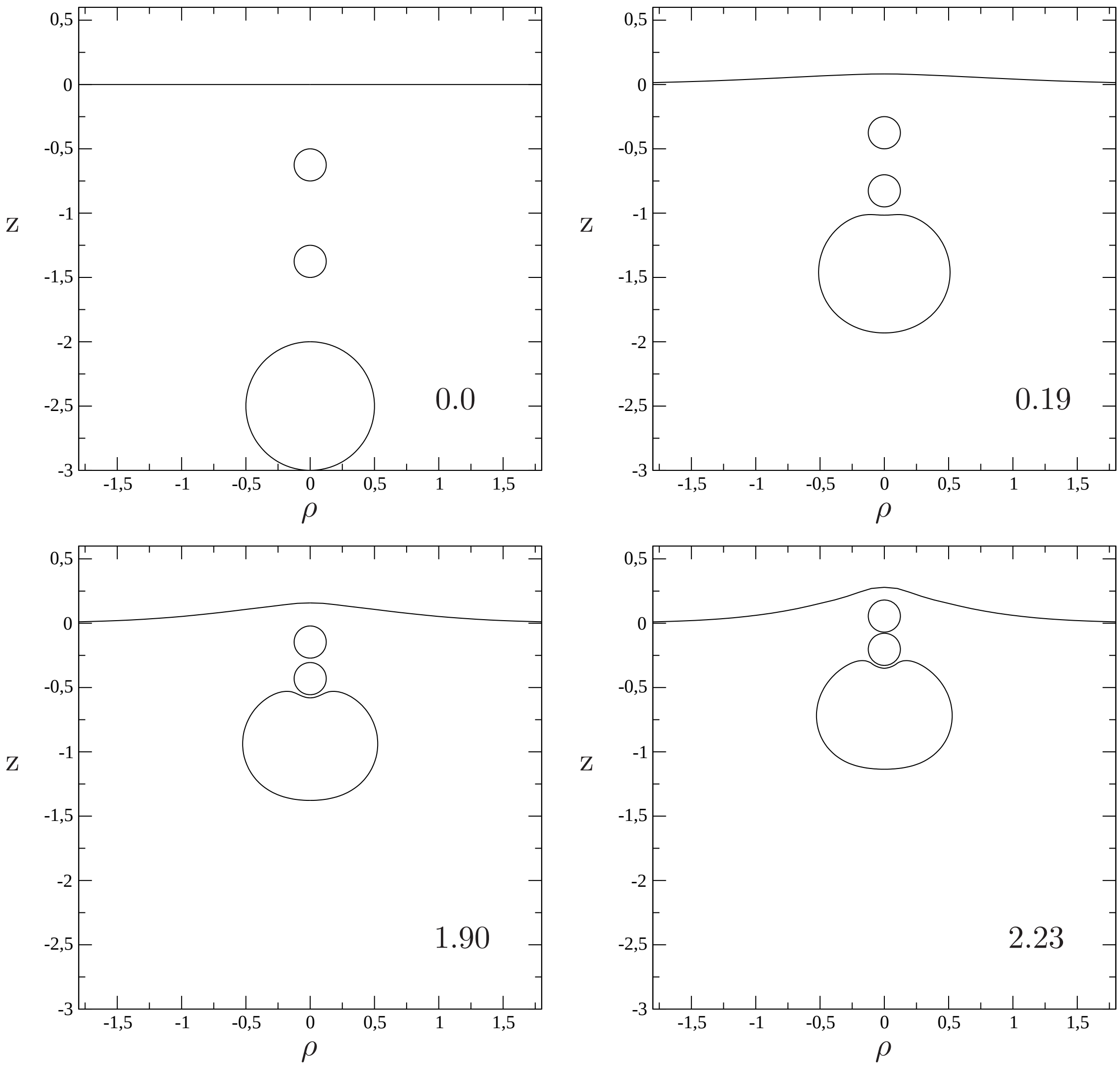

Figure 7.21: Compared shapes obtained at four different normalized times $\bar{t} = 0$, $\bar{t} = 1.19$, $\bar{t} = 1.90$ and $\bar{t} = 2.23$ for a bubble and two solid sphere with size $a_s = a/4$ near a free surface at $\mathrm{Bo}_1 = 2$.

The case of two small solid spheres between a bubble and a free surface has been also addressed. Figure 7.21 displays the obtained shapes at $\mathrm{Bo}_1 = 2$ for two equal spheres with radius $a_s = a/4$ and density $\rho_1/\rho_l = \rho_2/\rho_l = 0.94$ pushed by a bubble toward a free surface. The big bubble rises faster than the solid sphere and then catches up quickly with the two spheres. Then the bubble interacts with the solid spheres and encounters deformation. Finally, the cluster made of the bubble and the two solid spheres moves together toward the free surface which is weakly disturbed in this case. The bubble is indeed slowed down by the additional solid sphere and therefore the cluster is still far from the free surface.

Figure 7.22 depicts the film thickness $h_1(t)$ sensitivity to the number of solid spheres between the bubble and the free surface at $\mathrm{Bo}_1 = 1$. Clearly, as the number of solid spheres increases, the thinning rate decreases and therefore the drainage dynamics of the liquid film $h_1(t)$ is slowed down. The difference is especially large when comparing the case of one bubble near a free surface and one bubble and a solid sphere near a free surface. The solid sphere induces a screening effect on the bubble-free surface interaction.

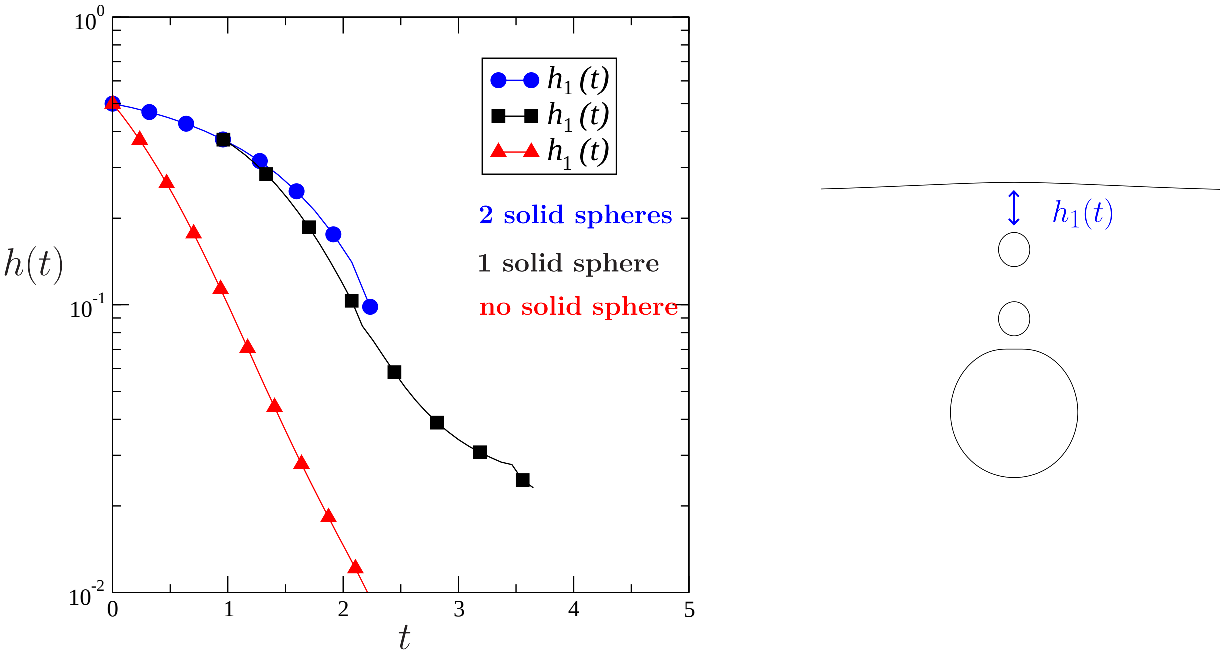

Figure 7.22: Film thickness evolution in time of $h_1(t)$ at $\mathrm{Bo}_1 = 1$. Comparing the three cases, one bubble only (red curve), bubble-solid sphere cluster (black curve) and a cluster made of one bubble and two solid sphere (blue curve).

7.3 Conclusion

The case of two particles (bubble(s) and/or solid body(ies)) rising toward a free surface has been examined depending on the surface tension and the Bond number. In the case of two equal bubbles having the same surface tension, the film drainage taking place between the upper bubble and the free surface exhibits a similar behavior to the case of one bubble interacting with a free surface. This film is mostly affected by the change of surface tension at small Bond number and the drainage dynamics of the liquid film is enhanced as the surface tension increases. A second liquid film, occurring later between the two bubbles, is deeply sensitive to the surface tension ratio and also the Bond number. As the surface tension increases, this film drainage is enhanced. Moreover, as the Bond number increases, the film drains faster. This liquid film is indeed more dependent on the gravity force than the upper bubble-free surface interaction. The lower bubble is thus less sensitive to the change of surface tension of the free surface due to its large distance.

Furthermore, by changing only the surface tension of the bubble, the liquid film h_1 is then sensitive to the surface tension ratio. When the upper bubble is half the size of the lower bubble, the two liquid films occur at the same time and exhibit a similar behavior. The film drainage h_2 is still slightly more affected by the change of surface tension ratio. However, their behavior differ as the Bond number changes. At small Bond number, the liquid film between the two bubbles is enhanced whereas at large Bond number, the film drainage taking place between the upper bubble and the free surface is then faster.

In the case of clusters made of a bubble and solid sphere(s), the no-slip boundary condition at the solid sphere(s) surface induces a different behavior for the liquid film h_1.

In this case, the liquid film between the bubble and a neutrally buoyant solid sphere drains faster than the one occurring between the solid body and the free surface. These two rising regimes are due to the fast rising of the bubble at the beginning which get stuck below the solid sphere, then the bubble and the solid body rise slowly together to the free surface.

As the Bond number increases, the two liquid films drain slower. When the solid sphere is reduced by half its size, the film drainage is enhanced for both h_1 and h_2. Finally, when the number of solid bodies is increased of one unit, the film drainage taking place between the solid particle and the free surface is slower.

Bibliography

[1] G. Debrégeas, P.-G. de Gennes, and F. Brochard-Wyart. The life and death of “bare” viscous bubbles. *Science*, 279:1704–1707, 1998.

[2] F. Pigeonneau and A. Sellier. Low-Reynolds-Number gravity-driven migration and deformation of bubbles near a free surface. *Phys. Fluids*, 23:092302, 2011.

Conclusion

Devoted to the interaction of bubbles or and solid particles with a free surface, this Ph. D. work carried out numerical and analytical predictions. With the glass melting in mind, the framework is limited to creeping flows.

The first part has been dedicated to a numerical and an asymptotic analysis of a bubble near a free surface in 2d-axisymmetric configuration. A BEM code has been developed and tested to performed the numerical analysis.

Firstly, the case of a bubble interacting with a free surface with unequal but uniform surface tensions has been numerically investigated. Two dimensionless numbers are involved: i) the Bond number corresponding to the ratio of the gravity to surface tension forces and ii) the ratio of the two surface tensions of the free surface and bubble interface. The numerical computations have been achieved for a large range of Bond number and surface tension ratio. Two phenomena have been investigated i) the film drainage taking place between the bubble and the free surface interfaces and ii) the time-dependent interface shapes.

At small Bond number, the interface shapes and the film drainage dynamics exhibit a strong sensitivity to the surface tension ratio. When the surface tension ratio is smaller than unity, the free surface is strongly disturbed whereas the bubble remains quasi-spherical and then, the film drainage dynamics is slow. In contrast, at large surface tension ratio, the free surface strongly resists to the bubble action and the film drainage dynamics is enhanced. Moreover, using a relation between the contact area of the film and its thinning rate [3], the results obtained with a model based on the static bubble shape following Princen and Mason [4] (the bubble and the free surface are in contact with a liquid film without thickness) and with the numerical procedure have been compared and a good agreement have been found. We point out here the important effect of the free surface deformation in the drainage dynamics. The larger the free surface deformation, the slower the drainage dynamics. This result comes from that the pressure due to the buoyancy force is more spread when the free surface is strongly deformed reducing the film drainage dynamics. Conversely, at small deformation, i.e. small Bond number, the buoyancy pressure is applied on a narrow area giving a fast drainage.

Secondly, an asymptotic analysis at small Bond and capillary numbers has been developed and performed for a particle (solid sphere or bubble) near a free surface. The zeroth-order problem when the particle is spherical near a rigid flat free surface has been wholly solved employing the bipolar coordinates. The free surface shape has been sought using two methods. The former is an analytic solution using the zeroth-order component of the normal stress written in cylindrical coordinates whatever the particle location. By this way, we extend the previous work achieved by Berdan and Leal (1982) [1] limited to a particle location far away the interface. The latter method appeals to the bipolar coordinates, the free surface shape has been obtained and successfully compared to former method using the cylindrical coordinates. Moreover, the free surface shapes obtained with these asymptotic methods have been compared with the computed one for different surface tension ratios and a suitable agreement has been shown. Furthermore, free surface shapes have been determined employing the asymptotic analysis at small Bond number for three different bubble locations. Finally, an analytical solution for the bubble shape has been established and compared to the computed ones at relatively small Bond number.

In a second part of this thesis, the dynamic of bubble(s) and/or solid sphere(s) has been numerically investigated in 2d-axisymmetric configuration.

The previous numerical analysis has been extended to the study of two bubbles interacting with a free surface. First, the case of two bubbles having identical size and surface tension has been investigated for a large range of Bond number and surface tension ratio. Two liquid films are examined, a first one occurring between the first bubble and the free surface and a second liquid film taking place between the two bubbles. The film drainage is enhanced when adding one bubble, in particular at small Bond number. A similar behavior for the first drainage in case of two bubbles with the one obtained for one bubble has been observed. In contrast, the second drainage, which takes place later than the first one, has shown a strong sensitivity to the change of surface tension even for moderate Bond number. In addition, the second bubble shape is weakly sensitive to the surface tension ratio whereas the first bubble shape deformation increases with the surface tension ratio whatever the Bond number.

Furthermore, the dynamic of one bubble and solid sphere(s) near a free surface has been carefully examined when the solid sphere(s) are pushed by the bubble toward the free surface.

First the case of a neutraly buoyant solid sphere that is pushed by a bubble twice in size has been considered. Two rising regimes have been identified: at the beginning, the bubble rises quickly and catches up the solid sphere, then the cluster made of the bubble and the solid sphere slowly moves toward the free surface. The film drainage h_1 taking place between the solid sphere and the free surface decays slowly compared with the one h_2 occurring between the bubble and the solid sphere. Moreover, keeping the same configuration, the sensitivity of the film drainage h_1 to the Bond number has been shown. When the size of the particle decreases, the film drainage h_1 is enhanced. By adding a second solid sphere between the bubble and the free surface, the film drainage dynamics of h_1 is slower than in the previous configuration.

In summary, the introduction of small particles between a rising bubble and the free surface induces a strong effect on the drainage dynamics. Consequently, bubbles are stuck due to the presence of particles which is qualitatively in agreement with observations (see Chapter 6 in [2]).

An asymptotic analysis has been developed for a bubble at a given location using the zeroth-order flow and associated traction. Tracking in time the interface can be performed with this zeroth-order quantities, however, the obtained solution will quickly differs from the real solution observed experimentally. The corrected force and velocity are therefore required to capture adequately the interface motion. Such a task can be achieved by appealing to the reciprocal theorem. Those first-order quantities can be expressed on the undisturbed interface and can then be calculated. Nevertheless, dealing with the bipolar coordinates is a non trivial task and since no result for a bubble is available for comparison purposes in the literature (at least to our very best knowledge) the main issue is to adequately test each velocity and normal components in order to obtain the corrected force and velocity and finally calculate the time-dependent film thickness. This film drainage will extend the ones obtained with the BEM code at small Bond number.

The restricted choice of 2d-axisymmetric configuration has been motivated for the case of one bubble where no instabilities appear and makes it simplier to obtain preliminary results in the case of several particles (bubbles or solid spheres). However, in reality bubble-bubble interaction induces instabilities which tend to shift the upper bubble away from the vertical axis due to the slip boundary condition on the bubble surface. A 3D configuration is therefore required to detect and further examine these behaviors. The main issue in a 3D numerical code using boundary-integral equations is to accurately calculate the mean curvature of each disturbed surface. Such a code will give a better understanding of the mixing in a glass furnaces.

Bibliography

[1] C. Berdan and L. G. Leal. Motion of a sphere in the presence of a deformation interface. I. Perturbation of the interface from flat: The effects on drag and torque. *J. Colloid Interface Sci.*, 87:62–80, 1982.

[2] J. Grynberg. *Mécanismes physiques et chimiques mis en jeu lors de la fusion du mélange SiO2-Na2CO3.* PhD thesis, Université Pierre et Marie Curie - Paris VI, 2012.

[3] H. Kočárková. *Stabilité des mousses de verre: Expériences à l'échelle d'une bulle ou d'un film vertical.* PhD thesis, Université Paris-Est, 2011.

[4] H. M. Princen and S.G. Mason. Shape of a fluid drop at a liquid-liquid interface. I. Extension and test of two-phase theory. *J. Colloid Interface Sci.*, 20(2):156–172, 1965.

Appendix A

Simple and double-layer operators in axisymmetric formulation

For $\mathbf{x}_0$ and $\mathbf{x}$ having cylindrical coordinates (r_0, z_0) and (r, z) respectively, one gets for the single-layer matrix $\mathbf{B}$ (recall ((2.1)) the following components [2]

$$\begin{aligned}
B_{zz}(\mathbf{x},\mathbf{x}_0) &= r\left(I_{10} + \hat{z}^2 I_{30}\right), &\text{(A.1)}\\
B_{zr}(\mathbf{x},\mathbf{x}_0) &= r\hat{z}\left(rI_{30} - r_0 I_{31}\right), &\text{(A.2)}\\
B_{rz}(\mathbf{x},\mathbf{x}_0) &= r\hat{z}\left(rI_{31} - r_0 I_{30}\right), &\text{(A.3)}\\
B_{rr}(\mathbf{x},\mathbf{x}_0) &= r\left[I_{11} + (r^2+r_0^2)I_{31} - r_0 r(I_{30}+I_{32})\right] &\text{(A.4)}
\end{aligned}$$

with $\hat{z} = z - z_0$ and, setting $\mathbf{n}(\mathbf{x}) = n_r\mathbf{e}_r + n_z\mathbf{e}_z$, the additionnal relations

$$\begin{aligned}
C_{zz}(\mathbf{x},\mathbf{x}_0) &= -6r\hat{z}^2\left[\hat{z}I_{50}n_z + (rI_{50} - r_0 I_{51})n_r\right], &\text{(A.5)}\\
C_{zr}(\mathbf{x},\mathbf{x}_0) &= -6r\hat{z}^2\left[(rI_{50} - r_0 I_{51})n_z + (r_0^2 I_{52} + r^2 I_{50} - 2rr_0 I_{51})n_r\right], &\text{(A.6)}\\
C_{rz}(\mathbf{x},\mathbf{x}_0) &= -6r\hat{z}^2\left\{(rI_{51} - r_0 I_{50})n_z + \left[(r^2+r_0^2)I_{51} - rr_0(I_{50}+I_{52})\right]n_r\right\}, &\text{(A.7)}\\
C_{rr}(\mathbf{x},\mathbf{x}_0) &= -6r\left\{\hat{z}[(r^2+r_0^2)I_{51} - rr_0(I_{50}+I_{52})]n_z\right.\\
&\quad \left.+[r^3 I_{51} - r_0^2 r(I_{50}+2I_{52}) + rr_0^2(I_{53}+2I_{51}) - r^3 I_{52}\right] n_r\Big\} &\text{(A.8)}
\end{aligned}$$

for the double-layer matrix $\mathbf{C}$ (recall ((2.1)). Moreover, the occuring quantities I_{mn} are defined as

$$I_{mn}(r, r_0, \hat{z}) = \frac{4k^m}{(4rr_0)^{m/2}}\int_0^{\pi/2}\frac{(2\cos^2\phi - 1)^n}{(1-k^2\cos^2\phi)^{m/2}}d\phi, \quad k^2 = \frac{4rr_0}{\hat{z}^2 + (r+r_0)^2}. \tag{A.9}$$

Actually, each term I_{mn} is obtained from the evaluation of the following complete elliptic integrals of the first and second kind

$$F(k) = \int_0^{\pi/2}\frac{d\phi}{(1-k^2\cos^2\phi)^{1/2}}, \qquad E(k) = \int_0^{\pi/2}(1-k^2\cos^2\phi)^{1/2}d\phi. \tag{A.10}$$

More precisely, one actually gets for the needed quantities I_{mn} involved in (A.5)-(A.8) the relations

$$
\begin{aligned}
I_{10} &= \frac{2k}{\sqrt{rr_0}} F(k), && \text{(A.11)}\\
I_{11} &= \frac{2}{k\sqrt{rr_0}} \left[(2-k^2)F(k) - 2E(k)\right], && \text{(A.12)}\\
I_{30} &= \frac{k^3}{2(rr_0)^{3/2}} \frac{E(k)}{1-k^2}, && \text{(A.13)}\\
I_{31} &= \frac{k}{2(rr_0)^{3/2}} \left[(2-k^2)\frac{E(k)}{1-k^2} - 2(1-k^2)F(k)\right], && \text{(A.14)}\\
I_{32} &= \frac{1}{2k(rr_0)^{3/2}} \left\{\left[\frac{(2-k^2)^2}{1-k^2} + 4\right] E(k) - 4(2-k^2)F(k)\right\}, && \text{(A.15)}\\
I_{50} &= \frac{k^5}{24(rr_0)^{5/2}(1-k^2)^2} \left[2(2-k^2)E(k) - (1-k^2)F(k)\right], && \text{(A.16)}\\
I_{51} &= \frac{k^3}{24(rr_0)^{5/2}(1-k^2)^2} \left\{2\left[(2-k^2)^2 - 3(1-k^2)\right] E(k)\right.\\
&\qquad \left. -(2-k^2)(1-k^2)F(k)\right\}, && \text{(A.17)}\\
I_{52} &= \frac{k}{24(rr_0)^{5/2}(1-k^2)^2} \left\{2(2-k^2)\left[(2-k^2)^2 - 6(1-k^2)\right] E(k)\right.\\
&\qquad \left. - \left[12(1-k^2) - (2-k^2)^2(1-k^2)F(k)\right]\right\}, && \text{(A.18)}\\
I_{53} &= \frac{1}{24k(rr_0)^{5/2}(1-k^2)^2} \left\{2\left[(2-k^2)^4 - 9(2-k^2)^2\,(1-k^2)\right.\right.\\
&\qquad \left.\left. -12(1-k^2)\right] E(k) + (1-k^2)(2-k^2)\left[36(1-k^2) - (2-k^2)^2\right] F(k)\right\}, && \text{(A.19)}
\end{aligned}
$$

In practice, the required integrals $E(k)$ and $F(k)$ are accurately computed by appealing to a polynomial approximation (see [2]) of [1].

Bibliography

[1] M. Abramowitz and I. A. Stegun. *Handbook of mathematical functions.* Dover Publications, Inc., New York, 1965.

[2] C. Pozrikidis. *Boundary integral and singularity methods for linearized viscous flow.* Cambridge University Press, Cambridge, 1992.

Appendix B

Static shapes problem

Contents

B.1 Bubble-liquid interface equation

Consider a Newtonian liquid at rest with uniform pressure p. At the bubble-liquid interfaces, sketched in Figure B.1, the Laplace equation reads

$$p_b = p + 2H\gamma_1, \tag{B.1}$$

with p_b and γ_1 the bubble pressure and surface tension.

Expressing the mean curvature H in terms of the principal radii of curvature R_1 and R_2, on gets

$$p_b = p + \gamma_1 \left(\frac{1}{R_1} + \frac{1}{R_2} \right). \tag{B.2}$$

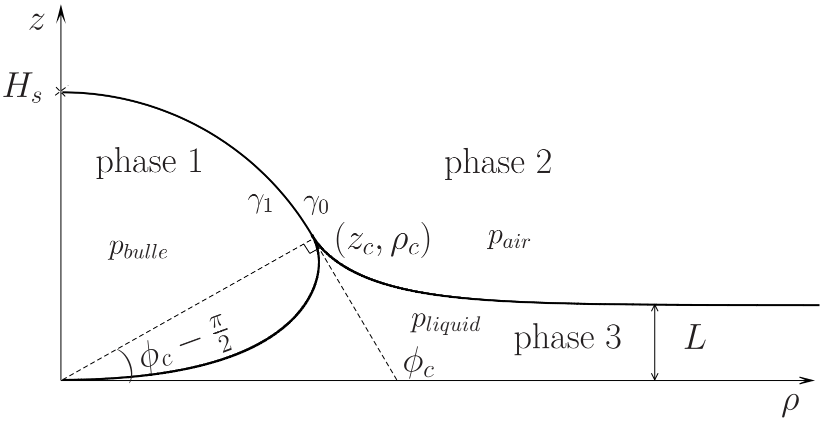

Figure B.1: Cylindrical coordinate system adopted in [1]to describe the bubble and free surface shapes for a three-phase (bubble, ambiant air, liquid) and axisymetric system.

At the lowest point of the bubble surface S_1, located on the z-axis, the bubble shape is approximated by a sphere with radius b and the liquid has pressure p_b. Thus, one has the relation

$$p_b = p_l + \frac{2}{b}\gamma_1 \tag{B.3}$$

Since the motionless liquid is subject to the uniform gravity field $\mathbf{g} = -g\mathbf{e}_z$, at any point in the liquid with coordinate z the pressure reads $p = p_l - \rho g z$. Combining (B.2) with (B.3) then yields

$$\frac{1}{R_1} + \frac{1}{R_2} = \frac{\rho g}{\gamma_1} + \frac{2}{b} \tag{B.4}$$

with the curvature radii R_1 and R_2 defined in Chapter 3 by the relation (3.5). Normalizing (B.4) with b and the Bond number $\mathrm{Bo}_p = \rho g b^2/\gamma_1$ then yields the announced link

$$\frac{1}{R_1/b} + \frac{\rho}{\sin\phi} = \frac{z}{b}\mathrm{Bo}_p + 2 \qquad \text{for } z < z_c, \rho < \rho_c \tag{B.5}$$

B.2 Bubble-free surface (contact area) interface equation

In the case of bubble-free surface interface, the pressure jump between the bubble-liquid interface and the free surface- air interface leads to the relations

$$p_{liquid} = p_{air} + 2\gamma_0\, H_1 \tag{B.6}$$
$$p_{bubble} = p_{liquid} + 2\gamma_1\, H_2 \tag{B.7}$$

Combining (B.6) and (B.7), one yields

$$2(H_1 - H_2)(\gamma_0 + \gamma_1) = p_{bubble} - p_{air} \tag{B.8}$$

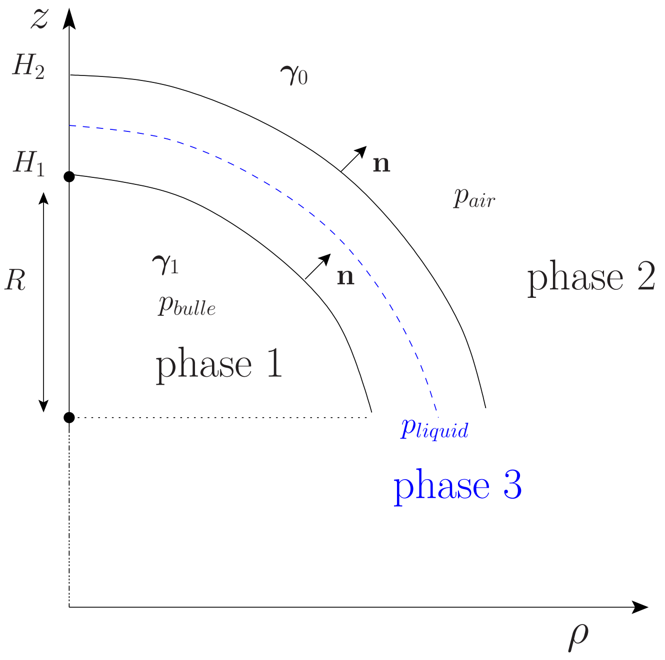

Figure B.2: Scheme of the bubble-free surface interfacial layer in the contact area.

This relation holds for the entire contact area (dashed line in Figure B.2) and at the top of the bubble, one has

$$2H_2(\gamma_0 + \gamma_1) = 2H_1(\gamma_0 + \gamma_1), \tag{B.9}$$

where $2H_1$ denotes the mean curvature at the bubble top. Approximating near its top the bubble shape with a sphere having radius R, one gets $H_1 = 1/R$. From (B.8) it follows that

$$\frac{2}{R} = \frac{1}{R_1} + \frac{1}{R_2} \tag{B.10}$$

One remarks that this relation is similar to (B.4) in which one sets $\rho = 0$ because of the equal densities on both sides of the film.

B.3 Bulk interface equation

B.3.1 Equation for the fluid interface shape

The free surface-liquid interface gives the two relations (see Figure B.1)

$$2H\gamma_0 = p'_{liq} - p_{air} \text{ for } \rho = \rho_c \ , \quad 2H\gamma_0 = p_{liq} - p_{air} \text{ for } \rho > \rho_c \tag{B.11}$$

Note that for large value of ρ, we have $p'_{liq} = p_{air}$ because the tail becomes flat far from the $z = 0$-axis. Normalizing (B.11), one has

$$\frac{b}{R_1} + \frac{b}{R_2} = \frac{\gamma_1}{\gamma_0} \, \mathrm{Bo}_p \, \frac{(z - L)}{b} \tag{B.12}$$

where $z = L$ is the asymptotic location of the tail far from the $z = 0$ axis.

B.3.2 Boundary condition to calculate the asymptotic value L

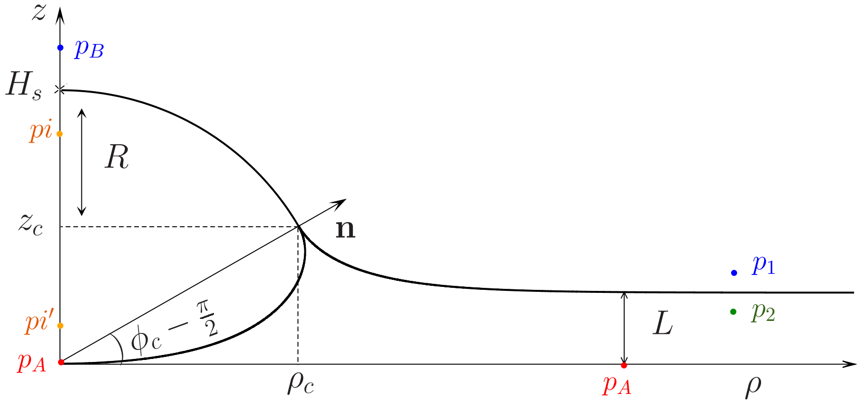

Figure B.3: Scheme of the bubble shape at a fluid interface in three-phase system

The bubble and free surface interfaces are motionless, then the pressure is constant in the ambient air and along the free surface implying $p_B = p_1$ (see in Figure B.3) since the ambiant gas has zero density. Therefore, the pressure on the $z = 0$-axis is $p_A = \rho g L + p_2$. In addition, the hydrostatics pressure inside the bubble can be expressed as follows

$$p_i' = p_A + \frac{2\gamma_1}{b} = \rho g L + p_2 + \frac{2\gamma_1}{b}, \tag{B.13}$$

$$p_i = p_B + \frac{2}{R}(\gamma_1 + \gamma_0) = p_2 + \frac{2}{R}(\gamma_1 + \gamma_0) \tag{B.14}$$

where $p_1 = p_2$ for large value of ρ. Since the pressure inside the bubble is constant, one has $p_i' = p_i$. Accordingly,

$$\rho g L + \frac{2\gamma_1}{b} = \frac{2}{R}(\gamma_1 + \gamma_0). \tag{B.15}$$

From (B.11), we obtain the following expression of L

$$\frac{L}{b} = \frac{2}{\mathrm{Bo}}\left[\frac{(1 + \gamma_0/\gamma_1)}{R/b} - 1\right]. \tag{B.16}$$

Bibliography

[1] H. M. Princen. Shape of a fluid drop at a liquid-liquid interface. *J. Colloid Interface Sci.*, 18:178–195, 1963.

Appendix C

Bipolar coordinates

Contents

C.1 Definition

The usual relations between the Cartesian coordinates (x, y, z) system and the cylindrical coordinates (ρ, ϕ, z) are

$$x = \rho \cos \phi, \qquad y = \rho \sin \phi. \tag{C.1}$$

As illustrated in Figure C.1 and in [2], the bipolar coordinates system (ζ, η, ϕ) is generated by the conform transformation

$$z + i\rho = ic \cot \frac{1}{2}(\eta + i\zeta), \tag{C.2}$$

with ζ real, $\eta \in [0, \pi]$, the real number $c > 0$ and i the imaginary unit number such that $i^2 = -1$ and $Im(i) = 1$. One then obtains the relations

$$z = \frac{c \sinh \zeta}{\cosh \zeta - \cos \eta}, \qquad \rho = \frac{c \sin \eta}{\cosh \zeta - \cos \eta}. \tag{C.3}$$

Each point of the space is then located using the coordinates (ζ, η, ϕ) with

$$0 \leq \eta \leq \pi, \qquad -\infty < \zeta < +\infty\,, \qquad 0 \leq \phi < 2\pi. \tag{C.4}$$

Eliminating η from (C.2), we obtain

$$(z - c \coth \zeta)^2 + \rho^2 = c^2 \operatorname{csch}^2 \zeta. \tag{C.5}$$

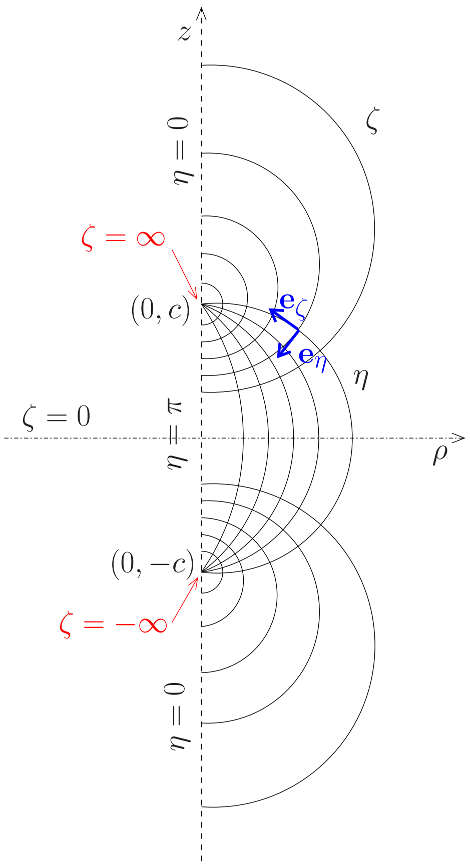

Figure C.1: Bipolar coordinates system in a meridian ($\phi = cst$) view.

Hence, the $\zeta = cte$ surfaces turn out to be a family of non-intersecting, coaxial spheres whose centers lie along the z axis. The $\zeta = \zeta_0$ sphere lies above the $z = 0$ plane for $\zeta_0 > 0$ and below for $\zeta_0 < 0$ while the $\zeta = 0$ surface is a sphere of infinite radius and then reduces to the $z = 0$ plane. For $\zeta = \pm\infty$ the sphere radius is zero, these values of ζ being the limiting points of the system and the corresponding surfaces reduce to the points $\rho = 0, z = \pm c$. For $\zeta = -\zeta_p$ with $\zeta_p > 0$, the associated sphere lies below the $z = 0$ plan and has radius $a = c \operatorname{csch} \zeta_p$ and center with cartesian coordinates $x = y = 0$ and $z = -c$. The distance l between the sphere center and the $z = 0$ plane therefore reads

$$l = c \coth \zeta_p. \tag{C.6}$$

Combining the previous expressions obtained for the radius a and the distance l, one gets the links (recalling here that $\zeta_p \geq 0$

$$\zeta_p = \cosh^{-1}\left(\frac{l}{a}\right) = \ln\left[\frac{l}{a} + \sqrt{\left(\frac{l}{a}\right)^2 - 1}\right], \tag{C.7}$$

$$c = a \sinh \zeta_p. \tag{C.8}$$

For $\phi = cst$, the $\eta = constant$ curves are arcs of circles having their centers on the $z = 0$ plane and their extremities are the limiting points $-c, +c$ of the system. The value of $\eta = 0$ corresponds to the two segments of the z-axis which lie above $z = +c$ and below

$z = -c$. The segment $]-c, +c[$ is for $\eta = \pi$ while $\eta = \pi/2$ gives the sphere with center $x = y = z = 0$ and radius c.

Setting the origin of the system at $\eta = \pi, \zeta = 0$, the distance r from this origin to a point having coordinates (ρ, ϕ, z) is

$$r = \sqrt{\rho^2 + z^2} = c \left(\frac{\cosh\zeta + \cos\eta}{\cosh\zeta - \cos\eta} \right)^{1/2}, \tag{C.9}$$

with $\cosh\zeta - \cos\eta \leq 0$. The value $r = \infty$ is reached only when $\cosh\zeta - \cos\eta = 0$, implying that $\zeta = \eta = 0$.

C.2 Vectors and metric coefficients

Since Bipolar coordinates are a right-handed system of orthogonal, curvilinear coordinates, its scale factors are

$$h_1 = h_2 = h = \frac{\cosh\zeta - \cos\eta}{c}, \qquad h_3 = \frac{\cosh\zeta - \cos\eta}{c \sin\eta}. \tag{C.10}$$

C.2.1 Transformation of partial derivatives

From the relation (A-6.3) in the Appendix of [1], the partial differential operators

$$\frac{\partial A}{\partial \rho} = \mathbf{e}_\rho \cdot \boldsymbol{\nabla} A \qquad \text{and} \qquad \frac{\partial A}{\partial z} = \mathbf{e}_z \cdot \boldsymbol{\nabla} A \tag{C.11}$$

are given by the relations

$$\frac{\partial A}{\partial \rho} = h^2 \left(\frac{\partial \rho}{\partial \eta} \frac{\partial A}{\partial \eta} + \frac{\partial \rho}{\partial \zeta} \frac{\partial A}{\partial \zeta} \right), \qquad \frac{\partial A}{\partial z} = h^2 \left(\frac{\partial z}{\partial \eta} \frac{\partial A}{\partial \eta} + \frac{\partial z}{\partial \zeta} \frac{\partial A}{\partial \zeta} \right). \tag{C.12}$$

C.2.2 Associated unit vectors and Jacobian

The unit vectors $(\mathbf{e}_\zeta, \mathbf{e}_\eta, \mathbf{e}_\phi)$ of the Bipolar coordinates system are related to the usual cylindrical unit vectors $(\mathbf{e}_\rho, \mathbf{e}_z, \mathbf{e}_\phi)$ using the following relations

$$\mathbf{e}_\zeta = h \left[\frac{\partial \rho}{\partial \eta} \mathbf{e}_\rho + \frac{\partial z}{\partial \eta} \mathbf{e}_z \right], \qquad \mathbf{e}_\eta = h \left[\frac{\partial \rho}{\partial \zeta} \mathbf{e}_\rho + \frac{\partial z}{\partial \zeta} \mathbf{e}_z \right], \qquad \mathbf{e}_\phi = \mathbf{e}_\phi. \tag{C.13}$$

Therefore, the unit vectors $(\mathbf{e}_\zeta, \mathbf{e}_\eta)$ are expressed in terms of the unit vectors relations $(\mathbf{e}_\rho, \mathbf{e}_z)$ as follows

$$\mathbf{e}_\zeta = -\frac{\sin\eta \sinh\zeta}{\cosh\zeta - \cos\eta} \mathbf{e}_\rho + \frac{1 - \cos\eta \cosh\zeta}{\cosh\zeta - \cos\eta} \mathbf{e}_z, \tag{C.14}$$

$$\mathbf{e}_\eta = -\frac{1 - \cos\eta \cosh\zeta}{\cosh\zeta - \cos\eta} \mathbf{e}_\rho - \frac{\sin\eta \sinh\zeta}{\cosh\zeta - \cos\eta} \mathbf{e}_z. \tag{C.15}$$

$$\tag{C.16}$$

The Jacobian J of the transformation $(\zeta, \eta, \phi) \to (\rho, \phi, z)$ is

$$J = \frac{\partial(\rho, z, \phi)}{\partial(\zeta, \eta, \phi)} = \frac{1}{h_1 h_2 h_3}. \tag{C.17}$$

By virtue of (C.10), one arrives at the useful relations

$$J = \frac{c^3 \sin\eta}{(\cosh\zeta - \cos\eta)^3}, \;\; d\Omega = J\, d\zeta d\eta d\phi = \frac{c^3 \sin\eta\, d\zeta d\eta d\phi}{(\cosh\zeta - \cos\eta)^3}, \tag{C.18}$$

where $d\Omega$ denotes the elementary volume $d\Omega = dxdydz$.

Bibliography

[1] J. Happel and H. Brenner. *Low Reynolds number hydrodynamics.* Martinus Nijhoff Publishers, The Hague, 1983.

[2] M. Stimson and G. B. Jeffery. The motion of two spheres in a viscous fluid. *Prod. R. Soc. London, Serie A*, 111:110–116, 1926.

Appendix D

Free surface shape functions using cylindrical coordinates

Contents

D.1 Solution to the homogenous differential equation

As seen in §4.3.2, the linear second-order differential equation governing the free surface shape function $f(\rho)$ is the following

$$\rho f''(\rho) + f'(\rho) - \rho t f(\rho) = R(\rho), \tag{D.1}$$

with $R = \rho[\mathbf{n}_0 \cdot \boldsymbol{\sigma}_0 \cdot \mathbf{n}_0]\,(z = 0)$ and $t = 12\mathrm{Bo}$ where $[\mathbf{n}_0 \cdot \boldsymbol{\sigma}_0 \cdot \mathbf{n}_0]\,(z = 0)$ is the normal stress component. Introducing a new function F such that $f(\rho) = F(\beta\rho)$ with $\beta > 0$ a constant, (D.1) also writes

$$\rho^2\beta^2\, F'' + \beta\rho\, F' - \rho^2 t F = R(\rho). \tag{D.2}$$

Setting $X = \beta\rho$, one obtains a second-order linear differential equation which reads

$$X^2\, F'' + X\, F' - X^2 \frac{t}{\beta^2}\, F = R(\rho). \tag{D.3}$$

Adopting $\beta = \sqrt{t}$ gives $t/\beta^2 = 1$. In that case, the homogeneous counter part of (D.3) becomes the usual Bessel differential equation admitting a general solution $F(\beta\rho)$ of the form

$$F(\sqrt{t}\rho) = A\, K_0(\sqrt{t}\rho) + B\, I_0(\sqrt{t}\rho) \tag{D.4}$$

where I_0 and K_0 designates the modified Bessel function of the first and second kind, respectively, given in [1].

D.2 The free surface shape function

The free surface shape function obeying (4.76)-(4.77) are here obtained. First, we give the general solution to the second-order differential equation

$$f''(\rho) + \frac{1}{\rho} f'(\rho) - t\, f(\rho) = \frac{R(\rho)}{\rho}. \tag{D.5}$$

To do so we employ the functions y_1 and y_2 such that $y_1 = K_0(\sqrt{t}\rho)$ and $y_2 = I_0(\sqrt{t}\rho)$. As seen in (D.1), such solutions obey the homogeneous counterpart of (D.5). Then the solution f to (D.5) is sought under the form $f = \lambda y_1 + \mu y_2$ with $\lambda = \lambda(\rho)$ and $\mu = \mu(\rho)$ two unknown functions such that

$$\lambda'\, y_1 + \mu'\, y_2 = 0, \quad \lambda'\, y_1' + \mu'\, y_2' = d(\rho). \tag{D.6}$$

In other words, the general solution f to (D.5) writes

$$f(\rho) = \lambda(\rho)\, K_0(\sqrt{t}\rho) + \mu(\rho)\, I_0(\sqrt{t}\rho) \tag{D.7}$$

where the function $\lambda(\rho)$ and $\mu(\rho)$ obeys

$$\lambda'(\rho)\, K_0(\sqrt{t}\rho) + \mu'(\rho)\; I_0(\sqrt{t}\rho) = 0, \tag{D.8}$$

$$\sqrt{t}\left(\lambda'(\rho)\, K_0'(\sqrt{t}\rho) + \mu'(\rho)\; I_0'(\sqrt{t}\rho)\right) = \frac{R(\rho)}{\rho}. \tag{D.9}$$

For further purpose, we introduce the Wronskian function as

$$W(\rho) = y_1(\rho)y_2'(\rho) - y_1'(\rho)y_2(\rho). \tag{D.10}$$

Because $K_0'(\rho) = -K_1(\rho)$ and $I_0'(\rho) = I_1(\rho)$, the Wronskian becomes

$$W(\rho) = \sqrt{t}\left\{I_1(\sqrt{t}\rho)K_0(\sqrt{t}\rho) + I_0(\sqrt{t}\rho)K_1(\sqrt{t}\rho)\right\}. \tag{D.11}$$

In addition, one has (see [1]) the property

$$I_0(u)K_1(u) + I_1(u)K_0(u) = \frac{1}{u}, \;\; u > 0. \tag{D.12}$$

Accordingly, one easily arrives at

$$W(\rho) = \frac{1}{\rho}. \tag{D.13}$$

Now we solve (D.8)-(D.9) to get the functions $\lambda(\rho)$ and $\mu(\rho)$. Combining (D.8)-(D.9) one immediately gets

$$\lambda'(\rho) = -I_0(\sqrt{t}\rho)\, R(\rho). \tag{D.14}$$

It follows that

$$\lambda(\rho) = -\int_0^\rho I_0(\sqrt{t}\, u)\, R(u)\, du + A \tag{D.15}$$

with A an arbitrary constant.

In a similar fashion, one also arrives at

$$\mu'(\rho) = K_0(\sqrt{t}\rho)\, R(\rho) \tag{D.16}$$

and the function $\mu(\rho)$ therefore takes the following form

$$\mu(\rho) = -\int_{\rho}^{\infty} K_0(\sqrt{t}\, u)\, R(u)\, du, +B \tag{D.17}$$

with B an arbitrary constant. In summary, the general solution to the second-order differential equation (D.1) is

$$\begin{aligned} f(\rho) = &\left[A - \int_0^{\rho} I_0(\sqrt{t}\, u)\, R(u)\, du\right] K_0(\sqrt{t}\rho) \\ &+ \left[B - \int_{\rho}^{\infty} K_0(\sqrt{t}\, u)\, R(u)\, du\right] I_0(\sqrt{t}\rho)\,. \end{aligned} \tag{D.18}$$

In a second step, the desired free surface shape function $f(\rho)$ is obtained by selecting in (D.18) the two unknown quantities A and B in order to ensure the two following boundary conditions

$$f'(\rho) = 0 \ \text{ for } \rho = 0, \ f(\rho) \to 0 \,\text{as}\, \rho \to \infty. \tag{D.19}$$

The modified Bessel functions satisfy, as $u \to 0$, $K_0(u) \sim -\ln u$, $I_0(u) \sim 1$. One then obtains $A = 0$. In addition, since $I_0(u) \sim e^u/u$ while $K_0(u) \sim e^{-u}/u$ as $u \to \infty$, one also arrives at $B = 0$. Accordingly (and as announced in Chapter 2) the free surface shape function $f(\rho)$ reads

$$f(\rho) = I_0(\sqrt{t}\rho) \int_{\rho}^{\infty} K_0(\sqrt{t}\, u)\, R(u)\, du - K_0(\sqrt{t}\rho) \int_0^{\rho} I_0(\sqrt{t}\, u)\, R(u)\, du \tag{D.20}$$

with $t = 12\mathrm{Bo}$ and $R(u) = u\sigma_{0\zeta\zeta}(u)$.

Bibliography

[1] M. Abramowitz and I. A. Stegun. *Handbook of mathematical functions.* Dover Publications, Inc., New York, 1965.

Appendix E

Solution to the linear problem for the bubble shape

In this Appendix we derive the solution ξ to the linear problem (4.127)-(4.129). Such a problem reads

$$2\xi \sin\theta + \frac{d}{d\theta}\left[\sin\theta \frac{d\xi}{d\theta}\right] = S(\theta)\sin\theta, \tag{E.1}$$

$$\int_0^\pi \xi(\theta)\sin\theta d\theta = \xi(\theta)\sin\theta\cos\theta d\theta = 0, \tag{E.2}$$

$$\frac{d\zeta}{d\theta} \text{ for } \theta = 0 \text{ and } \theta = \pi, \tag{E.3}$$

and we add the compatibility relations for the function $S(\theta)$

$$\int_0^\pi S(\theta)\sin\theta d\theta = 0, \ \int_0^\pi S(\theta)\sin\theta\cos\theta d\theta = 0. \tag{E.4}$$

We write $\xi = f\cos\theta$ and look at the function f. Setting $h = df/d\theta = f'$, the differential equation (E.1) yields

$$\sin 2\theta\, h' + (3\cos 2\theta - 1)\, h = 2\sin\theta\, S(\theta)\,. \tag{E.5}$$

The solution h is thus sought under the following form

$$h(\theta) = \frac{v(\theta)}{2\sin(\theta)\cos^2(\theta)} = \frac{v(\theta)}{\sin(2\theta)\cos(\theta)}. \tag{E.6}$$

Injecting (E.6) into (E.5) then gives

$$v'(\theta) = \frac{dv}{d\theta} = 2\sin\theta\cos(\theta)\, S(\theta)\,. \tag{E.7}$$

Accordingly,

$$v(\theta) = C + \int_0^\theta S(u)\cos(u)\sin(u)du \tag{E.8}$$

with C a constant to be later obtained. Therefore, one arrives at

$$h = f' = \frac{df}{d\theta} = \frac{C}{\sin(2\theta)\cos(\theta)} + \frac{1}{\sin(2\theta)\cos(\theta)}\int_0^\theta S(u)\cos(u)\sin(u)du. \tag{E.9}$$

Integrating over θ the relation (E.9) immediately gives the solution

$$\begin{aligned} f =& A + C\left[\frac{1}{\cos\theta} + \log\left(\tan(\theta/2)\right)\right] \\ &+ \left[\frac{1}{\cos\theta} + \log\left(\tan(\theta/2)\right)\right]\int_0^\theta \sin(u)\cos(u)\,S(u)\,du \\ &- \int_0^\theta\left[\frac{1}{\cos(t)} + \log(\tan(t/2))\right]\sin(t)\cos(t)\,S(t)\,dt\,. \end{aligned} \tag{E.10}$$

with A a second unknown constant.

Curtailing elementary manipulations, one finally gets

$$\begin{aligned} \xi(\theta) = f\cos\theta = A\cos\theta + C'\left[1+\cos\theta\log\left(\tan(\theta/2)\right)\right] \\ + \left[1+\cos\theta\log\left(\tan(\theta/2)\right)\right]\int_0^\theta \sin(u)\cos(u)\,S(u)\,du \\ - \cos\theta\int_0^\theta\left[1+\cos(t)\log(\tan(t/2))\right]\,\sin(t)\,S(t)\,dt\,. \end{aligned} \tag{E.11}$$

Because we require ξ to be bounded at $\theta = 0$ we have $C = 0$. Moreover ξ is also bounded at $\theta \to \pi$ whatever the constants A. Note that

$$\begin{aligned} \frac{d\xi}{d\theta} = \xi'(\theta) = -\,A\sin\theta + \left[\frac{\cos\theta}{\sin\theta} - \sin\theta\log\left(\tan(\theta/2)\right)\right]\int_0^\theta \sin(u)\cos(u)\,S(u)\,du \\ + \sin\theta\int_0^\theta\left[1+\cos(t)\log(\tan(t/2))\right]\,\sin(t)\,S(t)\,dt \end{aligned} \tag{E.12}$$

Inspecting (E.12) easily reveals that $\xi'(0) = 0$. In addition (E.12) also shows that

$$\xi'(\pi-\alpha) = +\frac{1}{\alpha}\left[\int_0^\pi \sin(t)\cos(t)\,S(t)\,dt\right] + \mathcal{O}(\alpha^2) \qquad \text{as } \alpha \to 0. \tag{E.13}$$

Accordingly, $\xi'(0) = 0$ at $\theta = \pi$ (as requested by (E.3)) as soon as the second compatibility conditions (E.4) holds.

In summary, the solution ξ writes

$$\begin{aligned} \xi(\theta) = A\cos\theta + \int_0^\theta \Big\{\left[1+\cos(\theta)\log(\tan(\theta/2))\right]\cos(u) \\ - \left[1+\cos(u)\log(\tan(u/2))\right]\cos\theta\Big\} S(u)\,\sin(u)\,du. \end{aligned} \tag{E.14}$$

By virtue of the first compatibility condition (E.4), this solution then satisfies the first condition (E.2). The second conditions (E.2) is enforced by adequately choosing the unknown constant A. One then arrives at the announced (see Chapter 4) solution

$$\xi(\theta) = -\frac{3}{2}\left[\int_0^\pi f_S(u)\cos(u)\sin(u)du\right]\cos\theta + f_S(\theta) \tag{E.15}$$

with function f_S depending upon the function S as follows

$$\begin{aligned} f_S(\theta) = \int_0^\theta \Big\{\left[1+\cos(\theta)\log(\tan(\theta/2))\right]\cos(u) \\ - \left[1+\cos(u)\log(\tan(u/2))\right]\cos\theta\Big\} S(u)\,\sin(u)\,du \end{aligned} \tag{E.16}$$

Appendix F

Expression of the zeroth-order stress and velocity components in bipolar coordinates

Contents

F.1 Expression of the zeroth-order velocity in bipolar coordinates

On the $\zeta = 0$ plane free surface and the $\zeta = -\zeta_p$ on the undisturbed bubble surface, one has $\mathbf{n}_0 = \mathbf{e}_\zeta$. Accordingly, the zeroth-order normal velocity component reads

$$[\mathbf{u}_0 \cdot \mathbf{n}_0]\,(\zeta, \eta) = \mathbf{u}_0 \cdot \mathbf{e}_\zeta\,(\zeta, \eta) = u_{0\zeta}(\zeta, \eta) \tag{F.1}$$

Moreover, the boundary condition on thesurface S_1 or solid sphere boundary Σ and on the free surface imply that

$$u_{0\zeta}(0, \eta) = 0 \quad \text{on } S_0' \text{ (free surface)}, \tag{F.2}$$

$$u_{0\zeta}(-\zeta_p, \eta) = U\,\mathbf{e}_z \cdot \mathbf{e}_\zeta \quad \text{on } S_1' \text{ (bubble)}, \tag{F.3}$$

$$u_{0\zeta}(-\zeta_p, \eta) + u_{0\eta}(-\zeta_p, \eta) = U\,\mathbf{e}_z \qquad \text{on } \Sigma \text{ (solid sphere)} \tag{F.4}$$

for a rigid bubble or solid sphere translating with velocity $\mathbf{U}\cdot\mathbf{e}_z$ where S_0' and S_1' denote the undisturbed free surface and bubble surface, respectively. The unit vector $\mathbf{e}_z$ is expressed in bipolar coordinates in terms of the local vectors $\mathbf{e}_\zeta$ and $\mathbf{e}_\eta$ on the $\zeta = -\zeta_p$ surface as

$$\mathbf{e}_z = \frac{(1 - \cosh\zeta_p\,\chi)}{(\cosh\zeta_p - \chi)}\,\mathbf{e}_\zeta - \frac{\sin\eta\,\sinh\zeta_p}{(\cosh\zeta_p - \chi)}\,\mathbf{e}_\eta \tag{F.5}$$

with $\chi = \cos\eta$ and $\eta \in [0, \pi]$. One then obtains the scalar product $\mathbf{e}_z \cdot \mathbf{e}_\zeta$ on the surface S'_1 or Σ as follows

$$\mathbf{e}_z \cdot \mathbf{e}^{nd}_\zeta = \frac{(1-\cosh\zeta_p\,\chi)}{(\cosh\zeta_p - \chi)}. \tag{F.6}$$

In summary, the zeroth-order normal velocity component are given by

$$u_{0\zeta}(0,\eta) = 0 \quad \text{on } S_0, \tag{F.7}$$

$$u_{0\zeta}(-\zeta_p,\eta) = U\,\frac{(1-\cosh\zeta_p\,\chi)}{(\cosh\zeta_p - \chi)} \quad \text{on } S_1, \tag{F.8}$$

$$u_{0\zeta}(-\zeta_p,\eta) = U\,\frac{(1-\cosh\zeta_p\,\chi)}{(\cosh\zeta_p - \chi)},\; u_{0\eta}(-\zeta_p,\eta) = -U\,\frac{\sin\eta\sinh\zeta_p\,\chi)}{(\cosh\zeta_p - \chi)} \quad \text{on } \Sigma. \tag{F.9}$$

The condition (F.8) is actually valid both for the solid sphere and the spherical bubble.

F.2 Zeroth-order stress tensor at the undisturbed free surface in terms of the Legendre polynomials.

Combining (4.41) and the stream function defined in Chapter §4.1, the quantity $u_{0\eta}(\zeta,\eta)$ is expressed using the Legendre polynomial $P_n(\chi)$

$$u_{\zeta\eta}(\zeta,\eta) = -\frac{(\cosh(\zeta)-\chi)^2}{c^2}\frac{\partial\psi}{\partial\chi} \tag{F.10}$$

with $\chi = \cos\eta$ and $\eta \in [0, \pi]$. The general expression of the stress tensor is

$$\boldsymbol{\sigma}_0 = -p_0\mathbf{I} + \mu\left(\boldsymbol{\nabla}\mathbf{u}_0 + \boldsymbol{\nabla}\mathbf{u}_0^T\right) \tag{F.11}$$

In getting (F.11), one needs the pressure p_0. It is gained by first expressing the pressure gradient in terms of the stream function $\psi(\zeta,\eta)$ (defined in Chapter §4.3) as

$$\frac{\partial p_0}{\partial\zeta} = -\frac{\mu(\cosh\zeta-\chi)}{c}\frac{\partial E^2(\psi)}{\partial\chi}, \tag{F.12}$$

$$\frac{\partial p_0}{\partial\eta} = -\frac{\mu(\cosh\zeta-\chi)}{c\sin\eta}\frac{\partial E^2(\psi)}{\partial\zeta} \tag{F.13}$$

where the harmonic operator E^2 is defined in Chapter §4.3. In addition, the pressure defined by [1] in bipolar coordinates writes

$$p_0(\zeta,\chi) = \frac{(\cosh\zeta-\chi)^{1/2}}{c^3}\sum_{n=0}^{\infty}\alpha_n\cosh[(n+\frac{1}{2})\zeta]\,P_n(\chi)\,, \tag{F.14}$$

with the coefficients α_n

$$\alpha_n = \sum_{n=1}^{n-1}\frac{(2m+1)b_m}{m(m+1)} + \frac{(2n+1)b_n}{n} + \alpha_0 \tag{F.15}$$

with by virtue of the velocity boundary conditions on the free surface, the relation

$$b_n = -(2n-1)B_n + (2n+3)D_n + \frac{2n(2n+3)}{2n+1}B_{n+1} - \frac{2(n-1)(2n-1)}{2n+1}D_{n-1}\,. \qquad \text{(F.16)}$$

Since the pressure vanishes far for the particle, the coefficient α_0 reads

$$\alpha_0 = -\lim_{n\to\infty}\left[\sum_{n=1}^{n-1}\frac{(2m+1)b_m}{m(m+1)} + \frac{(2n+1)b_n}{n}\right]. \qquad \text{(F.17)}$$

Furthemore, the components of the viscous part $\boldsymbol{\tau} = \mu\,(\boldsymbol{\nabla}\mathbf{u}_0 + \boldsymbol{\nabla}\mathbf{u}_0^T)$ of the stress tensor is expressed in terms of the stream function as follows

$$\tau_{\zeta\zeta}(\zeta,\chi) = 2\mu\, h\left(\frac{\partial u_\zeta}{\partial\zeta} + h\,\frac{\partial}{\partial\eta}\frac{1}{h}u_\eta\right), \quad \tau_{\eta\eta}(\zeta,\chi) = 2\mu\, h\left(\frac{\partial u_\eta}{\partial\eta} + h\,\frac{\partial}{\partial\zeta}\frac{1}{h}u_\zeta\right), \qquad \text{(F.18)}$$

$$\tau_{\zeta\eta}(\zeta,\chi) = \mu\left(\frac{\partial(h\,u_\zeta)}{\partial\eta} + \frac{\partial(h\,u_\eta)}{\partial\zeta}\right) \qquad \text{(F.19)}$$

with the scale factor $h = c/(\cosh\zeta - \cos\eta)$.

The previous relations are expresses in terms of the stream function $\psi(\zeta,\eta)$ as follows

$$\frac{\tau_{\zeta\zeta}}{\mu}(\zeta,\chi) = -2\frac{(\cosh\zeta-\chi)}{c^3}\left\{\frac{\partial}{\partial\zeta}\left[(\cosh\zeta-\chi)^2\frac{\partial\psi}{\partial\chi}\right] - (\cosh\zeta-\chi)^2\frac{\partial\psi}{\partial\zeta}\right\}, \qquad \text{(F.20)}$$

$$\frac{\tau_{\eta\eta}}{\mu}(\zeta,\chi) = -2\frac{(\cosh\zeta-\chi)^2}{c^3}\left\{(\cosh\zeta-\chi)\left[\sinh\zeta\frac{\partial\psi}{\partial\zeta} - \frac{\partial\psi}{\partial\chi\partial\zeta}\right] - 2\frac{\partial\psi}{\partial\chi}\right\}, \qquad \text{(F.21)}$$

$$\begin{aligned}\frac{\tau_{\zeta\eta}}{\mu}(\zeta,\chi) = \frac{\sigma_{0\zeta\eta}}{\mu}(\zeta,\eta) = \frac{(\cosh\zeta-\chi)^2}{(1-\chi)^{1/2}}\ &\left\{(1-\chi^2)\left[(\cosh\zeta-\chi)\frac{\partial^2\psi}{\partial\chi^2} - 3\frac{\partial\psi}{\partial\chi}\right]\right.\\ &\left.-\left[(\cosh\zeta-\chi)\frac{\partial^2\psi}{\partial\zeta^2} - 3\sinh\zeta\frac{\partial\psi}{\partial\zeta}\right]\right\}. \qquad \text{(F.22)}\end{aligned}$$

Appealing to the Legendre polynomial properties and using the previous general relations for the velocity and the needed stress tensor, the zeroth-order quantities on the $\zeta = 0$ free surface read

$$u_{0\eta}(0,\eta) = \frac{(1-\chi)(1+\chi)^{1/2}}{c^2}\sum_{n=1}^{\infty}\frac{2n+1}{n(n+1)}\,P_n'(\chi)\,U_n'(0) \qquad \text{(F.23)}$$

$$\begin{aligned}\tau_{0\zeta\zeta}(0,\eta) = \frac{(1-\chi)^{1/2}}{c^3}\sum_{n=0}^{\infty}P_n(\chi)\Big\{&(2n-1)\,U_{n-1}'(0) - 2(2n+1)U_n'(0)\\ &+ (2n+3)U_{n+1}'(0)\Big\} \qquad \text{(F.24)}\end{aligned}$$

Similarly, on the $\zeta = -\zeta_p$ undisturbed bubble surface, one gets

$$\begin{aligned}u_{0\eta}(-\zeta_p,\eta) = -\frac{(\cosh\zeta_p-\chi)^{-1/2}}{2\sin\eta\, c^3}\sum_{n=1}^{\infty}V_n(\chi)\Big\{&3\sinh\zeta_p U_n(\zeta_p)\\ &+ 2(\cosh\zeta_p-\chi)U_n''(\zeta_p)\Big\} \qquad \text{(F.25)}\end{aligned}$$

while the stress components write

$$\begin{aligned}\tau_{0\zeta\zeta}(-\zeta_p,\eta) = -\,\frac{(\cosh\zeta_p-\chi)^{-1/2}}{2\,c^3}\sum_{n=1}^{\infty}\Big\{&\sinh\zeta_p U_n(\zeta_p)\Big[2(\cosh\zeta_p-\chi)V_n'(\chi)\\ &- 3V_n(\chi)\Big] - 2(\cosh\zeta_p-\chi)U_n'(\zeta_p)\Big[V_n(\chi) + 2(\cosh\zeta_p-\chi)V_n'(\chi)\Big]\Big\} \qquad \text{(F.26)}\end{aligned}$$

Bibliography

[1] G. B. Jeffery. On a form of the solution of Laplace's Equation suitable for problems relating to two spheres. *Prod. R. Soc. London, serie A*, 87:109–120, 1912.

Résumé/Abstract

La thèse porte sur les interactions entre des bulles et/ou des particules solides situées à proximité de la frontière d'un liquide soumis à l'action de la pesanteur. Cette situation est notamment rencontrée pour les bains de verre liquide dans lesquels les bulles et les impuretés se concentrent sous l'action de la seule gravité au voisinage immédiat de la surface du verre. Ce travail étudie numériquement, dans le cadre des écoulements visqueux, l'évolution temporelle de la déformation de chaque interface (bulle(s) et surface du verre) et de l'épaisseur du film liquide entre deux surfaces proches (phénomène de drainage). Sur chaque interface interviennent des forces capillaires (mesurées par la tension de surface uniforme), des forces de pesanteur et enfin des forces visqueuses dues à l'écoulement. L'importance relative de ces efforts est mesurée par le nombre de Bond (comparant termes de gravité et termes capillaires) et le nombre capillaire (comparant termes visqueux et termes capillaires) qui pour nos particules d'inertie négligeable sont du même ordre de grandeur. L'influence des tensions de surface et du nombre de Bond a ainsi été mise en évidence et commentées dans les cas d'une seule bulle, de plusieurs bulles et enfin de bulles et de sphères solides.

Mots clés : Écoulement de Stokes, hydrodynamique de bulles, particules solides, éléments de frontières, nombre de Bond, tension de surface, élaboration du verre.

This thesis is devoted to the bubble(s) and solid particle(s) interactions near the surface of a liquid subject to gravity. Such case occurs during industrial glass process when bubbles and impurities, driven by gravity, gather below the surface of the liquid molten glass. The present work numerically investigates, in the viscous flow regime, the evolution in time of each interface (bubbles and molten glass surface) shape together with the thickness of the film occurring between two closes surfaces (drainage phenomenon). On each interface a competition takes place between different forces: the capillary one modeled by the interface uniform surface tension, the gravity one and the viscous one due to the liquid flow. The relative magnitude of these effects is estimated using the Bond number (comparing the gravity term to the capillary term) and the capillary number (comparing the viscous term to the capillary term) which are of the same order for particles with negligible inertia. The surface tension effect has been then quantified and discussed in a large range of Bond number for one bubble, several bubble(s) and clusters made of bubble(s) and solid particle(s).

Keywords : Stokes flow, bubbles, hydrodynamic, solid sphere, melting glass process, surface tension, boundary element method, 2D-axisymmetric, Bond number.